Scattering Properties of Jovian Cloud and Haze from Cassini Imaging Science Subsystem Limb-Darkening Observations

Doctor Thesis
博士論文

Scattering Properties of Jovian Cloud and Haze from Cassini Imaging Science Subsystem Limb-Darkening Observations

（Cassini ISS データを用いた 木星エアロゾルの散乱特性に関する研究）

東北大学
大学院理学研究科地球物理学専攻

Takao SATO
佐藤　隆雄

指導教員
笠羽　康正　教授

論文審査委員
岡野　章一　教授　(主査)
佐藤　毅彦　教授　(JAXA/ISAS)
村田　功　准教授　(環境科学研究科)
坂野井　健　准教授

平成 23 年

"Imagination is more important than knowledge.

For knowledge is limited to all we now know and understand,

while imagination embraces the entire world,

and all there ever will be to know and understand."

Albert Einstein (1879-1955)

Acknowledgments

I want to express gratitude to many people for their continuing supports. I can’t accomplish my study in the doctor’s course without their supports and encouragements.

I express my deepest gratitude to Professor Dr. Yasumasa Kasaba for his shrewd advices and extensive supports throughout the entire course of this study. When I am in trouble with my study, he gives me many pointed advices and the direction of my study.

I extend my gratitude to Professor Dr. Takehiko Satoh at the Institute of Space and Astronautical Science (ISAS) for his proper suggestions, meaningful discussions, and continuing encouragements. This study described in this thesis does not come to fruition without his collaboration.

In this study, I made use of the Cassini ISS images available at the NASA Planetary Data System (PDS) and the SPICE toolkit and kernels available at the Navigation and Ancillary Information Facility (NAIF). I am grateful to the Cassini ISS team for providing valuable data and express my appreciation to people involved in the NASA PDS and the NAIF. I wish to thank Dr. Robert West and Dr. Benjamin Knowles for their helpful discussions about data calibration.

I have been supported by a Grant-in-Aid for Scientific Research from the Japan Society for the Promotion of Science (JSPS) for three years of the doctor’s course.

I express my continuing gratitude to Professor Dr. Hitoshi Fujiwara now at Seikei University. His continuing supports and encouragements have been instrumental in the progress I have made in my study to date. Whenever I ask questions about my study, he always gives me many useful comments. I would like to express my appreciation to Dr. Isao Murata for his guidance and helpful comments in the laboratory. I express my sincere thanks and appreciation to Professor Dr. Yukihiro Takahashi now at Hokkaido University. Much is owned to him especially during the first days of my research. I am greatly obliged to Dr. Hiromu Nakagawa for his valuable suggestions and kindness since I belonged

to the laboratory.

I extend my deep thanks to all other staffs of C-group: Professor Dr. Shoichi Okano, Professor Dr. Takayuki Ono, Professor Dr. Takahiro Obara, Dr. Hiroaki Misawa, Dr. Takeshi Sakanoi, Dr. Atsushi Kumamoto, Dr. Naoki Terada, Dr. Fuminori Tsuchiya, and Dr. Yuto Katoh for their valuable comments and advices on my study.

I owe a lot to all members in the Planetary Atmosphere Physics Laboratory for their supports and encouragements in many ways. The time to spend with my colleagues is precious for me. Especially, I am deeply grateful to Dr. Naoya Hoshino, who joined the laboratory in the same year. Thanks to his encouragements and supports in not only research but also private life, I have enjoyed my campus life and manage to conduct my study. I am obliged to Ms. Yoshie Aizawa for helping my life in the laboratory. By her favor, I have been able to conduct my research with an easy mind.

Finally, needless to say, I would like to express my profound gratitude to my family for their moral and financial supports for nine years since I entered Tohoku University. There are no words to express how grateful I am for their continuous supports.

Takao SATO

Sendai, Miyagi, Japan

December, 2011

Abstract

For centuries, Jupiter has attracted the curiosity of humans by the varying shapes and colors of its cloud appearance. Jupiter is covered with dense clouds organized in two distinctly-different bands referred to as zones and belts. The appearance of these, as well as of small-scale features such as the Great Red Spot (GRS), is attributed to different vertical cloud structure and/or different optical and physical properties of atmospheric aerosols. Thus, baseline cloud models of Jupiter are important to quantitatively describe the spatial and temporal variations. Furthermore, the detailed knowledge about the vertical cloud structure and aerosols' properties lead to the understanding of the thermal balance of Jupiter. Such models have gradually been developed as theories have become more sophisticated, spacecrafts have sent more data back to the Earth, and laboratory measurements have accumulated. With respect to the scattering properties of aerosols which are essential to deduce the vertical distributions of aerosols, to the present, we have commonly applied two different scattering phase functions. One is the scattering phase functions (referred to as the Pioneer HG functions) described in the form of a double Henyey-Greenstein function that were derived by Tomasko et al. (1978) from the Pioneer 10 Imaging Photopolarimeter (IPP) data in red (640 nm) and blue (440 nm) channels over a wide range of solar phase angles. The other is the Mie scattering phase functions for NH_3 ice particles which are believed to compose the visible cloud layer. There are, however, several major problems that need to be overcome in both scattering phase functions. In the former case, they cannot provide any physical meanings such as the particle size and composition, and are not validated for other wavelengths. In the latter case, there are no detections of spectroscopic signatures of such small NH_3 ice particles.

This thesis provides new observational constraints on the scattering properties of aerosols in the Jovian upper troposphere and stratosphere. To achieve this objectives, we have analyzed new and high-quality imaging data during the Cassini flyby of Jupiter (October 2000–March 2001) by utilizing its onboard Imaging Science Subsystem (ISS). The Cassini data, covering a wide range of solar phase angles (0°–140°), provide the first opportunity to improve observationally-based scattering phase functions for the Jovian aerosols since Tomasko et al. (1978) derived those from the

Pioneer 10 data.

In this thesis, we present the analysis results of four sets of limb-darkening curves extracted along a bright zone (the South Tropical Zone: STrZ) and a dark belt (the north component of the South Equatorial Belt: SEBn) from Jovian images in CB2 (effective wavelength: 750 nm) and BL1 (effective wavelength: 455 nm). The selection of these regions and wavelengths allows us to directly compare our results to Tomasko et al.'s. There are three major advantages of the Cassini data sets used in this study over the Pioneer 10 data sets. First, the Cassini data sets were taken at a constant gain setting for all solar phase angles, which is theoretically free from unwanted photometric inconsistency due to cross-calibration of the data acquired at different settings like the Pioneer 10 data. Second, the transmission bandwidth of the Cassini ISS CB2 filter is so narrow that we can infer more monochromatic optical properties of aerosols, which is suitable for applying the Mie scattering theory, than the Pioneer 10 IPP red-channel data. Finally, the Cassini data sets have a better solar phase angle coverage with much smaller gap in solar phase angles (19°–54°) than the Pioneer 10 IPP's larger gap (34–109°), although the largest available solar phase angle of the Pioneer 10 data (150°) surpasses the Cassini data (140.1°) by 10 degrees.

To explain the solar phase angle behaviors of limb-darkening curves for each data set, we perform the radiative transfer calculations with a simple cloud model and the Mie scattering theory applied to scattering of aerosols (Type II-Mie model), and successfully derive the scattering properties of aerosols for all data sets.

From the results of our radiative transfer calculations, we find two important characteristics of cloud particles. One is the effective radius of cloud ($r_{\mathrm{eff,cloud}}$). The best-fit $r_{\mathrm{eff,cloud}}$ is obtained at two different values, depending on the wavelength (not on the region): $r_{\mathrm{eff,cloud}}$ = 0.3 μm in CB2 and $r_{\mathrm{eff,cloud}}$ = 0.2 μm in BL1. These values are in good agreement with those inferred from previous studies (Sromovsky and Fry, 2010a, 2010b) for the diffuse and ubiquitous layer of small particles in the upper troposphere as described in the synthesis works by West et al. (1986, 2004). The other is the real part of the refractive index of cloud ($n_{\mathrm{r,cloud}}$). The best-fit $n_{\mathrm{r,cloud}}$ for all data sets except for the CB2/SEBn data set ($n_{\mathrm{r,cloud}}$ = 1.8) show an identical value ($n_{\mathrm{r,cloud}}$ = 1.85). Such values of $n_{\mathrm{r,cloud}}$ are found to be significantly higher than experimental values of n_{r} for NH_3 ice particles (n_{r} ~ 1.4) measured by Martonchik et al. (1984). Thus, we conclude that the best-fit combination of $n_{\mathrm{r,cloud}}$ and $r_{\mathrm{eff,cloud}}$ would strongly suggest the idea that the abundant small particle population in the upper troposphere is not composed of pure NH_3 ice. This suggestion does not conflict with lack of spectrally identifiable ammonia clouds (SIACs) (Baines et al., 2002) and

source of the 3-μm absorption anomaly (Sromovsky and Fry, 2010a, 2010b) inferred from near-infrared spectra. What actually eliminates the spectral signature of NH_3 ice around the 3-μm wavelength, despite the fact that significant depletion of NH_3 vapor has been observed for pressure levels of visible cloud layer, is unclear at this moment. The high real refractive index obtained in this study may hint at the composition of cloud particles for further studies.

As described above, the scattering properties of cloud particles for both the STrZ and the SEBn are found to show much the same characteristics, which suggests that the cloud particles themselves are less likely to be related to the visual difference between the zones and belts. We find that only the single scattering albedo of cloud (ω_{cloud}) shows a remarkable difference between two regions (ω_{cloud} gets a higher value for the STrZ than that for the SEBn). Particles in cloud layer for the SEBn ($1-\omega_{\mathrm{cloud}}$ = 0.031) absorb about ten times as many photons as those for the STrZ ($1-\omega_{\mathrm{cloud}}$ = 0.0035) in BL1, while particles for the SEBn ($1-\omega_{\mathrm{cloud}}$ = 0.0068) absorb twice as many photons as those for the STrZ ($1-\omega_{\mathrm{cloud}}$ = 0.0032) in CB2. Thus, we conclude that only ω_{cloud} is one key parameter which causes the visual difference between the zones and belts. Our results support the idea proposed by West et al. (1986). Such difference in absorption would be likely to be due to chromophores (unknown coloring agents) since all of condensate clouds predicted from thermochemical equilibrium theory and photochemically produced stratospheric haze are white at visible wavelengths.

Although the optical and physical properties of the stratospheric haze are not well constrained, we also find several key characteristics of the stratospheric haze. First, the large haze particles ($r_{\mathrm{eff,haze}}$ = 0.5 μm) are found to improve the model's fit either for the near-limb points in most solar phase angles or for higher reflectivity seen at the two largest solar phase angles from the analysis of the CB2/STrZ data set. Second, the large value of the imaginary part of the refractive index ($n_{\mathrm{i,haze}} \geq$ 0.04) is required to reproduce the BL1/STrZ data set well. This requirement becomes less important for fitting the CB2/STrZ data set. Finally, the characteristic common to all data sets is that the stratospheric haze is optically thin (τ_{haze} = 0.06 even at the optically thickest case for the CB2/STrZ data set). Conversely, we find that there are a considerable gap in the value of τ_{haze} between ours and those deduced from previous studies in which the Pioneer HG functions were used to reproduce the ground-based photometric data (e.g., Satoh and Kawabata, 1992, 1994; Kuehn and Beebe, 1993).

On the basis of these results, we compare our best-fit Mie scattering phase functions for cloud obtained from all data sets with the Pioneer HG functions. The overall shapes of our Mie scattering phase functions are found to be much flatter than those of the Pioneer HG functions. Our Mie

scattering phase functions can reproduce the Pioneer 10 observations well. In contrast, the Pioneer HG function does not reproduce the Cassini ISS observations. This is attributed to the fact that their scattering phase function is under-constrained, primarily due to a considerable gap in observations for intermediate solar phase angles (34°–109°).

A set of our new Mie scattering phase functions has two advantages over the Pioneer HG functions:

(1) since the Cassini data do not have a large gap in solar phase angle, the new Mie scattering phase functions are better constrained;

(2) the Mie scattering phase function can easily be applied to different wavelengths.

With such characteristics, we now have a set of reliable baseline scattering phase functions that can be used to interpret the ever-changing appearance of Jovian clouds as changes of the vertical cloud structure and/or distribution of chromophores in the atmosphere.

Contents

List of Figures

List of Tables

Chapter 1

Introduction

In this chapter, we introduce the basic characteristics of Jupiter and its cloud appearance in **Section 1.1**. **Section 1.2** gives the current status of our knowledge about Jovian atmosphere which are mainly relevant to thermal structure, vertical distributions of clouds and haze, and their optical and physical properties. Outstanding problems to be revealed in this thesis are mentioned in **Section 1.3**. Finally, we present the objectives and outlines of this thesis in **Section 1.4**.

1.1. Jupiter overview

1.1.1. Basic characteristics of Jupiter

Jupiter, the fifth planet from the Sun, is the largest in our solar system and represents the jovian planets or so-called gas giants. The jovian planets include Saturn, Uranus, and Neptune as well, and are characterized by massive fluid envelopes with relatively small solid (rocky or icy) cores. The jovian planets are thought to be formed by capturing the primordial gas during the formation of the solar system, while the terrestrial planets were formed from a meager amount of refractory materials. Thus, the jovian planets are believed to retain more or less the bulk composition of the solar nebula. Because of the difference of their beginnings, the basic characteristics of these two types of planets are quite different from each other. The basic parameters of Jupiter and the Earth are compared in **Table 1.1**. For example, Jupiter is over 300 times more massive than the Earth and its radius is over ten times as larger. While the Earth's atmosphere is mainly composed of nitrogen (~78.1%) and oxygen (~21.0%), the atmospheric composition of Jupiter is primarily hydrogen (~86.0%) with a small portion of helium (~13.6%). Note that Venus and Mars have atmospheres of mostly carbon dioxide, better representing the atmosphere of terrestrial planets without biological alteration. As a

consequence of H_2 + He atmosphere, the overall density of Jupiter (= 1.33 g/cm^3) is little more than that of liquid water. Since Jupiter rotates faster than the Earth, its shape is noticeably oblate with the polar radius being ~6.5% less than the equatorial radius. Furthermore, Jupiter emits 1.67 times more radiation than it receives from the Sun, which indicates the existence of the substantial internal heat source and presumably vigorous convection. Conversely, in the case of the Earth, the power due to internal heat source is negligible compared with the power due to absorption of solar radiation. Of course, Jupiter has no topography, i.e., no continents or oceans.

Table 1.1. The basic parameters of Jupiter and the Earth.

Parameter	Jupiter	Earth
Physical properties		
Mass [kg]	1.8986×10^{27}	5.9736×10^{24}
Mean density [g/cm^3]	1.326	5.515
Rotational period	9h 55m 29.71s (System III)	23h 56m 3.1s
Equatorial surface gravity [m/s^2]	23.12 (at 1 bar)	9.78
Equatorial radius [km][a]	71492	6378.1
Polar radius [km]	66854	6356.8
Equilibrium radiating temperature [K]	110	255
Geometric albedo	0.52	0.367
Compositional information of atmosphere		
Volume mixing ratio [%][b]	H_2 (86.0), He (13.6), CH_4 (0.18), NH_3 (0.07)[c]	N_2 (78.08), O_2 (20.95), Ar (0.9), CO_2 (0.0345)
Mean molecular weight [g/mol][d]	2.32	28.95
Orbital characteristics		
Mean distance from the Sun [AU][e]	5.203	1.000
Sidereal orbital period [years]	11.9	1.0
Orbital eccentricity	0.048	0.017
Obliquity [degrees]	3.12[f]	23.45

Most data are taken from de Pater and Lissauer (2010).

a: The equatorial radii quoted refer to the 1 bar pressure level.

b:The volume mixing ratios of Jovian atmosphere are taken from Table 4.2 of Taylor et al. (2004).

c: The volume mixing ratios of H_2, He, and CH_4 are constant with altitude in the upper troposphere and the lower stratosphere. Such gases are well mixed in these regions. For NH_3, the volume mixing ratio decreases with increasing altitude. The observed vertical profiles of NH_3 volume mixing ratio are shown in **Figure 5.2**.

d: The mean molecular weights are calculated with the volume mixing ratios listed in the table.

e: 1 AU is one astronomical unit, the mean distance of the Earth from the Sun equals to 1.496×10^8 km.

f: It is expected that there is very little seasonal variation on Jupiter because of the small obliquity.

1.1.2. Jovian cloud appearance

Although the basic characteristics of Jupiter and the Earth are completely different from each other as discussed in **Section 1.1.1**, within the outermost skin surrounding the interior fluid envelope, we can find some atmospheric phenomena that are similar to those found in the Earth's troposphere and stratosphere. One of the important similarities is the existence of cloud. For centuries, Jupiter has attracted the curiosity of humans by the varying shapes and colors of its cloud appearance. The most salient features of Jovian cloud appearance are mainly classified into three groups: banded structures, ovals (vortices) as typified by the Great Red Spot (GRS) which is the largest and long-lived vortex in the atmosphere, and discrete storms. **Figure 1.1** shows the comparisons of Jovian cloud appearance in 1979 and 2000 taken by Voyager 2 and Cassini, respectively. In spite of a gap of 21 years between two images, the general banded structures appear to be stable. The bright and dark bands seen at visible wavelengths are traditionally called "zones" and "belts", respectively. **Figure 1.2** illustrates the Jovian traditional zonal nomenclature. These banded structures are also characterized by well-defined zonal wind at cloud top altitude as shown in **Figure 1.3**. The banded structures are roughly correlated with ~30 zonal winds and the zonal winds are strongest on boundaries between the zones and belts. In other words, the belts are regions where the latitudinal shear in the zonal winds is cyclonic, while the zones are anticyclonic regions. Although small changes in the zonal wind profile are seen at some latitudes, the stability of zonal wind is a remarkable feature of its atmosphere.

While the general banded structures of Jupiter appear to be stable with well-defined belts and zones, some bands (e.g., the South Equatorial Belt: SEB) have often changed dramatically with timescales ranging from days to years. Most recently, the most dramatic changes in appearance occurred in the SEB in 2009–2010. **Figure 1.4** shows the nominal dark and the faint states of the SEB on August 4, 2009 and on May 8, 2010, respectively.

The appearance of banded structures, as well as of small-scale features such as the GRS, is attributed to different vertical cloud structures and/or different optical and physical properties of atmospheric aerosols. Thus, baseline cloud models of Jupiter are important to quantitatively describe the spatial and temporal variations mentioned above. Such models have gradually been developed as theories have become more sophisticated, spacecrafts have sent more data back to the Earth, and laboratory measurements have accumulated. In next section, we introduce the current status of our knowledge with respect to the Jovian atmosphere.

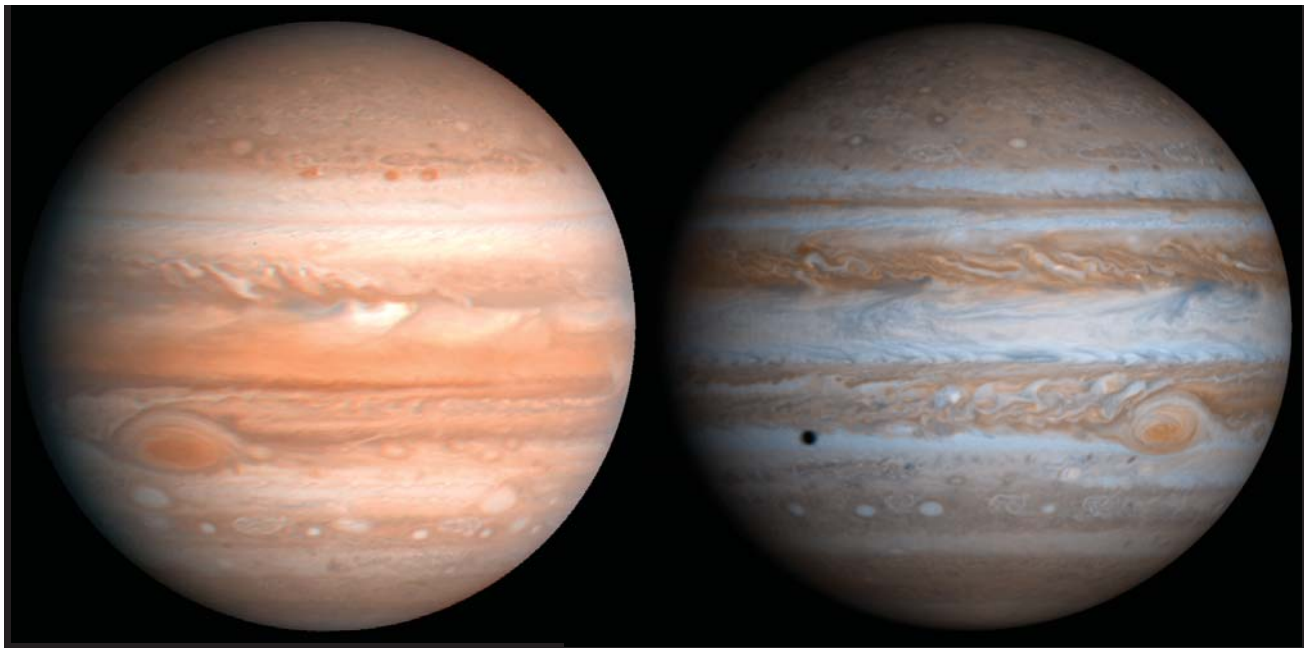

Figure 1.1. The comparison of the Jovian cloud appearance between 1979 and 2000. The left image was taken by Voyager 2 in June 1979 and the right image was taken by Cassini in November 2000. Although the overall shift and the contrast in color are attributable to the different instruments and the different processing methods, many real changes are apparent (from Ingersoll et al., 2004).

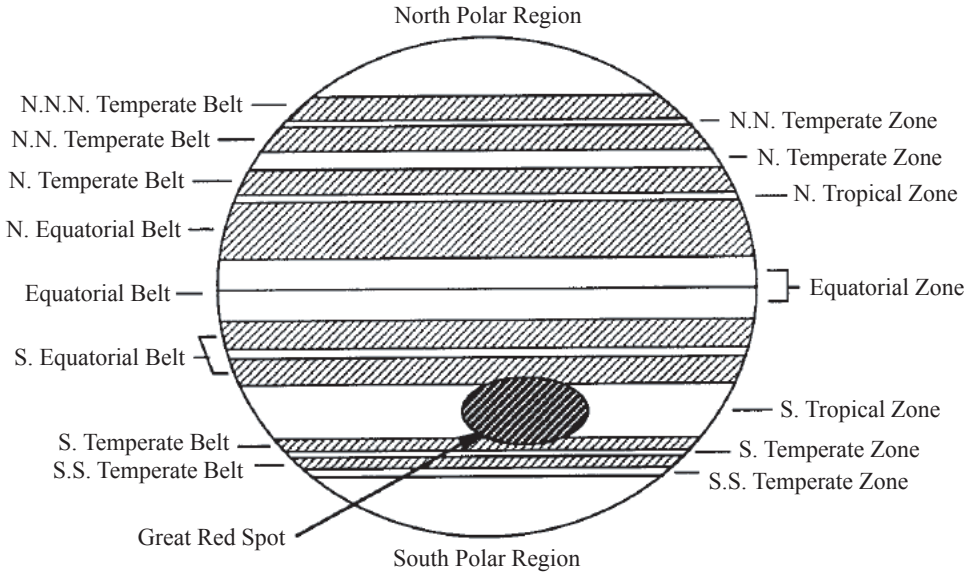

Figure 1.2. The typical Jovian zonal nomenclature. The shaded oval located in the South Tropical Zone is the Great Red Spot (GRS) (from Irwin, 1999).

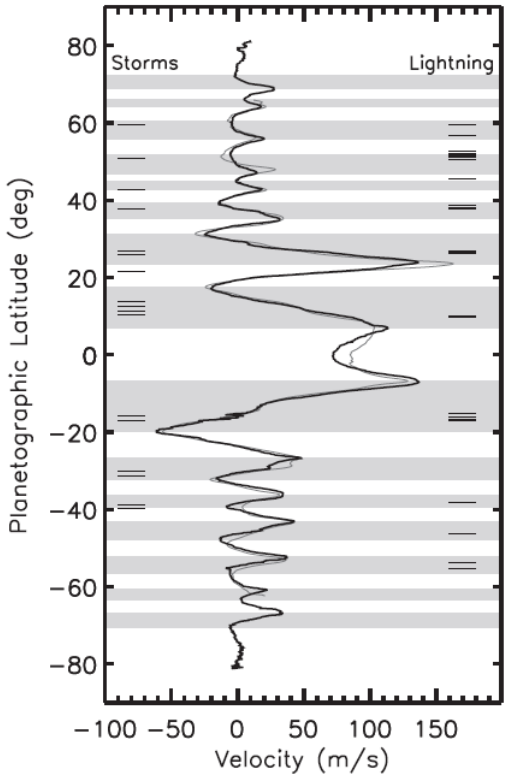

Figure 1.3. Zonal wind profiles vs. latitude in 1979 and 2000. The thick line shows the zonal wind speeds measured by Porco et al. (2003) from the Cassini images. The thin line shows those measured by Limaye (1986) from the Voyager 2 images. These profiles are remarkably similar to each other, although some changes (e.g., at 24° N) are apparent. Shaded (clear) bands mark regions of cyclonic (anticyclonic) shear in the zonal winds (from Vasavada and Showman, 2005).

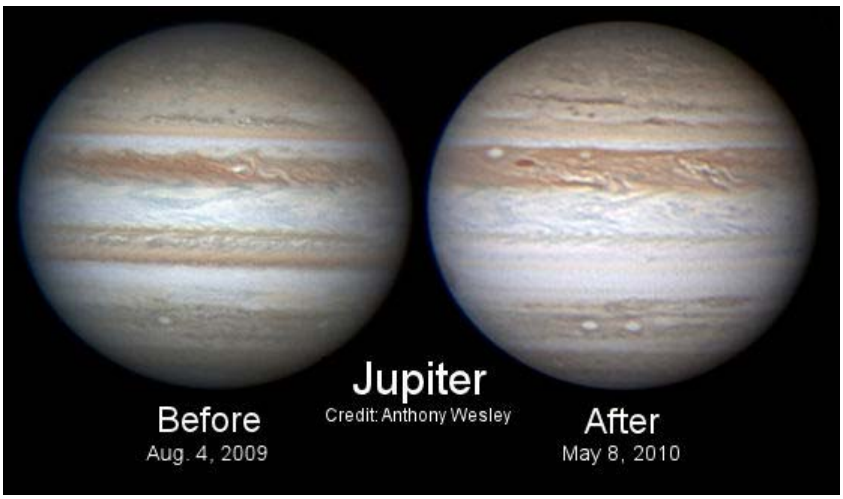

Figure 1.4. The nominal dark and the faint states of the SEB on August 4, 2009 and May 8, 2010, respectively (credit: Anthony Wesley).

1.2. The current status of our knowledge of Jovian atmosphere

1.2.1. Thermal structure

Our knowledge of thermal structure of the Jovian atmosphere comes from a number of observations: star occultations by Jupiter with ground-based telescopes, radio occultation and remote thermal measurements from the Voyager missions, and direct in-situ measurement from the Galileo entry probe. Lindal et al. (1981) showed that the Voyager radio occultation profiles at the South Equatorial Belt (SEB) and the Equatorial Zone (EZ) were quite similar and almost identical at pressures greater than 0.2 bar. Their results implied remarkable uniformity in the temperature field regardless different visual appearance between the zones and belts, while small horizontal temperature differences near 0.3 bar, of the order of a few Kelvin or less, were inferred from the Voyager Infrared Spectrometer (IRIS) measurements (Conrath et al., 1981; Flaser et al., 1981). Based on these data and the data from the Galileo entry probe (Seiff et al., 1998), the vertical structure of the atmosphere in the outer "observable" depth is classified into three regions; the stratosphere, the upper troposphere, and the lower troposphere. In the stratosphere ($p \leq 0.1$ bar), the atmosphere is completely stably stratified, no convection occurs and the thermal structure is determined by radiation balance. Thus, no condensation clouds are expected in this altitude, except for aerosols which are produced by photochemical reactions or by chemistry initiated by auroral particle impacts. In the upper troposphere ($0.1 \leq p \leq 0.6$ bar), the radiative process starts to dominate and the atmosphere appears to be stably stratified with dynamical overturning time constants on the order of a few days (Conrath et al., 1998). In the lower troposphere ($p \geq 0.6$ bar), the temperature profile appears to be close to adiabatic, implying active convection and existence of condensation clouds. A diagram of the Jovian thermal structure with definitions of the three main observable atmospheric regions is shown in **Figure 1.5**.

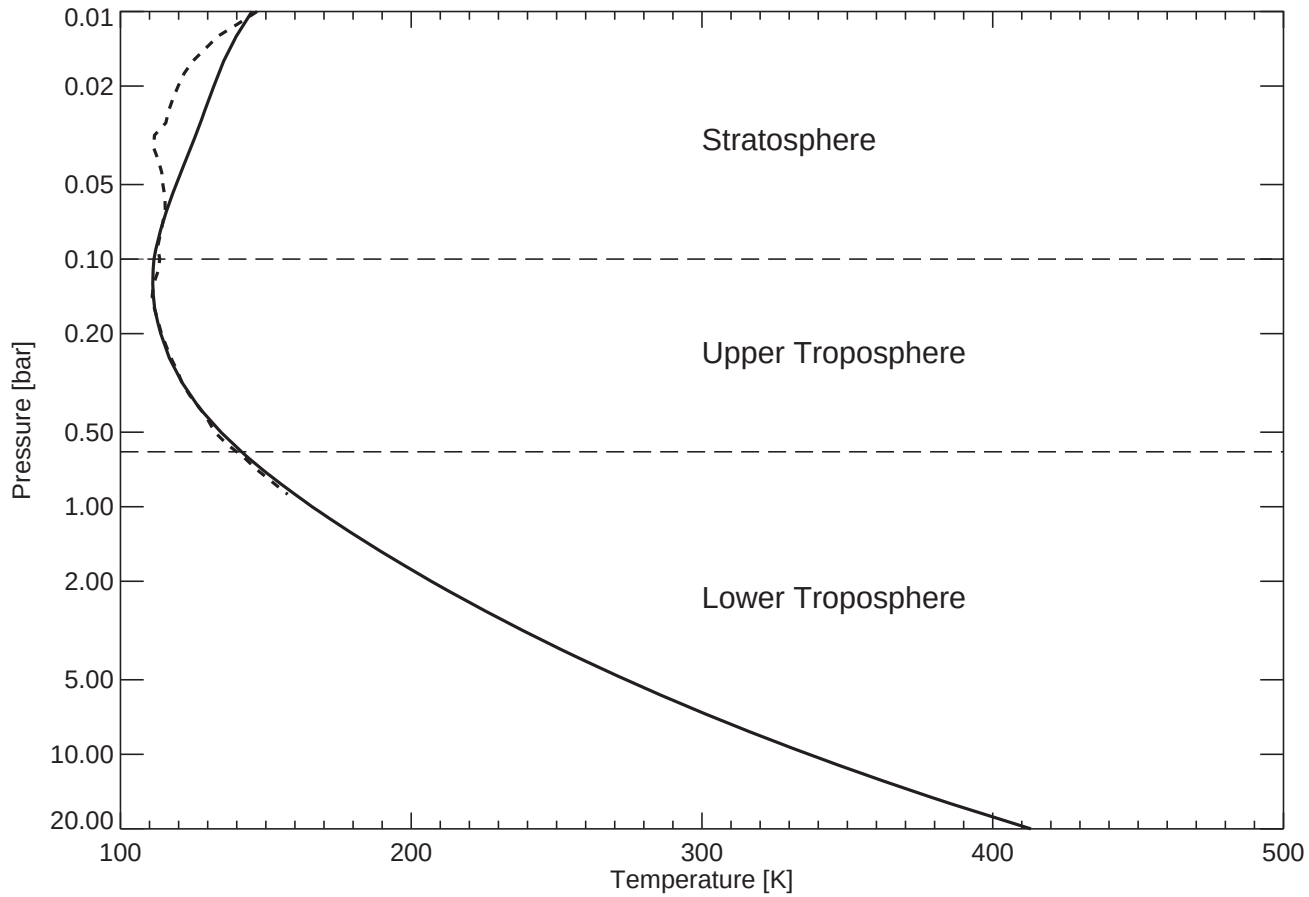

Figure 1.5. Jovian thermal structure, together with definitions of the three main atmospheric regions. Temperature profiles measured by the Galileo entry probe (Seiff et al., 1998) and the Voyager radio occultation (Lindal et al., 1981) are presented by solid and dashed curves, respectively.

1.2.2. Vertical distribution of clouds and haze in the troposphere

For decades, the vertical cloud structure of the Jovian atmosphere has been studied theoretically and observationally. The latter uses the imaging and spectroscopic data, such as those from spacecraft, those from Earth-orbiting telescopes, and those from the ground-based telescopes. An extensive review of the current knowledge about the Jovian cloud structure was summarized by West et al. (1986) for theory and observational results from Pioneer, Voyager, and ground-based telescopes prior to 1986 and by West et al. (2004) for theory and observational results mainly from Galileo and Cassini prior to 2004. In this section, we present only a brief summary of key theoretical and observational constraints.

Our first knowledge of the Jovian cloud structure (the composition and the vertical location) was provided by modeling studies based on thermochemical equilibrium theory (Lewis, 1969 and Weidenschilling and Lewis, 1973). Assuming that the bulk mixing ratio of the Jovian atmosphere was the solar composition, they predicted that there were three layers of condensate clouds: a water-ammonia (H_2O-NH_3) solution cloud with a base near 6 bar, an ammonia hydrosulfide (NH_4SH) cloud with a base near 2 bar, and an ammonia (NH_3) ice cloud with a base near 0.7 bar. Thereafter, Atreya et al. (1999) proposed a model with a different bulk mixing ratio (three times the solar composition) by referring to the latest observational results. The same three condensate cloud layers were found at slightly different pressure levels. The left panel of **Figure 1.6** shows the expected vertical cloud structures for various assumptions about the mixing ratios of condensable species relative to solar composition (Atreya et al., 2005). These fundamental studies have motivated researchers to confirm the existence of three predicted cloud layers and to understand the thermal balance of Jupiter by analyzing remote imaging and spectroscopy with the aid of radiative transfer calculations.

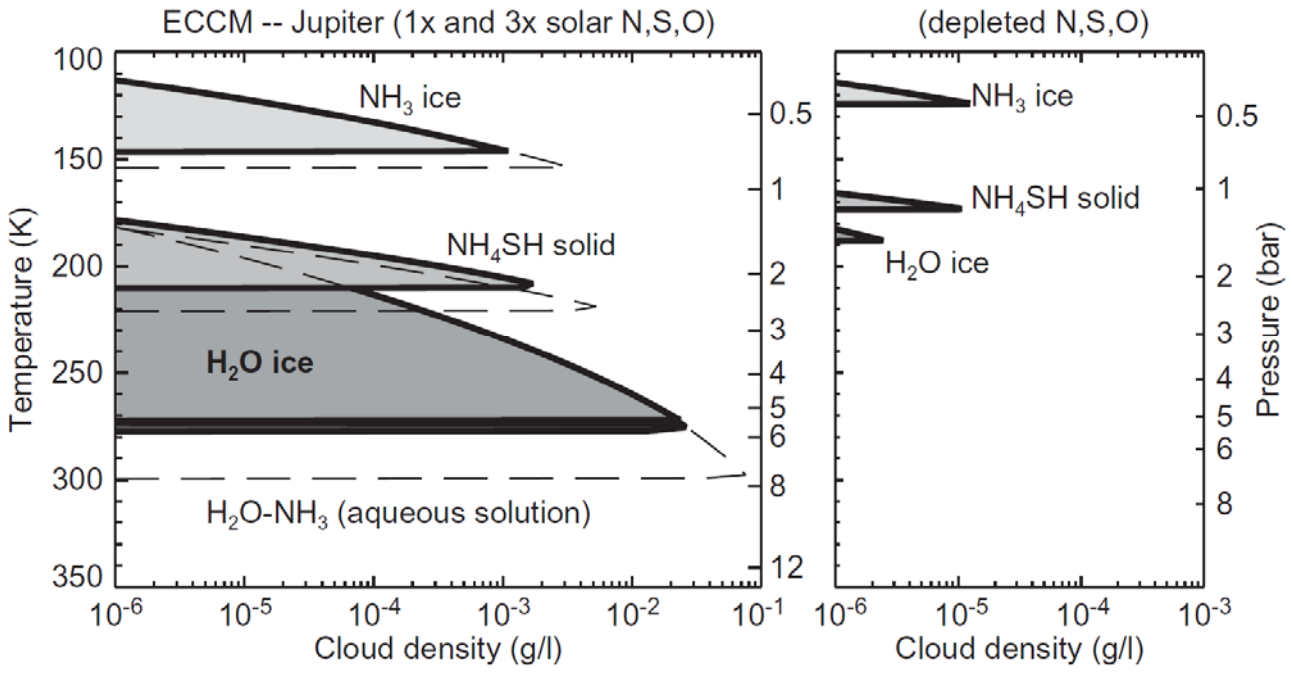

Figure 1.6. The results of the equilibrium cloud condensation model (ECCM) for different bulk mixing ratios. (Left panel) the condensable volatile abundances were taken at 1 × solar (solid area) and 3 × solar (dashed lines) compositions. (Right panel) the depleted condensable volatile abundances relative to solar: H_2O: 0.01%; NH_3: 1%; H_2S: 0.5% (from Atreya et al., 2005).

Analyses of spacecraft (Pioneer, Voyager, Galileo, and Cassini) data along with the Hubble Space Telescope (HST) and ground-based data have steadily revealed the vertical cloud structure in the troposphere. The current view of tropospheric cloud structure is depicted in **Figure 1.7**. The main characteristics are as follows:

- The upper tropospheric haze layer (indicated by circles in **Figure 1.7**) populated by sub-micron particles (r ~ 0.5 μm) ubiquitously covers all latitudes, extending in the pressure range 0.2–0.5 bar. Its optical thickness at visible wavelengths is between 2 and 10, depending on latitude. The effective cloud top pressure level (see **Figure 1.7**) varies from ~0.2 bar above the equator and the GRS to ~0.3 bar at ±10° latitudes. The upper tropospheric haze likely consists of NH_3 ice particles with some chromophores (unknown coloring agents). This haze accounts for limb-darkening curves obtained from methane (CH_4) band photometry (e.g., West, 1979; West and Tomasko, 1980; Satoh and Kawabata, 1992, 1994; Kuehn and Beebe, 1993) and for scattering phase functions inferred from the Pioneer 10 Imaging Photopolarimeter (IPP) photometric measurements (Tomasko et al., 1978), which is described in detail in **Section 1.2.3**. The main difference between the zones and belts at visible wavelengths has been explained by the decreased continuum single scattering albedo in the belts which may reflect a greater concentration of chromophores there or a mechanism, such as sublimation of NH_3 ice mantles, which increases chromophore visibility in the belts.
- A vertically compact cloud layer populated by large particles (r ~ 3–100 μm) is located near NH_3 condensation level (~0.7 bar), which is denser in zones than in belts. This cloud is needed to account for cloud opacity inferred from the Voyager IRIS spectra at 45 μm wavelength (Gierasch et al., 1986). This cloud is in partial responsible for modulation of 5-μm thermal radiation. Banfield et al. (1998) analyzed the small-scale (~30 km) cloud features obtained by the Galileo Solid State Imager (SSI) and concluded that the contrast of these features were mainly caused by optical thickness variations of tropospheric cloud near 0.75±0.25 bar.
- An inhomogeneous cloud layer is located near 2 bar. This cloud is probably composed of NH_4SH. The variability of this cloud layer accounts for the large variations in cloud opacity seen at 5 μm. Irwin et al. (1998) concluded, from analysis of the Galileo Near Infrared Mapping Spectrometer (NIMS) spectra (0.7–5.2 μm), that large particles of the NH_4SH near 1.4 bar were responsible for the main 5-μm cloud opacity.
- There is almost no observational evidence for a deep water cloud, although such cloud is pictured in **Figure 1.7**. It is difficult or impossible to retrieve this cloud in regions where the

overlying clouds are optically thick (i.e., zones). Lightning discovered by Galileo (Little et al., 1999; Gierasch et al., 2000) and Cassini (Dyudina et al., 2004) would give a clue to detection of water clouds by analogy with lightning on the Earth's atmosphere.

- The first and the only in-situ observations of the clouds in the Jovian atmosphere were conducted by the Galileo entry probe at a location of 6.5°N, 4.9°W (Young, 1998). During descent, the instruments on board the probe directly investigated composition, cloud properties, thermal structure, and radiative energy balance. Since the probe entered an unrepresentative "5-μm hot spot", which had abnormally low cloud and a low abundance of volatiles, the Nephelometer and the Net Flux Radiometer detected unexpectedly very tenuous clouds (Ragent et al., 1998; Sromovsky et al., 1998). These cloud altitudes were much higher than those expected from the theoretical models (ECCM) as shown in the left panel of **Figure 1.6**. Such tenuous cloud structure was also modeled by Atreya et al. (1997) (the right panel of **Figure 1.6**). A series of odd observations have been interpreted either as regions of extremely rapid downdraft or as a part of an atmospheric wave system, where the air column is vertically stretched and compressed with the hotspots occurring at the stretching phase.

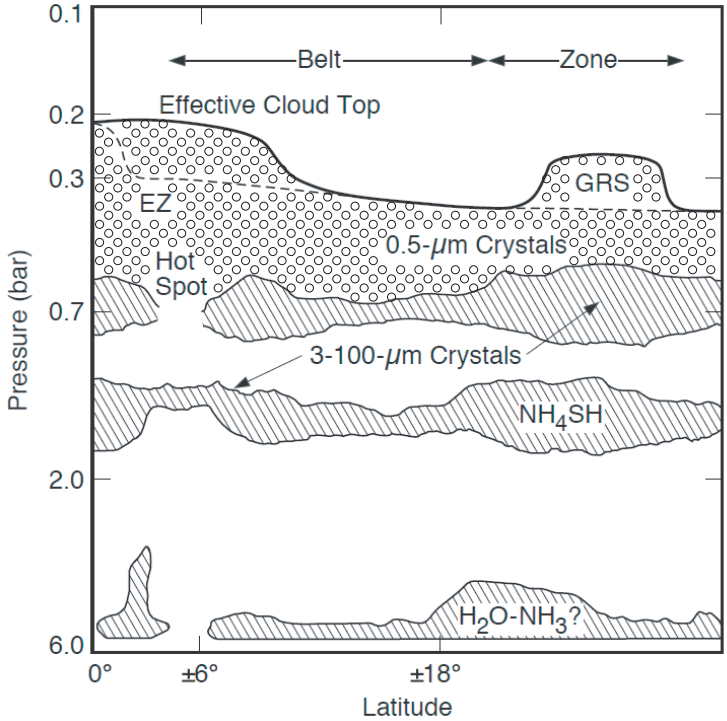

Figure 1.7. The schematic representation illustrating the current ideas about tropospheric cloud structure gathered from a large collection of observations after the Cassini encounter (from West et al., 2004). The effective cloud top pressure levels in the south and north hemispheres are represented by solid and dashed curves, respectively. The main characteristics of tropospheric cloud structure are summarized in text.

1.2.3. Optical and physical properties of tropospheric clouds and haze

In general, knowledge of the optical properties (scattering phase function, polarization, and absorption and scattering cross sections) of aerosols is indispensable not only to estimate the size, shape, and composition of aerosols, but also to infer the vertical cloud structure (molecular abundance, as well) from any remote sensing data. Furthermore, these information leads to the understanding of the thermal balance of Jupiter. Such knowledge, of course, can only be obtained through observations of the planet at a wide variety of illumination conditions (solar phase angles). However, the solar phase angle of Jupiter accessible from ground-based and Earth-orbit telescopes is always smaller than ~12°. The Pioneer 10 IPP (hereafter referred to as P10/IPP) provided photometric measurements at large solar phase angles (12°–150°), for the first time, during its Jupiter encounter in 1973. Tomasko et al. (1978) analyzed the P10/IPP data for two regions: a bright zone (the South Tropical Zone: STrZ) and a dark belt (the north component of the South Equatorial Belt: SEBn), in two colors: red (640 nm) and blue (440 nm). They derived the scattering phase functions of tropospheric aerosols for these regions (hereafter referred to as the Pioneer HG functions) in the form of a double Henyey-Greenstein function:

$$P_{\mathrm{DHG}}(f, g_1, g_2, \Theta) = f \cdot P_{\mathrm{HG}}(g_1, \Theta) + (1 - f) \cdot P_{\mathrm{HG}}(g_2, \Theta), \tag{1.1}$$

and

$$P_{\mathrm{HG}}(g, \Theta) = \frac{1 - g^2}{(1 + g^2 - 2g\cos\Theta)^{\frac{3}{2}}}, \tag{1.2}$$

where Θ is the scattering angle, f $(0 \leq f \leq 1)$ is the fraction of forward scattering, and g is the asymmetry factor, $P_{\mathrm{HG}}(g, \Theta)$ is more forwardly (backwardly) scattering if g is positive (negative), and becomes an isotropic scattering if g is zero. They also derived the scattering phase functions of stratospheric haze for these regions with a single Henyey-Greenstein function, although the shapes of the functions were not very well constrained. The best fit values of parameters g_1, g_2, f for tropospheric aerosols and stratospheric haze in the STrZ and SEBn at two wavelengths are given in **Table 1.2**. The Pioneer HG functions are also depicted in **Figure 1.8**.

Doose et al. (1986) extended Tomasko et al.'s analyses to other latitudes and concluded that the scattering phase functions of aerosols in mid-latitudes were very similar to those for the STrZ and SEBn derived by Tomasko et al. (1978), except at high latitudes where a population of particles having a measurably different scattering phase functions were apparent.

Table 1.2. The best fit parameters of double Henyey-Greenstein functions for tropospheric aerosols and single Henyey-Greenstein functions for stratospheric haze in two regions at two wavelengths (Tomasko et al., 1978).

Region	Blue (440 nm)				Red (640 nm)			
	g_1	g_2	f	ω^*	g_1	g_2	f	ω^*
STrZ	0.80	–0.80	0.969	0.995	0.80	–0.70	0.938	0.997
SEBn	0.80	–0.75	0.979	0.970	0.80	–0.65	0.938	0.991
Stratosphere	0.75	0.0	1.0	0.995	0.75	0.0	1.0	0.95

* ω stands for single scattering albedo.

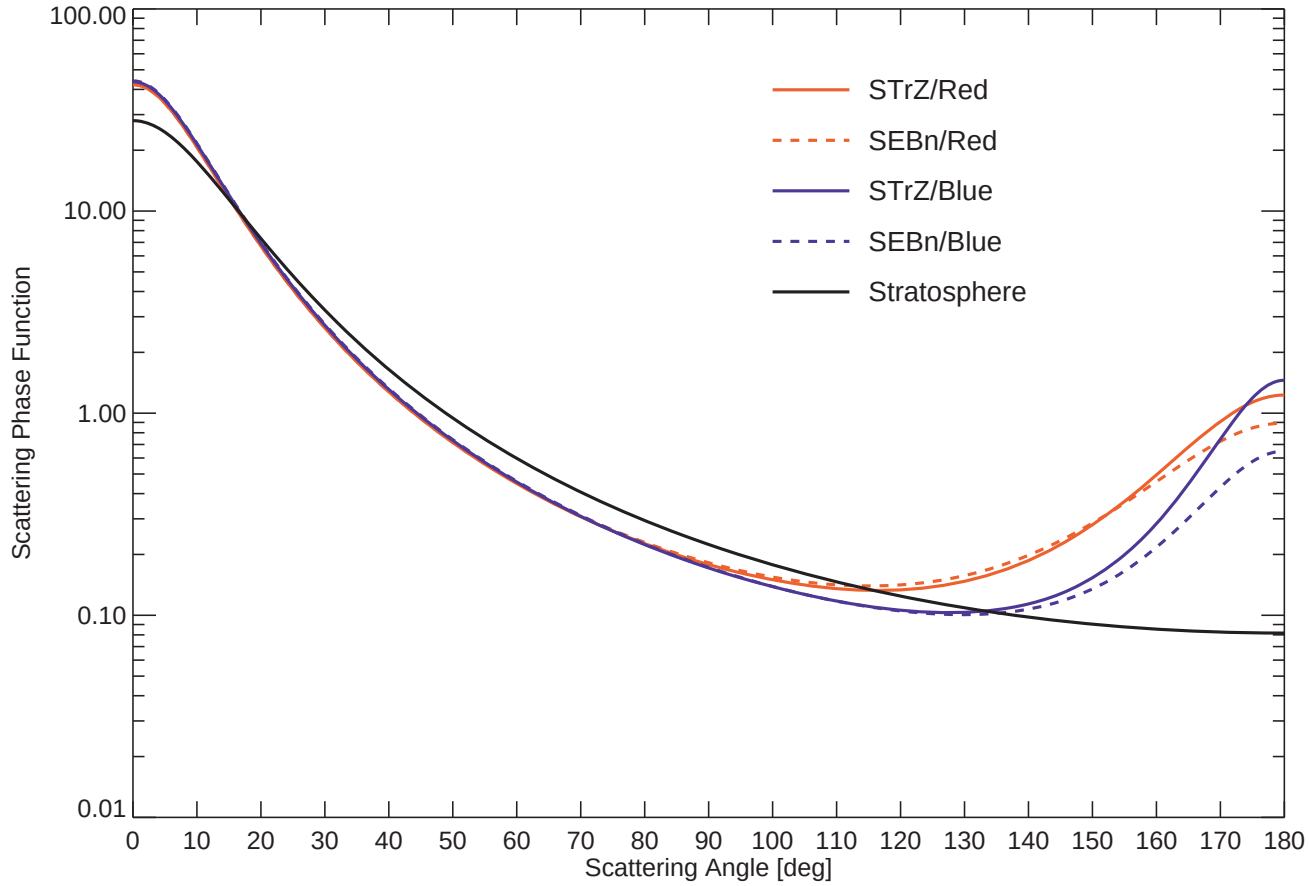

Figure 1.8. The scattering phase functions for tropospheric aerosols and stratospheric haze in the STrZ and the SEBn at blue- and red-channels deduced from the Pioneer 10 IPP data (Tomasko et al., 1978).

Aside from the above observational constraints, Martonchik et al. (1984) provided, from the laboratory measurements, the complex refractive index (n_r, n_i) for NH_3 ice in the cubic phase covering a wide spectral range, 50–71,000 cm^{-1} (0.14–200 μm). Pope et al. (1992) reported laboratory-measured scattering phase functions of NH_3 ice that, to a certain degree, resembled the Pioneer HG functions and could be simulated by Mie scattering with Martonchik et al.'s refractive index for NH_3 ice. Thus, these fundamental studies seem to have confirmed the validity of the Pioneer HG functions and to justify the use of either the Pioneer HG functions or Mie scattering phase functions for NH_3 ice, as "a priori" knowledge, to interpret the photometric data acquired at small solar phase angles. The Pioneer HG functions were commonly used in the analyses of ground-based data (e.g., West, 1979; West and Tomasko, 1980; Satoh and Kawabata, 1992, 1994; Kuehn and Beebe, 1993) and the data from the HST (Chanover et al., 1997; Sromovsky and Fry, 2002), while some researchers used the Mie scattering phase functions for NH_3 ice particles (e.g., Banfield et al., 1998; Simon-Miller et al., 2001).

There has been, however, a conflict between the theoretical predictions and the observations. Until the last decade, there were no detections of spectroscopic signatures indicating any condensate clouds as expected from thermochemical models. The first spectral indication of these clouds was made by Brooke et al. (1998). They analyzed the spatially averaged spectra in 2.7–3.2 μm region with moderate spectral resolution obtained by the Infrared Space Observatory (ISO) and concluded that large particles (~10 μm) of NH_3 ice were needed to reproduce the broad and shallow absorption seen in the spectra. Irwin et al. (2001) found a similar absorption anomaly near 3 μm in the Galileo NIMS spectra, but pointed out that large NH_3 ice particles would introduce additional features in other parts of infrared spectra that were not evident in existing data. Baines et al. (2002) showed, from the Galileo NIMS data, that spectrally identifiable ammonia clouds (SIACs) were associated with strong vertical uplifts as shown in **Figure 1.9** and covered only <1% of the globe. Conversely, Wong et al. (2004) found a more widespread distribution of NH_3 ice, at least in some latitude bands, from the thermal infrared (9.4 μm) spectra obtained by the Cassini Composite Infrared Spectrometer (CIRS), but only if the particles were assumed to be nonspherical. More recently, Sromovsky and Fry (2010a) reanalyzed the ISO spectra with new NH_3 gas absorption models and showed that large particles (~15 μm) of NH_4SH, not NH_3 ice, were mainly responsible for the 3-μm absorption feature. Sromovsky and Fry (2010b) found that 3-μm absorption anomaly were widely distributed on Jupiter from spatially-resolved Cassini Visual Infrared Mapping Spectrometer (VIMS) data (**Figure 1.10**) and made a similar conclusion with Sromovsky and Fry (2010a).

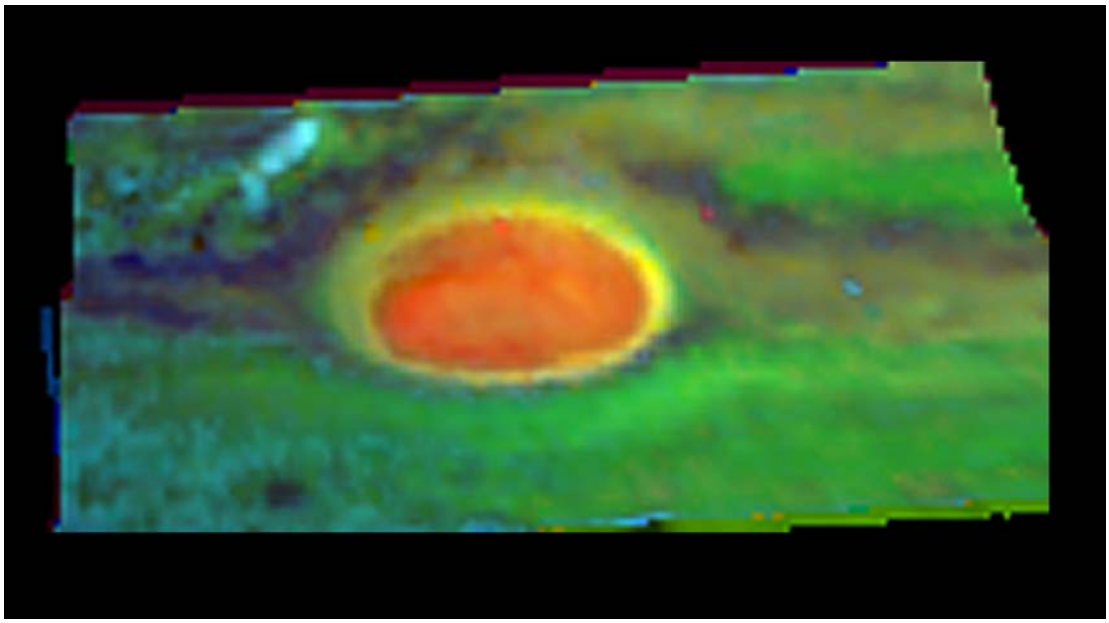

Figure 1.9. False color image of the GRS constructed from near-infrared data obtained by the Galileo NIMS. Reddish-orange areas show region of high-level clouds, yellow areas depict mid-level clouds, and green areas depict lower-level clouds. The darker areas are cloud-free regions. The light blue region to the north-west of the GRS has been identified as middle-to-high level ammonia pure ice clouds (from Baines et al., 2002).

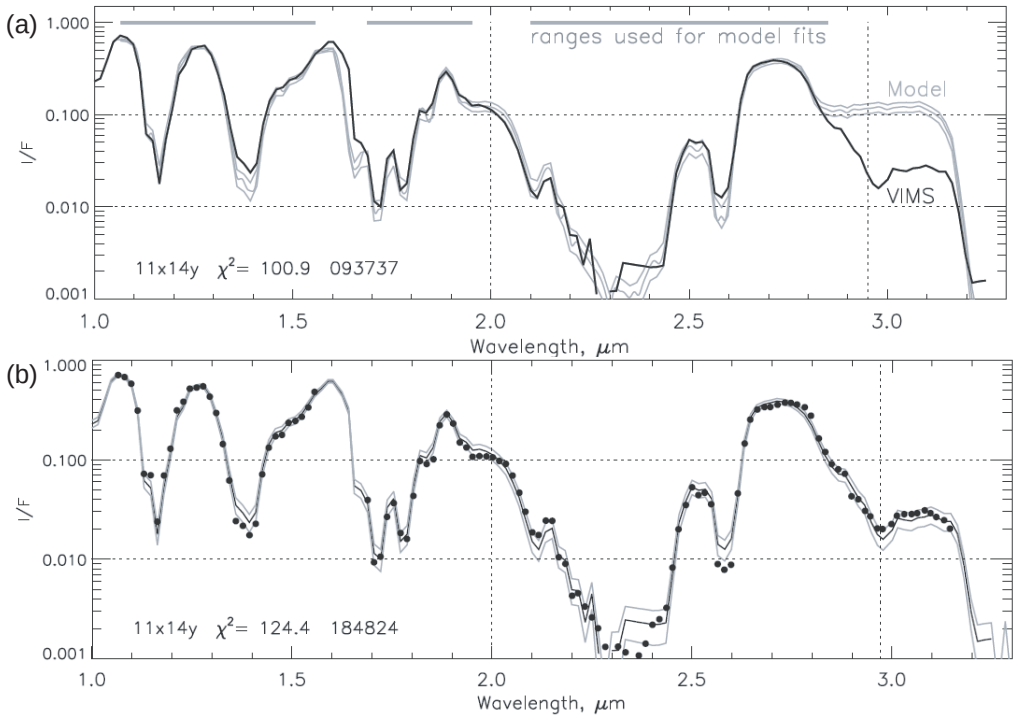

Figure 1.10. The 3-μm absorption anomaly from the Cassini VIMS spectra at low solar phase angle (from Sromovsky and Fry, 2010b). (a) The model that did not contain any cloud as an absorber could not reproduce the observed spectra. (b) The model with NH_4SH as 3-μm absorber (filled circles) accounted for the observed spectra (lines).

1.2.4. Optical and physical properties of stratospheric haze

Stratospheric haze, which reduces the contrast and sharpness of Jovian cloud appearance as well as tropospheric haze, has also been investigated in the range from ultraviolet (UV) to near-infrared. Stratospheric haze is probably produced from higher mass photolysis products of CH_4 and/or from hydrazine (N_2H_4) ice being photolysis product of NH_3. However, the haze particles in the polar regions are strongly UV-absorbing and appear brighter in CH_4 bands centered at 0.89 μm and 2.3 μm, indicating their altitudes are higher compared with other latitudes. In these regions, the haze would be produced by a different mechanism possibly by interaction with charged particles from the magnetosphere and atmospheric molecules in the upper atmosphere.

Smith (1980) performed ground-based Galilean satellite eclipse observations and deduced the aerosol distribution in the lower stratosphere and the upper troposphere. He concluded that some aerosols above the tropopause, which were tenuous (optical thickness at 1.05 μm was less than 0.07) and varied with altitude, were required to fit the observations.

Tomasko et al. (1978) mentioned that a thin layer of strongly forward scattering haze particles at ~0.1 bar above both the STrZ and the SEBn was required to fit very high intensity at a solar phase angle of 150° as observed with the P10/IPP. The scattering phase function for stratospheric haze is represented by a single Henyey-Greenstein function as given in **Table 1.2** and **Figure 1.8**. From combination of photometric and polarimetric data taken by the Pioneer 10 and 11 IPP, Smith and Tomasko (1984) extended Tomasko et al.'s analyses and showed that stratospheric haze of positively polarizing with an optical thickness of a few tenths was located at ~0.12 bar.

West (1988) deduced the nature of high stratospheric haze by analyzing the limb brightness at a large solar phase angle of ~177° taken by the Voyager 2 wide angle camera with two wavelengths (430 nm and 600 nm) and found smaller particles (<0.1 μm) at ~0.5 mbar.

Rages et al. (1999) also analyzed limb intensity variations obtained from the Galileo SSI at high solar phase angles (146° and 157°) to retrieve the vertical profiles of aerosol extinction at two wavelengths (410 nm and 756 nm). For the equatorial region (9°N), the best-fit model was obtained with mean particle radius ~0.32 μm at ~16 mbar probed primarily in 410 nm and mean particle size ~0.45 μm at ~96 mbar sensed in 756 nm. For the high latitude region (60°N), there were two possible solutions: one was similar structure to that for the equatorial region except for slightly changes in particle radii and their locations; another was that stratospheric haze layer was placed between 1–2 mbar at both wavelengths, with mean particle size of 0.6 μm in 410 nm and 1.3 μm in 756 nm.

The behavior of stratospheric haze in UV has also been deduced by Tomasko et al. (1986). They

analyzed the International Ultraviolet Explorer (IUE) data and found that stratospheric haze particles with radii between 0.2–0.5 μm were required for fit to the reflectivity and limb-darkening curves. Sromovsky and Fry (2002) proposed that stratospheric haze should be composed of particles with a mean radius ~0.5 μm and a very narrow size distribution to satisfy wavelength dependence of its optical thickness (increasing optical thickness with wavelength) inferred from previous studies (Tomasko et al., 1978; West, 1979; Smith, 1986) and the HST observations.

1.3. Outstanding problems in Jovian aerosol studies to be revealed in this thesis

As mentioned in the above, vertical distribution of clouds and haze in the troposphere and stratosphere and their optical and physical properties have been extensively investigated and revealed by effort of researchers. From these reviews, we realize that information on the scattering properties of aerosols is essential to deduce the vertical distribution of aerosols and determination of such vertical distributions relies strongly on accuracy of the scattering properties of aerosols.

To the present, when we examine these distributions with remote sensing such as CH_4 band photometry, we have commonly applied two different scattering phase functions to scattering of aerosols in the Jovian atmosphere: the Pioneer HG functions and the Mie scattering phase functions for NH_3 ice particles. Both scattering phase functions, however, have several major problems that need to be overcome. We make reference to these problems separately.

- The Pioneer HG functions

First, the Pioneer HG functions cannot provide us any physical meanings such as the particle size and composition since these functions, which are described in the form of the Henyey-Greenstein function, are no more than mathematical (not physical) expression. Second, the Pioneer HG functions are not validated for other wavelengths, although these functions at red-channel have been extensively used as a substitute for analyses of CH_4 band photometry. In general, since the scattering properties of aerosols are as a function of wavelength, application of these functions to other wavelengths would result in additional ambiguity to determination of vertical distribution of aerosols.

- The Mie scattering phase functions for NH_3 ice particles

These scattering phase functions have been used on the grounds of the theoretical expectations that

small NH_3 ice particles are populated in the upper troposphere where we can see at visible to near-infrared wavelengths. If such small particles are abundant in the region, strong absorption features should be seen near 3 μm and near 9.4 and 26 μm. Recently, although large particles of either NH_3 ice or NH_4SH are found to be responsible for the 3-μm absorption anomaly, there are still no observational evidences of small particles. Thus, it is highly possible that these functions do not accurately describe the scattering properties of tropospheric haze.

1.4. The objectives of this thesis

In this thesis, in order to contribute to the field of the Jovian atmospheric studies, we aim to provide the scattering properties of aerosols in the Jovian upper troposphere and stratosphere observationally by analyzing new and high-quality imaging data obtained by Cassini.

Cassini, en route to Saturn, performed the Jovian observations during its flyby between October 2000 and March 2001 (the closest approach was on December 30, 2000). The Imaging Science Subsystem (ISS) on board Cassini collected a set of high spatial resolution Jovian images with several filters, including continua and three CH_4 bands, over a wide range of solar phase angles, 0°–140° (Porco et al., 2003). Such photometric data provide the first opportunity to improve observationally-based scattering phase functions for these aerosols since Tomasko et al. (1978) derived the scattering phase functions from the P10/IPP data. In addition to this, these data also have a potential to sound the vertical cloud structure with CH_4 band filters and multi-angle viewing, although this is beyond the scope of this thesis.

This thesis will mainly address the following questions:

(1) What optical and physical properties does the tropospheric haze have?

Although there are no spectroscopic evidences of small particles consisting of the tropospheric haze layer, such small population in the upper troposphere is needed to account for limb-darkening curves sampled at visible to near-infrared wavelengths. The optical and physical properties (i.e., refractive indices and effective radii) of such particles can be deduced by applying Mie scattering theory, not a mathematical expression such as the Henyey-Greenstein function, to scattering of aerosols when we reproduce the limb-darkening curves at a wide range of solar phase angles with the radiative transfer calculations. The obtained optical properties (especially, the real part of the refractive index, n_r) should hint at the composition of this

tropospheric haze, which has not yet been conclusively identified.

(2) What cause the visual difference between two distinctly-different bands: zones and belts?

It has long been thought that the visual difference is due to the low continuum single scattering albedo in the belts. However, this view is mainly based on the results of photometric and polarimetric measurements at a wide variety of solar phase angles from the Pioneer 10 and 11 IPP because we cannot distinguish the effects of scattering phase function from those of optical properties when we analyze photometric data measured at only small solar phase angles. Thus, this thesis answers whether this current view still works even in the case of the Cassini data.

(3) Can new scattering phase functions for aerosols reproduce other photometric data?

There are not so many chances to sound aerosols in the Jovian atmosphere by spacecraft. Therefore, we should provide new scattering phase functions for aerosols to researchers as a new "a priori" knowledge. In that context, the application of new scattering phase functions to other photometric data is important to verify these scattering phase functions against other data.

(4) Can conventional scattering phase functions for aerosols also reproduce new Cassini imaging data?

Conversely, it is also essential to validate the accuracy of conventional scattering phase functions such as the Pioneer HG functions with the Cassini multi-angle viewing data. If the Pioneer HG functions cannot reproduce these data, the need to modify the current view of Jovian tropospheric cloud structure will arise to a certain degree.

The outline of this thesis is as follows. We present details of the Cassini ISS observations and data reduction processes in **Chapter 2**. To answer the above questions, we concentrate on imaging data taken with two filters: CB2 (effective wavelength: 750 nm) and BL1 (effective wavelength: 455 nm) and on two latitude regions: a bright zone (the STrZ) and a dark belt (the SEBn). We refer to the advantage of the Cassini data over the Pioneer 10 data. In closing this chapter, we describe the behaviors of limb-darkening curves as a function of solar phase angle for all combinations of two wavelengths and two distinctly-different regions.

Chapter 3 explains the principle of radiative transfer in a scattering atmosphere, our model assumptions for explaining the obtained limb-darkening curves in **Chapter 2**, and the fitting strategy. In this thesis, we have newly developed a radiative transfer code for analyzing remote sensing data of planetary atmospheres. The accuracy of this code is validated in this chapter.

In **Chapter 4**, we show the radiative transfer calculation results of four data sets described in **Chapter 2**. In closing this chapter, we present a brief summary of these results.

In **Chapter 5**, we discuss the scattering properties of aerosols in the Jovian upper troposphere and stratosphere obtained in **Chapter 4**, along with comparison with previous studies. Answers for questions (1) and (2) are argued in **Section 5.1**. Answers for questions (3) and (4) are also mentioned in **Section 5.3** and **Section 5.4**, respectively. Sensitivity of our results for the assumed parameters is confirmed in **Section 5.2**.

Finally, we describe the summary and conclusions of this thesis in **Chapter 6**. Our future works to be accomplished are also given in **Chapter 7**.

In **Chapters 3**–**5**, we use the term “cloud” instead of the term “tropospheric haze” to clearly distinguish it from the haze in the stratosphere.

Chapter 2

Cassini ISS observations and data analysis

In this chapter, we present a summary of the Cassini spacecraft and the Jovian observations during its flyby in **Section 2.1** and a brief overview of the ISS on board Cassini in **Section 2.2**. The data reduction process is described in detail in **Section 2.3**. We explain the principle of limb-darkening analysis in **Section 2.4**. The criteria for selecting data used in this study are given in **Section 2.5**. The characteristics of limb-darkening curves for a bright zone and a dark belt in near-infrared and blue lights at a wide variety of solar phase angles are discussed in **Section 2.6**.

2.1. Cassini spacecraft

Cassini/Huygens is an international mission to the Saturnian system that consists of the Cassini Orbiter and the Huygens Probe. The Cassini Orbiter, carrying twelve scientific instruments, was designed for investigating Titan, the magnetosphere, icy satellites, the Saturnian ring system, and Saturn itself as well as the many interactions among them. The Huygens Probe, carrying six scientific instruments, was targeted for entry into the Titan atmosphere. The instruments on board the Cassini Orbiter and the Huygens Probe are briefly presented with their main scientific objectives in **Table 2.1** and **Table 2.2**, respectively. Cassini/Huygens was launched from Launch Complex 40 at Cape Canaveral in Florida by a Titan IVB/Centaur launch vehicle on October 15, 1997. After the launch, Cassini/Huygens followed a trajectory called the Venus-Venus-Earth-Jupiter gravity assist (VVEJGA) for traveling to Saturn over three billion km. The interplanetary trajectory is shown in **Figure 2.1**. For the sake of brevity, we hereafter use just “Cassini” instead of “Cassini/Huygens”.

The Cassini flyby of Jupiter was performed slowly and at nearly equatorial plane. Cassini began observations on October 1, 2000 when the spacecraft was at 84.7 million km away from Jupiter with

a solar phase angle of 20°, and elevation of 3.8° above the Jovian equatorial plane. After the period of a solar phase angle of 0° (December 13, 2000), the spacecraft had the month-long sweep observations with a wide range of solar phase angles. The closest approach was on December 30, 2000, at a distance of 9.8 million km which corresponds to 137 Jovian radii (R_J ~ 71,490 km). At the time, the apparent diameter of Jupiter was 0.84° (= 14.6 mrad). By January 15, 2001, the spacecraft moved on an asymptotic trajectory out of the Jovian system, looking back on the crescent Jupiter from a distance of 18 million km with a solar phase angle of 120°, and elevation of 3° below the Jovian equatorial plane. The last Jovian images were taken on March 22, 2001, at a distance of 76 million km (Porco et al., 2003). The solar phase angle and the distance between Cassini and Jupiter during its flyby are presented in **Figure 2.2**.

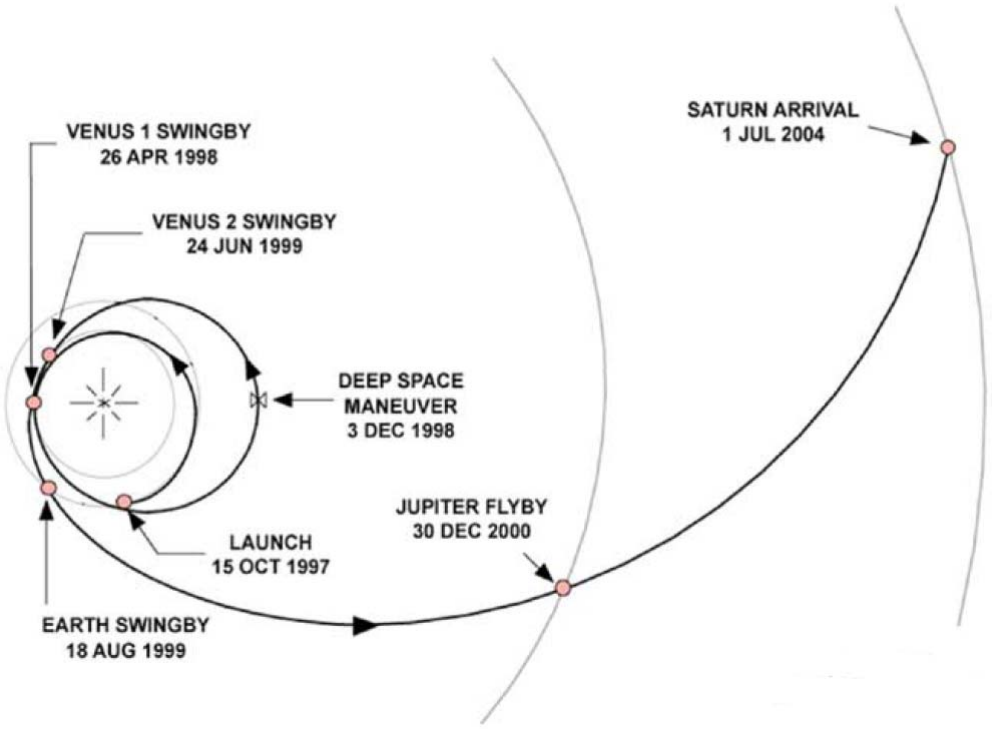

Figure 2.1. The Cassini mission interplanetary trajectory (VVEJGA) from launch on October 16, 1997, to Saturn orbit insertion on July 1, 2004 (from Matson et al., 2002).

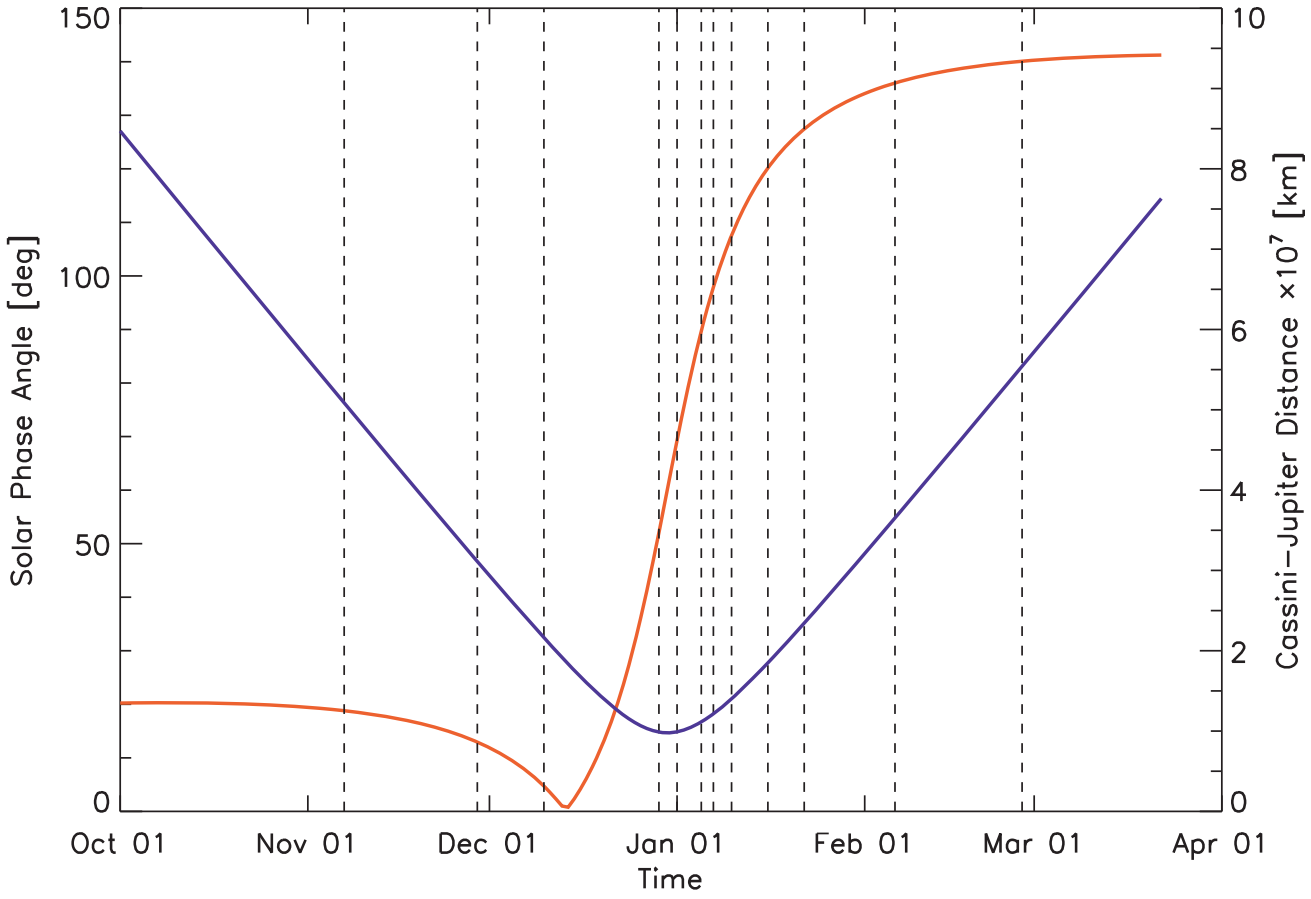

Figure 2.2. The solar phase angle (red curve) and the distance between Cassini and Jupiter (blue curve) during the Cassini flyby of Jupiter. The vertical dashed lines indicate the observation dates on which the Cassini data used in the analyses for the STrZ were taken. The Cassini started observations on October 1, 2000 and ended on March 22, 2001. The solar phase angle decreased to the minimum value ($\alpha = 0°$) on December 13, 2000. The closest approach was on December 30, 2000.

Table 2.1. The twelve scientific instruments on board the Cassini Orbiter (from Matson et al., 2002).

Instrument (Acronym)	Scientific objectives
Cassini Plasma Spectrometer (CAPS)	In-situ study of plasma within and near the Saturnian magnetic field
Cosmic Dust Analyzer (CDA)	In-situ study of ice and dust grains in the Saturnian system
Composite Infrared Spectrometer (CIRS)	Temperature and composition of surfaces, atmospheres, and rings within the Saturnian system
Ion and Neutral Mass Spectrometer (INMS)	In-situ compositions of neutral and charged particles within the Saturnian magnetosphere
Imaging Science Subsystem (ISS)	Multispectral imaging of Saturn, Titan, rings, and the icy satellites to observe their properties
Dual Technique Magnetometer (MAG)	Study of the Saturnian magnetic field and interactions with the solar wind
Magnetospheric Imaging Instrument (MIMI)	Global magnetospheric imaging and in-situ measurements of the Saturnian magnetosphere and solar wind interactions
Cassini Radar (RADAR)	Radar imaging, altimetry, and passive radiometry of the Titan's surface
Radio and Plasma Wave Science (RPWS)	Measure the electric and magnetic fields and electron density and temperature in the interplanetary medium and within the Saturnian magnetosphere
Radio Science Subsystem (RSS)	Study of atmospheric and ring structure, gravity fields, and gravitational waves
Ultraviolet Imaging Spectrograph (UVIS)	Spectra and low resolution imaging of atmospheres and rings for structure, chemistry, and composition
Visible and Infrared Mapping Spectrometer (VIMS)	Spectral mapping to study composition and structure of surfaces, atmospheres, and rings

Table 2.2. The six scientific instruments on board the Huygens Probe (from Matson et al., 2002).

Instrument (Acronym)	Scientific objectives
Aerosol Collector Pyrolyser (ACP)	In-situ study of clouds and aerosols in the Titan's atmosphere
Descent Imager and Spectral Radiometer (DISR)	Temperatures and images of the Titan's atmospheric aerosols and surface
Doppler Wind Experiment (DWE)	Study of winds from their effect on the Probe during the Titan descent
Gas Chromatograph and Mass Spectrometer (GCMS)	In-situ measurement of chemical composition of gases and aerosols in the Titan's atmosphere
Huygens Atmospheric Structure Instrument (HASI)	In-situ study of the physical and electrical properties of the Titan's atmospheric
Surface Science Package (SSP)	Measurement of the physical properties of the Titan's surface

2.2. Instrument characteristics of ISS

The Imaging Science Subsystem (ISS) on board the Cassini Orbiter is the highest-resolution two-dimensional imaging device ever carried into the outer solar system, and was designed for investigations of the Saturnian atmosphere, its rings, icy satellites, Titan, and their mutual interactions. The ISS was built by the Jet Propulsion Laboratory (JPL), California Institute of Technology.

The ISS consists of two telescopes with fixed focal length (*f.l.*), called "cameras": the narrow angle camera (NAC, *f.l.* = 2000 mm) and wide angle camera (WAC, *f.l.* = 200 mm). They sit on the Remote Sensing Palette (RSP), fixed to the body of the Cassini Orbiter, between the Visual Infrared Mapping Spectrometer (VIMS), the Composite Infrared Spectrometer (CIRS), and the Ultraviolet Imaging Spectrometer (UVIS). The apertures and radiators of both telescopes are parallel to each other. **Figure 2.3** shows the position of the ISS and the other scientific instruments on board the Cassini orbiter.

Both the NAC and the WAC use a UV-coated charge-coupled device (CCD) detector consisting of a 1024 × 1024-pixels square array with pixel size of 12 μm. The NAC is an f/10.5 Ritchey-Chretien design reflector telescope for better image quality and resolution compared to what were recorded by Voyager. The corresponding field of view (FOV) is 0.35° (= 6.1 mrad) and the pixel angular size is 1.2 [arcsec/pixel]. It carries 24 spectral filters, 12 filters on each of two filter wheels, in the spectral range from 200 nm to 1100 nm, including three methane band filters for vertical sounding of the Saturnian atmosphere. The WAC is an f/3.5 refractor telescope whose optics is a Voyager flight spare, while the detector and filter wheel were exclusively designed for the WAC of the Cassini ISS. The FOV is 3.5° (= 61.2 mrad) and the pixel angular size is 12.3 [arcsec/pixel]. The spectral range of the WAC is 380–1100 nm, which is narrower than that of the NAC because of the UV-blocking glass materials in the refractor design. It carries nine filters on each of two filter wheels, for a total of 18 filters. The ISS instrument and investigation are described in detail by Porco et al. (2004).

In this study, we use Jovian images obtained from the NAC to obtain limb-darkening curves at a wide variety of solar phase angles with sufficient spatial resolution. The schematic view of the NAC appears in **Figure 2.4**. The characteristics of CCD and spectral filters on board the NAC are summarized in **Table 2.3** and **Table 2.4**, respectively. The transmission curves of several key filters on board the NAC are also described along with those of the P10/IPP blue- and red-channels (Pellicori et al., 1973) and the Karkoschka's ground-based Jovian full-disk albedo spectrum (Karkoschka, 1998) in **Figure 2.5**. For the NAC, the transmission curves are given as the

non-wavelength-integrated system transmission values ($T_0 \times T_1 \times T_2 \times QE$). Definitions of variables are presented in **Table 2.5**.

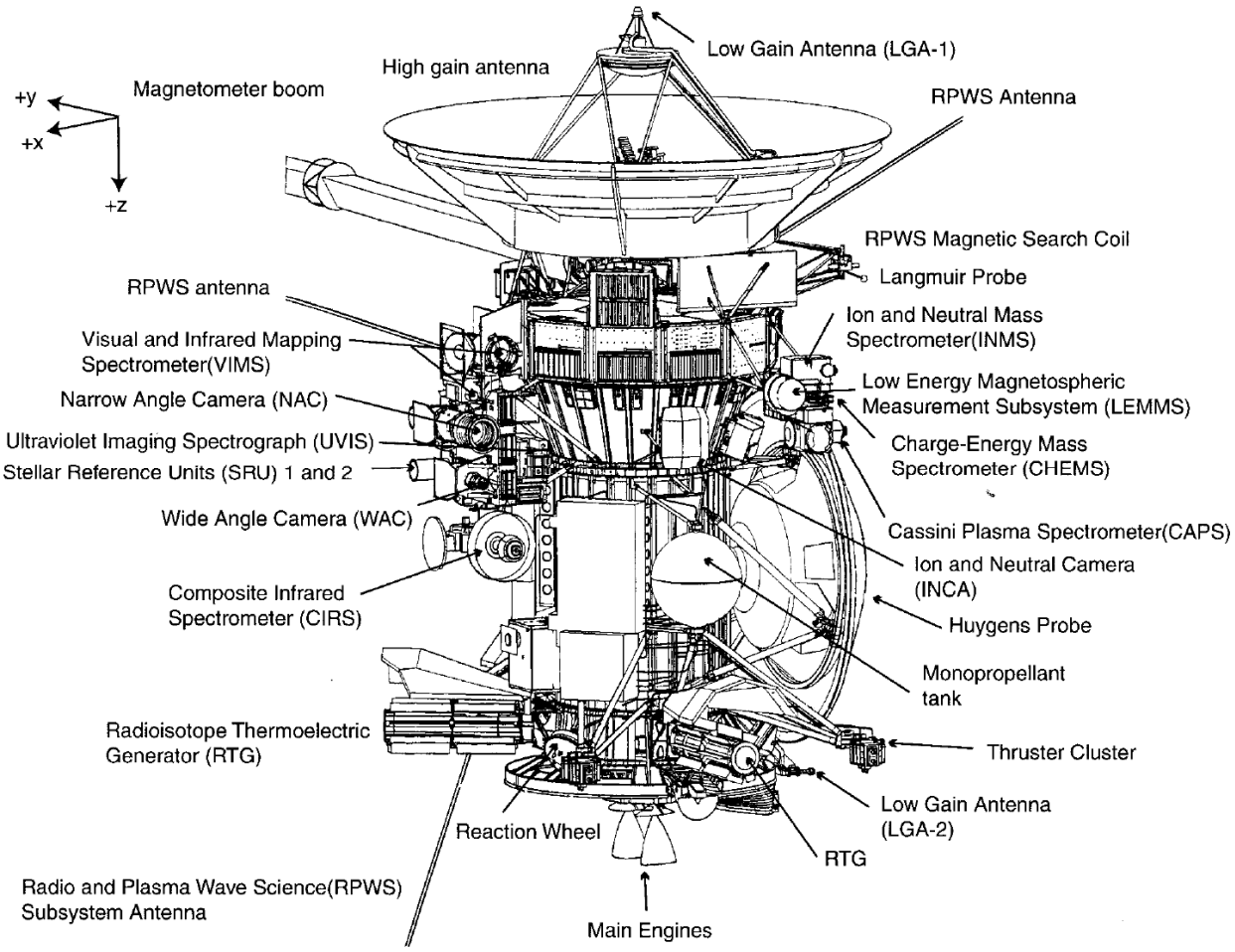

Figure 2.3. The schematic diagram of the Cassini Orbiter, showing the positions of the twelve scientific instruments and some of the engineering subsystems. The magnetometer boom is aligned with the +*y* axis, and the high-gain antenna is pointed toward –*z* axis (from Burton et al., 2001).

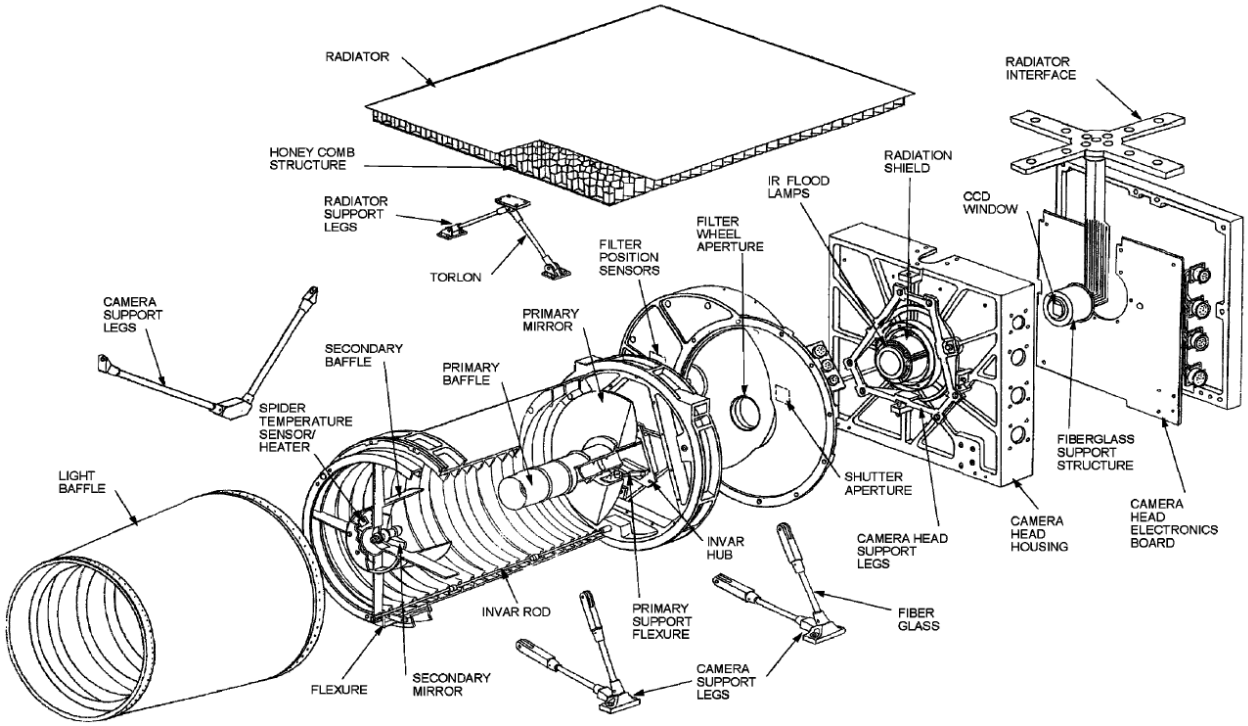

Figure 2.4. The schematic diagram of the Cassini ISS NAC, showing optical, structural, and sensor components (from Porco et al., 2004).

Table 2.3. The Cassini ISS NAC CCD and optical characteristics (from Porco et al., 2004).

Parameter	Value
Common design	
CCD	Three-phase, front-side illuminated, UV-coated
Pixel size	12 μm
Format	1024 × 1024
Available exposure	64 commandable settings, 5 ms–1200 s
Signal digitization	12 bits, 4095 DN
Summation modes	1 × 1, 2 × 2, 4 × 4
NAC	
Type	Reflector
F/N	10.5
Focal length	2002.70 ± 0.07 mm
Pixel angular size	5.9907 μrad/pixel (= 1.2 arcsec/pixel)
FOV*	6.134 mrad (= 0.35°)
FWHM* of PSF*	1.3 pixels
Spectral range	200–1050 nm
Filter positions	12 × 2 filters wheels
Gain state	0: 1: 2: 3
Gain values [electrons/DN*]	233: 99: 30: 13
Gain state factors	0.13: 0.31: 1.0: 2.36

* abbreviations
FOV: field of view
FWHM: full width at half maximum
PSF: point spread function
DN: digit number

Table 2.4. The Cassini ISS NAC filter characteristics (from Porco et al., 2004).

Filter	$\lambda_{cen, NAC}$	$\lambda_{eff, NAC}$	Scientific justification
UV1	258W	264	Aerosols
UV2	298W	306	Aerosols, broad-band filter
UV3	338W	343	Aerosols, broad-band color, polarization
BL2	440M	441	Medium-band color, polarization
BL1	451W	455	Broad-band color
GRN	568W	569	Broad-band color
MT1	619N	619	Methane band, vertical sounding
CB1	619N	619	Two-lobed continuum for MT1
CB1a	635	635	
CB1b	603	603	
RED	650W	649	Broad-band color
HAL	656N	656	H-alpha/lightning
MT2	727N	727	Methane band, vertical sounding
CB2	750N	750	Continuum for MT2
IR1	752W	750	Broad-band color
IR2	862W	861	Broad-band color; ring absorption band
MT3	889N	889	Methane band, vertical sounding
CB3	938N	938	Continuum for MT3; see through Titan haze
IR3	930W	928	Broad-band color
IR4	1002LP	1001	Broad-band color
CL1	611	651	Wide open, combine with wheel 2 filters
CL2	611	651	Wide open, combine with wheel 1 filters
P0	617	633	Visible polarization 0°
P60	617	633	Visible polarization 60°
P120	617	633	Visible polarization 120°
IRP0	746	738	IR polarization; see through Titan haze

All wavelengths are given in units of nm. Central wavelengths (“cen”) are computed using the full system transmission function. These numbers are taken to be the numerical name assigned to the filter. Effective wavelengths (“eff”) are computed using the full system transmission function convolved with a solar spectrum. Bandpass type: W: wide; M: middle; N: narrow; and LP: long wavelength cutoff.

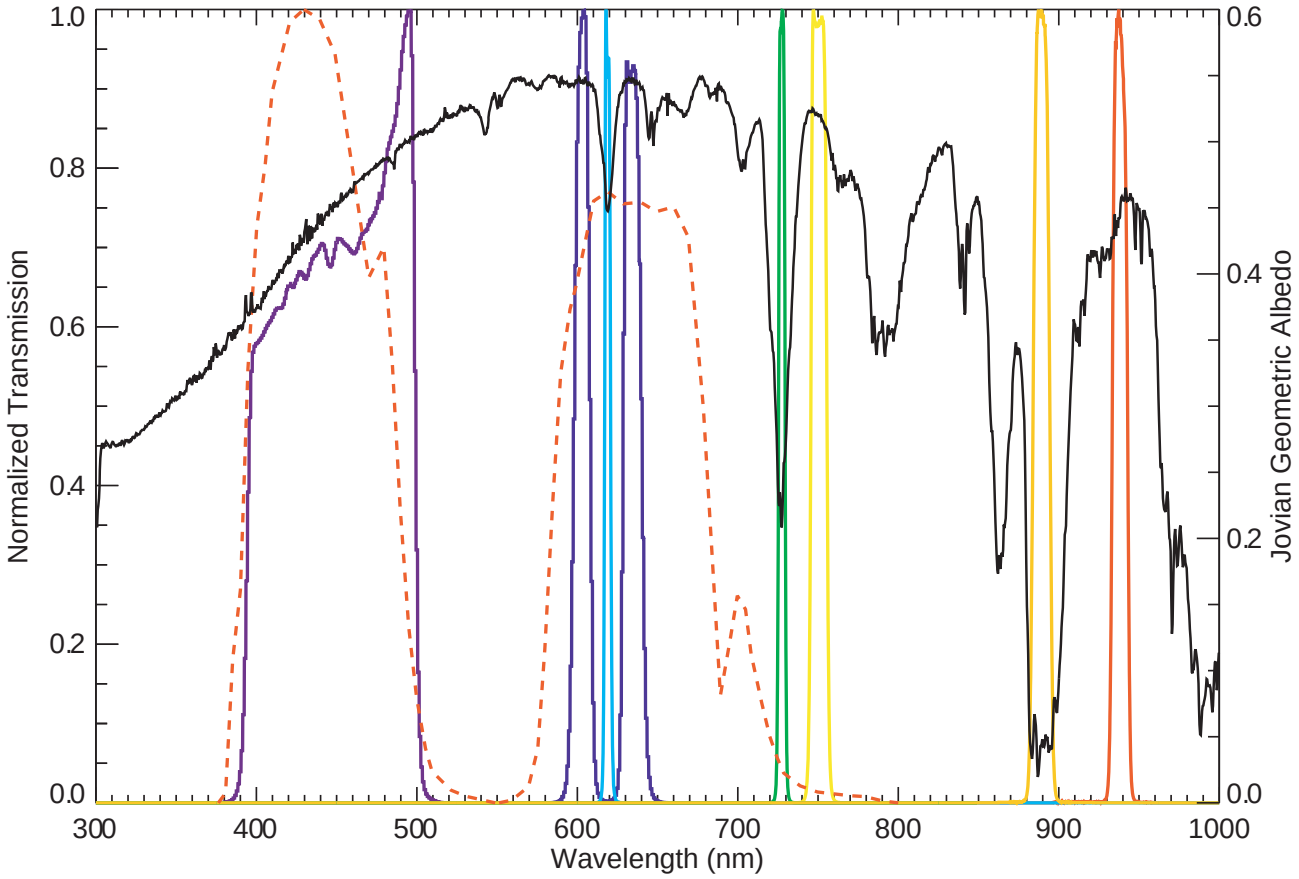

Figure 2.5. The transmission curves of several key filters on board the ISS NAC along with those of the Pioneer 10 IPP blue- and red-channels (red dashed curves) (Pellicori et al., 1973) and the Karkoschka's ground-based Jovian full-disk albedo spectrum (black solid curve) (Karkoschka, 1998). Filters for the NAC are as follows: BL1 (purple); MT1 (aqua); CB1 (blue); MT2 (yellow-green); CB2 (yellow); MT3 (orange); and CB3 (red).

2.3. Data reduction

Jovian images used in this study are available on the NASA Planetary Data System (PDS) website at http://img.pds.nasa.gov/volumes/iss.html. We perform the standard ISS data reduction with version 3.6 (the latest as of the time of this work) of the Cassini Imaging Science Subsystem Calibration tool (CISSCAL) software (Porco et al., 2004), which is available at the PDS Imaging Node website at http://pds-imaging.jpl.nasa.gov/data/cassini/cassini_orbiter/coiss_0011_v2/extras/. CISSCAL works under IDL version 5.5 or newer, on Linux and Unix environments. The calibration procedures are summarized as follows:

(1) LUT conversion

Data from the analog-to-digital converter (ADC) are encoded to 12-bit digit numbers (DN). If images, which are passed through data conversion from 12-bit range (0–4096 DNs) to 8-bit range (0–255 DNs) in the ISS flight software (such images are tagged by DATA_CONVERSION_TYPE = “TABLE”), are calibrated, it is required to convert the pixel values from 8-bit range to 12-bit range again.

(2) Bitweight correction

The electrons on the CCD are shifted to an output register and then to the ADC. The ADC introduces a slight error in the DN levels because of a process called uneven bit weighting. For the correction, some of the DN values are under-populated and some are over-populated instead of a one-to-one linear correspondence between input signal and output DN.

(3) Subtract bias

The bias, which means the zero-exposure DN level of the CCD chip, is removed from image either by simply subtracting the BIAS_STRIP_MEAN value found in the image header, or by using the over-clocked pixel array taken out of the binary line prefix.

(4) Remove 2-Hz noise

“2-Hz noise” is a coherent noise that results in a horizontal banding pattern across the image. This noise is introduced during image readout. The removal of this noise is accomplished either by looking at the over-clocked pixels, or by looking at dark sky areas in the image itself, and constructing a 2-Hz signal by use of an image mean.

(5) Subtract dark

Dark current consists both of the traditional, slowly-increasing kind (i.e. dark current), and of an effect called residual bulk image (RBI). The latter is caused by the leaking of electrons into the pixel wells from whatever image was on the CCD previous to the current exposure.

The removal of these dark current is conducted either with in-flight dark images, or with dark images created by a model.

(6) A-B pixel pairs

Correction for the bright/dark pixel pair artifacts created by the anti-blooming mode. This option is skipped if images with ANTIBLOOMING_STATE_FLAG = "OFF" are calibrated.

(7) Linearize

Correction for non-linearity of the CCD response.

(8) Flat field

Correction for pixel-to-pixel response due to dust ring and the CCD chip itself.

(9) Convert DN to flux (reflectivity)

The relationship between the measured signal S [DN] and the intensity I [photons/(cm^2 s nm steradian)] is given by

$$\begin{aligned} S &= ge_p \\ &= gC(f_1, f_2)A\Omega t(i)FF(i,j,f_1,f_2)\int I(i,j,\lambda)T_0(\lambda)T_1(\lambda)T_2(\lambda)QE(\lambda)d\lambda\,. \end{aligned} \tag{2.1}$$

Definitions of variables are presented in **Table 2.5**. Then, intensity averaged over the passband of the given filter with non-wavelength-integrated system transmission function $T_0(\lambda)T_1(\lambda)T_2(\lambda)QE(\lambda)$ is written by

$$\bar{I}(i,j) = \int I(i,j,\lambda)T_0(\lambda)T_1(\lambda)T_2(\lambda)QE(\lambda)d\lambda \Big/ \int T_0(\lambda)T_1(\lambda)T_2(\lambda)QE(\lambda)d\lambda\,. \tag{2.2}$$

The solar flux weighted by the passband of the filter is also obtained as follows:

$$\bar{F} = \int F_1(\lambda)T_0(\lambda)T_1(\lambda)T_2(\lambda)QE(\lambda)d\lambda \Big/ \pi R^2 \int T_0(\lambda)T_1(\lambda)T_2(\lambda)QE(\lambda)d\lambda\,, \tag{2.3}$$

where F_1 is the solar flux at 1 AU and R is the distance between the Sun and target body in units of AU. Therefore, the observed reflectivity (I/F) taken with the given filter can be calculated by dividing equation (2.2) by equation (2.3).

(10) Correction factor

Dividing the image array by filter-specific correction factors to match the actual observed flux with the theoretical flux derived from the integrated system transmission function.

(11) Geometric correction

Correction for the geometric distortion resulted from the optical system. Fortunately, distortion of the ISS camera is quite insignificant in most cases (Porco et al., 2004).

With the exception of the geometric correction, all other calibration options are automatically

performed for images by default. The calibration methodology and in-flight calibration performance are described in detail by Porco et al. (2004) and West et al. (2010).

Table 2.5. Definitions of variables for calibration (from Porco et al., 2004).

Quantity	Units	Definition
Ω	steradian	Solid angle sampled by one pixel
A	cm^2	Collecting area of camera optics $0.25\pi d^2$, d is the primary mirror or lens diameter
$C(f_1, f_2)$		Absolute sensitivity correction factor determined from in-flight calibration
$e_p(i,j)$	electrons	Electrons produced by photons striking the CCD
f_1, f_2		Filter 1 in wheel 1, filter 2 in wheel 2
$FF(i,j,f_1,f_2)$		Flat filed relative sensitivity*
g	electrons/DN	Gain constant (**Table 2.3**)
$I(i,j,\lambda)$	photons/(cm^2 s nm steradian)	Intensity at pixel (i,j) and λ
$Line$		The vertical coordinate (1:1024) of the image. Index j indicates line number
$QE(i,j,\lambda)$	electrons/photon	CCD quantum efficiency
$RBI(i,j,mode)$	DN	Residual bulk image
$Sample$		The horizontal coordinate (1:1024) of the image. Index i indicates sample number
$t(i)$	seconds	Shutter open time, depends on sample number
$T_0(i,j,\lambda)$		Optics transmission. Accounts for beam obscuration as well as losses at lens and mirror surfaces
$T_1(i,j,\lambda)$		Filter 1 transmission
$T_2(i,j,\lambda)$		Filter 2 transmission

* FF is normalized to unity, i.e., $(1/N^2)\sum_{j=1}^{N}\sum_{i=1}^{N} FF(i,j,f_1,f_2) = 1.0$.

Figure 2.6 shows comparison between the CISSCAL-calibrated full-disk albedo in eight filters and the full-disk albedo spectrum in 1995 by Karkoschka (1998). Both values are obtained at a solar phase angle of 6.8°. The CISSCAL-calibrated full-disk albedo at the solar phase angle of 6.8° is derived by extrapolating from those at solar phase angles in the range 17.7°–~19° at which Cassini was far enough from Jupiter to capture full-disk snapshot images with the NAC (B. Knowles, private communication). Clearly, the values of the CISSCAL-calibrated full-disk albedo in several filters are higher than those of the Karkoschka's full-disk albedo although they are within expected absolute calibration error (±10%) (R. West, private communication). Although it may have something to do

with the post-Jupiter NAC contamination event (B. Knowles, private communication) and, of course, the "true" temporal changes of cloud brightness between 1995 and 2000 may be partially responsible for this difference, however, at this time, there is no concrete conclusion by the Cassini ISS team for what explains this discrepancy. In this study, as an additional photometric correction, we multiply nominal reflectivity obtained from CISSCAL by an absolute scale factor C_{abs} in order to match the CISSCAL-calibrated full-disk albedo with the Karkoschka's full-disk albedo convolved with non-wavelength-integrated system transmission function for the given filter,

$$(I/F)_{\text{corr}} = (I/F)_{\text{CISSCAL}} \times C_{abs}. \quad (2.4)$$

C_{abs} is determined with respect to each filter and the values for eight filters are presented in **Table 2.6**. This is said to be valid only for data during the Cassini flyby of Jupiter (B. Knowles, private communication).

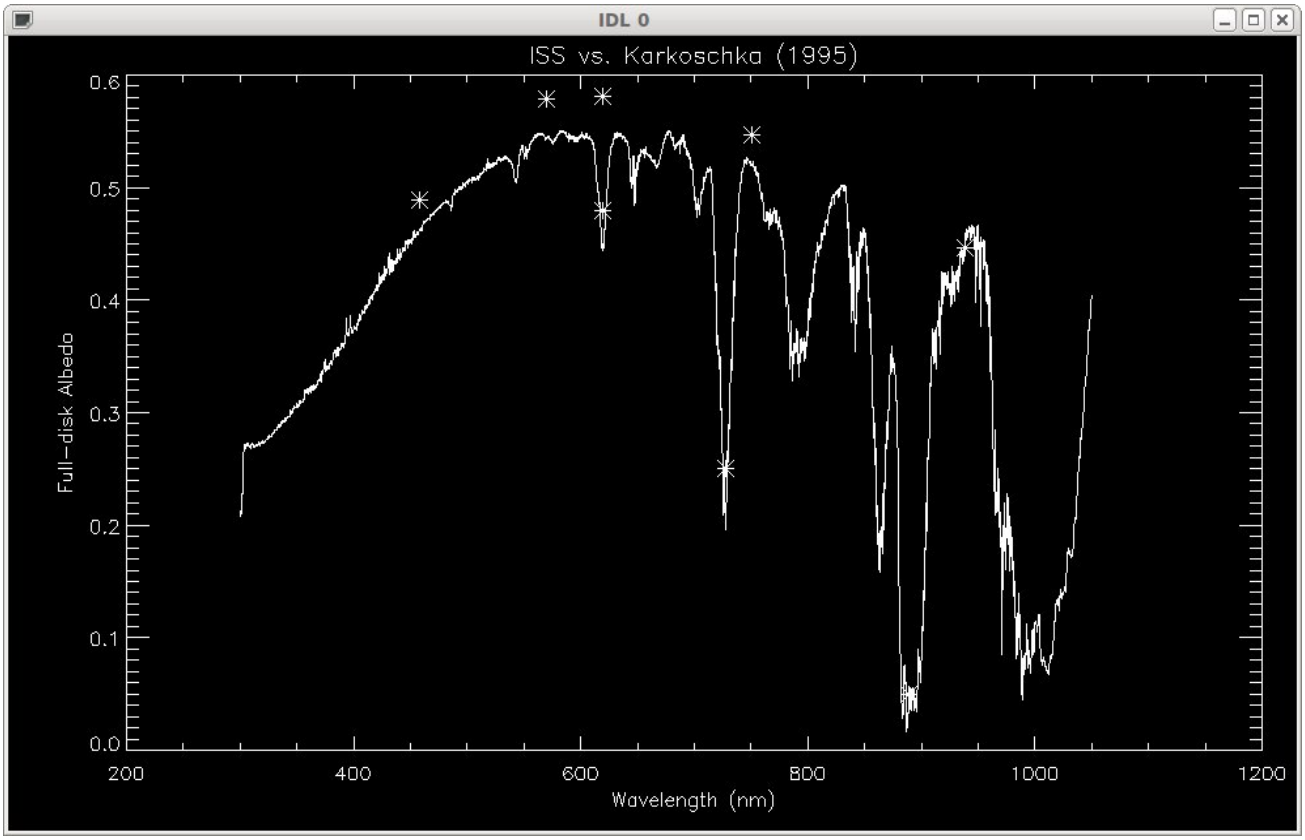

Figure 2.6. Comparison between the CISSCAL-calibrated full-disk albedo in eight filters (asterisks) and the Jovian full-disk albedo spectrum in 1995 by Karkoschka (1998) (solid curve). Both values are obtained at the same solar phase angle (α = 6.8°). The CISSCAL-calibrated full-disk albedo is obtained by extrapolating from images at solar phase angles in the range 17.7°–~19° at which Cassini was far enough from Jupiter to allow the NAC to capture full-disk snapshot images (courtesy of Dr. B. Knowles).

Table 2.6. The absolute scale factor (C_{abs}) for the additional photometric correction.

Filter	Eff. wavelength [nm]*	C_{abs}	1-σ standard deviation
BL1, CL2	455	0.932	0.005
CL1, GRN	569	0.914	0.004
CL1, MT1	619	0.953	0.003
CL1, CB1	619	0.937	0.003
CL1, MT2	727	0.935	0.001
CL1, CB2	750	0.952	0.003
CL1, MT3	889	0.9228	0.0005
CL1, CB3	938	1.001	0.003

* "Eff." is the effective wavelength.

After the photometric calibration, we allocate the latitude–longitude coordinate to Jovian images. First, we calculate the sub-solar point, the sub-observer point, the north polar orientation (δ, see **Figure 2.7a**), and the distance between Cassini and Jupiter (D_{CJ}) with the SPICE toolkit developed at the Navigation and Ancillary Information Facility (NAIF). The SPICE toolkit and data (often referred to as "kernels") can be found at the NAIF website at http://naif.jpl.nasa.gov/naif/toolkit.html and http://naif.jpl.nasa.gov/naif/data_outer.html, respectively.

Second, the planetary limb in an image is enhanced by the Sobel filter. The Sobel filter is a discrete differentiation filter, computing an approximation of the gradient of the image intensity function. An example of Jovian image and the same image after enhancing with the Sobel filter are shown in **Figure 2.8a** and **Figure 2.8b**, respectively. The pixels, the gradient value at which is the largest in each horizontal line, are plotted by green dashed-dotted curve in **Figure 2.8c**. After that, the pixels, which evidently are not planetary limb, are replaced with the probable pixels by eye (red dashed-dotted curve in **Figure 2.8c**).

Third, the detected planetary limb points are fitted with an ellipse by using the Levenberg-Marquardt method to determine the center coordinate (X_0, Y_0) shown in **Figure 2.7a**. Since the geometric distortion of NAC images are known to be quite small and the location of Cassini was much far from Jupiter ($137R_J$, even at the time of the closest approach), the ellipse to be fit is simply given by

$$\{[(X - X_0)\cos\delta - (Y - Y_0)\sin\delta]/a\}^2 + \{[(X - X_0)\sin\delta + (Y - Y_0)\cos\delta]/b'\}^2 = 1, \qquad (2.5)$$

where (X, Y) is a two-dimensional coordinate system for image opened in IDL, a is the equatorial radius of Jupiter in units of pixels, and b' is the apparent polar radius of Jupiter in units of pixels. a and b' are obtained with the polar radius of Jupiter b [pixel]:

$$\mathrm{a} = \sqrt{\left(R_e/D_{CJ}\right)^2 / \left[1 - \left(R_e/D_{CJ}\right)^2\right]}/ifov\,, \tag{2.6}$$

$$b' = \sqrt{\left(a\sin\theta_{pc,0}\right)^2 + \left(b\cos\theta_{pc,,0}\right)^2}, \tag{2.7}$$

$$b = \sqrt{\left(R_p/D_{CJ}\right)^2 / \left[1 - \left(R_p/D_{CJ}\right)^2\right]}/ifov\,, \tag{2.8}$$

where R_e and R_p are the equatorial (= 71,492 km) and polar (= 66,854 km) radii of Jupiter, respectively, D_{CJ} is the distance between Cassini and Jupiter in units of km, $ifov$ (= 5.9907 × 10^{-6} [rad/pixel]) stands for instantaneous field of view, and $\theta_{pc,0}$ is the sub-observer planetocentric latitude in units of radians. Although the uncertainty of the center coordinate is sensitive to the coverage of planetary limb, the uncertainty of the center coordinate of images used in this study should be ±1 pixel as a conservative estimate.

Once the center coordinate is determined, the coordinate transformation from the coordinate system for image (X, Y) to the Jovian body-fixed frame (x, y, z) can be performed as follows (see also **Figure 2.7a** and **Figure 2.7b**):

$$\begin{pmatrix} X' \\ Y' \end{pmatrix} = \begin{pmatrix} \cos\delta & -\sin\delta \\ \sin\delta & \cos\delta \end{pmatrix} \begin{pmatrix} X - X_0 \\ Y - Y_0 \end{pmatrix}, \tag{2.9}$$

$$\begin{pmatrix} x \\ y \\ z \end{pmatrix} = A \begin{pmatrix} X' \\ Y' \\ Z' \end{pmatrix}, \tag{2.10}$$

where A is a rotation matrix, which is calculated with longitude λ_0 [rad] in System III and planetocentric latitude $\theta_{pc,0}$ for the Sub-observer point. The rotation matrix A is given by

$$A = \begin{pmatrix} \cos\lambda_0 & 0 & -\sin\lambda_0 \\ 0 & 1 & 0 \\ \sin\lambda_0 & 0 & \cos\lambda_0 \end{pmatrix} \begin{pmatrix} 1 & 0 & 0 \\ 0 & \cos\theta_{pc,0} & \sin\theta_{pc,0} \\ 0 & -\sin\theta_{pc,0} & \cos\theta_{pc,0} \end{pmatrix}. \tag{2.11}$$

An axis Z' for the coordinate system (X', Y', Z'), which is perpendicular to image, can also be derived as follows:

$$Z' = \left(-k_3 + \sqrt{{k_3}^2 - k_1 k_2}\right)/k_1\,, \qquad \text{if} \quad {k_3}^2 - k_1 k_2 \geq 0, \tag{2.12}$$

$$k_1 = \left(\sin\theta_{pc,0}/b\right)^2 + \left(\cos\theta_{pc,0}/a\right)^2, \tag{2.13}$$

$$k_2 = (1/a^2)X'^2 + \left[\left(\cos\theta_{pc,0}/b\right)^2 + \left(\sin\theta_{pc,0}/a\right)^2\right]Y'^2 - 1, \tag{2.14}$$

$$k_3 = \left\{\cos\theta_{pc,0}\sin\theta_{pc,0}[(1/a^2) - (1/b^2)]\right\}Y'. \tag{2.15}$$

Note that if ${k_3}^2 - k_1 k_2 < 0$, Jupiter is not projected onto such pixel.

Finally, planetographic latitude θ_{pg}, longitude λ in System III, and the local scattering geometries (i.e., μ, cosine of the local zenith angle to the observer; μ_0, cosine of the local zenith angle to the Sun; and $\Delta\phi$, the local azimuth angle between the direction to the Sun and the observer) are computed for each pixel by

$$\tan\lambda = -x/z, \tag{2.16}$$

$$\tan\theta_{pg} = (a/b)^2\tan\theta_{pc} = (a/b)\tan\theta = (a/b)^2(y/z)\cos\lambda, \tag{2.17}$$

$$\mu = n_x c_x + n_y c_y + n_z c_z, \tag{2.18}$$

$$\mu_0 = n_x s_x + n_y s_y + n_z s_z, \tag{2.19}$$

$$\cos\alpha = c_x s_x + c_y s_y + c_z s_z, \tag{2.20}$$

$$\cos\Delta\phi = (\mu\mu_0 - \cos\alpha)/\sqrt{(1-\mu^2)(1-\mu_0^2)}, \tag{2.21}$$

where $\vec{n} = (n_x, n_y, n_z)$ is a unit normal vector at each pixel, $\vec{c} = (c_x, c_y, c_z)$ is an orientation vector of Cassini, which is normalized to unity, $\vec{s} = (s_x, s_y, s_z)$ is an orientation vector of the Sun, which is normalized to unity, and α is solar phase angle. The relationship among parameter θ, planetocentric latitude θ_{pc}, and planetographic latitude θ_{pg} is depicted in **Figure 2.7c**. **Figure 2.8d** shows latitude–longitude coordinates superimposed on the Jovian image.

In this study, we focus on two prominent latitude regions: the South Tropical Zone (STrZ) and the north component of the South Equatorial Belt (SEBn). There are two reasons why we choose these regions: one is for direct comparison with the results of Tomasko et al. (1978) and the other is that these regions look most longitudinally uniform bands in all latitude bands, which is suitable for the limb-darkening analysis. Thus, the limb-darkening curves are extracted along –25° planetographic latitude in the STrZ and –10° planetographic latitude in the SEBn. Note that we average out the reflectivity and local scattering geometry over $n \times n$ pixels for two reasons:

(1) to have similar spatial resolution in each image;
(2) to lessen unwanted deviation from a smooth limb-darkening curve due to small localized cloud patterns that are visible in high spatial resolution images.

The areas of the STrZ and the SEBn are shown by red squares in **Figure 2.8e** and **Figure 2.8f**, respectively. The limb-darkening curves are extracted from images by averaging out the reflectivity and local scattering geometry surrounded by red square. In practice, the data points with either μ_0 and μ smaller than 0.15 are excluded because of using the plane-parallel approximation in the following radiative transfer modeling described in **Chapter 3**.

The primary source of relative (pixel-to-pixel) uncertainty in a processed image is the off-focus dust rings in the flat field, amplitude of which is estimated to be less than 1% (R. West, private communication). Aside from this, the relative uncertainty resulting from navigation error (uncertainty of the central coordinate) is also considered. We estimate this uncertainty using the following equation:

$$err_{navigation} = \frac{100}{(I/F)_j}\sqrt{\frac{1}{n}\sum_{k=1}^{n}\left[(I/F)_{j,k} - (I/F)_j\right]^2}, \tag{2.22}$$

where n is the number of center coordinates which are shifted from the best-fit center coordinate (X_0, Y_0) by 1 pixel (n = 8), i.e., $(X_0 + 1,\ Y_0)$, $(X_0 - 1,\ Y_0)$, $(X_0,\ Y_0 + 1)$, $(X_0,\ Y_0 - 1)$, $(X_0 + 1/\sqrt{2},\ Y_0 + 1/\sqrt{2})$, $(X_0 + 1/\sqrt{2},\ Y_0 - 1/\sqrt{2})$, $(X_0 - 1/\sqrt{2},\ Y_0 + 1/\sqrt{2})$, and $(X_0 - 1/\sqrt{2},\ Y_0 - 1/\sqrt{2})$, $(I/F)_j$ is the value of reflectivity of the *j*th data point derived with the best-fit center coordinate, and $(I/F)_{j,k}$ is the value of reflectivity of the *j*th data point derived with the *k*th center coordinate which is shifted from the best-fit center coordinate by 1 pixel. From such estimation, as a result, this uncertainty is found to be ~0.5% on average.

The relative uncertainties combined with the above two factors are included in the following radiative transfer modeling. The absolute uncertainty of nominal reflectivity calculated by CISSCAL is estimated to be ±10% (R. West, private communication). In **Chapter 3**, we do not consider this absolute uncertainty in determining the scattering phase functions. Instead of this, the sensitivity test for this absolute uncertainty is conducted in **Section 5.2**.

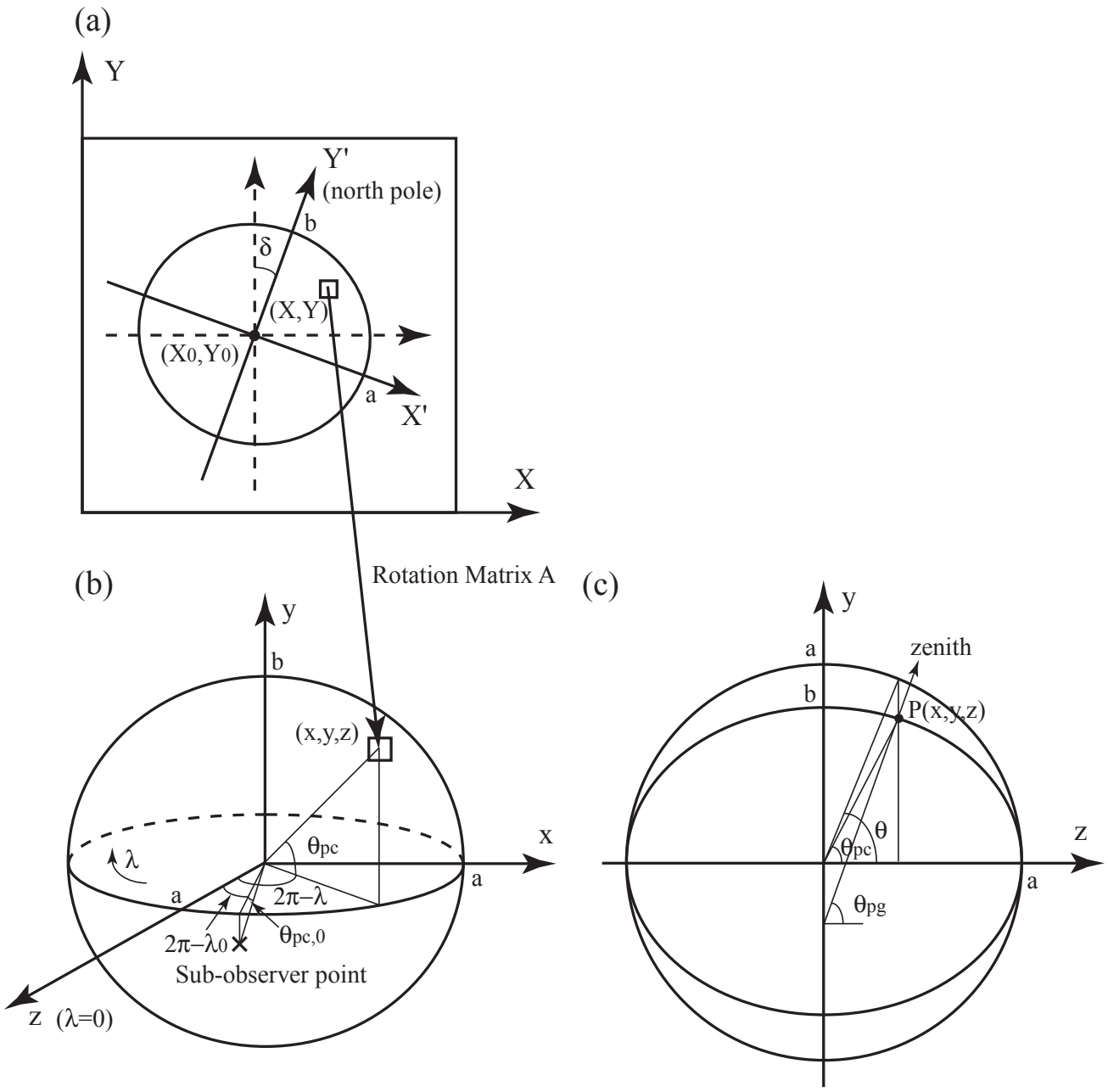

Figure 2.7. Correspondence relationship between a coordinate system for image opened in IDL and the Jovian body-fixed frame: (a) a two-dimensional coordinate system for image defined in this study; (b) the Jovian body-fixed frame; and (c) the relationship among parameter θ, planetocentric latitude θ_{pc}, and planetographic latitude θ_{pg}.

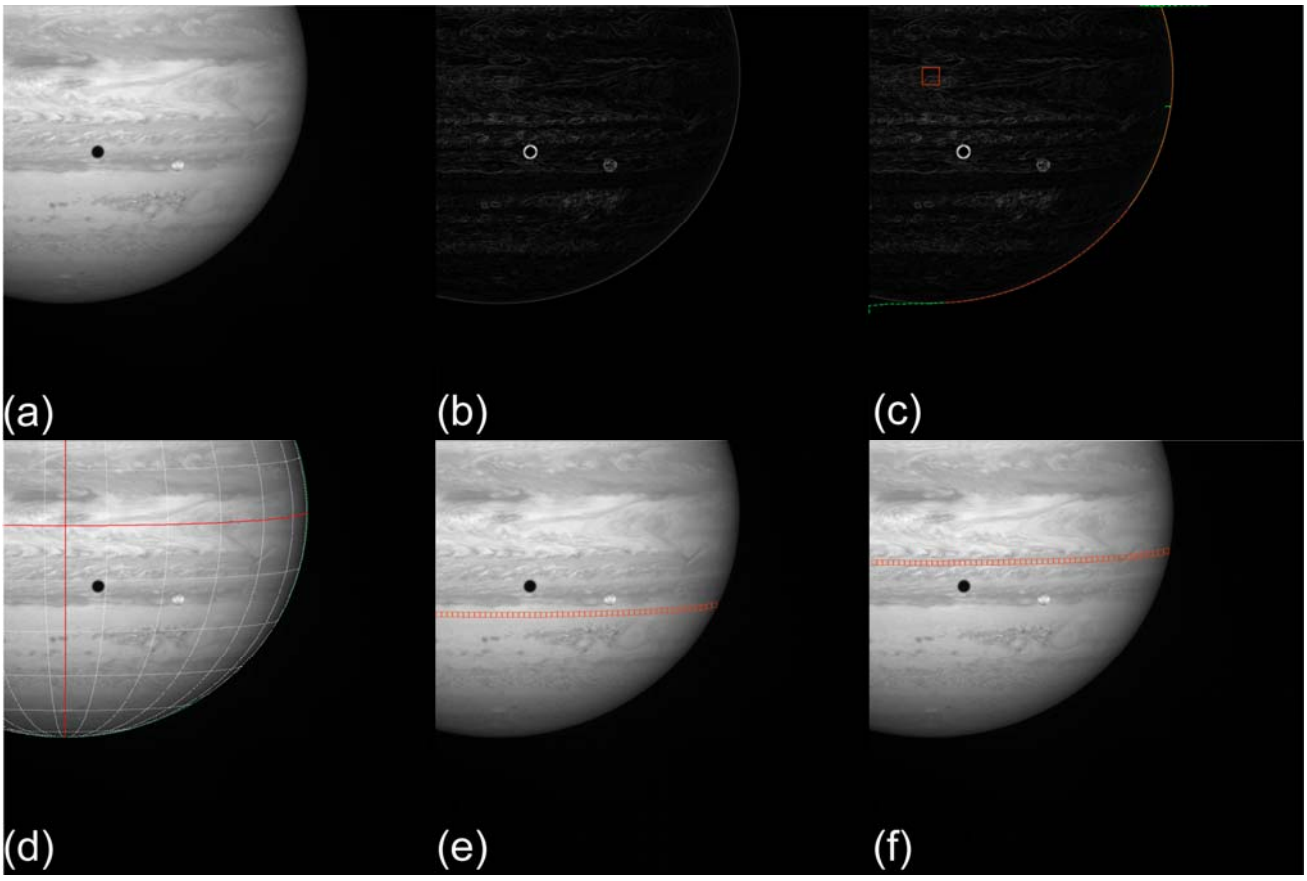

Figure 2.8. Sequence of data reduction process for extracting limb-darkening curves: (a) an example of Jovian image; (b) the same image after enhancing planetary limb with the Sobel filter; (c) detection of planetary limb (red dashed-dotted curves); (d) latitude–longitude coordinates with 15° intervals for both latitude and longitude are superimposed on the image (horizontal and vertical red curves indicate the equator and central meridional longitude (CML), respectively); (e) the area of the STrZ to be extracted is showed by red squares; and (f) same as (e) except for the SEBn.

2.4. Principle of limb-darkening analysis

In this study, we analyze the limb-darkening curves extracted from the latitude bands determined in **Section 2.3**. The analysis of the limb-darkening curve (longitudinal variation of reflectivity at a given latitude band) is a powerful tool to investigate the vertical cloud structure and has been commonly conducted by many researchers (e.g., Tomasko et al., 1978; West et al., 1979; West and Tomasko, 1980; Smith and Tomasko et al., 1984; Satoh and Kawabata, 1992, 1994; Kuehn and Beebe, 1993). In this section, we briefly explain the principle of this analysis.

The sensing atmospheric altitude varies along the limb-darkening curve because of the difference

in path length. Thus, the shape of the limb-darkening curve is strongly affected by the vertical distribution of scattering and absorbing materials in the atmosphere. Temma (2005) illustrated this picture with two simple examples shown in **Figure 2.9**. In Case (1) of **Figure 2.9**, a scattering aerosol layer lies above an absorbing gas layer. Because the path length of incident sunlight is shortest on the disk center (light beam: a), some of sunlight toward the disk center reaches the lower absorbing layer. Consequently, the reflectivity at the case is lower compared with one at the case where there exists only the scattering aerosol layer. In contrast, most of sunlight toward the limb (light beam: b) is reflected back without reaching the lower absorbing gas layer because of the relatively long path length. As a result, the observed limb-darkening curve becomes relatively flat compared with the case where there is no absorbing gas layer. In Case (2) of **Figure 2.9**, a scattering aerosol layer lies beneath an absorbing gas layer. While most of sunlight entering in the absorbing layer near the limb (light beam: c) is absorbed because of the relatively long path length, some of sunlight toward the disk center (light beam: d) is reflected back to space by the underlying scattering aerosol layer. As a result, the observed limb-darkening curve indicates a relatively steep shape.

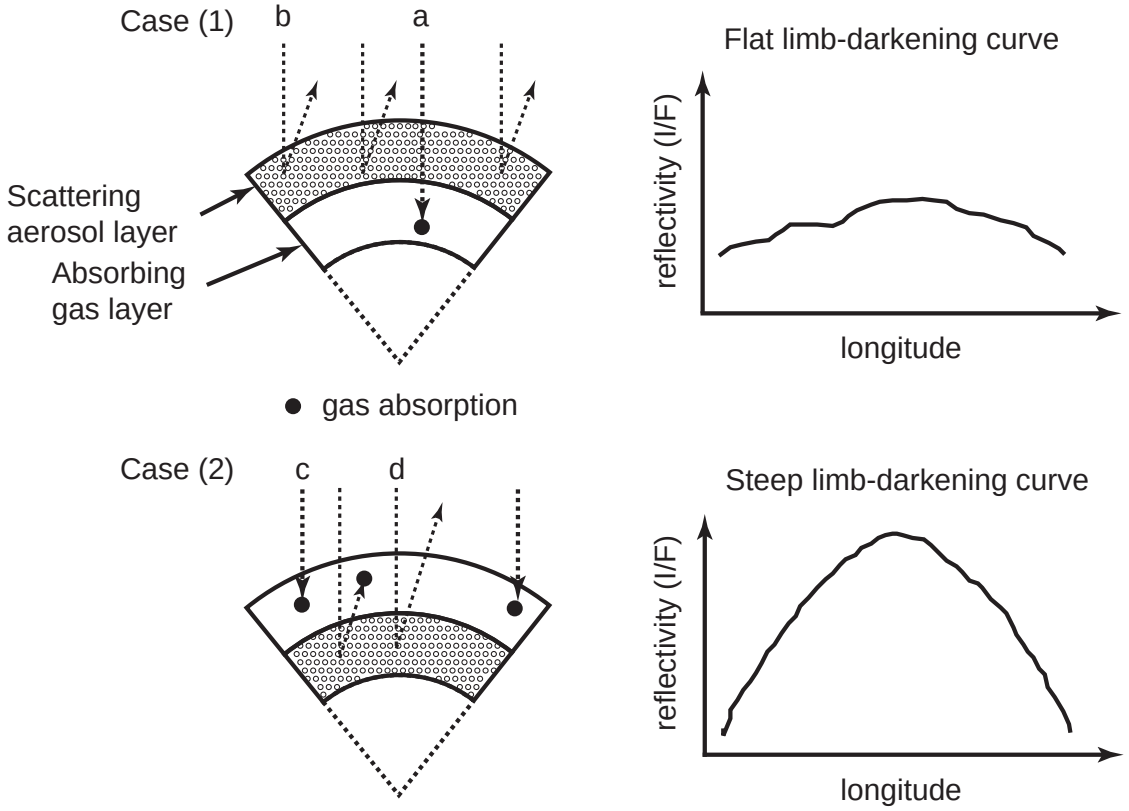

Figure 2.9. The schematic representation illustrating the principle of the limb-darkening analysis. The limb-darkening curve is strongly affected by the vertical distribution of scattering and absorbing materials in the atmosphere (from Temma, 2005).

In addition, the limb-darkening curves at small solar phase angles are sensitive to the backward scattering of aerosols. In contrast, those at large solar phase angles are sensitive to the forward scattering of aerosols. Thus, the solar phase angle dependence of the limb-darkening curves enables us to investigate the zonally-averaged vertical distribution of scattering and absorbing materials, and their optical properties.

2.5. Data selection

For constraining the scattering properties of aerosols in the Jovian atmosphere, we concentrate on analyzing images acquired by the CB2 filter (effective wavelength: 750 nm) and the BL1 filter (455 nm) from among images acquired by a variety of filters because:

- CB2 and BL1 images were taken almost regularly in the solar phase angle range between 0° and 140°;
- CB2 and BL1 images are less sensitive to other atmospheric parameters (i.e. cloud and haze altitudes) than ultraviolet (UV1) and methane band (MT1, MT2, and MT3) images;
- The scattering properties inferred from CB2 and BL1 images enable to make a direct comparison with those inferred from the P10/IPP red-channel (intensity-weighted average wavelength: 640 nm) and blue-channel (440 nm) data with minimizing the effect of wavelength difference.

Selection of CB2 and BL1 images is done so as to satisfy the following criteria:

- sufficient sampling intervals for the solar phase angle (at intervals of ~10°);
- the same gain mode (gain state “2”: 30 [electrons/DN]) for smallest possible image-to-image photometric uncertainties;
- broad coverage of limb for precise determination of the center coordinate;
- relatively similar longitudinal coverage, if at all possible.

We find that the last criterion is of great importance for selection of images to be analyzed. **Figure 2.10**–**Figure 2.13** show limb-darkening curves for the STrZ and the SEBn, which are extracted from CB2 and BL1 images at a solar phase angle of ~19° as an example. The difference in color indicates the different longitudinal coverage. Two limb-darkening curves presented in same color but different symbols represent those extracted from similar longitudinal coverage but acquired at different time.

From **Figure 2.10**–**Figure 2.13**, although the small difference of image acquisition time causes little change in reflectivity, it is clearly seen that the difference in reflectivity due to the difference of longitudinal coverage is not so small except for the reflectivities in the STrZ obtained with CB2 filter (**Figure 2.10**). We also find that such difference lessens as the solar phase angle gets larger. Therefore, we choose the longitudinal coverage which was acquired for all three small solar phase angles (<~19°). Note that Jupiter rotates rapidly near the equator than it does at the pole. The System I (rotation period: $9^h50^m30^s.003$) and the System II (rotation period: $9^h55^m40^s.632$) are used for the SEBn and the STrZ to check the longitudinal coverage for each image, respectively. The relationship among System I, System II and System III (rotation period: $9^h55^m29^s.711$) are given by:

$$\lambda_{\mathrm{I}} = \lambda_{\mathrm{III}} - 217.85 + 7.364(t - t_0), \tag{2.23}$$

$$\lambda_{\mathrm{II}} = \lambda_{\mathrm{III}} - 241.65 - 0.266(t - t_0), \tag{2.24}$$

where λ_{I}, λ_{II}, and λ_{III} denote the System I, System II, and System III longitudes in units of degrees, t is Julian day (JD), and t_0 = 2451545 (JD) or 12:00 UT, January 1, 2000. That is, during the Cassini flyby of Jupiter (approximately six months), clouds in the equator rotated 3.7 extra times than those in the mid-latitudes did.

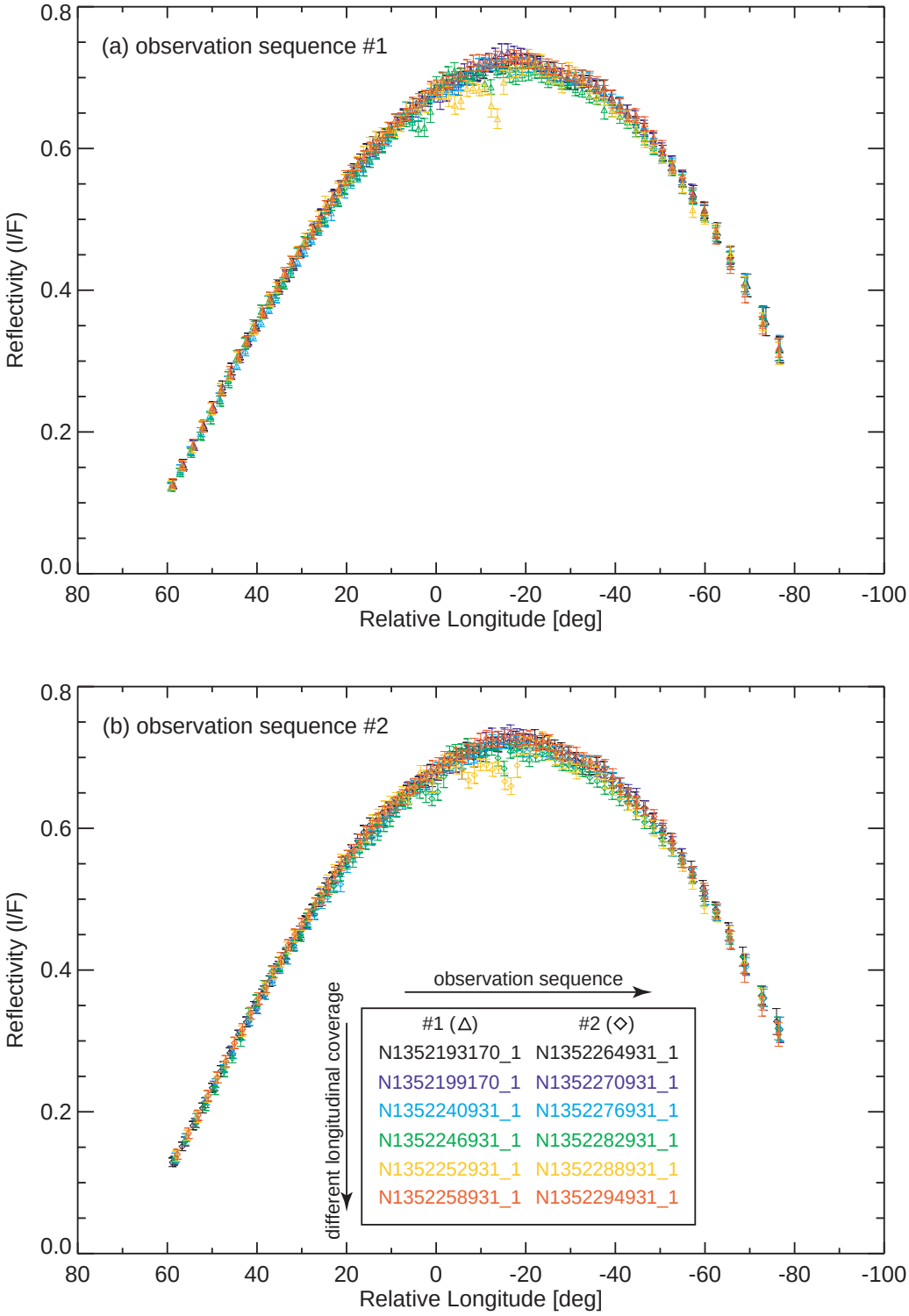

Figure 2.10. Twelve limb-darkening curves for the STrZ which are extracted from CB2 images at a solar phase of ~19°: (a) observation sequence #1 (9:02 UT on November 6–3:18 UT on November 7, 2000); and (b) observation sequence #2 (4:58–13:18 UT on November 7, 2000). The difference in color indicates the different longitudinal coverage. Two limb-darkening curves presented in same color but different symbols represent those extracted from similar longitudinal coverage but acquired at different time.

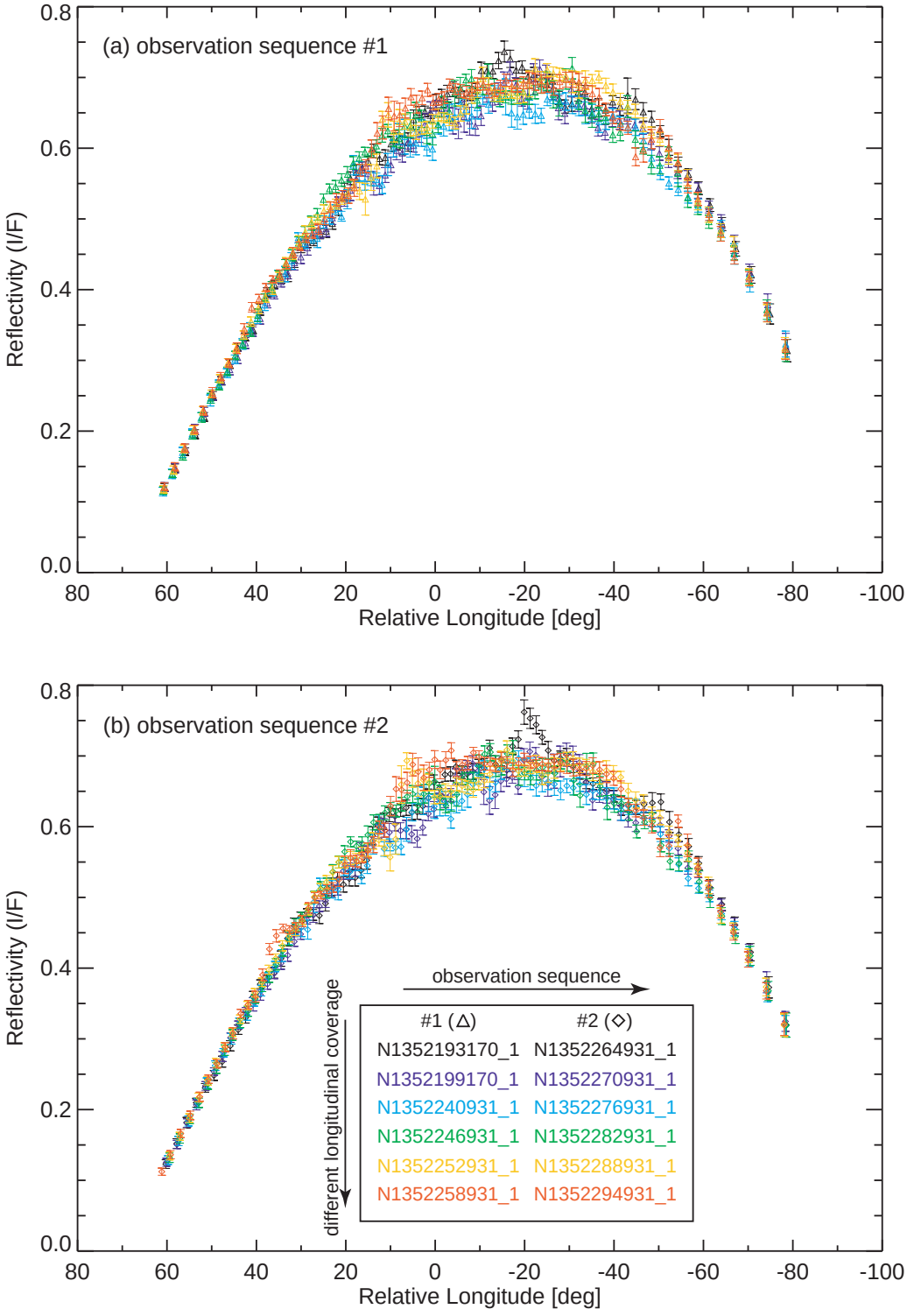

Figure 2.11. Same as Figure 2.10, except for the SEBn.

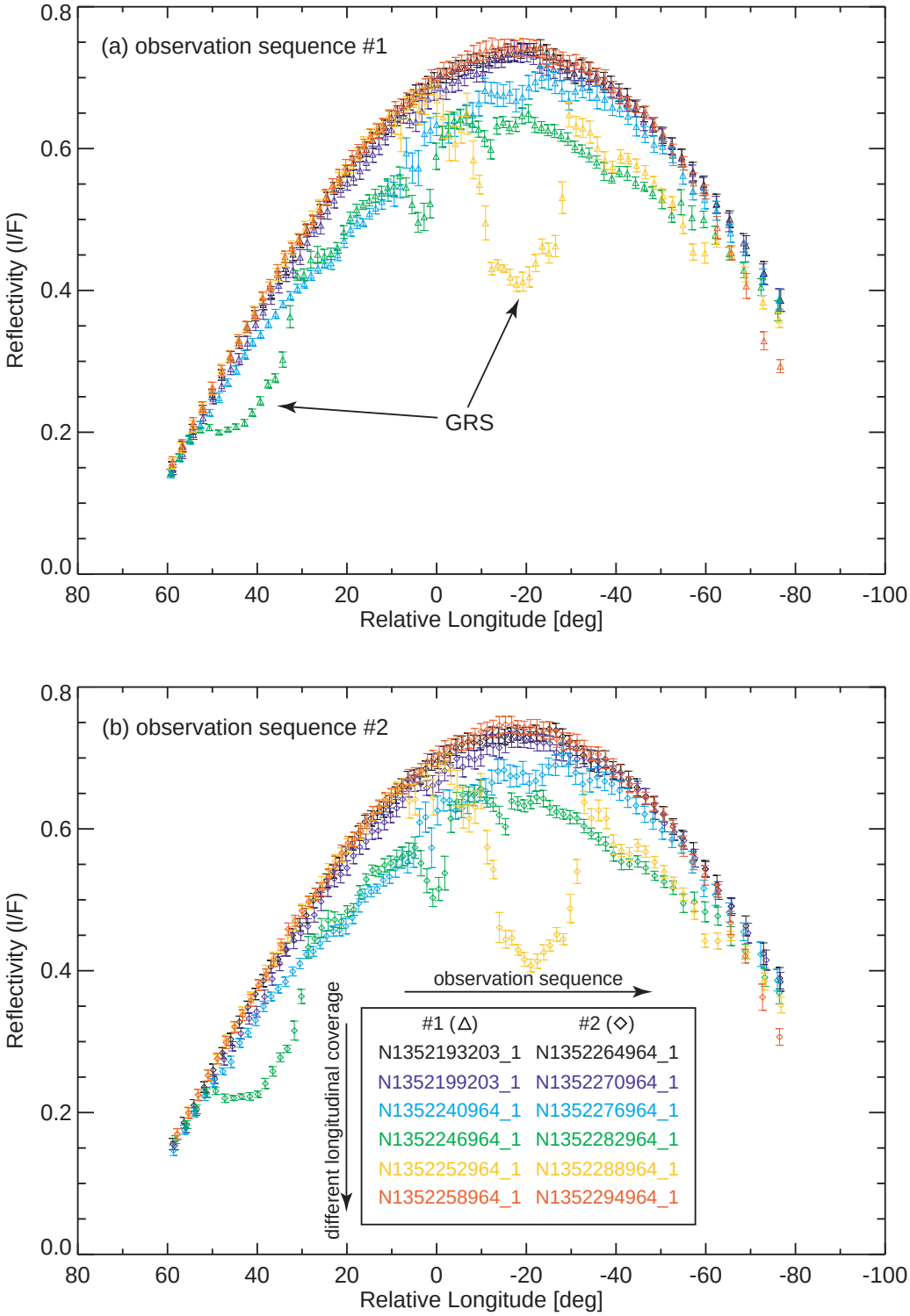

Figure 2.12. Twelve limb-darkening curves for the STrZ which are extracted from BL1 images at a solar phase of ~19°: (a) observation sequence #1 (9:02 UT on November 6–3:18 UT on November 7, 2000); and (b) observation sequence #2 (4:58–13:18 UT on November 7, 2000). The difference in color indicates the different longitudinal coverage. Two limb-darkening curves presented in same color but different symbols represent those extracted from similar longitudinal coverage but acquired at different time.

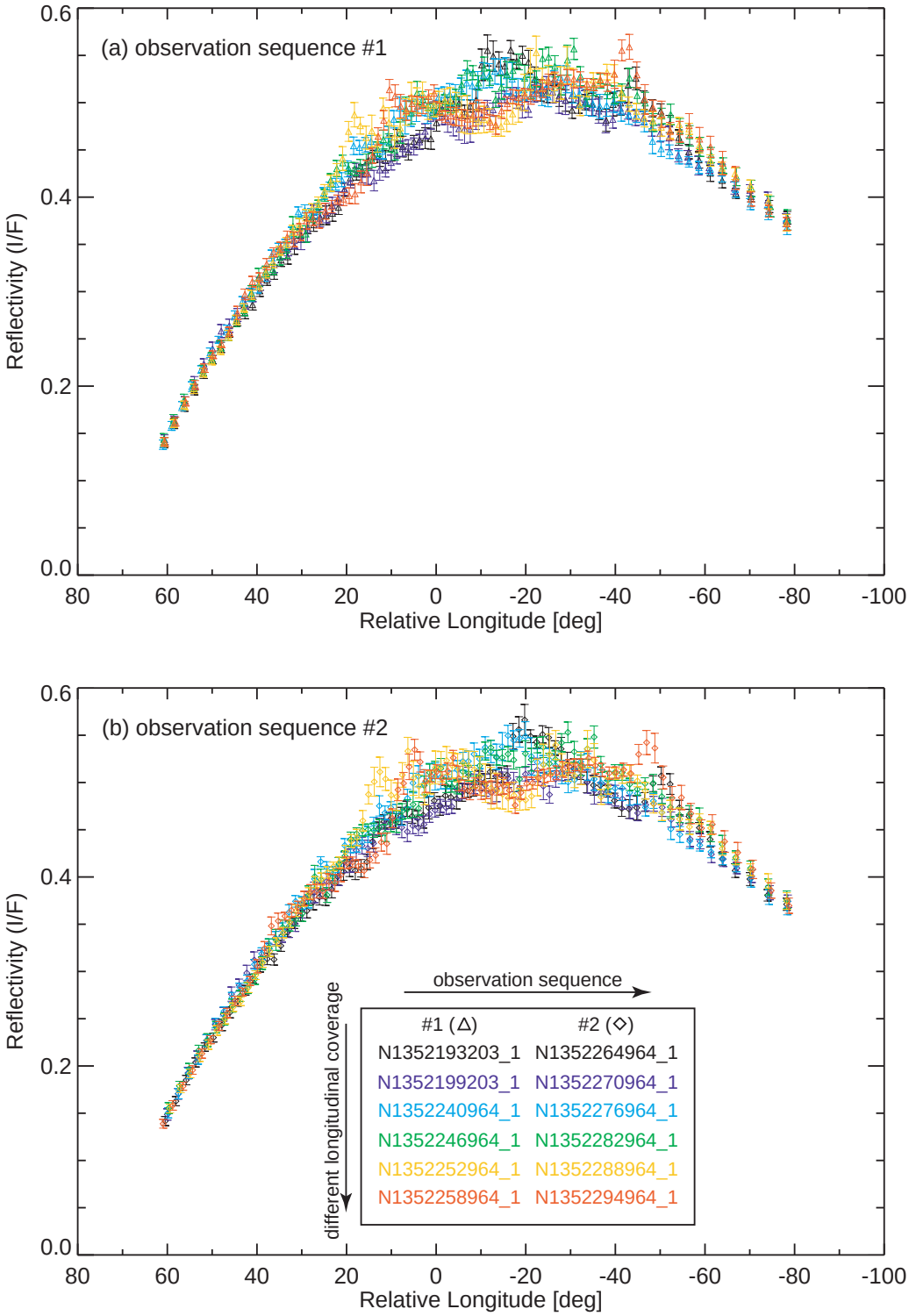

Figure 2.13. Same as Figure 2.12, except for the SEBn.

Figure 2.14–**Figure 2.17** show processed CB2 and BL1 images with the latitude–longitude coordinates used in this study. The areas of the STrZ and the SEBn are indicated by red curves. The selected CB2 and BL1 images for the STrZ and the SEBn are summarized with basic parameters (e.g., observation date, exposure time, and solar phase angle) in **Table 2.7**–**Table 2.10**. Note that no images for solar phase angles in the range from ~20° to ~50° were acquired because of the critical mission operation around the closest approach.

It should be emphasized that the Cassini ISS data sets used in this study have advantages over the P10/IPP data sets:

- the Cassini ISS data sets were acquired at a constant gain setting for all solar phase angles, while the P10/IPP data sets were acquired with three different gain settings (Tomasko et al., 1978);
- the transmission bandwidth of the ISS CB2 filter is so narrow ($\Delta\lambda^*$ = 10 nm) that we can infer more monochromatic optical properties of aerosols than the P10/IPP red-channel ($\Delta\lambda$ = 102 nm), although the transmission bandwidth of the ISS BL1 filter ($\Delta\lambda$ = 76 nm) is not so different from that of the P10/IPP blue-channel ($\Delta\lambda$ = 85 nm).

* The transmission width of each filter $\Delta\lambda$ is calculated by

$$\Delta\lambda = \int T_0(\lambda)T_1(\lambda)T_2(\lambda)QE(\lambda)\mathrm{d}\,\lambda. \quad (2.25)$$

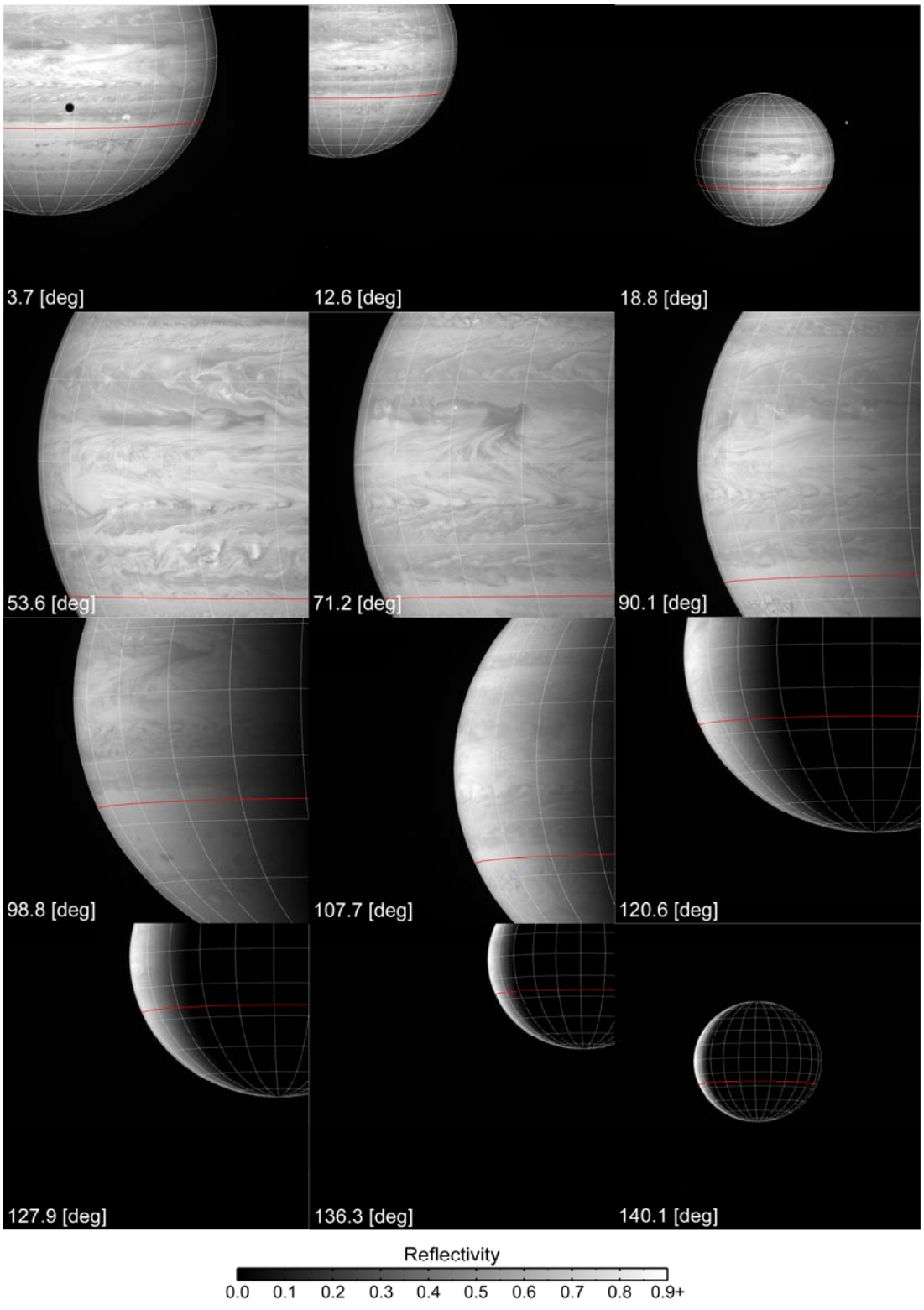

Figure 2.14. The processed Jovian images in CB2 used for analysis of the STrZ. The bottom-left number denotes solar phase angle in units of degrees. Latitude–longitude coordinates with 15° intervals for both latitude and longitude are superimposed on these images. The red curve indicates –25° planetographic latitude in the STrZ.

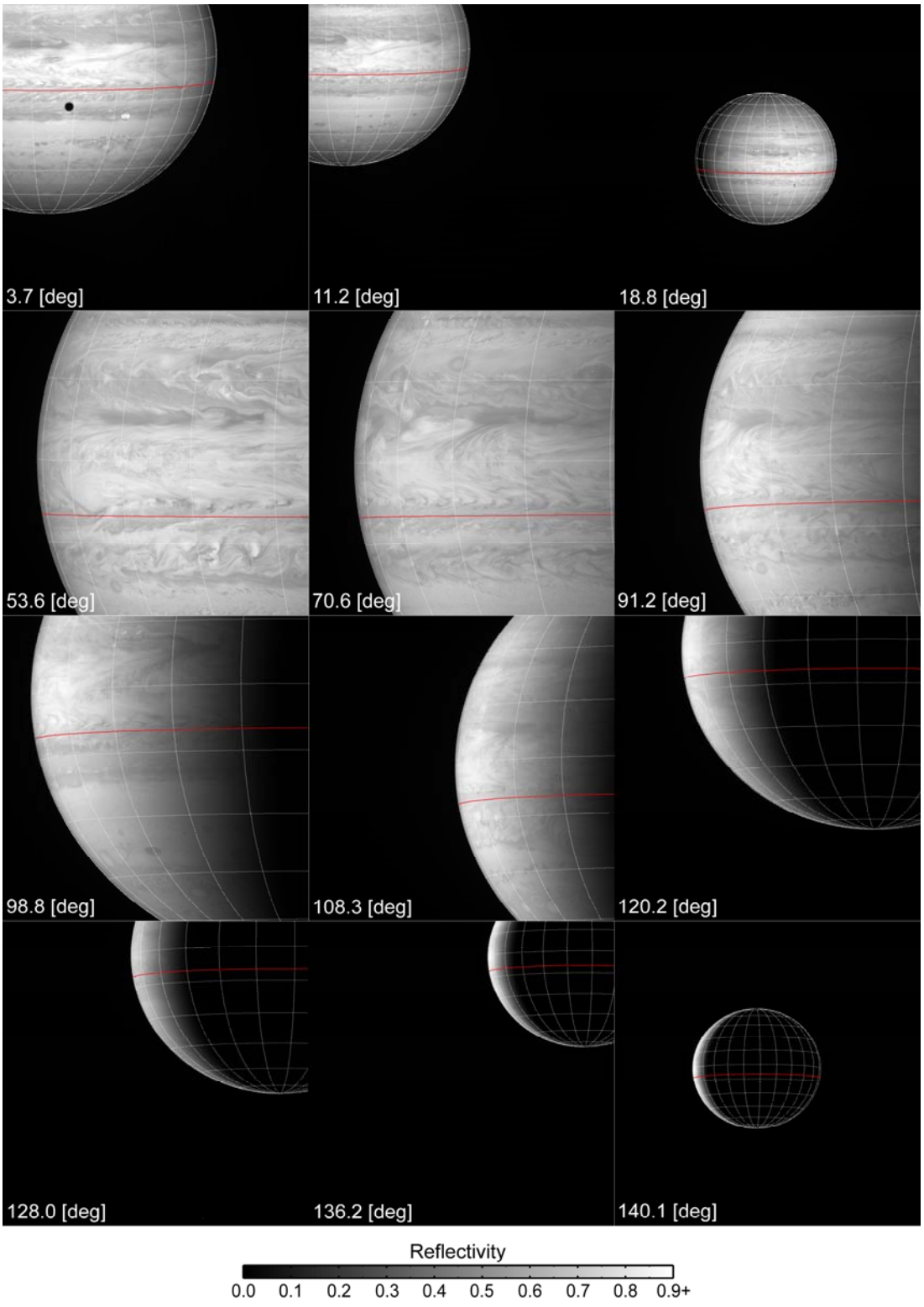

Figure 2.15. The processed Jovian images in CB2 used for analysis of the SEBn. The bottom-left number denotes solar phase angle in units of degrees. Latitude–longitude coordinates with 15° intervals for both latitude and longitude are superimposed on these images. The red curve indicates –10° planetographic latitude in the SEBn.

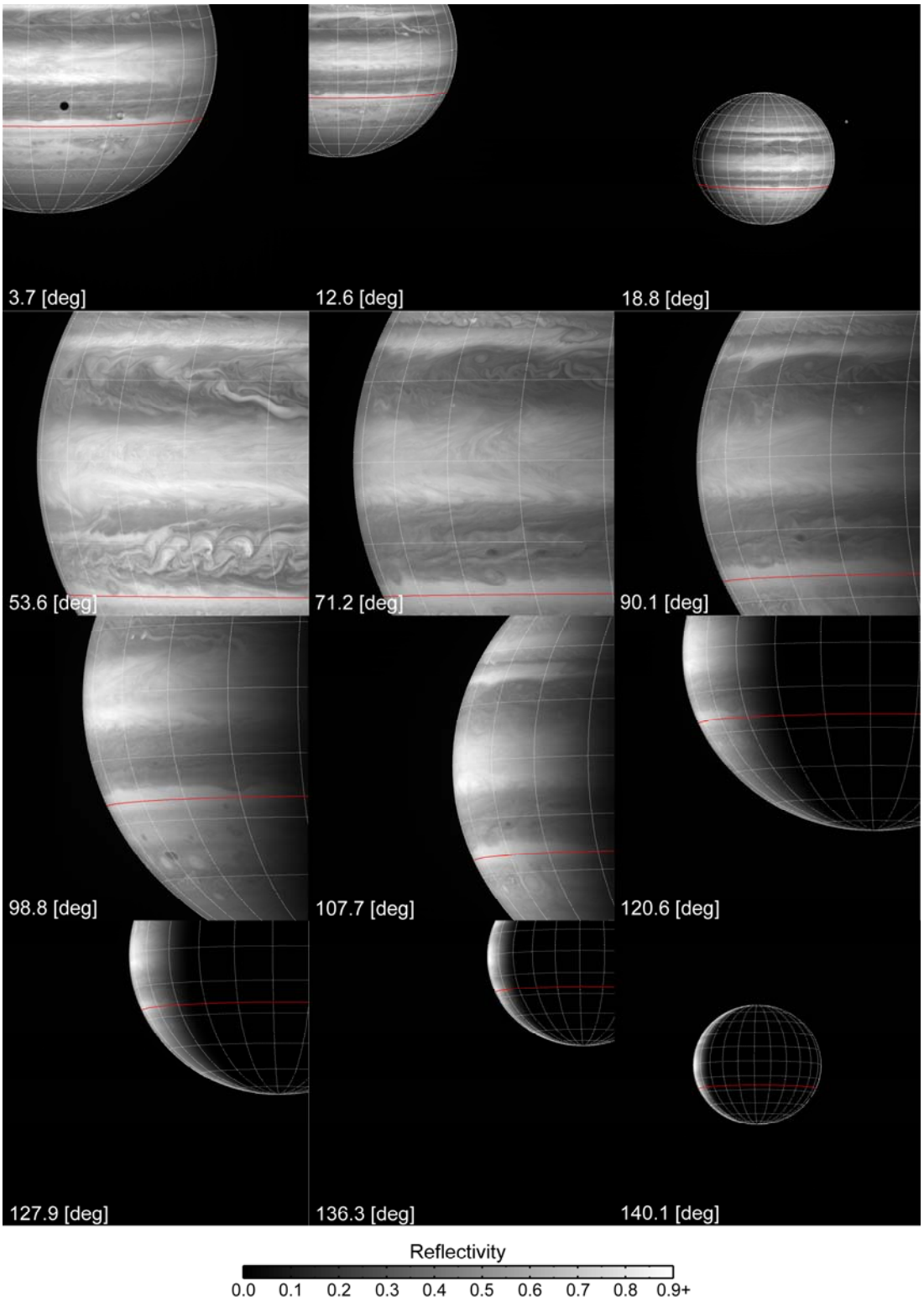

Figure 2.16. Same as Figure 2.14, except for the Jovian images in BL1.

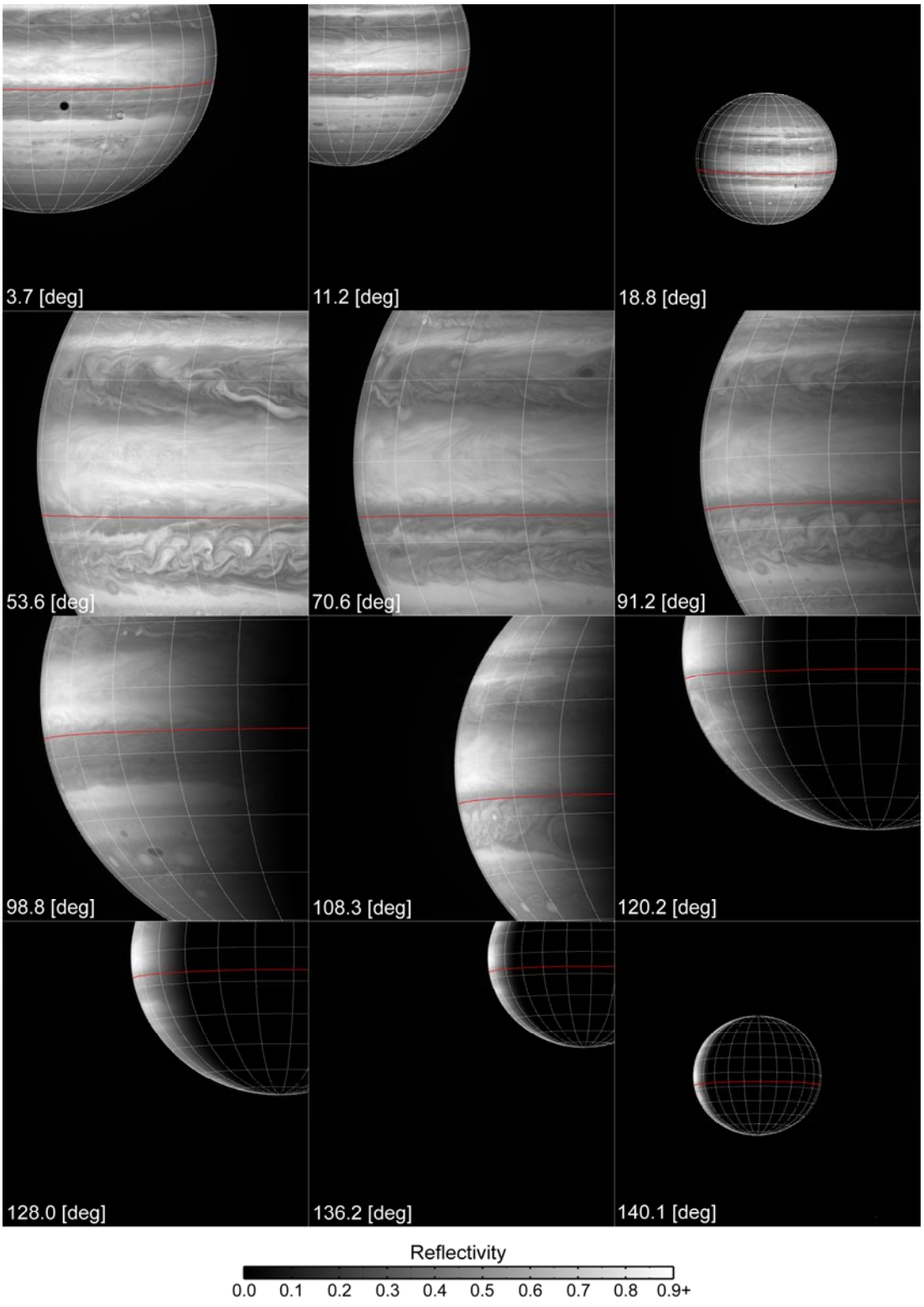

Figure 2.17. Same as Figure 2.15, except for the Jovian images in BL1.

Table 2.7. Summary of the CB2 images for the STrZ used in this study.

Image ID	Observation date	Exposure time [ms]	Solar phase angle [degrees]	Spatial resolution [km/pixel]	Longitudinal coverage* [degrees]	Averaging size ($n \times n$)
N1352270931_1.IMG	2000.11.7	820	18.8	303.2	162–297	5
N1354204200_1.IMG	2000.11.29	1000	12.6	183.0	194–286	9
N1355170848_1.IMG	2000.12.10	1000	3.7	125.4	203–296	13
N1356762148_1.IMG	2000.12.29	1200	53.6	59.0	71–133	25
N1357027730_1.IMG	2001.1.1	1000	71.2	59.7	212–272	25
N1357350916_1.IMG	2001.1.5	1200	90.1	66.9	211–269	23
N1357538658_1.IMG	2001.1.7	1000	98.8	73.7	293–352	21
N1357780751_1.IMG	2001.1.10	1200	107.7	84.2	212–263	17
N1358317720_1.IMG	2001.1.16	1200	120.6	112.0	222–259	13
N1358855829_1.IMG	2001.1.22	1000	127.9	142.9	244–273	11
N1360177398_1.IMG	2001.2.6	1000	136.3	223.1	236–259	7
N1361962971_1.IMG	2001.2.27	460	140.1	334.4	225–243	5

Table 2.8. Summary of the CB2 images for the SEBn used in this study.

Image ID	Observation date	Exposure time [ms]	Solar phase angle [degrees]	Spatial resolution [km/pixel]	Longitudinal coverage* [degrees]	Averaging size ($n \times n$)
N1352258931_1.IMG	2000.11.7	820	18.8	303.9	40–178	5
N1354425363_1.IMG	2000.12.2	1000	11.2	169.5	258–353	9
N1355170848_1.IMG	2000.12.10	1000	3.7	125.4	201–294	13
N1356762148_1.IMG	2000.12.29	1200	53.6	59.0	71–134	25
N1357018786_1.IMG	2001.1.1	1000	70.6	59.6	120–183	25
N1357373277_1.IMG	2001.1.5	1200	91.2	67.7	73–134	23
N1357539800_1.IMG	2001.1.7	1000	98.8	73.7	303–4	21
N1357800891_1.IMG	2001.1.10	1200	108.3	85.2	53–105	17
N1358297880_1.IMG	2001.1.16	1200	120.2	110.9	20–60	13
N1358865549_1.IMG	2001.1.22	1000	128.0	143.4	339–11	11
N1360148238_1.IMG	2001.2.6	1000	136.2	221.3	301–325	7
N1361957571_1.IMG	2001.2.27	460	140.1	334.1	169–188	5

* Longitudinal coverage is presented in System III.

Table 2.9. Summary of the BL1 images for the STrZ used in this study.

Image ID	Observation date	Exposure time [ms]	Solar phase angle [degrees]	Spatial resolution [km/pixel]	Longitudinal coverage* [degrees]	Averaging size ($n \times n$)
N1352270964_1.IMG	2000.11.7	260	18.8	303.2	162–297	5
N1354204098_1.IMG	2000.11.29	260	12.6	183.0	193–285	9
N1355170728_1.IMG	2000.12.10	320	3.7	125.4	202–294	13
N1356762029_1.IMG	2000.12.29	380	53.6	59.0	70–132	25
N1357027693_1.IMG	2001.1.1	380	71.2	59.7	212–271	25
N1357350879_1.IMG	2001.1.5	380	90.1	66.9	210–269	23
N1357538402_2.IMG	2001.1.7	460	98.8	73.7	291–350	21
N1357780714_1.IMG	2001.1.10	460	107.7	84.2	211–262	17
N1358317687_1.IMG	2001.1.16	380	120.6	112.0	222–259	13
N1358855796_1.IMG	2001.1.22	320	127.9	142.9	243–273	11
N1360177365_1.IMG	2001.2.6	320	136.3	223.1	236–258	7
N1361962938_1.IMG	2001.2.27	150	140.1	334.4	225–243	5

Table 2.10. Summary of the BL1 images for the SEBn used in this study.

Image ID	Observation date	Exposure time [ms]	Solar phase angle [degrees]	Spatial resolution [km/pixel]	Longitudinal coverage* [degrees]	Averaging size ($n \times n$)
N1352258964_1.IMG	2000.11.7	260	18.8	303.9	40–179	5
N1354425261_1.IMG	2000.12.2	260	11.2	160.6	257–352	9
N1355170728_1.IMG	2000.12.10	320	3.7	125.4	200–293	13
N1356762029_1.IMG	2000.12.29	380	53.6	59.0	70–133	25
N1357018749_1.IMG	2001.1.1	380	70.6	59.6	120–182	25
N1357373240_1.IMG	2001.1.5	380	91.2	67.7	73–133	23
N1357539544_1.IMG	2001.1.7	460	98.8	73.7	301–1	21
N1357800854_1.IMG	2001.1.10	460	108.3	85.2	53–104	17
N1358297847_1.IMG	2001.1.16	380	120.2	110.9	19–59	13
N1358865516_1.IMG	2001.1.22	320	128.0	143.4	339–10	11
N1360148205_1.IMG	2001.2.6	320	136.2	221.3	301–324	7
N1361957538_1.IMG	2001.2.27	150	140.1	334.1	169–188	5

* Longitudinal coverage is presented in System III.

2.6. Characteristics of CB2 and BL1 limb-darkening curves

Figure 2.18 shows the reflectivity variations in CB2 and BL1 for the STrZ and the SEBn as a function of μ_0 for 12 solar phase angles.

As a first step, we describe the characteristics of reflectivity variations in CB2 for the STrZ (**Figure 2.18a**) because these are the easiest to understand compared with the others. As is known through ground-based observations, the reflectivity varies almost linearly with μ_0 at small solar phase angles (i.e., 3.7° and 12.6°). It is found that the same is true for the data at a solar phase angle of 18.8°. In other words, the reflected sunlight from Jupiter, if observed at small solar phase angles, follows the simple Lambert's law. Conversely, as solar phase angle gets larger than 53.6°, the deviation from the Lambert surface appears to be significant. The least bright peak is found for a solar phase angle of 98.8°: the peak value of the reflectivity increases as the solar phase angle gets smaller or larger than 98.8°. These characteristics are similar to those of residual data sets, to a certain degree, although the solar phase angle for which the least bright peak is seen is different from each other: 108.3° for the CB2/SEBn data set, 98.8° for the BL1/STrZ data set, and 70.6° for the BL1/SEBn data set. The comparisons among four data sets are discussed in detail below.

The STrZ seen in CB2 and BL1

For three small solar phase angles, the difference in peak reflectivity between CB2 and BL1 ($I/F_{\mathrm{peak,CB2}} - I/F_{\mathrm{peak,BL1}}$) is not so significant (≤ 0.013). As the solar phase angle gets larger than 53.6°, however, such difference becomes larger, reaching a value of 0.19 at the solar phase angle of 140.1°. The remarkable difference in peak reflectivity at large solar phase angles should be explained by wavelength dependence of the forward scattering of cloud particles and/or the optical (scattering) properties of the stratospheric haze. In addition, the slopes of reflectivity variations in BL1 for two smallest solar phase angles at 3.7° and 12.6° are found to be more gradual with decreasing μ_0, which is not seen in CB2.

The SEBn seen in CB2 and BL1

Although the reflectivity variations in CB2 and BL1 for the SEBn do not necessarily show smooth curves due to the existence of small localized cloud patterns, which are more obvious in small solar phase angles, there are also several notable characteristics through the comparison between the CB2/SEBn data set and the BL1/SEBn data set. It is highly noticeable that the slopes of reflectivity variations in BL1 for two solar phase angles at 3.7° and 12.6° are significantly gradual for the entire

μ_0 range and these curves seem not to intercept with those for the other solar phase angles around μ_0 ~ 0, which is not seen in CB2. The difference in peak reflectivity between CB2 and BL1 ranges from 0.14 at the solar phase angle of 18.8° to 0.245 at the solar phase angle of 140.1°. Such difference for the SEBn is found to be always larger than that for the STrZ over the entire solar phase angles.

Visual difference in CB2 between the STrZ and the SEBn

The reflectivity variations in CB2 for the SEBn are similar to those both in CB2 for the STrZ and in BL1 for the STrZ rather than those in BL1 for the SEBn. For three small solar phase angles, the values of peak reflectivity in the STrZ are somewhat higher than those in the SEBn by up to 0.04 (at the solar phase angle of 18.8°), even though μ_0 at the peak value for the STrZ is always smaller than that for the SEBn. Conversely, as the solar phase angle is larger than 53.6°, the values of peak reflectivity in the STrZ become smaller than those in the SEBn by up to 0.03 (at the solar phase angle of 140.1°). It seems that the peak reflectivities at large solar phase angles in CB2 would simply depend on μ_0.

Visual difference in BL1 between the STrZ and the SEBn

As mentioned above, the difference of reflectivity in BL1 between the STrZ and the SEBn is significantly apparent in particular for three small solar phase angles. In contrast, such difference decreases with increasing solar phase angle, reaching a value of 0.02 at the solar phase angle of 140.1°. Although μ_0 at the peak value for the STrZ is always smaller than that for the SEBn, the values of peak reflectivity in the STrZ are always higher than those in the SEBn over the entire solar phase angles unlike the CB2 case. This would suggest that the reflectivity variations for all 12 solar phase angles are affected in varying degrees by blue absorbent(s) that may be more abundant in the SEBn than in the STrZ in the Jovian atmosphere beyond the effect of μ_0.

A part of characteristics discussed above can be read from the P10/IPP red- and blue-channel data for the STrZ and the SEBn at seven solar phase angles (12°, 23°, 34°, 109°, 120°, 127°, and 150°) shown in **Figure 2.19**. As is clear in **Figure 2.18** and **Figure 2.19**, the Cassini ISS data sets have a better solar phase angle coverage with a much smaller gap in solar phase angles (19°–54°) than the P10/IPP's larger gap (34°–109°).

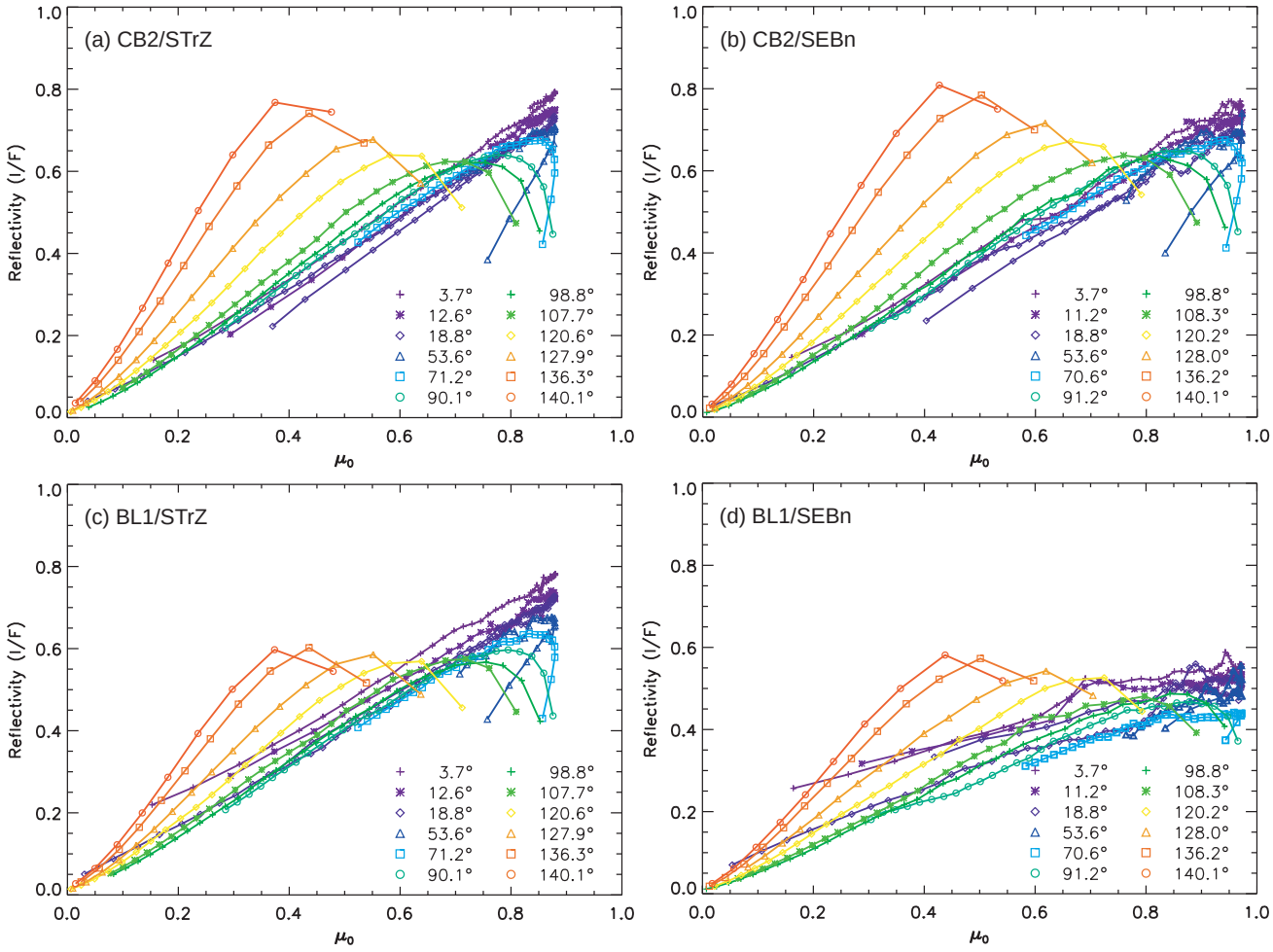

Figure 2.18. The reflectivity variations as a function of μ_0 and solar phase angle α from the Cassini ISS observations: (a) the reflectivity variations in CB2 for the STrZ; (b) those in CB2 for the SEBn; (c) those in BL1 for the STrZ; and (d) those in BL1 for the SEBn. The bottom-right numbers denote solar phase angles in units of degrees. Note that the data points with μ_0 (and also μ) smaller than 0.15 are not used for radiative transfer calculation.

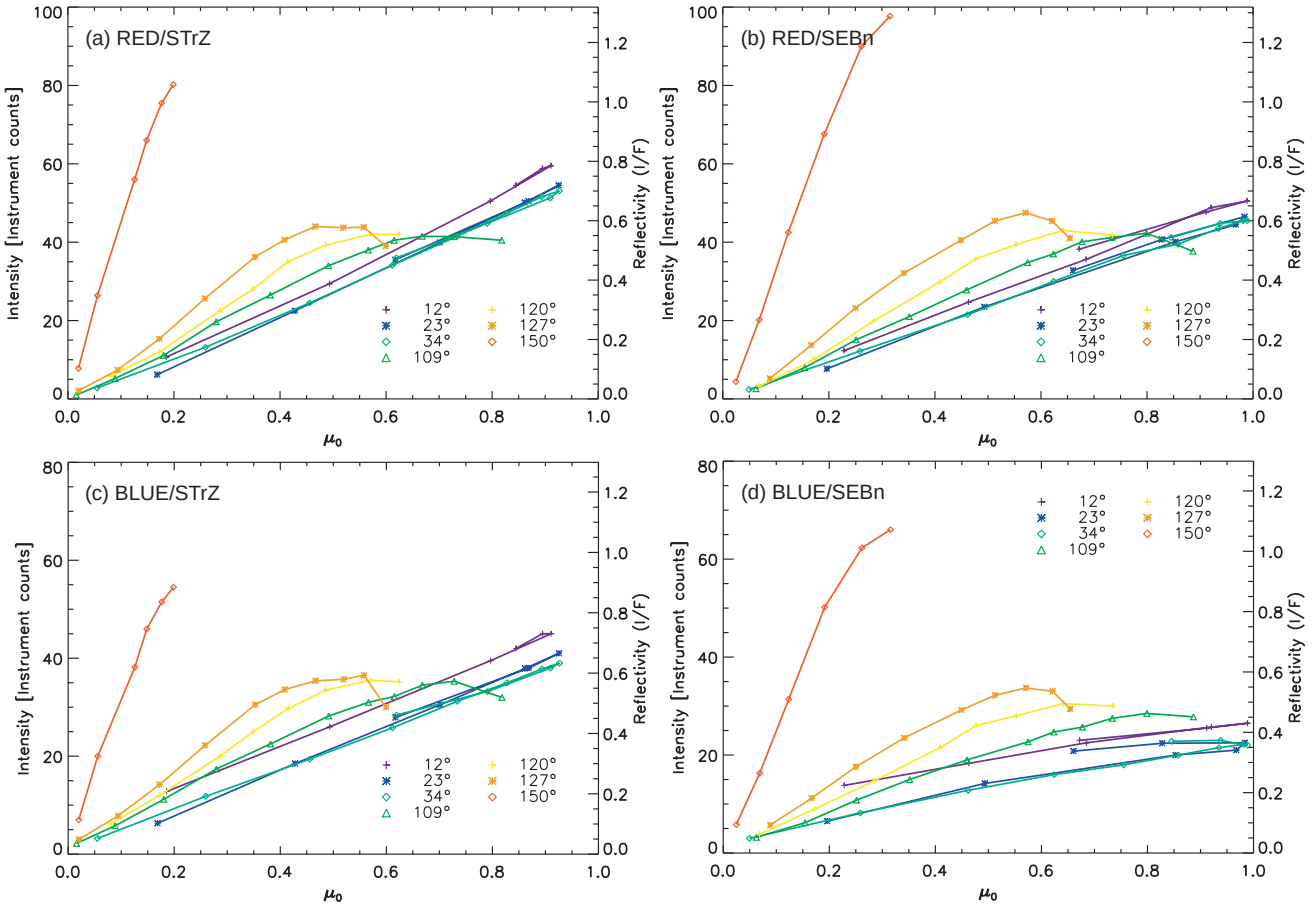

Figure 2.19. The intensity variations as a function of μ_0 and solar phase angle α from the Pioneer 10 IPP observations: (a) the intensity variations in red-channel for the STrZ; (b) those in red-channel for the SEB; (c) those in blue-channel for the STrZ; and (d) those in blue-channel for the SEBn. The bottom-right numbers denote solar phase angles in units of degrees. The reflectivity is calculated with the nominal value of a conversion factor F_p (Tomasko et al., 1978).

Figure 2.20 shows the coverage curves, in the μ_0–μ space, for the CB2 data in the STrZ and the SEBn used in this study. Note that only a small portion of these diagrams, as shown by plots at solar phase angles of 3.7° and 12.6°, can be obtained from observations by ground-based telescopes and the HST. The CB2 (also BL1) data sets for both the STrZ and the SEBn fully cover the μ_0–μ space where both μ_0 and μ of data points are larger than 0.15. The data set for the SEBn covers more broad range of μ_0–μ space compared with the data set for the STrZ in area where either μ_0 or μ of data points is larger than ~0.9. This is because the Cassini observations were conducted at nearly equatorial plane. For comparison, the relationships between μ_0 and μ for the P10/IPP red-channel data in the STrZ and the SEBn are shown in **Figure 2.21**. In the case of the scattering geometries over a planetary disk as viewed with large solar phase angle (>140°), very few points are found to satisfy the condition (both μ_0 and μ of data point are larger than 0.15) (courtesy of Dr. T. Satoh). This can also be read from plots at the solar phase angle of 150° in **Figure 2.21**. This means that simulation of high solar phase angle (>140°) data by the radiative transfer calculation based on the plane-parallel approximation should be treated carefully or possibly avoided.

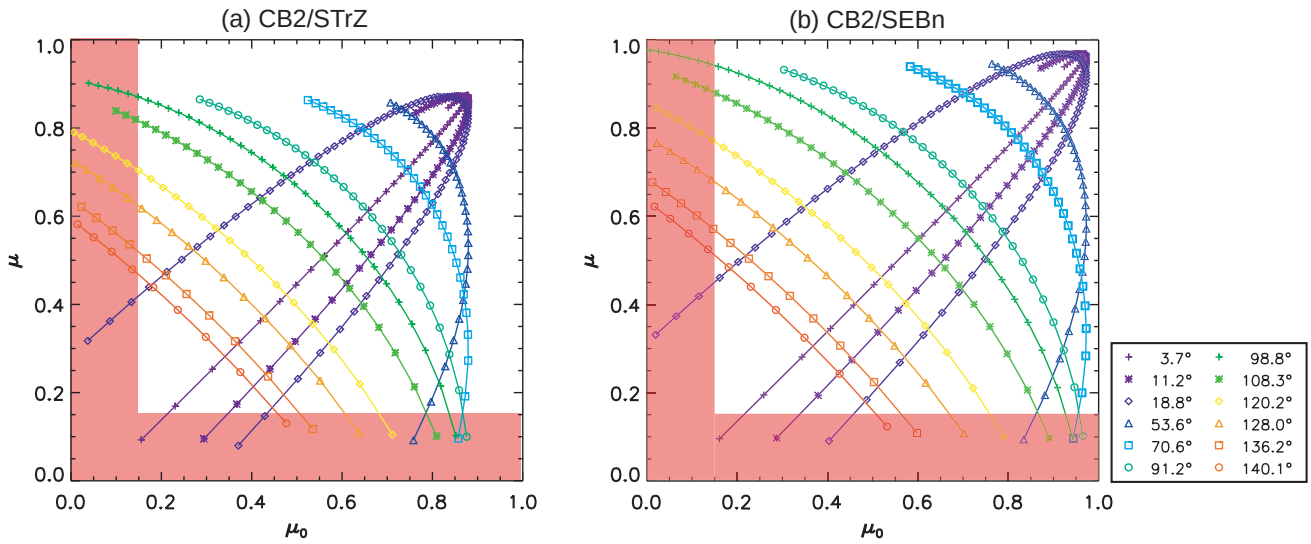

Figure 2.20. The coverage curves in the μ_0–μ space for the CB2 data used in this study: (a) the STrZ; and (b) the SEBn. Only a small portion of the combination of μ_0 and μ shown by purple pluses (3.7°) and blue asterisks (12.6°) can be observed by ground-based telescopes and the HST. Note that the data points with either μ_0 and μ smaller than 0.15 in red shaded area are not used for radiative transfer calculation because such geometries prevent from using a plane-parallel approximation.

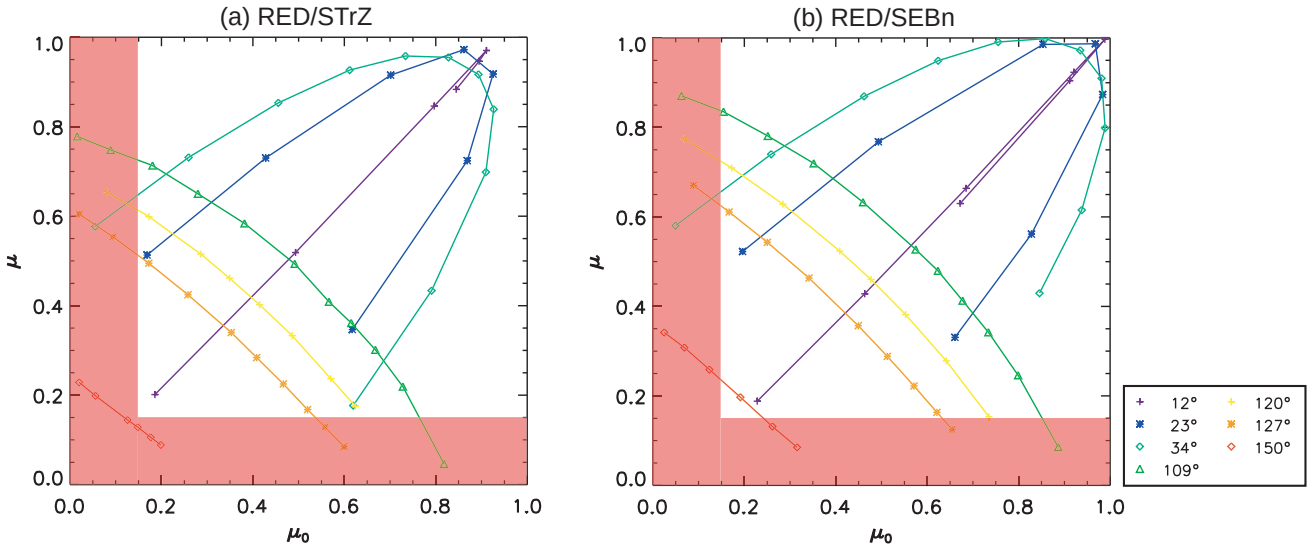

Figure 2.21. The coverage curves in the μ_0–μ space for the Pioneer 10 IPP red-channel data: (a) the STrZ; and (b) the SEBn. In the case of the scattering geometries for a solar phase angle of 150° in the SEBn, there is only one point which satisfies the criteria (both μ_0 and μ of data point are larger than 0.15) for use of a plane-parallel approximation.

Chapter 3

Radiative transfer modeling

In this chapter, we explain fundamentals of radiative transfer in a scattering atmosphere and a numerical solution approach using the doubling and adding method in **Section 3.1**. The accuracy of our radiative transfer code used in this study is validated in **Section 3.2**. The Jovian cloud model for reproducing the observed limb-darkening curves at a wide variety of solar phase angles discussed in **Section 2.6** is described in detail in **Section 3.3**. Finally, the fitting strategy is mentioned in **Section 3.4**.

3.1. Solution of radiative transfer in a scattering atmosphere

3.1.1. General description of radiative transfer in a plane-parallel atmosphere

In practice, when dealing with local radiation fields, it is appropriate to consider the planetary atmosphere as a vertical stack of layers that are horizontally uniform and infinite. This is so-called plane-parallel approximation. In this approximation, the atmospheric parameters (e.g., temperature, composition, and aerosol contents) vary in vertical (i.e., height and pressure) but homogeneous in horizontal. Consequently, the radiation field is also a function of the height. In this section, we explain the fundamental equation governing the radiative transfer of direct and diffuse solar radiation and thermal radiation in plane-parallel atmospheres. The term *diffuse* is associated with multiple scattering processes and is differentiated from *direct* solar radiation. As **Figure 3.1** shows, the differential change of diffuse intensity ΔI emergent from below the layer in a differential thickness Δz is caused by the following four processes: (1) reduction from the extinction attenuation; (2) increase from the single scattering of the unscattered direct solar flux from the direction $-\Omega_0(-\mu_0, \phi_0)$ to $\Omega(\mu, \phi)$; (3) increase from multiple scattering of the diffuse intensity from

directions $\Omega'(\mu', \phi')$ to $\Omega(\mu, \phi)$; and (4) increase from emission within the layer in the direction $\Omega(\mu, \phi)$

$$\begin{aligned}\Delta I(z;\mu,\phi) = &-\frac{\sigma_e(z)n(z)\Delta z}{\mu} I(z;\mu,\phi) \\ &+\frac{\sigma_s(z)n(z)\Delta z}{\mu}\pi F_0 \exp\left(-\int_z^\infty \sigma_e(z)n(z)\Delta z/\mu_0\right)\frac{P(\mu,\phi;-\mu_0,\phi_0)}{4\pi} \\ &+\frac{\sigma_s(z)n(z)\Delta z}{\mu}\int_0^{2\pi}\int_{-1}^{1} I(z;\mu',\phi')\frac{P(\mu,\phi;\mu',\phi')}{4\pi}d\mu' d\phi' \\ &+\frac{\sigma_a(z)n(z)\Delta z}{\mu} B[T(z)],\end{aligned} \tag{3.1}$$

where σ_e, σ_s, and σ_a denote the extinction, scattering, and absorption cross sections of a sample of particles, n is the number density, z is the height, πF_0 is the incident solar flux, $P(\mu, \phi; \mu', \phi')$ is the scattering phase function which describes the amount of light scattered from the incoming direction $\Omega'(\mu', \phi')$ to the outgoing direction $\Omega(\mu, \phi)$, $B[T(z)]$ is the Planck function given by temperature $T(z)$, and definitions of incoming direction $\Omega'(\mu', \phi')$ and outgoing direction $\Omega(\mu, \phi)$ are described in **Figure 3.2**.

By introducing the optical thickness τ and the single scattering albedo ω, which is the ratio of the scattering cross section to the extinction cross section,

$$\omega \equiv \sigma_s/\sigma_e = (1-\sigma_a)/\sigma_e, \tag{3.2}$$

$$\tau \equiv \int_z^\infty \sigma_e(z)n(z)dz, \tag{3.3}$$

equation (3.1) can be rewritten as follows:

$$\begin{aligned}\mu\frac{dI(\tau;\mu,\phi)}{d\tau} &\equiv I(\tau;\mu,\phi) - J(\tau;\mu,\phi) \\ &= I(\tau;\mu,\phi) \\ &\quad -\frac{\omega}{4\pi}\pi F_0 P(\mu,\phi;-\mu_0,\phi_0)\exp(-\tau/\mu_0) \\ &\quad -\frac{\omega}{4\pi}\int_0^{2\pi}\int_{-1}^{1} I(\tau;\mu',\phi')P(\mu,\phi;\mu',\phi')d\mu' d\phi' \\ &\quad -(1-\omega)B[T(\tau)],\end{aligned} \tag{3.4}$$

where $J(\tau; \mu, \phi)$ is the source function. This is the general ratidative transfer equation in plane-parallel atmospheres to be solved. When dealing with the planetary applications in the visible wavelength region, it is practical to ignore the last term on the right-hand side of equation (3.4) as the thermal emission from the ground or the atmosphere is orders of magnitude weaker than the solar

radiation at such wavelengths. Henceforth, we omit this term in the following description.

The scattering phase function $P(\mu, \phi; \mu', \phi')$ is generally written as a function of the scattering angle Θ. The scattering angle Θ is the angle between the incoming direction $\Omega'(\mu', \phi')$ and the outgoing direction $\Omega(\mu, \phi)$, as shown in **Figure 3.2**, can be written as:

$$\cos\Theta = \mu\,\mu' + \sqrt{(1-\mu^2)(1-\mu'^2)}\cos(\phi - \phi'). \tag{3.5}$$

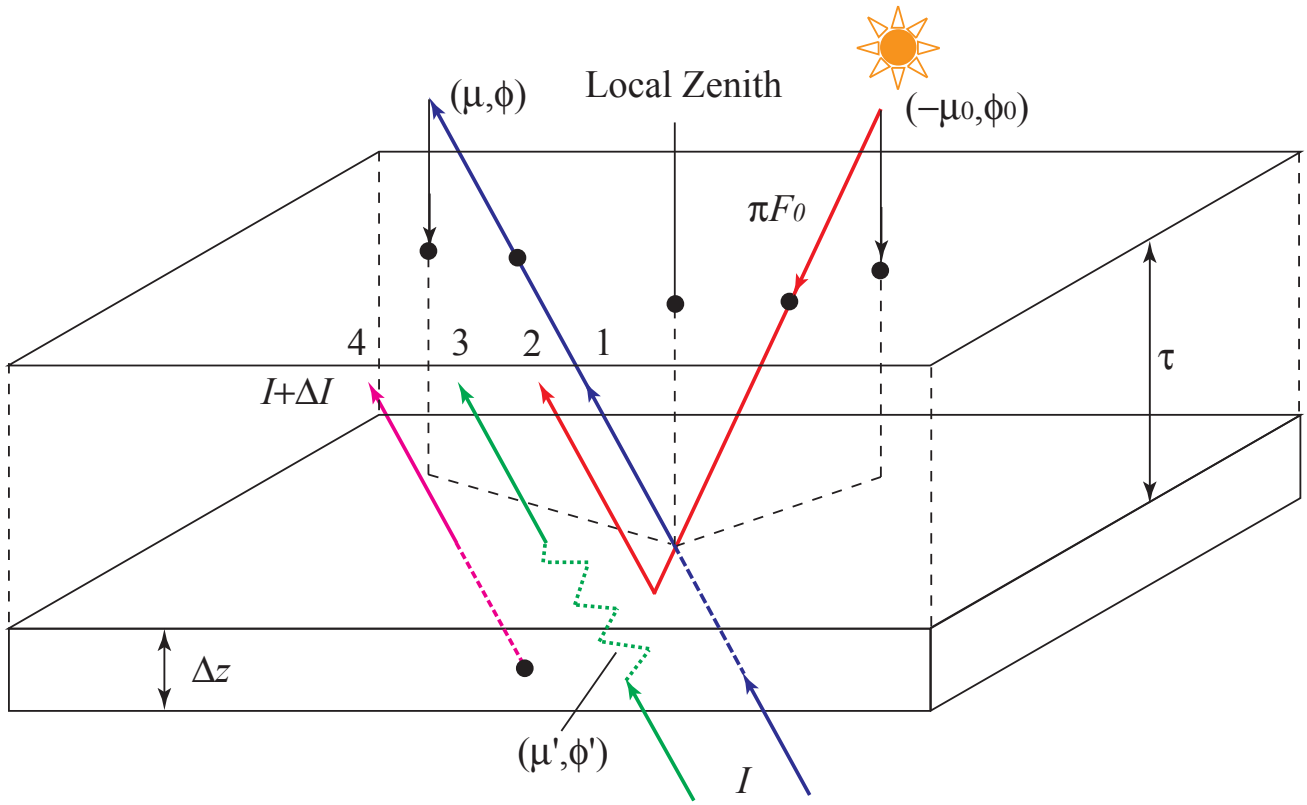

Figure 3.1. Transfer of diffuse solar intensity from below in plane-parallel layers: (1) attenuation by extinction; (2) single scattering of the unscattered direct solar flux; (3) multiple scattering; and (4) emission from the layer. The notations are defined in the text (from Liou, 2002).

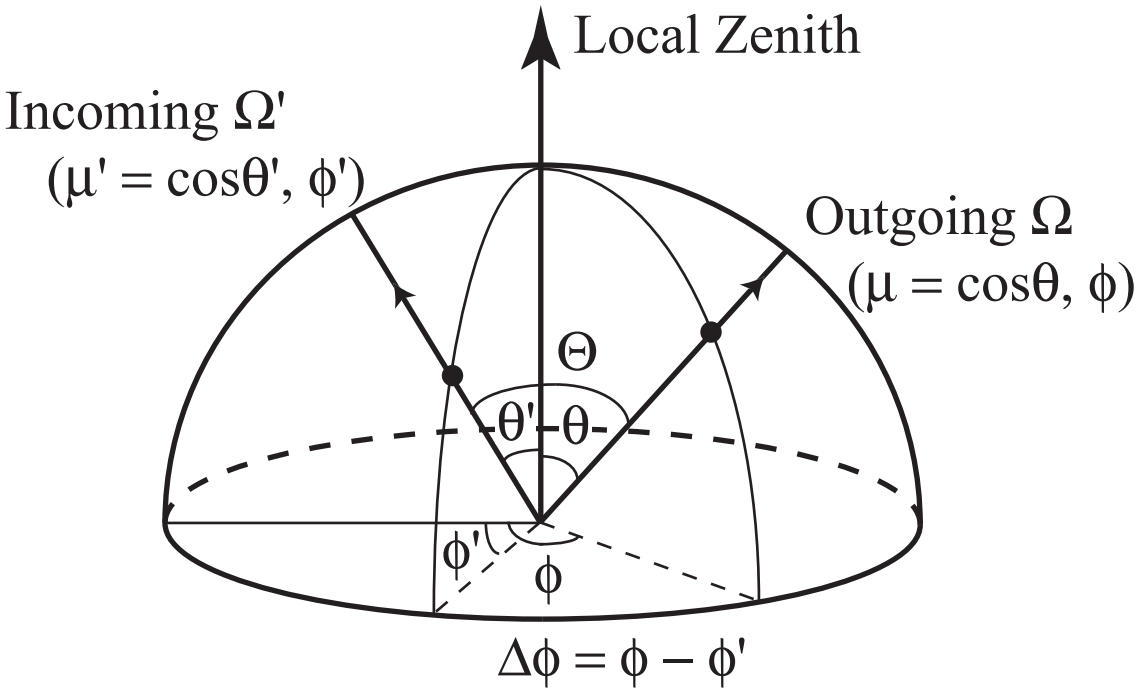

Figure 3.2. Relation of scattering (Θ), zenith (θ, θ'), and azimuth (ϕ, ϕ') angles. μ and μ' denote cosine of zenith angle θ and θ', respectively.

In the case of considering an optically thin layer where most scattering events are dominated by single scattering of the solar radiation, and there are no diffuse intensities from the top $(\tau = 0)$ and the bottom $(\tau = \tau_a)$ of the layer, the source function $J(\tau; \mu, \phi)$ in equation (3.4) is represented by

$$J(\tau; \mu, \phi) \cong \frac{\omega}{4\pi} \pi F_0 P(\mu, \phi; -\mu_0, \phi_0) \exp(-\tau/\mu_0). \tag{3.6}$$

In such case, the upward intensity $I(\tau = 0; \mu, \phi)$ at the top of the atmosphere and the downward intensity $I(\tau = \tau_a; -\mu, \phi)$ at the bottom of the atmosphere can be solved analytically in the form

$$I(\tau = 0; \mu, \phi) = \frac{\omega \mu_0 F_0}{4(\mu + \mu_0)} P(\mu, \phi; -\mu_0, \phi_0) \left\{ 1 - \exp\left[-\tau_a \left(\frac{1}{\mu} + \frac{1}{\mu_0} \right) \right] \right\}, \tag{3.7}$$

$$I(\tau = \tau_a; -\mu, \phi)$$

$$= \begin{cases} \dfrac{\omega \mu_0 F_0}{4(\mu - \mu_0)} P(-\mu, \phi; -\mu_0, \phi_0) \left[\exp\left(-\dfrac{\tau_a}{\mu} \right) - \exp\left(-\dfrac{\tau_a}{\mu_0} \right) \right], & (\mu \neq \mu_0), \\ \dfrac{\omega \tau_a F_0}{4\mu_0} P(-\mu_0, \phi; -\mu_0, \phi_0) \exp\left(-\dfrac{\tau_a}{\mu_0} \right), & (\mu = \mu_0). \end{cases} \tag{3.8}$$

Conversely, in the case of considering multiple scattering of the diffuse intensity, equation (3.4) should be solved numerically with a method mentioned in next section.

3.1.2. Doubling and adding method

There are a variety of numerical calculation techniques (e.g., Chandrasekhar's X and Y functions, discrete ordinates, doubling and adding, invariant imbedding, Monte Carlo, and successive orders) to solve radiative transfer in a scattering atmosphere (see Chandrasekhar, 1960; Hansen and Travis, 1974; Liou, 1980, 2002; van de Hulst, 1980; and Goody and Young, 1989). In this study, we choose the doubling and adding method for solving the radiative transfer equation. The principle of this method for radiative transfer was stated by Stokes (1862), who considered the reflection and transmission by a stack of glass plates. van de Hulst (1963) developed this method for multiple scattering that is now commonly employed. The doubling and adding method uses a straightforward geometrical ray tracing technique. In essence, if the reflection and transmission properties of two individual layers are known, the reflection and transmission properties of the combined layers can be obtained by computing the successive reflections back and forth between the two layers. When the two layers have the identical optical properties (both the reflection and transmission), the adding method is referred to as the doubling method. The adding method provides traceable mathematical and physical deductions of the reflection and the transmission of light.

This method has five advantages:

- physical interpretation of results is possible at each step;
- simple mathematical operations such as matrix multiplications;
- the reflection and transmission functions are obtained for all incident and emergent angles at once;
- computation for isotropic and anisotropic scattering is equivalent, although more quadrature points are needed to describe complex radiation field of the latter case;
- results are obtained for a range of optical thickness between the final value and the initial value.

and also two disadvantages:

- its application is restricted to layered geometries with uniform irradiation;
- it is necessary that each layer has homogeneous optical properties.

In the adding method, instead of solving for the specific intensities, we use the reflection and transmission properties of a medium with the simple combination laws discussed below. The diffuse reflection and transmission functions for a plane-parallel layer bounded by $\tau = \tau_1$ and $\tau = \tau_2$ $(\tau_a = \tau_2 - \tau_1)$ are defined by following equations:

$$I_R^+(\tau_1, \mu, \phi) = \frac{1}{\pi}\int_0^{2\pi}\int_0^1 R(\tau_a; \mu, \phi; \mu', \phi') I^-(\tau_1, \mu', \phi')\mu' d\mu' d\phi', \tag{3.9}$$

$$I_T^-(\tau_2, \mu, \phi) = \frac{1}{\pi}\int_0^{2\pi}\int_0^1 T(\tau_a; \mu, \phi; \mu', \phi') I^-(\tau_1, \mu', \phi')\mu' d\mu' d\phi', \tag{3.10}$$

$$I_R^-(\tau_2, \mu, \phi) = \frac{1}{\pi}\int_0^{2\pi}\int_0^1 R^*(\tau_a; \mu, \phi; \mu', \phi') I^+(\tau_2, \mu', \phi')\mu' d\mu' d\phi', \tag{3.11}$$

$$I_T^+(\tau_1, \mu, \phi) = \frac{1}{\pi}\int_0^{2\pi}\int_0^1 T^*(\tau_a; \mu, \phi; \mu', \phi') I^+(\tau_2, \mu', \phi')\mu' d\mu' d\phi', \tag{3.12}$$

where $I_R^+(\tau_1, \mu, \phi)$ and $I_T^+(\tau_1, \mu, \phi)$ indicate the upward reflected and transmitted intensities at the upper boundary $(\tau = \tau_1)$, $I_R^-(\tau_2, \mu, \phi)$ and $I_T^-(\tau_2, \mu, \phi)$ are the downward reflected and transmitted intensities at the lower boundary $(\tau = \tau_2)$, R and T denote reflection and transmission functions for the downward incident radiation, and R^* and T^* denote the corresponding functions for the upward incident radiation. The incident sunlight on the top of a layer with $\tau_1 = 0$ and $\tau_2 = \tau_a$ can be represented by the Dirac δ function,

$$I^-(\tau_1, \mu, \phi) = \delta(\mu - \mu_0)\delta(\phi - \phi_0)\pi F_0. \tag{3.13}$$

By substituting equation (3.13) to equations (3.9) and (3.10), the reflected and transmitted intensities are given by

$$I_R^+(0, \mu, \phi) = R(\tau_a; \mu, \phi; \mu_0, \phi_0)\mu_0 F_0, \tag{3.14}$$

$$I_T^-(\tau_a, \mu, \phi) = T(\tau_a; \mu, \phi; \mu_0, \phi_0)\mu_0 F_0. \tag{3.15}$$

If a layer is extremely optically thin (e.g., $\tau \approx 2^{-20}$), it's quite unlikely that multiple scattering occurs. Under such case, by comparing equations (3.14) and (3.15) with equations (3.7) and (3.8), we obtain the following reflected and transmission functions,

$$R(\tau_a; \mu, \phi; \mu_0, \phi_0) = \frac{\omega}{4(\mu + \mu_0)} P(\mu, \phi; -\mu_0, \phi_0)\left\{1 - \exp\left[-\tau_a\left(\frac{1}{\mu} + \frac{1}{\mu_0}\right)\right]\right\}, \tag{3.16}$$

$$T(\tau_a; \mu, \phi; \mu_0, \phi_0) = \begin{cases} \dfrac{\omega}{4(\mu - \mu_0)} P(-\mu, \phi; -\mu_0, \phi_0)\left[\exp\left(-\dfrac{\tau_a}{\mu}\right) - \exp\left(-\dfrac{\tau_a}{\mu_0}\right)\right], & (\mu \neq \mu_0), \\ \dfrac{\omega\tau_a}{4\mu_0^2} P(-\mu_0, \phi; -\mu_0, \phi_0)\exp\left(-\dfrac{\tau_a}{\mu_0}\right), & (\mu = \mu_0). \end{cases} \tag{3.17}$$

In the same way,

$$R^*(\tau_a;\mu,\phi;\mu_0,\phi_0)=\frac{\omega}{4(\mu+\mu_0)}\,P(-\mu,\phi;\mu_0,\phi_0)\left\{1-\exp\left[-\tau_{\mathrm{a}}\left(\frac{1}{\mu}+\frac{1}{\mu_0}\right)\right]\right\}, \tag{3.18}$$

$$T^*(\tau_a;\mu,\phi;\mu_0,\phi_0)$$

$$=\begin{cases}\dfrac{\omega}{4(\mu-\mu_0)}\,P(\mu,\phi;\mu_0,\phi_0)\left[\exp\left(-\dfrac{\tau_{\mathrm{a}}}{\mu}\right)-\exp\left(-\dfrac{\tau_{\mathrm{a}}}{\mu_0}\right)\right], & (\mu\neq\mu_0),\\ \dfrac{\omega\tau_{\mathrm{a}}}{4\mu_0^2}\,P(\mu_0,\phi;\mu_0,\phi_0)\exp\left(-\dfrac{\tau_{\mathrm{a}}}{\mu_0}\right), & (\mu=\mu_0).\end{cases} \tag{3.19}$$

It is known that the phase functions of both Mie scattering for spherical particles and scattering for randomly-oriented nonspherical particles can be decomposed by Fourier series for $(\phi-\phi')$. It is also known that corresponding reflection or transmission functions can be presented in Fourier decomposition

$$X(\tau;\mu,\phi;\mu',\phi')=\sum_{m=0}^{M}(2-\delta_{0m})X^m(\tau;\mu,\mu')\cos m(\phi-\phi'), \tag{3.20}$$

where $X=R$, T, R^*, and T^*. Replacing the relevant functions in equations (3.9)–(3.12) by their appropriate Fourier series, we obtain *m*th Fourier component $(m>0)$ as follows:

$$I_R^{+m}(\tau_1,\mu)=2\int_0^1 R^m(\tau_a;\mu,\mu')I^{-m}(\tau_1,\mu')\mu'd\mu', \tag{3.21}$$

$$I_T^{-m}(\tau_2,\mu)=2\int_0^1 T^m(\tau_a;\mu,\mu')I^{-m}(\tau_1,\mu')\mu'd\mu', \tag{3.22}$$

$$I_R^{-m}(\tau_2,\mu)=2\int_0^1 R^{*m}(\tau_a;\mu,\mu')I^{+m}(\tau_2,\mu')\mu'd\mu', \tag{3.23}$$

$$I_T^{+m}(\tau_1,\mu)=2\int_0^1 T^{*m}(\tau_a;\mu,\mu')I^{+m}(\tau_2,\mu')\mu'd\mu'. \tag{3.24}$$

Note that the right-hand sides of equations (3.21)–(3.24) should be divided by a factor of two for m = 0.

The integrals in equations (3.21)–(3.24) should also be replaced by summation over a finite number of quadrature points. For any function $f(x)$, Gaussian quadrature is expressed by

$$\int_{-1}^{1}f(x)dx=2\int_0^1 f(x)dx\approx\sum_{j=-N}^{N}w_jf(x_j), \tag{3.25}$$

where x_j and w_j are the Gaussian points and corresponding weights, respectively.

With equation (3.25), equations (3.21)–(3.24) are replaced to the following matrix representations:

$$\boldsymbol{I}_R^{+m}(\tau_1) = \boldsymbol{R}_a{}^m \boldsymbol{I}^{-m}(\tau_1), \tag{3.26}$$

$$\boldsymbol{I}_T^{-m}(\tau_2) = \boldsymbol{T}_a{}^m \boldsymbol{I}^{-m}(\tau_1), \tag{3.27}$$

$$\boldsymbol{I}_R^{-m}(\tau_2) = \boldsymbol{R}_a^{*m} \boldsymbol{I}^{+m}(\tau_2), \tag{3.28}$$

$$\boldsymbol{I}_T^{+m}(\tau_1) = \boldsymbol{T}_a^{*m} \boldsymbol{I}^{+m}(\tau_2), \tag{3.29}$$

where $\boldsymbol{I}^{\pm m}(\tau)$ are the N-vectors for the upward and downward intensities, i.e., $\boldsymbol{I}^{\pm m}(\tau) = [\boldsymbol{I}^m(\tau, \pm\mu_1), \boldsymbol{I}^m(\tau, \pm\mu_2), \ldots, \boldsymbol{I}^m(\tau, \pm\mu_N)]$. Reflection and transmission functions are represented by $N \times N$ matrix whose elements are given by

$$\boldsymbol{X}_{a_{ij}}{}^m = 2X^m(\tau_a; \mu_i, \mu_j)\mu_j w_j, \tag{3.30}$$

for $\boldsymbol{X}_a{}^m = \boldsymbol{R}_a{}^m$ or $\boldsymbol{R}_a^{*m}$, and by

$$\boldsymbol{Y}_{a_{ij}}{}^m = \exp(-\tau_a/\mu_i)\delta_{ij} + 2Y^m(\tau_a; \mu_i, \mu_j)\mu_j w_j, \tag{3.31}$$

for $\boldsymbol{Y}_a{}^m = \boldsymbol{T}_a{}^m$ or $\boldsymbol{T}_a^{*m}$. The first and second terms on the right-hand side of equation (3.31) represent the direct and diffuse transmissions, respectively.

Up to here, we discuss the reflection and transmission functions for an optically thin layer. Next, we explain principle of combining two layers using the reflection and transmission functions. Although all reflection and transmission functions ($X(\tau; \mu, \mu') = R,\ \tilde{T},\ R^*,\ \widetilde{T^*},\ \widetilde{D},\ U$) should be labeled with the Fourier term index, m, we omit this index in the below for readability.

Figure 3.3 illustrates the multiple scattering processes between two layers (layer A and layer B). Assume that radiation comes from the top of layer A (flux: πF_0). Let $\boldsymbol{R}_A$ and $\widetilde{\boldsymbol{T}}_A$ denote the reflection and total (direct + diffuse) transmission functions for the first layer and $\boldsymbol{R}_B$ and $\widetilde{\boldsymbol{T}}_B$ for the second layer, and define $\widetilde{\boldsymbol{D}}$ and $\boldsymbol{U}$ for the combined total transmission and reflection functions between layer A and layer B. Photons should undergo one to an infinite number of scattering events.

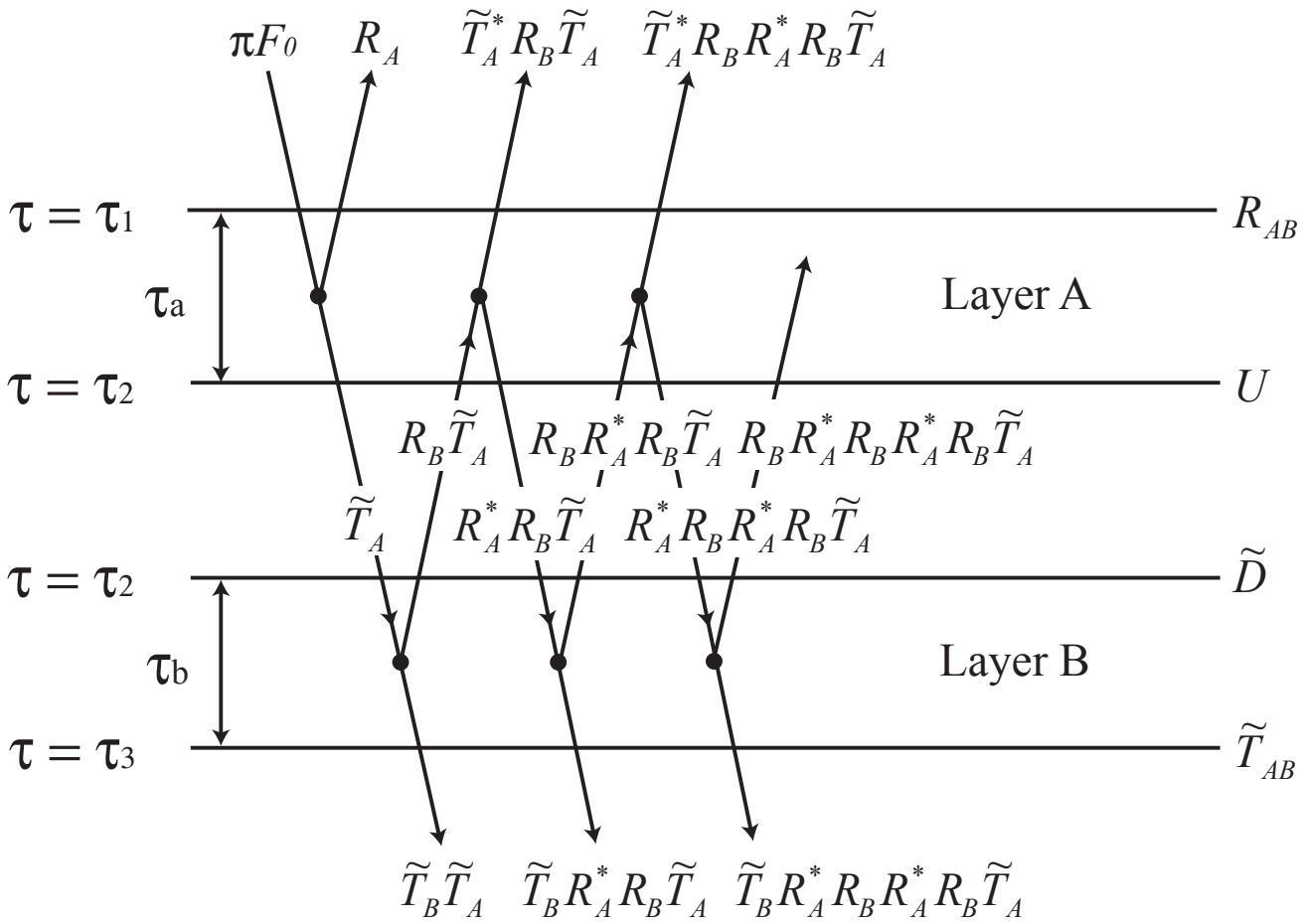

Figure 3.3. The schematic representation of the adding method. For convenience, layer A with optical thickness τ_a and layer B with optical thickness τ_b are illustrated as if they were physically separated.

Under such case, the combined reflection $\boldsymbol{R}_{AB}$ and transmission $\widetilde{\boldsymbol{T}}_{AB}$ functions are described by

$$\begin{aligned}\boldsymbol{R}_{AB} &= \boldsymbol{R}_A + \widetilde{\boldsymbol{T}^*}_A\boldsymbol{R}_B\widetilde{\boldsymbol{T}}_A + \widetilde{\boldsymbol{T}^*}_A\boldsymbol{R}_B\boldsymbol{R}^*{}_A\boldsymbol{R}_B\boldsymbol{R}^*{}_A\boldsymbol{R}_B\widetilde{\boldsymbol{T}}_A + \cdots \\ &= \boldsymbol{R}_A + \widetilde{\boldsymbol{T}^*}_A\boldsymbol{R}_B[\mathbf{1} + \boldsymbol{R}^*{}_A\boldsymbol{R}_B + (\boldsymbol{R}^*{}_A\boldsymbol{R}_B)^2 + \cdots]\widetilde{\boldsymbol{T}}_A \\ &= \boldsymbol{R}_A + \widetilde{\boldsymbol{T}^*}_A\boldsymbol{R}_B(\mathbf{1} - \boldsymbol{R}^*{}_A\boldsymbol{R}_B)^{-1}\widetilde{\boldsymbol{T}}_A,\end{aligned} \tag{3.32}$$

$$\begin{aligned}\widetilde{\boldsymbol{T}}_{AB} &= \widetilde{\boldsymbol{T}}_B\widetilde{\boldsymbol{T}}_A + \widetilde{\boldsymbol{T}}_B\boldsymbol{R}^*{}_A\boldsymbol{R}_B\widetilde{\boldsymbol{T}}_A + \widetilde{\boldsymbol{T}}_B\boldsymbol{R}^*{}_A\boldsymbol{R}_B\boldsymbol{R}^*{}_A\boldsymbol{R}_B\widetilde{\boldsymbol{T}}_A + \cdots \\ &= \widetilde{\boldsymbol{T}}_B[\mathbf{1} + \boldsymbol{R}^*{}_A\boldsymbol{R}_B + (\boldsymbol{R}^*{}_A\boldsymbol{R}_B)^2 + \cdots]\widetilde{\boldsymbol{T}}_A \\ &= \widetilde{\boldsymbol{T}}_B(\mathbf{1} - \boldsymbol{R}^*{}_A\boldsymbol{R}_B)^{-1}\widetilde{\boldsymbol{T}}_A.\end{aligned} \tag{3.33}$$

The combined reflection $\boldsymbol{U}$ and transmission $\widetilde{\boldsymbol{D}}$ functions between layer A and layer B are also formulated as follows:

$$\begin{aligned}\boldsymbol{U} &= \boldsymbol{R}_B\widetilde{\boldsymbol{T}}_A + \boldsymbol{R}_B\boldsymbol{R}^*{}_A\boldsymbol{R}_B\widetilde{\boldsymbol{T}}_A + \boldsymbol{R}_B\boldsymbol{R}^*{}_A\boldsymbol{R}_B\boldsymbol{R}^*{}_A\boldsymbol{R}_B\widetilde{\boldsymbol{T}}_A + \cdots \\ &= \boldsymbol{R}_B[\mathbf{1} + \boldsymbol{R}^*{}_A\boldsymbol{R}_B + (\boldsymbol{R}^*{}_A\boldsymbol{R}_B)^2 + \cdots]\widetilde{\boldsymbol{T}}_A \\ &= \boldsymbol{R}_B(\mathbf{1} - \boldsymbol{R}^*{}_A\boldsymbol{R}_B)^{-1}\widetilde{\boldsymbol{T}}_A,\end{aligned} \tag{3.34}$$

$$\begin{aligned}\widetilde{\boldsymbol{D}} &= \widetilde{\boldsymbol{T}}_A + \boldsymbol{R}^*{}_A\boldsymbol{R}_B\widetilde{\boldsymbol{T}}_A + \boldsymbol{R}^*{}_A\boldsymbol{R}_B\boldsymbol{R}^*{}_A\boldsymbol{R}_B\widetilde{\boldsymbol{T}}_A + \cdots \\ &= [\mathbf{1} + \boldsymbol{R}^*{}_A\boldsymbol{R}_B + (\boldsymbol{R}^*{}_A\boldsymbol{R}_B)^2 + \cdots]\widetilde{\boldsymbol{T}}_A \\ &= (\mathbf{1} - \boldsymbol{R}^*{}_A\boldsymbol{R}_B)^{-1}\widetilde{\boldsymbol{T}}_A = (\mathbf{1} + \boldsymbol{S})\widetilde{\boldsymbol{T}}_A,\end{aligned} \tag{3.35}$$

$$\boldsymbol{S} \equiv \boldsymbol{R}^*{}_A\boldsymbol{R}_B(\mathbf{1} - \boldsymbol{R}^*{}_A\boldsymbol{R}_B)^{-1}. \tag{3.36}$$

From equations (3.32)–(3.36), the combined reflection $\boldsymbol{R}_{AB}$ and transmission $\widetilde{\boldsymbol{T}}_{AB}$ functions can simply be written in the following forms

$$\boldsymbol{R}_{AB} = \boldsymbol{R}_A + \widetilde{\boldsymbol{T}}_A\boldsymbol{U}, \tag{3.37}$$

$$\widetilde{\boldsymbol{T}}_{AB} = \widetilde{\boldsymbol{T}}_B\widetilde{\boldsymbol{D}}, \tag{3.38}$$

$$\boldsymbol{U} = \boldsymbol{R}_B\widetilde{\boldsymbol{D}}. \tag{3.39}$$

In equations (3.32)–(3.39), the product of any two parameters implies that integration over solid angle is to be performed so as to take into account all the possible multiple scattering contributions,

$$\boldsymbol{X}_A\boldsymbol{Y}_B = 2\int_0^1 X(\tau_a;\mu,\mu')Y(\tau_a;\mu',\mu_0)\mu' d\mu', \tag{3.40}$$

in which X and Y can be any functions: R, $\tilde{T}$, R^*, $\widetilde{T^*}$, $\widetilde{D}$, and U. In actual computation, equation (3.40) is treated by matrix representation. Furthermore, the total transmission function $\widetilde{\boldsymbol{T}}$ consists of the diffuse and direct components and can be expressed in isolation:

$$\widetilde{\boldsymbol{T}} = \boldsymbol{T} + \mathbf{1}\cdot\exp(-\tau/\mu'), \tag{3.41}$$

where $\mathbf{1}$ is unit matrix, $\mu' = \mu_0$ when transmission is associated with the incident sunlight and $\mu' = \mu$ when transmission is related to the emergent radiation in the direction μ.

In a similar way, $\widetilde{\boldsymbol{D}}$ and $\widetilde{\boldsymbol{T}}_{AB}$ are represented as follows:

$$\begin{aligned}\widetilde{\boldsymbol{D}} &= \boldsymbol{D} + \mathbf{1}\cdot\exp(-\tau_{\mathrm{a}}/\mu_0) = [\boldsymbol{T}_A + \mathbf{1}\cdot\exp(-\tau_{\mathrm{a}}/\mu_0)](\mathbf{1}+\boldsymbol{S}) \\ &= (\mathbf{1}+\boldsymbol{S})\boldsymbol{T}_A + \boldsymbol{S}\exp(-\tau_{\mathrm{a}}/\mu_0) + \mathbf{1}\cdot\exp(-\tau_{\mathrm{a}}/\mu_0),\end{aligned} \tag{3.42}$$

$$\begin{aligned}\widetilde{\boldsymbol{T}}_{AB} &= [\boldsymbol{T}_B + \mathbf{1}\cdot\exp(-\tau_{\mathrm{b}}/\mu)][\boldsymbol{D} + \mathbf{1}\cdot\exp(-\tau_{\mathrm{a}}/\mu_0)] \\ &= \exp(-\tau_{\mathrm{b}}/\mu)\boldsymbol{D} + \boldsymbol{T}_B\exp(-\tau_{\mathrm{a}}/\mu_0) + \boldsymbol{T}_B\boldsymbol{D} \\ &\quad + \mathbf{1}\cdot\exp[-(\tau_{\mathrm{a}}/\mu_0 + \tau_{\mathrm{b}}/\mu)]\ \delta(\mu-\mu_0),\end{aligned} \tag{3.43}$$

where parameters without tilt notation (~) denote only diffuse component of transmission. The fourth term on the right-hand side of equation (3.43) represents the direct transmission for the combined layer.

As a result, for the downward incident radiation, a set of iterative equations governing the diffuse transmission and reflection involving the two layers are given by

$$\boldsymbol{Q}_1 = \boldsymbol{R}^*{}_A\boldsymbol{R}_B, \tag{3.44}$$

$$\boldsymbol{Q}_n = \boldsymbol{Q}_1\boldsymbol{Q}_{n-1}, \tag{3.45}$$

$$\boldsymbol{S} = \sum_{n=1}^{\infty}\boldsymbol{Q}_n, \tag{3.46}$$

$$\boldsymbol{D} = \boldsymbol{T}_A + \boldsymbol{S}\boldsymbol{T}_A + \boldsymbol{S}\exp(-\tau_{\mathrm{a}}/\mu_0), \tag{3.47}$$

$$\boldsymbol{U} = \boldsymbol{R}_B\boldsymbol{D} + \boldsymbol{R}_B\exp(-\tau_{\mathrm{a}}/\mu_0), \tag{3.48}$$

$$\boldsymbol{R}_{AB} = \boldsymbol{R}_A + \exp(-\tau_{\mathrm{a}}/\mu)\,\boldsymbol{U} + \boldsymbol{T}^*{}_A\boldsymbol{U}, \tag{3.49}$$

$$\boldsymbol{T}_{AB} = \exp(-\tau_{\mathrm{b}}/\mu)\boldsymbol{D} + \boldsymbol{T}_B\exp(-\tau_{\mathrm{a}}/\mu_0) + \boldsymbol{T}_B\boldsymbol{D}. \tag{3.50}$$

In a similar way, the corresponding equations for the upward incident radiation are written in the forms

$$\boldsymbol{Q}_1 = \boldsymbol{R}_B\boldsymbol{R}^*{}_A, \tag{3.51}$$

$$\boldsymbol{Q}_n = \boldsymbol{Q}_1\boldsymbol{Q}_{n-1}, \tag{3.52}$$

$$\boldsymbol{S} = \sum_{n=1}^{\infty}\boldsymbol{Q}_n, \tag{3.53}$$

$$\boldsymbol{U} = \boldsymbol{T}^*{}_B + \boldsymbol{S}\boldsymbol{T}^*{}_B + \boldsymbol{S}\exp(-\tau_{\mathrm{b}}/\mu'), \tag{3.54}$$

$$\boldsymbol{D} = \boldsymbol{R}^*{}_A\boldsymbol{U} + \boldsymbol{R}^*{}_A\exp(-\tau_{\mathrm{b}}/\mu'), \tag{3.55}$$

$$\boldsymbol{R}^*{}_{AB} = \boldsymbol{R}^*{}_B + \exp(-\tau_{\mathrm{b}}/\mu)\,\boldsymbol{D} + \boldsymbol{T}_B\boldsymbol{D}, \tag{3.56}$$

$$\boldsymbol{T}^*{}_{AB} = \exp(-\tau_{\mathrm{a}}/\mu)\boldsymbol{U} + \boldsymbol{T}^*{}_A\exp(-\tau_{\mathrm{b}}/\mu') + \boldsymbol{T}^*{}_A\boldsymbol{U}, \tag{3.57}$$

where μ' is direction of the direct incident radiation.

Therefore, the actual procedure in the numerical computation consists mainly of following four items:

(1) In each homogeneous layer, optical thickness τ, single scattering albedo ω, and scattering phase function P are computed.

(2) The homogeneous layer derived in (1) is divided by a factor of two until light scatters only once in divided layer which allows to utilize equations (3.16)–(3.19).

(3) The reflection and transmission functions are calculated with the doubling method until optical thickness equals to that of the original homogeneous layer.

(4) Between inhomogeneous layers, the combined reflection and transmission functions are calculated with the adding method until "one" combined layer.

3.2. Accuracy validation of our radiative transfer code

We have newly developed a numerical computation code based on the doubling and adding method for analyzing remote sensing data of planetary atmospheres. This code has been validated by performing numerical computations for several cloud models described in Temma (2005) and by comparing our results with his. Temma's code was also written based on the doubling and adding method and was checked by comparing his results with several published ones. For Mie scattering, our computation results are also cross-matched with those of Dr. T. Satoh (private communication). **Table 3.1–Table 3.5** show several results of accuracy validation for our radiative transfer code. Accuracy of our radiative transfer code displayed in each Table is computed in the following manner:

$$Accuracy = \frac{|(I/F)_{\mathrm{Reference}} - (I/F)_{\mathrm{Ours}}|}{(I/F)_{\mathrm{Reference}}} \times 100. \tag{3.58}$$

Note that our code outputs the reflection function which, when multiplied by μ_0, becomes (I/F) in the above equation. As a result, we find that computation results of our radiative transfer code are in good agreement with their results with 0.5 % accuracy except for the case that μ (also μ_0) is close to zero. This accuracy should be enough for analyses of remote sensing data of planetary atmospheres. From this comparison, in this study, we conduct the radiative transfer calculation with a total of 22 quadrature points (N = 22) for the integration of μ_0 and μ, and 10 Fourier expansion terms (M = 10) for $\Delta\phi$ in aerosol scattering layers and only three Fourier expansion terms (M = 3) for $\Delta\phi$ in the Rayleigh gas layers.

Table 3.1. The result of accuracy validation for our radiative transfer code for isotropic scattering cases. The assumed cloud model consists of one layer with an optical thickness of 96. Scattering phase function in this layer is given by isotropic scattering phase function ($P(\Theta) = 1$). In this table, two single scattering albedo cases are presented. For additional information, see pp. 124 in Temma (2005).

$\omega = 0.5$					
Input parameters			Computed intensities (I/F)		
μ_0	μ	$\Delta\phi$	Ours	Temma's	Accuracy (%)
0.35	0.05	1.	0.1331	0.1321	0.73
0.95	0.10	1.	0.1511	0.1511	0.03
0.55	0.25	1.	0.1162	0.1161	0.12
0.65	0.45	1.	0.1055	0.1055	0.01
0.80	0.70	1.	0.1000	0.1000	0.01
0.15	0.85	1.	0.0254	0.0254	0.12
0.45	0.95	1.	0.0590	0.0590	0.03

$\omega = 0.975$					
Input parameters			Computed intensities (I/F)		
μ_0	μ	$\Delta\phi$	Ours	Temma's	Accuracy (%)
0.35	0.05	1.	0.3773	0.3764	0.23
0.95	0.10	1.	0.5933	0.5940	0.12
0.55	0.25	1.	0.4398	0.4399	0.02
0.65	0.45	1.	0.4731	0.4732	0.03
0.80	0.70	1.	0.5367	0.5369	0.04
0.15	0.85	1.	0.1006	0.1008	0.17
0.45	0.95	1.	0.2968	0.2969	0.03

Table 3.2. Same as Table 3.1, except for the case with isotropic scattering and the Rayleigh scattering. The assumed cloud structure consists of two layers as listed below. For additional information, see pp. 125 in Temma (2005).

Cloud model parameters			
Layer	τ	ω	$P(\Theta)$
1	10.0	1.0	Rayleigh scattering
2	128.0	0.1	Isotropic scattering

Input parameters			Computed intensities (I/F)		
μ_0	μ	$\Delta\phi$	Ours	Temma's	Accuracy (%)
0.60	0.60	0.0	0.5157	0.5158	0.02
0.60	0.20	0.0	0.5788	0.5787	0.015
0.60	0.60	90.0	0.5197	0.5200	0.06
0.60	0.20	90.0	0.5141	0.5145	0.08
0.60	0.60	180.0	0.6064	0.6068	0.07
0.60	0.20	180.0	0.6334	0.6338	0.06

Table 3.3. Same as Table 3.1, except for the Jovian aerosol scattering case. The assumed cloud structure consists of six layers as listed below. "HGF075" and "J.TTHGF" denote a single Henyey-Greenstein function with an asymmetry factor g = 0.75 and a double Henyey-Greenstein function with (f, g_1, g_2) = (0.938, 0.80, –0.70), respectively (Tomasko et al., 1978). For more information, see pp. 126 in Temma (2005).

Cloud model parameters			
Layer	τ	ω	$P(\Theta)$
1	0.01	0.995	Rayleigh scattering
2	1.0	0.980	HGF075
3	1.0	0.995	Rayleigh scattering
4	1.0	0.980	J.TTHGF
5	2.0	0.995	Rayleigh scattering
6	128.0	0.990	J.TTHGF

Input parameters			Computed intensities (I/F)		
μ_0	μ	$\Delta\phi$	Ours	Temma's	Accuracy (%)
0.3513	0.3911	180.9	0.2108	0.2114	0.27
0.6575	0.6877	181.5	0.4541	0.4556	0.32
0.8285	0.8478	183.0	0.5866	0.5888	0.37
0.9132	0.9217	185.8	0.6484	0.6511	0.42
0.9325	0.9300	172.9	0.6620	0.6647	0.41
0.8882	0.8746	175.7	0.6302	0.6327	0.39
0.7662	0.7415	177.8	0.5378	0.5396	0.33

Table 3.4. Same as Table 3.1, except for the Saturnian aerosol scattering case. The assumed cloud structure consists of six layers as listed below. "S.TTHGF" denotes a double Henyey-Greenstein function with (f, g_1, g_2) = (0.763, 0.620, –0.294) (Tomasko and Doose, 1984). For more information, see pp. 127 in Temma (2005).

Cloud model parameters			
Layer	τ	ω	$P(\Theta)$
1	0.05	0.998	Rayleigh scattering
2	0.5	0.960	S.TTHGF
3	0.1	0.998	Rayleigh scattering
4	5.0	0.999	S.TTHGF
5	0.2	0.998	Rayleigh scattering
6	128.0	0.980	S.TTHGF

Input parameters			Computed intensities (I/F)		
μ_0	μ	$\Delta\phi$	Ours	Temma's	Accuracy (%)
0.3572	0.2605	180.00	0.3623	0.3621	0.06
0.5695	0.4837	179.17	0.4835	0.4841	0.12
0.6919	0.6173	178.17	0.5628	0.5636	0.15
0.7842	0.7229	176.45	0.6243	0.6252	0.14
0.8573	0.8187	172.32	0.6734	0.6742	0.12
0.8357	0.8278	169.59	0.6570	0.6580	0.15
0.6745	0.6977	172.39	0.5450	0.5459	0.16
0.4900	0.5309	174.01	0.4199	0.4204	0.12
0.3860	0.4338	174.52	0.3520	0.3522	0.06
0.2858	0.3386	174.86	0.2895	0.2891	0.12

Table 3.5. Same as Table 3.1, except for the Mie scattering case. The assumed cloud model consists of one layer with an optical thickness of 128. Scattering phase function in this layer is given by a Mie scattering phase function with (n_r, n_i) = (1.4, 0.0) and the Hansen's size distribution (a, b) = (0.5 μm, 0.1). The definitions of variables for Mie scattering are described in Section 3.3.1. In this table, one single scattering albedo case is presented (courtesy of Dr. T. Satoh).

$\omega = 0.99$					
Input parameters			Computed intensities (I/F)		
μ_0	μ	$\Delta\phi$	Ours	Satoh's	Accuracy (%)
0.4292	0.2411	174.4	0.2347	0.2350	0.12
0.4842	0.3024	174.0	0.2666	0.2668	0.08
0.5696	0.3999	173.2	0.3162	0.3163	0.02
0.6579	0.5054	171.9	0.3685	0.3683	0.06
0.7227	0.5870	170.4	0.4073	0.4070	0.07
0.8133	0.7843	175.8	0.4661	0.4670	0.18
0.8784	0.8745	172.3	0.5051	0.5057	0.11

3.3. Model description

Tomasko et al. (1978) tested four atmospheric models (Type I–IV represented in Figure 13 of their paper) to reproduce the P10/IPP limb-darkening curves at seven solar phase angles. They concluded that reasonable fits to all four data (the blue- and red-channel data for the STrZ and the SEBn) were obtained only with the Type II model. We therefore conduct the radiative transfer modeling with a cloud structure similar to their Type II model. As shown in **Figure 3.4**, the Type II model consists of four layers: from the top to the bottom, the upper Rayleigh gas layer, the stratospheric haze, the lower Rayleigh gas layer, and the semi-infinite cloud layer. Assuming that the stratospheric haze and the cloud particles can be approximated by spherical particles, we perform the radiative transfer calculations using this model combined with the Mie scattering computations (hereafter Type II-Mie model). In this model, we assume no layer is mixed with aerosols and gas for simplicity.

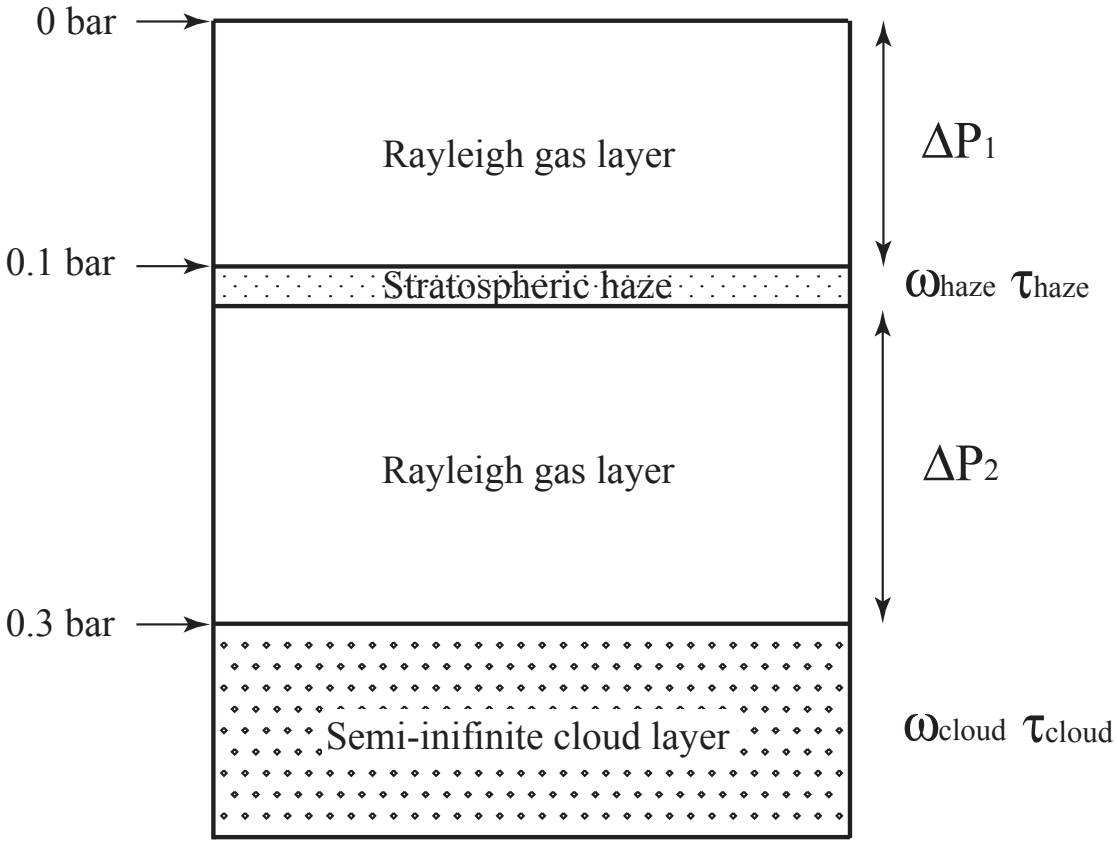

Figure 3.4. The diagram of the assumed vertical cloud structure (Type II model). This model is similar to the Type II model described by Tomasko et al. (1978). The pressure differences ΔP_1 and ΔP_2 are fixed at 0.1 and 0.2 [bar] because limb-darkening curves in CB2 are insensitive to vertical distributions of the stratospheric haze and cloud. The notations are defined in the text.

3.3.1. Scattering phase functions of cloud, haze, and gas

For a single aerosol particle (radius r [μm]), the Mie scattering of the incident light beam (wavelength λ [μm]) in the form of $P_{\mathrm{Mie,r}}(\Theta, r, n_{\mathrm{r}}, n_{\mathrm{i}})$, where $(n_{\mathrm{r}}, n_{\mathrm{i}})$ is the complex refractive index of the particle, can be computed with a Fortran code written by Bohren and Huffman (1998). The computation is repeated for a range of particle sizes to obtain an *averaged* scattering phase function. For the size distribution functions $n(r, a, b)$ for cloud and haze, we adopt the Hansen's size distribution (Hansen and Travis, 1974):

$$n(r, a, b) = n_0 r^{(1-3b)/b} e^{(-r/ab)}, \tag{3.59}$$

where n_0 is a constant*, and r is the radius; a and b are the effective radius (r_{eff}) and the effective variance (v_{eff}), respectively. An example of the Hansen's size distribution is shown in **Figure 3.5**. Thereafter, the "*scattering cross-section weighted*" average of Mie scattering phase function can be obtained as follows:

$$P_{\mathrm{Mie}}(\Theta, n_{\mathrm{r}}, n_{\mathrm{i}}, r_{\mathrm{eff}}, v_{\mathrm{eff}}) = \frac{\int_0^\infty Q_{\mathrm{s}}(r, n_{\mathrm{r}}, n_{\mathrm{i}}) \pi r^2 P_{\mathrm{Mie,r}}(\Theta, r, n_{\mathrm{r}}, n_{\mathrm{i}}) n(r, r_{\mathrm{eff}}, v_{\mathrm{eff}}) dr}{\int_0^\infty Q_{\mathrm{s}}(r, n_{\mathrm{r}}, n_{\mathrm{i}}) \pi r^2 n(r, r_{\mathrm{eff}}, v_{\mathrm{eff}}) dr}, \tag{3.60}$$

where Q_{s} is the scattering efficiency. A Mie scattering phase function for cloud or haze is thus obtained by specifying a combination of parameters $(n_{\mathrm{r}}, n_{\mathrm{i}}, r_{\mathrm{eff}}, v_{\mathrm{eff}})$. An example of the *averaged* Mie scattering phase function is also shown in **Figure 3.6**.

---

* Constant n_0 is written by

$$n_0 = N \cdot (ab)^{(2b-1)/b} / \Gamma[(1-2b)/b], \tag{3.61}$$

where N is the total number of particles per unit volume and Γ is the gamma function.

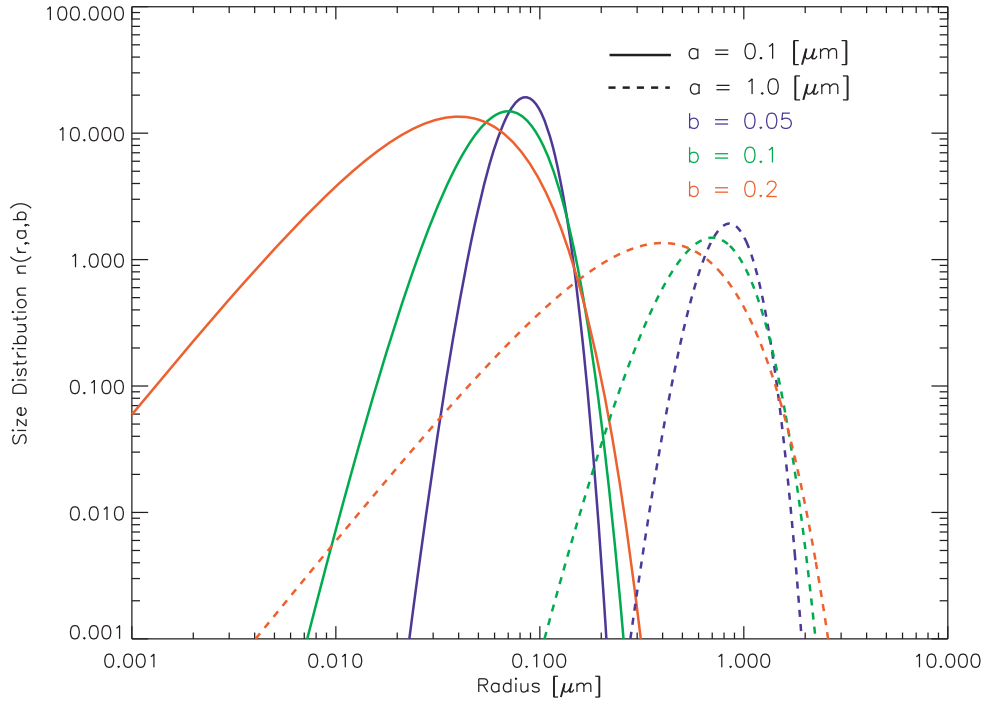

Figure 3.5. An example of the Hansen's size distribution for two values of a (0.1 and 1.0 μm) and three values of b (0.05, 0.1, and 0.2). The size distribution is normalized so that the integral over all sizes is $N = 1$.

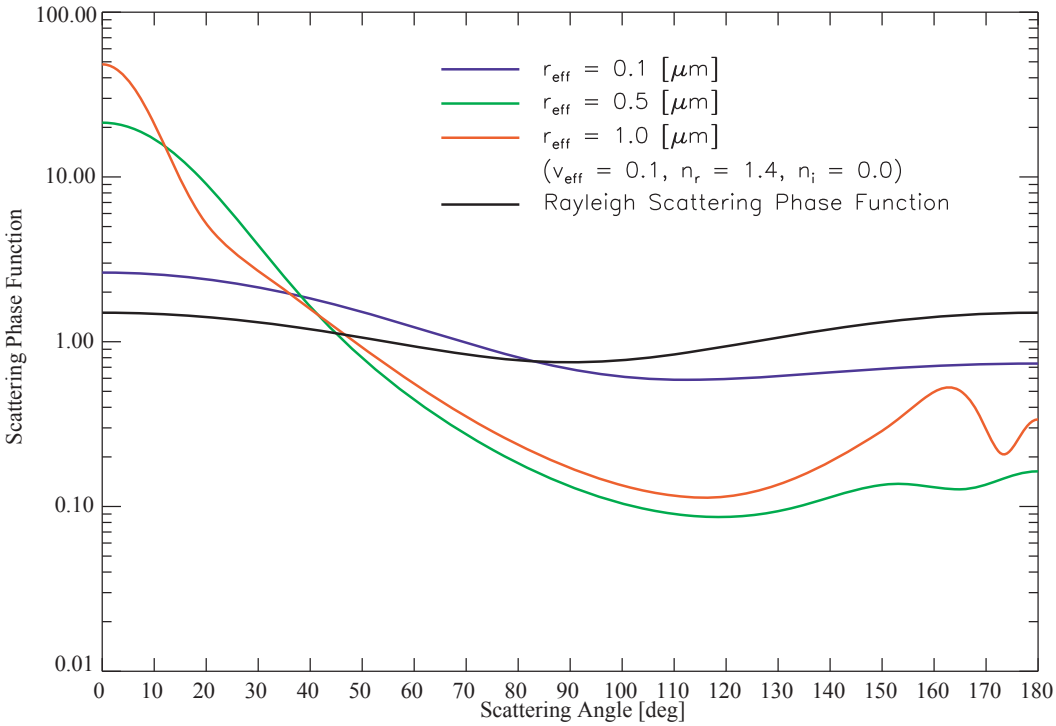

Figure 3.6. An example of the *averaged* Mie scattering phase functions in CB2 passband (effective wavelength: 750 nm) for three values of r_{eff} (0.1, 0.5, and 1.0 [μm]). Also plotted for comparison is the Rayleigh scattering phase function. The values of the other parameters (v_{eff}, n_{r}, and n_{i}) for calculating the Mie scattering phase functions are presented in this figure.

For cloud particles, the real part of the refractive index $(n_{\mathrm{r,cloud}})$ and the effective radius $(r_{\mathrm{eff,cloud}})$ are treated as free parameters. These are the two most important physical quantities in this study. In a Mie scattering calculation, we do not fix $n_{\mathrm{r,cloud}}$ to the laboratory-measured values of NH_3 ice because of the doubt to this simple assumption in the Jovian upper clouds, as mentioned in **Chapter 1**. We assume, however, the imaginary part of the refractive index $(n_{\mathrm{i,cloud}})$ is zero. To match the actual reflectivity variations, small amount of absorption in the cloud layer is allowed by adjusting the single scattering albedo of cloud $(\omega_{\mathrm{cloud}})$. Note that absorption in the cloud layer can be caused either by the cloud particles or by some absorbents amongst the cloud particles without any distinguishable differences. The effective variance $(v_{\mathrm{eff,cloud}})$ is set to 0.1.

For the stratospheric haze, Mie scattering for spherical particles has been proposed by several researchers. Tomasko et al. (1986) concluded that particles with n_{r} = 1.6 and an effective radius in the range 0.2–0.5 μm were needed to reproduce ultraviolet data from the IUE observations (the longest wavelength is 330 nm). Rages et al. (1999) found a similar particle mean radius (0.32–0.45 μm) from their analysis of the Galileo SSI high solar phase angle images. They used n_{r} = 1.29 for 410 and 756 nm wavelengths. In contrast, West (1988) showed smaller particles than 0.1 μm, with n_{r} = 1.4 and n_{i} = 0.02 (for 430 nm wavelength) and n_{i} = 0.0002 (for 600 nm wavelength), were required to match the limb brightness as seen from Voyager 2 during eclipse. The variation in the physical properties of the stratospheric haze should result from differences of observing altitude and model assumption. We therefore allow cloud models to have a range of parameters, $n_{\mathrm{r,haze}}$: 1.3, 1.4, 1.5, 1.6, and 1.7, and $r_{\mathrm{eff,haze}}$: 0.05, 0.1, 0.15, 0.2, 0.3, 0.4, and 0.5 μm, while the effective variance of haze is fixed ($v_{\mathrm{eff,haze}}$ = 0.1). The imaginary part of the refractive index $n_{\mathrm{i,haze}}$ is assumed to be zero.

In the molecular gas layers, the Rayleigh scattering phase function is described as follows:

$$P_{\mathrm{R}}(\Theta) = \frac{3}{4}(1 + \cos^2\Theta). \tag{3.62}$$

The upper and lower limits of free parameters and assumptions for other parameters are summarized in **Table 3.6**. If an acceptable fit to each data set cannot be obtained with these assumptions, we will relax the constraint on fixed parameters.

Table 3.6. Model parameters for the Type II-Mie model.

Layer	Parameter	Values	References
Stratospheric haze	τ_{haze}	variable	
	ω_{haze}	1.0	
	$P_{\mathrm{Mie}}(\Theta)$	Mie scattering	
	$n_{\mathrm{r,haze}}$	variable (1.3, 1.4, 1.5, 1.6, and 1.7)	Tomasko et al. (1986); West (1988); Rages et al. (1999)
	$n_{\mathrm{i,haze}}$	0.0	
	$r_{\mathrm{eff,haze}}$ [μm]	variable (0.05, 0.1, 0.15, 0.2, 0.3, 0.4, and 0.5)	Tomasko et al. (1986); West (1988); Rages et al. (1999)
	$v_{\mathrm{eff,haze}}$	0.1	
Semi-infinite cloud	τ_{cloud}	128	
	ω_{cloud}	variable	
	$P_{\mathrm{Mie}}(\Theta)$	Mie scattering	
	$n_{\mathrm{r,cloud}}$	variable (1.3–2.0)*	
	$n_{\mathrm{i,cloud}}$	0.0	
	$r_{\mathrm{eff,cloud}}$ [μm]	variable (0.1–1.0)*	
	$v_{\mathrm{eff,cloud}}$	0.1	

* We search $n_{\mathrm{r,cloud}}$ in the range from 1.3 to 2.0 at intervals of 0.05 and $r_{\mathrm{eff,cloud}}$ in the range from 0.1 μm to 1.0 μm at intervals of 0.1 μm.

3.3.2. Optical thickness and single scattering albedo of the Rayleigh gas layer

For calculating the optical thickness of the Rayleigh scattering and CH_4 absorption with hydrostatic equilibrium and the ideal gas equation, we use nominal values for the mole fractions of H_2, He, and CH_4, which are $f_{\mathrm{H_2}}$ = 0.86, f_{He} = 0.136, and $f_{\mathrm{CH_4}}$ = 0.018, respectively (Table 4.2 of Taylor et al., 2004). The optical thickness of the Rayleigh scattering is given by

$$\tau_R = \frac{\sigma_R}{\bar{m}g} \cdot \Delta P \cdot 10^5, \tag{3.63}$$

where σ_R [m^2] is the cross section of the Rayleigh scattering, $\bar{m}$ [kg/particle] is the mean molecular weight, g [m/s^2] is the gravity acceleration considering the flattening effect, and ΔP [bar] is the pressure difference between top and bottom of a gas layer. The cross section of the Rayleigh scattering σ_R is calculated with the effective polarizability of the Jovian atmosphere α_{eff}:

$$\sigma_R = \frac{128}{3} \cdot \frac{\pi^5}{\lambda^4} \cdot {\alpha_{\mathrm{eff}}}^2 \cdot 10^{24}, \tag{3.64}$$

$$\alpha_{\mathrm{eff}} = f_{\mathrm{H_2}}\alpha_{\mathrm{H_2}} + f_{\mathrm{He}}\alpha_{\mathrm{He}}, \tag{3.65}$$

where $\alpha_{\mathrm{H_2}}$ = 8.04 × 10^{-31} [m^3] and α_{He} = 2.05 × 10^{-31} [m^3] (Weast et al., 1990).

Conversely, the effective CH_4 absorption coefficient $\bar{k}$ [/km-amagat] is given by

$$\bar{k} = \int k(\lambda)S(\lambda)d\lambda \Big/ \int S(\lambda)d\lambda, \tag{3.66}$$

where $S(\lambda)$ is the instrument relative response function (considering quantum efficiency, and transmissions of optics and two filters: $S = T_0 \times T_1 \times T_2 \times QE$) as a function of wavelength, normalized to a unit maximum, and $k(\lambda)$ [/km-amagat] is the empirical CH_4 absorption coefficient taken from Karkoschka (1998). The optical thickness of CH_4 absorption is written by

$$\tau_M = \frac{f_{CH_4} \cdot \bar{k}}{\bar{m}gL_0} \cdot \Delta P \cdot 10^2, \tag{3.67}$$

where L_0 is the Loschmidt number, which is the number of atoms or molecules (2.6868×10^{25} [/m^3]) in a unit volume under standard temperature and pressure).

In cloud free regions, the Rayleigh scattering and CH_4 absorption determine the pressure level we can probe. **Figure 3.7** illustrates the pressure level at which atmospheric gas opacity reaches unity for a two-way nadir path ($\mu_0 = \mu = 1$) as a function of wavelength in cloud free regions. In the case of cloud-covered regions that we investigate in this study, the pressure level we can probe becomes lower (the altitude becomes higher) than that shown in **Figure 3.7** because of opacity caused by the aerosols (scattering and absorption).

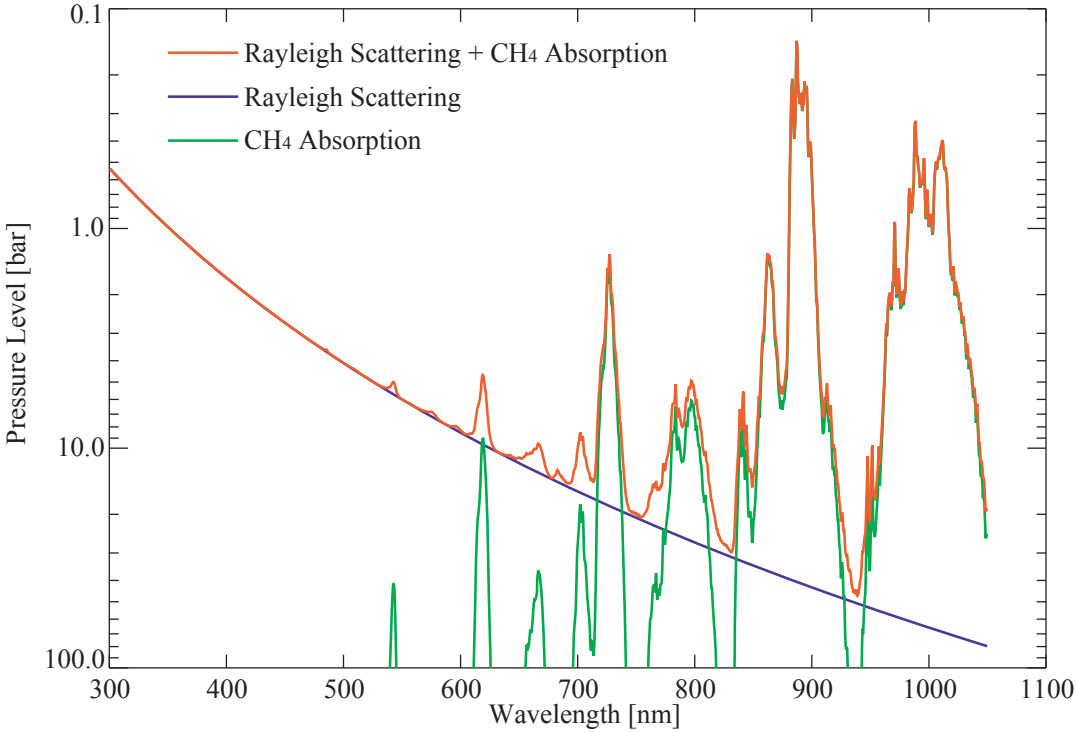

Figure 3.7. The pressure level at which atmospheric gas opacity reaches unity for a two-way nadir path ($\mu_0 = \mu = 1$) as a function of wavelength. For CH_4 absorption, the Karkoschka's 0.4 nm tabulated absorption coefficients are used.

With equations (3.63) and (3.67), the total optical thickness $(\tau_{total} = \tau_R + \tau_M)$ as a function of ΔP and the single scattering albedo $(\omega_R = \tau_R/\tau_{total})$ of the Rayleigh gas layer are computed in CB2 and BL1 for the STrZ and the SEBn as presented in **Table 3.7**. Since the gravity acceleration varies with latitude, the total optical thickness is slightly different from each other. As **Table 3.7** shows, the single scattering albedo in both CB2 and BL1 are found to be close to unity because of small CH_4 absorption in these continua. Furthermore, in the case of CB2, the Rayleigh scattering cross section is so small that the small difference of ΔP makes no change to our conclusion (A 4-bar pressure-thickness is required to produce an optical thickness of only 0.1). Therefore, we fix ΔP_1 and ΔP_2 shown in **Figure 3.4** to be 0.1 and 0.2 [bar], respectively. These values correspond to the nominal ones found in the previous studies (cf. West et al. 2004). For BL1, however, we are not sure that such assumption of pressure difference has no effect on our conclusion because the optical thickness in BL1 is thicker than that in CB2 by a factor of approximately eight. Thus, the sensitivity test for assumption of pressure differences ΔP_1 and ΔP_2 has to be conducted in **Chapter 4**.

Table 3.7. Total optical thickness and single scattering albedo of the Rayleigh gas layer calculated for CB2 and BL1 in the STrZ and the SEB.

	CB2		BL1	
	STrZ	SEBn	STrZ	SEBn
τ_R	$0.0234\Delta P$	$0.0239\Delta P$	$0.188\Delta P$	$0.193\Delta P$
τ_M	$9.39\times 10^{-4}\Delta P$	$9.60\times 10^{-4}\Delta P$	$1.62\times 10^{-4}\Delta P$	$1.65\times 10^{-4}\Delta P$
τ_{total}	$0.0243\Delta P$	$0.0249\Delta P$	$0.189\Delta P$	$0.193\Delta P$
ω_R	0.9614	0.9614	0.9991	0.9991

Table 3.8. The lower limit, the upper limit, and the initial values of two free parameters: optical thickness of haze τ_{haze} and single scattering albedo of cloud ω_{cloud}.

Parameter	Lower limit	Upper limit	Initial value
τ_{haze}	0.0	–	0.25, 0.5, 0.75
ω_{cloud}	0.0	1.0	0.975, 0.985, 0.995

3.4. Fitting strategy

The number of data points sampled at each of 12 solar phase angles is different for each angle. Taking the CB2/STrZ data set as an example, the number of data points sampled at a solar phase angle of 18.8° is 80, while that at a solar phase angle of 140.1° is only five due to the extreme crescent shape of the illuminated portion. We should treat goodness of fit for data obtained at each solar phase angle fairly. In order to judge goodness of fit between the observed and modeled limb-darkening curves, we therefore define the following χ^2:

$$\chi^2 \equiv \frac{1}{n}\sum_{i=1}^{n}\chi_i^2, \tag{3.68}$$

$$\chi_i^2 = \frac{1}{m_i}\sum_{j=1}^{m_i}\left[\frac{(I/F)_{i,j}^{\mathrm{obs}} - (I/F)_{i,j}^{\mathrm{mod}}}{\sigma_{i,j}}\right]^2, \tag{3.69}$$

where n is the number of solar phase angles used in this study (n = 12), χ_i^2 is the normalized chi-square for the *i*th solar phase angle, m_i is the number of data points for the *i*th solar phase angle, $(I/F)_{i,j}^{\mathrm{obs}}$ and $(I/F)_{i,j}^{\mathrm{mod}}$ are the values of observed and modeled reflectivity of the *j*th data point for the *i*th solar phase angle, respectively, and $\sigma_{i,j}$ is the relative uncertainty of the *j*th data point for the *i*th solar phase angle discussed in **Section 2.3**.

In the Type II-Mie model, there are six free parameters: the real part of the refractive index $(n_{\mathrm{r,haze}})$, the effective radius $(r_{\mathrm{eff,haze}})$, and the optical thickness of stratospheric haze (τ_{haze}); and the real part of the refractive index $(n_{\mathrm{r,cloud}})$, the effective radius $(r_{\mathrm{eff,cloud}})$, and the single scattering albedo of cloud $(\omega_{\mathrm{cloud}})$. It is not realistic to conduct a fitting process for determining all six parameters at once because of the risk of being captured in local minima of the parameter space. Instead, we set the four dimensional grid for $n_{\mathrm{r,haze}}$, $r_{\mathrm{eff,haze}}$, $n_{\mathrm{r,cloud}}$, and $r_{\mathrm{eff,cloud}}$ within the range between the upper and the lower limits presented in **Table 3.6**. In practice, we perform Mie scattering computations to prepare a set of scattering phase functions for each grid point by discretely changing the values for $n_{\mathrm{r,haze}}$, $r_{\mathrm{eff,haze}}$, $n_{\mathrm{r,cloud}}$, and $r_{\mathrm{eff,cloud}}$. Then, for each grid point, we perform radiative transfer computations until we obtain the best-fit combination of the other two free parameters, τ_{haze} and ω_{cloud}, by minimizing χ^2 through iterating the process with the aid of the Levenberg-Marquardt method. Generally, as a number of free parameters to be solved increases, the solutions of these parameters strongly depend on these initial conditions. Therefore, we also prepare nine types of initial value sets as presented in **Table 3.8** and start the iteration process from each

initial condition. In this study, the iteration process terminates when either the change in χ^2 drops 0.1 % (i.e., convergence), or the number of runs reaches a maximum of 30 iterations. In actual computations, the two free parameters always converge within 10 iterations although the number of iterations depends on the initial conditions.

In **Chapter 4**, we start the retrieval of the scattering properties of aerosols for the CB2/STrZ data set before the other data sets because:

- small pressure differences of ΔP_1 and ΔP_2 have no effects on the determination of scattering properties of aerosols in CB2;
- CB2 data, unlike BL1 data, would be little sensitive to the characteristics and vertical distribution of the blue absorbents (chromophores);
- compared with the SEBn, the STrZ is so longitudinally uniform that the scattering properties of aerosols should be determined without some interruption due to unwanted small cloud features.

Chapter 4

Results

In **Chapter 4**, we show the optical and physical properties of cloud and haze deduced from four data sets described in **Section 2.6** through radiative transfer calculations. Our analysis results for each data set are described in detail in **Section 4.1**–**4.4**. In closing this chapter, the summary of our analysis results is given in **Section 4.5**.

4.1. The CB2/STrZ data set

First of all, we check the dependence of the best-fit χ^2 value on $n_{\mathrm{r,haze}}$ in the range 1.3–1.7 and $r_{\mathrm{eff,haze}}$ in the range 0.05–0.5 μm as shown in **Figure 4.1**. The circle denotes the χ^2 value at the best-fit model obtained with a combination of $n_{\mathrm{r,haze}}$ and $r_{\mathrm{eff,haze}}$. While the χ^2 values for two large $r_{\mathrm{eff,haze}}$ cases ($r_{\mathrm{eff,haze}}$ = 0.4 and 0.5 μm) get monotonically smaller as the value of $n_{\mathrm{r,haze}}$ decreases and reach the minimum value at $n_{\mathrm{r,haze}}$ = 1.3 in the searching coverage, the χ^2 values for the other $r_{\mathrm{eff,haze}}$ cases ($r_{\mathrm{eff,haze}}$ = 0.05, 0.1, 0.15, 0.2, and 0.3 μm) vary little with the change of $n_{\mathrm{r,haze}}$. From this sensitivity test, we find that the determination of $n_{\mathrm{r,haze}}$ is more difficult than that of $r_{\mathrm{eff,haze}}$ because the χ^2 value is less dependent on $n_{\mathrm{r,haze}}$ than on $r_{\mathrm{eff,haze}}$. Therefore, we adopt $n_{\mathrm{r,haze}}$ = 1.3 in the following analyses of all four data sets.

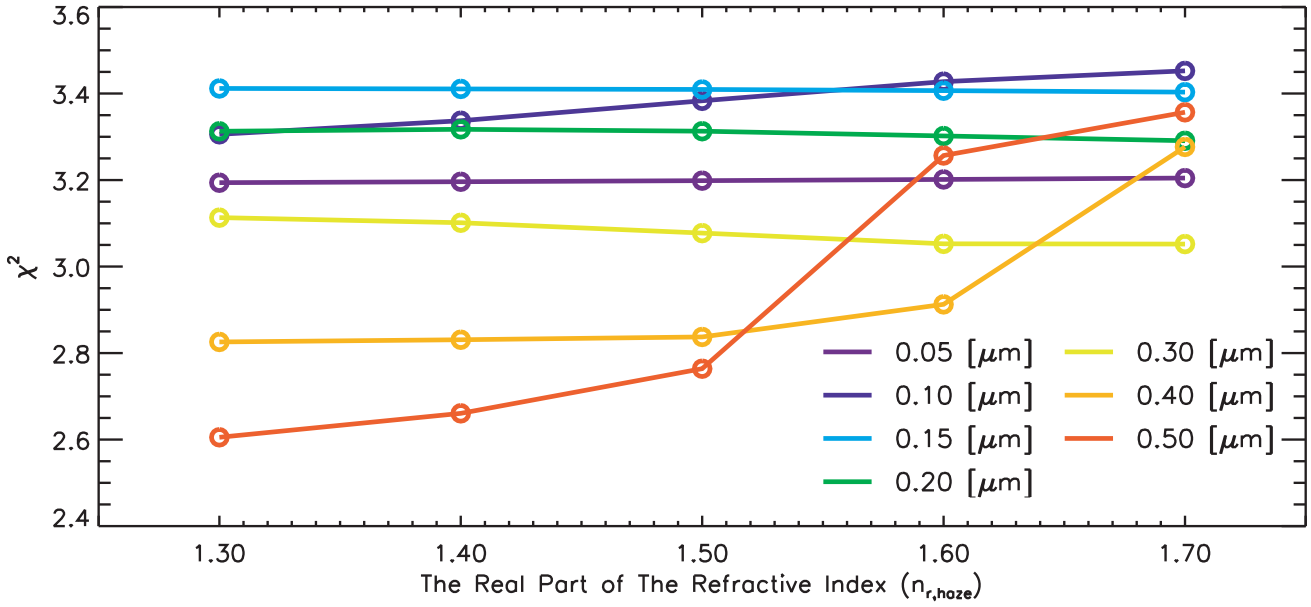

Figure 4.1. The dependence of the best-fit χ^2 value on $n_{\mathrm{r,haze}}$ in the range 1.3–1.7 and $r_{\mathrm{eff,haze}}$ in the range 0.05–0.5 μm for the case of the CB2/STrZ data set. The circle denotes the χ^2 value at the best-fit model obtained with a combination of $n_{\mathrm{r,haze}}$ and $r_{\mathrm{eff,haze}}$.

Figure 4.2 shows χ^2 variations as a function of $n_{\mathrm{r,cloud}}$ and $r_{\mathrm{eff,cloud}}$ for seven different $r_{\mathrm{eff,haze}}$ cases. As is evident in **Figure 4.2**, there are four significant characteristics as discussed below.

First, the χ^2 variations at two small $r_{\mathrm{eff,haze}}$ cases ($r_{\mathrm{eff,haze}}$ = 0.05 and 0.1 μm) show quite similar distributions to each other. The same holds for the χ^2 variations at four large $r_{\mathrm{eff,haze}}$ cases ($r_{\mathrm{eff,haze}}$ = 0.2, 0.3, 0.4, and 0.5 μm). Since the effective radius, which gives the size parameter $(2\pi r/\lambda)$ being equal to unity, is ~0.12 μm in CB2 (effective wavelength: 750 nm), it seems that the behavior of χ^2 is affected by the criterion of whether the size parameter of the stratospheric haze exceeds unity or not. In fact, the χ^2 variations at $r_{\mathrm{eff,haze}}$ = 0.15 μm, which gives size parameter of approximately unity, show different distributions from these variations at both small and large $r_{\mathrm{eff,haze}}$ cases.

Second, we find that smaller $r_{\mathrm{eff,cloud}}$ is required for a reasonable fit as the value of $n_{\mathrm{r,cloud}}$ increases as shown by warm colors, the trend of which is independent of $r_{\mathrm{eff,haze}}$.

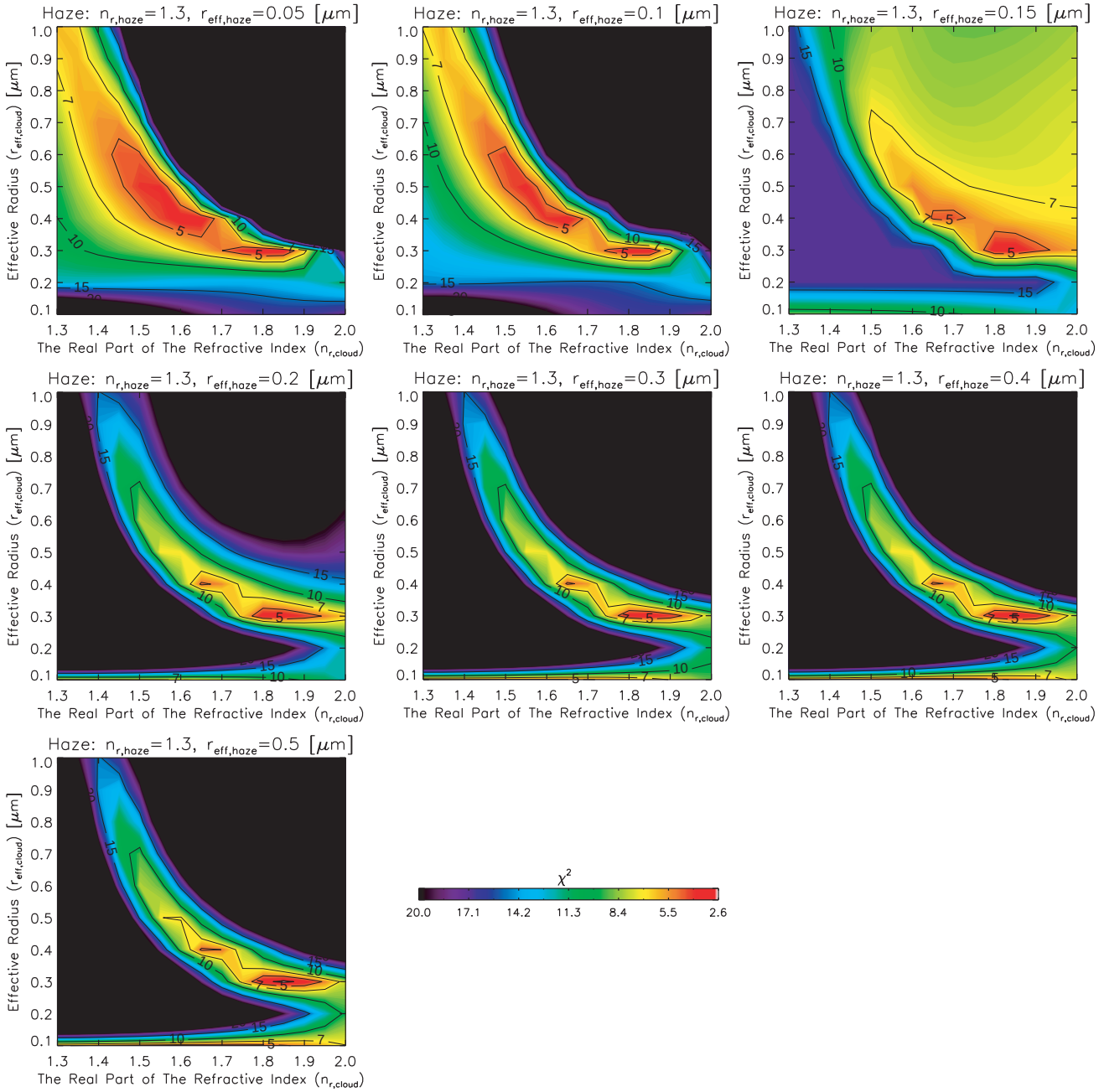

Figure 4.2. χ^2 variations as a function of the real part of the index of cloud ($n_{\mathrm{r,cloud}}$) and the effective radius of cloud ($r_{\mathrm{eff,cloud}}$) for seven different effective radii of haze ($r_{\mathrm{eff,haze}}$ = 0.05, 0.1, 0.15, 0.2, 0.3, 0.4, and 0.5 μm) in the CB2/STrZ data set. For each $r_{\mathrm{eff,haze}}$, the best-fit values of $n_{\mathrm{r,cloud}}$ and $r_{\mathrm{eff,cloud}}$, and χ^2 value for the best-fit model are presented in Table 4.1.

Third, $r_{\mathrm{eff,cloud}}$ = 0.1 μm is also found to give a small χ^2 value when $r_{\mathrm{eff,haze}}$ is larger than 0.15 μm. Careful examination of the Mie scattering phase functions in the range from $r_{\mathrm{eff,cloud}}$ = 0.05 μm to 0.35 μm ($n_{\mathrm{r,cloud}}$ = 1.80) indicates the followings (see **Figure 4.3**):

(1) the scattering phase function for $r_{\mathrm{eff,cloud}}$ = 0.05 μm almost resembles the Rayleigh scattering because the size parameter is significantly smaller than unity;

(2) the backward scattering peak, $P_{\mathrm{Mie}}(\Theta$ = ~180°), of the scattering phase function for $r_{\mathrm{eff,cloud}}$ = 0.1 μm (the size parameter ~0.84) is about the same as that for $r_{\mathrm{eff,cloud}}$ = 0.3 μm. This is why a marginally good fit to the data can be obtained with such small cloud particles;

(3) between $r_{\mathrm{eff,cloud}}$ = 0.15 μm and 0.25 μm, the backward scattering drops down to levels that are too low to reproduce the observed reflectivity at smaller solar phase angles, thereby yielding large χ^2 values.

In the following discussion, we do not consider such small cloud particles for two reasons. One is that the goodness of fit is not as good as the best-fit models. Another is that, as mentioned above, this may be a local minimum that occurs when the size parameter is around unity (the boundary between the Rayleigh scattering and the Mie scattering regimes). For BL1, a similar local minimum is also confirmed to occur for different particle radius (~0.05 μm) for the same reason (not shown again in **Section 4.3**).

Finally, when we use only $n_{\mathrm{r,cloud}}$ in the range of 1.4–1.45, which is similar value to the experimental value (1.423 at ~670 nm) of n_{r} for NH_3 ice (Martonchik et al., 1984), the models do not reproduce the observations well. That is, the χ^2 value is always >10 if $r_{\mathrm{eff,haze}}$ is larger than 0.15 μm. Even for models with smaller haze particles, the smallest achieved χ^2 value is 4.62 ($r_{\mathrm{eff,haze}}$ = 0.05 μm, $n_{\mathrm{r,cloud}}$ = 1.45, and $r_{\mathrm{eff,cloud}}$ = 0.6 μm), which is quite unsatisfactory.

For each $r_{\mathrm{eff,haze}}$ case, the values of best-fit parameters ($n_{\mathrm{r,cloud}}$, $r_{\mathrm{eff,cloud}}$, ω_{cloud}, and τ_{haze}) and χ^2 value for the best-fit model are summarized in **Table 4.1**. The best-fit modeled limb-darkening curves for each $r_{\mathrm{eff,haze}}$ case, together with the observed curves, are also presented in **Figure 4.4**.

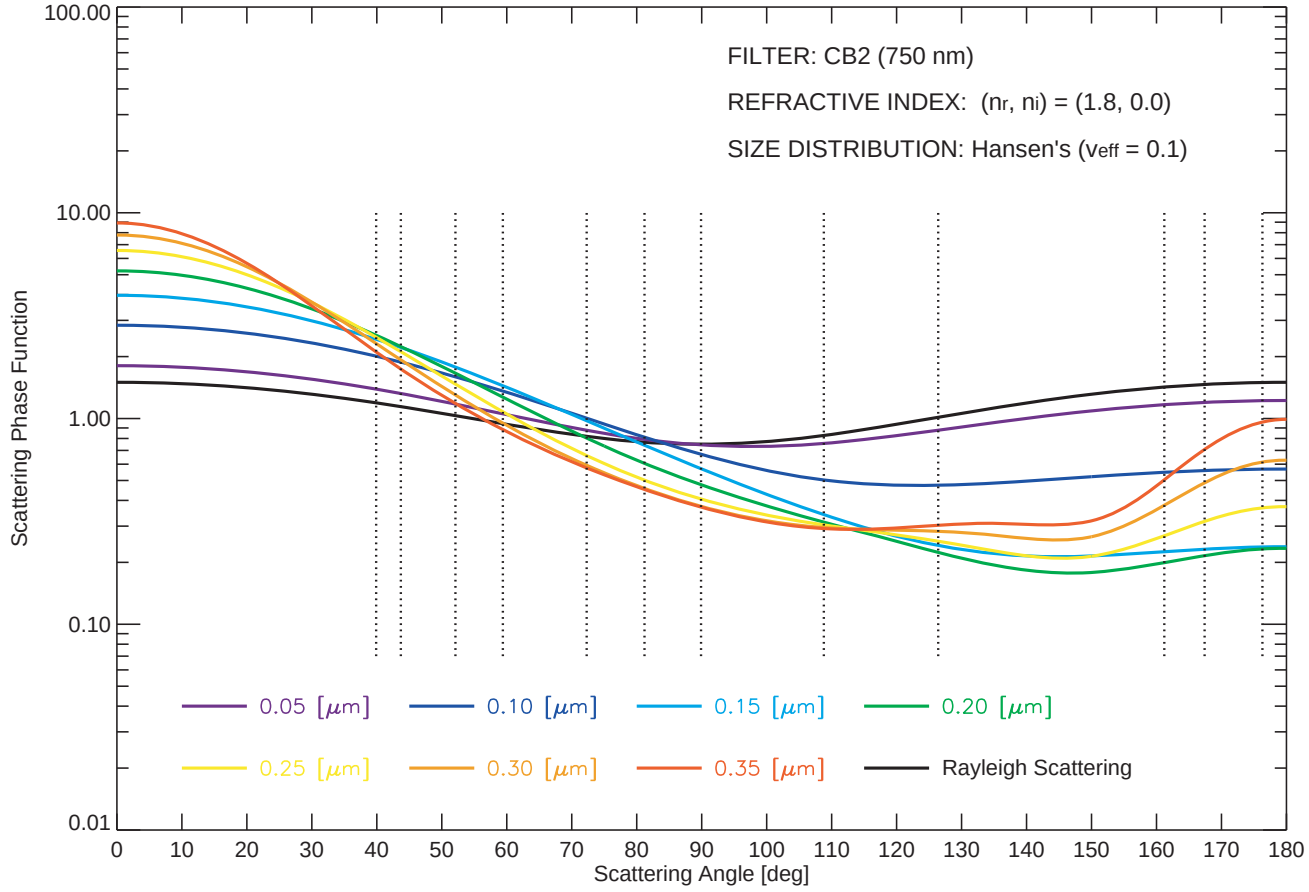

Figure 4.3. The comparison of scattering phase functions between the Mie scatterings in the range 0.05–0.35 μm and the Rayleigh scattering. The vertical dotted lines indicate scattering angles sampled at the Cassini ISS observations used in this study.

Table 4.1. The best-fit models of the Type II-Mie model for the case of $n_{\mathrm{r,haze}}$ = 1.3 in the CB2/STrZ data set.

The best-fit values					
$r_{\mathrm{eff,haze}}$ [μm]	$n_{\mathrm{r,cloud}}$	$r_{\mathrm{eff,cloud}}$ [μm]	ω_{cloud}	τ_{haze}	χ^2
0.05	1.80	0.3	0.9971	0.011	3.19
0.1	1.65	0.4	0.9975	0.043	3.31
0.15	1.85	0.3	0.9968	0.015	3.41
0.2	1.85	0.3	0.9968	0.016	3.31
0.3	1.85	0.3	0.9968	0.023	3.11
0.4	1.85	0.3	0.9968	0.039	2.83
0.5	1.85	0.3	0.9968	0.056	2.61

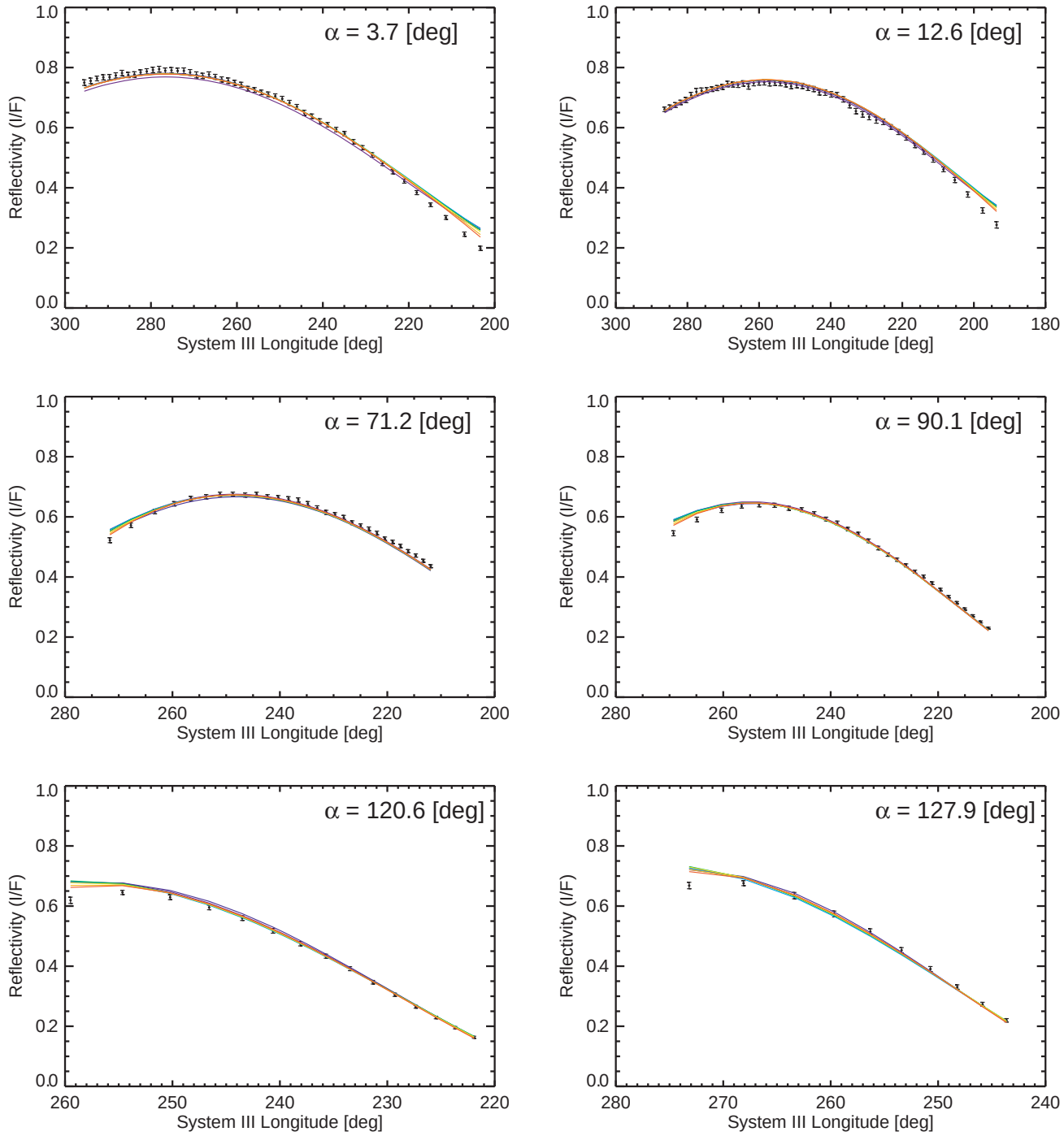

Figure 4.4. The best-fit models of the Type II-Mie model for seven different effective radii of haze ($r_{\mathrm{eff,haze}}$ = 0.05, 0.1, 0.15, 0.2, 0.3, 0.4, and 0.5 μm) in the CB2/STrZ data set. The best-fit model in all assumed cases is obtained with $n_{\mathrm{r,cloud}}$ = 1.85 and $r_{\mathrm{eff,cloud}}$ = 0.3 μm for cloud particles and $n_{\mathrm{r,haze}}$ = 1.3 and $r_{\mathrm{eff,haze}}$ = 0.5 μm for the stratospheric haze.

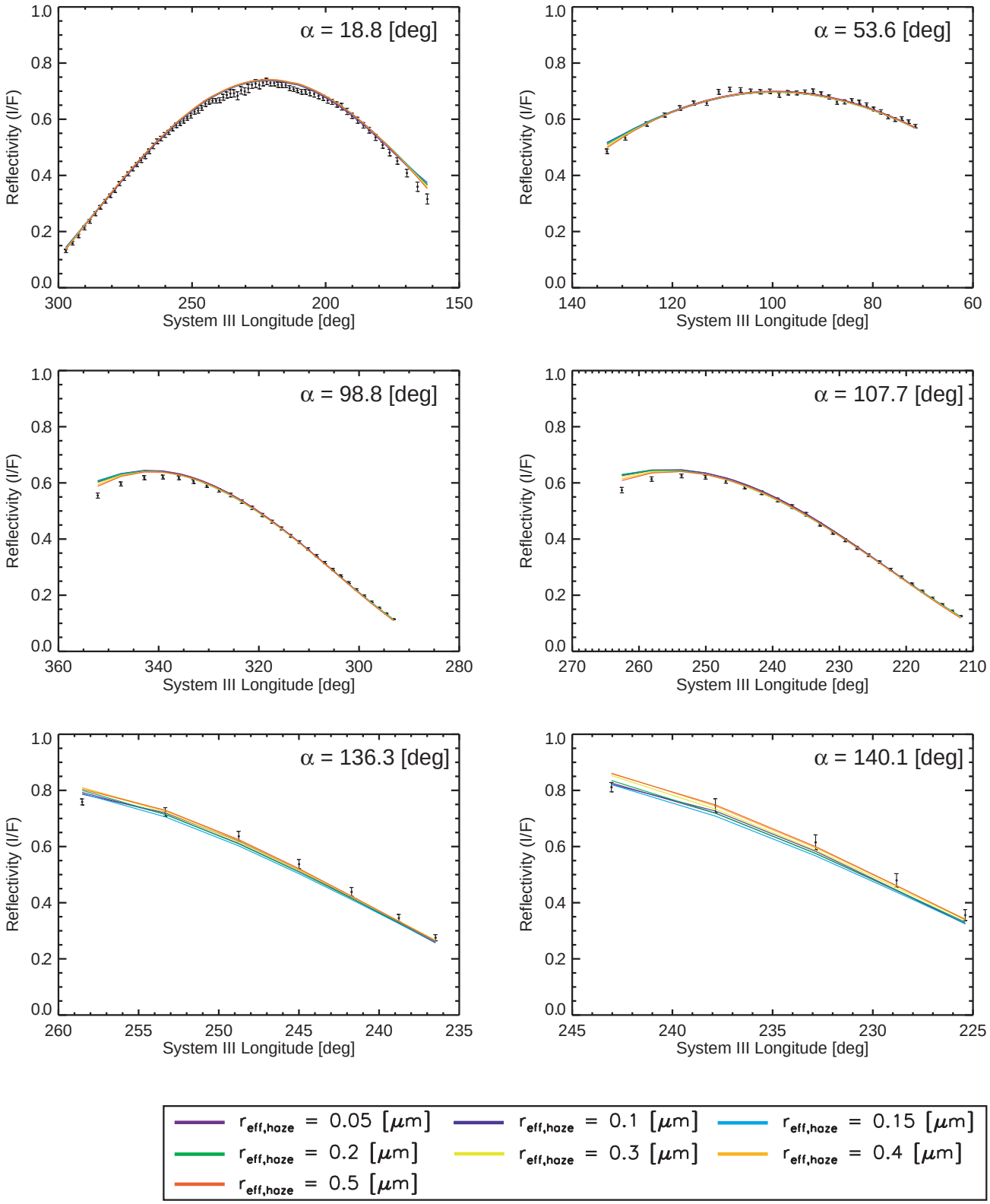

Figure 4.4–*Continued*

Although the general characteristics of the observed limb-darkening curves for a total of 12 solar phase angles can be reproduced well with any values of $r_{\mathrm{eff,haze}}$ as shown by **Figure 4.4**, the smallest χ^2 value (χ^2 = 2.61) is reached with the best-fit model of $r_{\mathrm{eff,haze}}$ = 0.5 μm series. This large $r_{\mathrm{eff,haze}}$ actually improves the model's fit for the near-limb points at 10 solar phase angles (3.7°–127.9°). At the same time, the two large solar phase angles (136.3° and 140.1°) also prefer such a large effective radius, as these data are very sensitive to the intensity of forward scattering. The relatively high reflectivity observed in these two solar phase angles indeed requires very strong forward scattering, which a larger $r_{\mathrm{eff,haze}}$ would produce (Rages et al., 1999). In the case of $r_{\mathrm{eff,haze}}$ = 0.5 μm, $n_{\mathrm{r,cloud}}$ and $r_{\mathrm{eff,cloud}}$ are optimized at 1.85 and 0.3 μm, respectively. The combination of these two parameters does not change with $r_{\mathrm{eff,haze}}$ if $r_{\mathrm{eff,haze}}$ is larger than or equal to 0.15 μm. This combination still gives a small χ^2 value in the other two cases for $r_{\mathrm{eff,haze}}$ = 0.05 μm and 0.1 μm, as shown in **Figure 4.2**.

In the best-fit models for seven different $r_{\mathrm{eff,haze}}$ cases, ω_{cloud} is optimized at a value of ~0.997, close to unity. For τ_{haze}, although the optimized τ_{haze} varies with the value of $r_{\mathrm{eff,haze}}$, the stratospheric haze is found to be optically thin (<0.06). The results of the best-fit model in all assumed cases for this data set are summarized in **Section 4.5**, along with those for other data sets. Comparisons of these optical and physical properties with those inferred from previous studies are described in detail in **Section 5.1**.

4.2. The CB2/SEBn data set

The same approach as that for the CB2/STrZ data set is applied to the CB2/SEBn data set. The χ^2 variations as a function of $n_{\mathrm{r,cloud}}$ and $r_{\mathrm{eff,cloud}}$ for seven different $r_{\mathrm{eff,haze}}$ cases are displayed in **Figure 4.5**. All four characteristics mentioned in **Section 4.1** can also be read from the behavior of such χ^2 variations. For each $r_{\mathrm{eff,haze}}$ case, the values of best-fit parameters ($n_{\mathrm{r,cloud}}$, $r_{\mathrm{eff,cloud}}$, ω_{cloud}, and τ_{haze}) and χ^2 value for the best-fit model are listed in **Table 4.2**. In this data set, the best-fit combination of $n_{\mathrm{r,cloud}}$ and $r_{\mathrm{eff,cloud}}$ is determined regardless of the value of $r_{\mathrm{eff,haze}}$. That is, $n_{\mathrm{r,cloud}}$ is optimized at 1.8, which is somewhat smaller than the best-fit value of $n_{\mathrm{r,cloud}}$ for the CB2/STrZ data set. $r_{\mathrm{eff,cloud}}$ as well as that for the CB2/STrZ data set is optimized at 0.3 μm. The best-fit modeled limb-darkening curves for each $r_{\mathrm{eff,haze}}$ case, together with the observed curves, are presented in **Figure 4.6**.

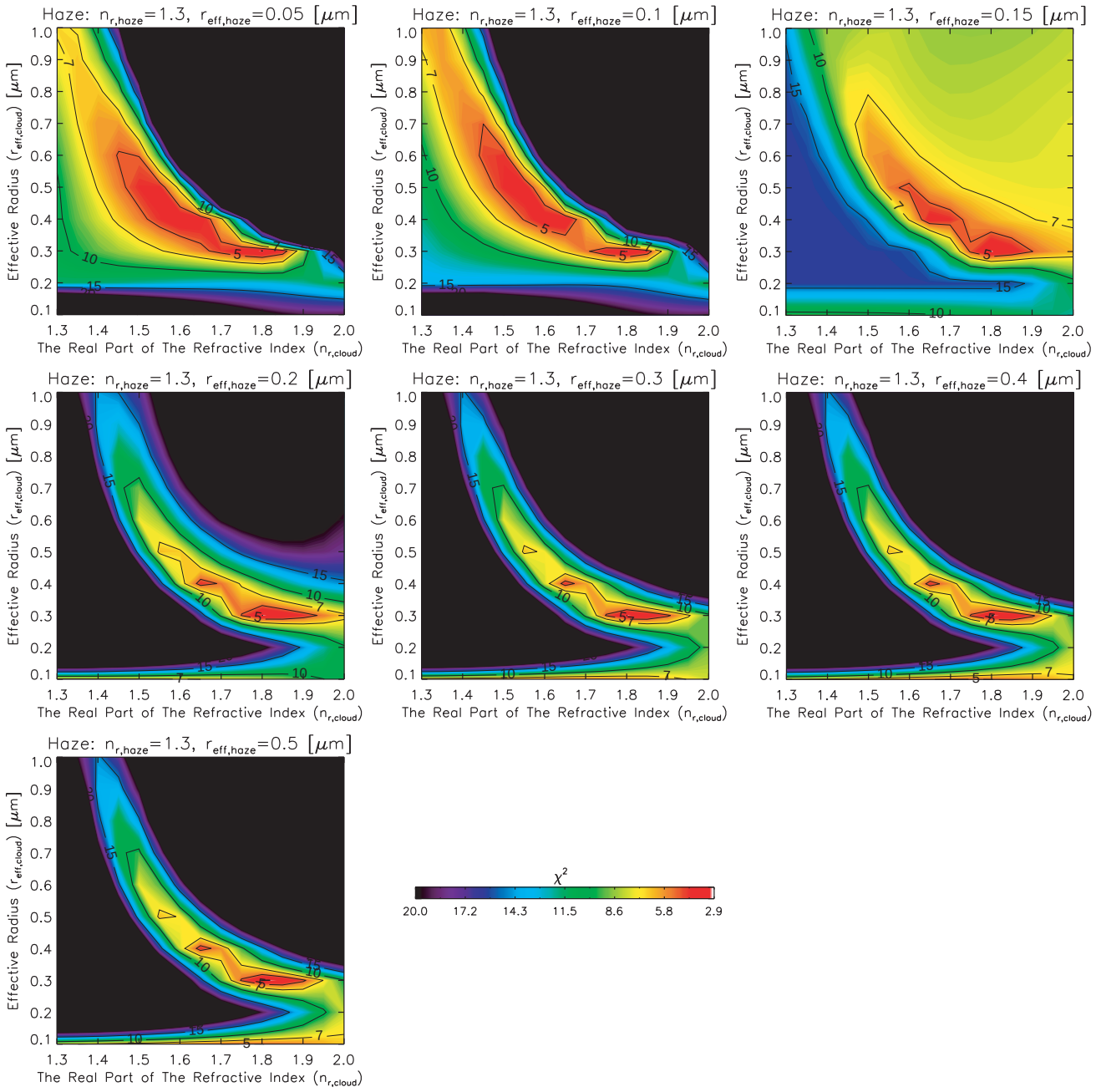

Figure 4.5. Same as Figure 4.2, except in the CB2/SEBn data set. For each $r_{\text{eff,haze}}$, the best-fit values of $n_{\text{r,cloud}}$ and $r_{\text{eff,cloud}}$, and χ^2 value for the best-fit model are presented in Table 4.2.

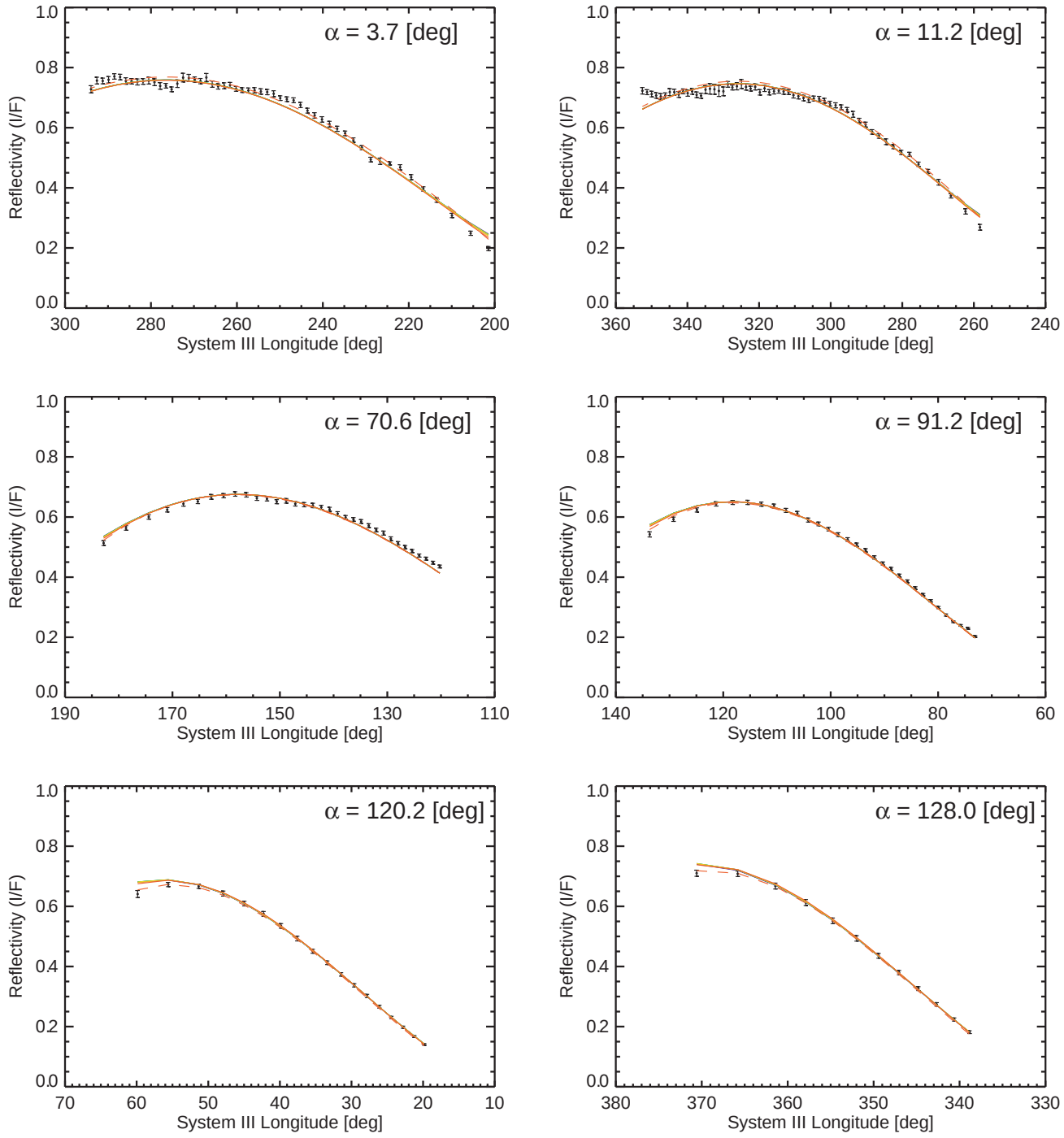

Figure 4.6. Same as Figure 4.4, except in the CB2/SEBn data set. The best-fit model in all assumed cases is obtained with $n_{\mathrm{r,cloud}}$ = 1.8 and $r_{\mathrm{eff,cloud}}$ = 0.3 μm for cloud particles and $n_{\mathrm{r,haze}}$ = 1.3 and $r_{\mathrm{eff,haze}}$ = 0.5 μm for the stratospheric haze. The best-fit model with the scattering phase function for cloud with values of $n_{\mathrm{r,cloud}}$ = 1.85 and $r_{\mathrm{eff,cloud}}$ = 0.3 μm is also presented with red dashed curves.

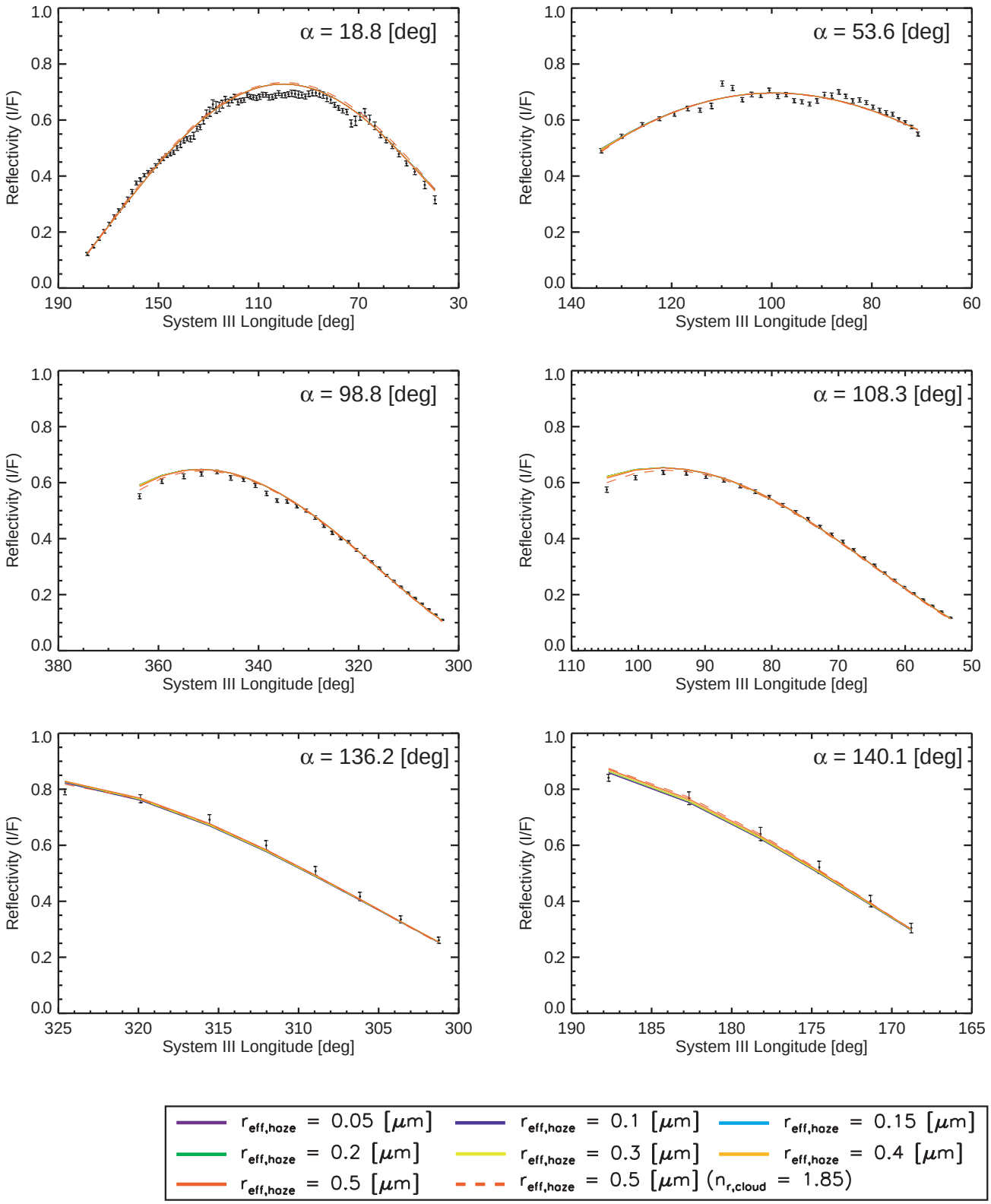

Figure 4.6–*Continued*

Table 4.2. Same as Table 4.1, except in the CB2/SEBn data set.

The best-fit values					
$r_{\mathrm{eff,haze}}$ [μm]	$n_{\mathrm{r,cloud}}$	$r_{\mathrm{eff,cloud}}$ [μm]	ω_{cloud}	τ_{haze}	χ^2
0.05	1.80	0.3	0.9933	0.0024	2.97
0.1	1.80	0.3	0.9933	0.0028	2.98
0.15	1.80	0.3	0.9933	0.0000	2.99
0.2	1.80	0.3	0.9933	0.0000	2.99
0.3	1.80	0.3	0.9933	0.0000	2.99
0.4	1.80	0.3	0.9932	0.0070	2.97
0.5	1.80	0.3	0.9932	0.0174	2.92

The obtained ω_{cloud}, the value of which is 0.9932, shows no change with $r_{\mathrm{eff,haze}}$ and is smaller than that for the CB2/STrZ data set (= 0.9968 at $r_{\mathrm{eff,haze}}$ = 0.5 μm). In general, single scattering co-albedo, $1-\omega$, gives the probability of absorption due to atmospheric molecules or aerosols in one scattering event. Thus, particles in cloud layer for the SEBn ($1-\omega$ = 0.0068) absorb twice as many photons as those for the STrZ ($1-\omega$ = 0.0032) per one scattering event at this wavelength. Conversely, unlike in the case of the CB2/STrZ data set, the stratospheric haze is not indispensable for fitting the observations for all $r_{\mathrm{eff,haze}}$ cases, while the best-fit model ($r_{\mathrm{eff,haze}}$ = 0.5 μm) in all assumed cases actually improves the model's fit for the same reasons mentioned in **Section 4.1** compared with no stratospheric haze models (i.e., $r_{\mathrm{eff,haze}}$ = 0.15–0.3 μm cases).

There is a remaining important question: can a cloud model with the best-fit combination of $n_{\mathrm{r,cloud}}$ (= 1.85) and $r_{\mathrm{eff,cloud}}$ (= 0.3 μm) obtained from the CB2/STrZ data set also make a reasonable fit to the CB2/SEBn data set? **Table 4.3** presents the optimized ω_{cloud} and τ_{haze}, and the best-fit χ^2 value for each $r_{\mathrm{eff,haze}}$ case. Under such combination of $n_{\mathrm{r,cloud}}$ and $r_{\mathrm{eff,cloud}}$, as $r_{\mathrm{eff,haze}}$ is larger, χ^2 value monotonically decreases and reaches the minimum value (= 3.13) at $r_{\mathrm{eff,haze}}$ = 0.5 μm. For $r_{\mathrm{eff,haze}}$ = 0.5 μm case, the obtained ω_{cloud} is 0.9928 which is slightly smaller than that (= 0.9932) for the best-fit model described above and τ_{haze} (= 0.064) is comparable to that (= 0.056) for the STrZ. The modeled limb-darkening curves for $r_{\mathrm{eff,haze}}$ = 0.5 μm case ($n_{\mathrm{r,cloud}}$ = 1.85 and $r_{\mathrm{eff,cloud}}$ = 0.3 μm) are shown using red dashed curves in **Figure 4.6**. The difference in χ^2 between two cloud models is only 0.21. To check the value of individual chi-square for each solar phase angle, we tabulate the normalized chi-square for the *i*th solar phase angle, χ_{i}^2, in two cloud models: ($n_{\mathrm{r,cloud}}$ = 1.8 and $r_{\mathrm{eff,cloud}}$ = 0.3 μm) and ($n_{\mathrm{r,cloud}}$ = 1.85 and $r_{\mathrm{eff,cloud}}$ = 0.3 μm) in **Table 4.4**. Although the relatively large differences in χ_{i}^2 ($\Delta\chi_{\mathrm{i}}^2$ > 1) are found at α = 3.7°, 18.8°, and 108.3°, even in such cases, it is highly difficult to judge the goodness

of fit from **Figure 4.6** because limb-darkening curves at small solar phase angles for the SEBn are not so smooth compared with those for the STrZ due to small cloud features. For large solar phase angles, the cloud model with $n_{\mathrm{r,cloud}}$ = 1.85 seems to bring better results with regard to the near-limb points because of the relatively-thick stratospheric haze. Therefore, we do not have any basis for suggesting that the difference of $n_{\mathrm{r,cloud}}$ in the best-fit models leads to the visual difference at this wavelength between the STrZ and the SEBn.

Table 4.3. The best-fit models in the CB2/SEBn data set when we use a cloud model with a combination of $n_{\mathrm{r,cloud}}$ = 1.85 and $r_{\mathrm{eff,cloud}}$ = 0.3 μm.

The best-fit values					
$r_{\mathrm{eff,haze}}$ [μm]	$n_{\mathrm{r,cloud}}$	$r_{\mathrm{eff,cloud}}$ [μm]	ω_{cloud}	τ_{haze}	χ^2
0.05	1.85	0.3	0.9929	0.0000	4.13
0.1	1.85	0.3	0.9928	0.0000	4.13
0.15	1.85	0.3	0.9928	0.049	3.73
0.2	1.85	0.3	0.9928	0.039	3.36
0.3	1.85	0.3	0.9928	0.035	3.34
0.4	1.85	0.3	0.9928	0.048	3.24
0.5	1.85	0.3	0.9928	0.064	3.13

Table 4.4. Comparison of chi-square for *i*th solar phase angle, χ_{i}^2, between two cloud models: ($n_{\mathrm{r,cloud}}$ = 1.8 and $r_{\mathrm{eff,cloud}}$ = 0.3 μm) and ($n_{\mathrm{r,cloud}}$ = 1.85 and $r_{\mathrm{eff,cloud}}$ = 0.3 μm).

Solar phase angle α	3.7°	11.2°	18.8°	53.6°	70.6°	91.2°	98.8°
$n_{\mathrm{r,cloud}}$ = 1.8	4.54	2.33	5.62	4.36	3.83	2.19	4.24
$n_{\mathrm{r,cloud}}$ = 1.85	2.26	3.20	7.87	4.63	4.31	2.81	4.05
	108.3°	120.2°	128.0°	136.2°	140.1°	average	
$n_{\mathrm{r,cloud}}$ = 1.8	2.76	0.82	0.98	2.23	1.10	2.92	
$n_{\mathrm{r,cloud}}$ = 1.85	3.82	0.93	0.80	1.60	1.27	3.13	

4.3. The BL1/STrZ data set

We run through the same routine for the BL1/STrZ data set. **Figure 4.7** shows χ^2 variations as a function of $n_{\mathrm{r,cloud}}$ and $r_{\mathrm{eff,cloud}}$ for seven different $r_{\mathrm{eff,haze}}$ cases. In spite of the wavelength difference between BL1 and CB2, the characteristics of χ^2 variations discussed in **Section 4.1** hold true in this data set. Note that the behavior of χ^2 at $r_{\mathrm{eff,haze}}$ = 0.05 μm is different from the others because the effective radius which gives the size parameter being equal to unity in BL1 is ~0.07 μm. Again, the models with NH_3 ice-like particles, $n_{\mathrm{r,cloud}}$ of which is in the range of 1.4–1.45, do not reproduce the observations well. The χ^2 value is always >17 if $r_{\mathrm{eff,haze}}$ is larger than 0.1 μm. Even for models with much small haze particle, the smallest achieved χ^2 value is 8.26 ($r_{\mathrm{eff,haze}}$ = 0.05 μm, $n_{\mathrm{r,cloud}}$ = 1.45, and $r_{\mathrm{eff,cloud}}$ = 0.5 μm), which is quite unsatisfactory.

For each $r_{\mathrm{eff,haze}}$ case, the values of best-fit parameters ($n_{\mathrm{r,cloud}}$, $r_{\mathrm{eff,cloud}}$, ω_{cloud}, and τ_{haze}) and χ^2 value for the best-fit model are listed in **Table 4.5**. The best-fit modeled limb-darkening curves for each $r_{\mathrm{eff,haze}}$ case, together with the observed curves, are shown in **Figure 4.8**.

Even though the limb-darkening curves for all solar phase angles in the STrZ are relatively smooth at both wavelengths (CB2 and BL1) used in this study (**Figure 4.4** and **Figure 4.8**), the best-fit χ^2 values calculated from the BL1/STrZ data set are significantly large than those calculated from the CB2/STrZ data set (**Table 4.1** and **Table 4.5**). As is evident in **Figure 4.8**, mismatches between the observed and modeled limb-darkening curves become apparent toward the limb at three small solar phase angles (3.7°, 12.6°, and 18.8°). For this reason, we relax the constraint on fixed parameters in the cloud model to improve the model's fit in the followings.

Table 4.5. Same as Table 4.1, except in the BL1/STrZ data set.

The best-fit values					
$r_{\mathrm{eff,haze}}$ [μm]	$n_{\mathrm{r,cloud}}$	$r_{\mathrm{eff,cloud}}$ [μm]	ω_{cloud}	τ_{haze}	χ^2
0.05	1.85	0.2	0.9949	0.054	5.33
0.1	1.90	0.2	0.9943	0.0043	6.04
0.15	1.90	0.2	0.9943	0.0036	6.04
0.2	1.90	0.2	0.9943	0.012	5.92
0.3	1.90	0.2	0.9943	0.035	5.45
0.4	1.90	0.2	0.9943	0.049	5.27
0.5	1.90	0.2	0.9943	0.050	5.36

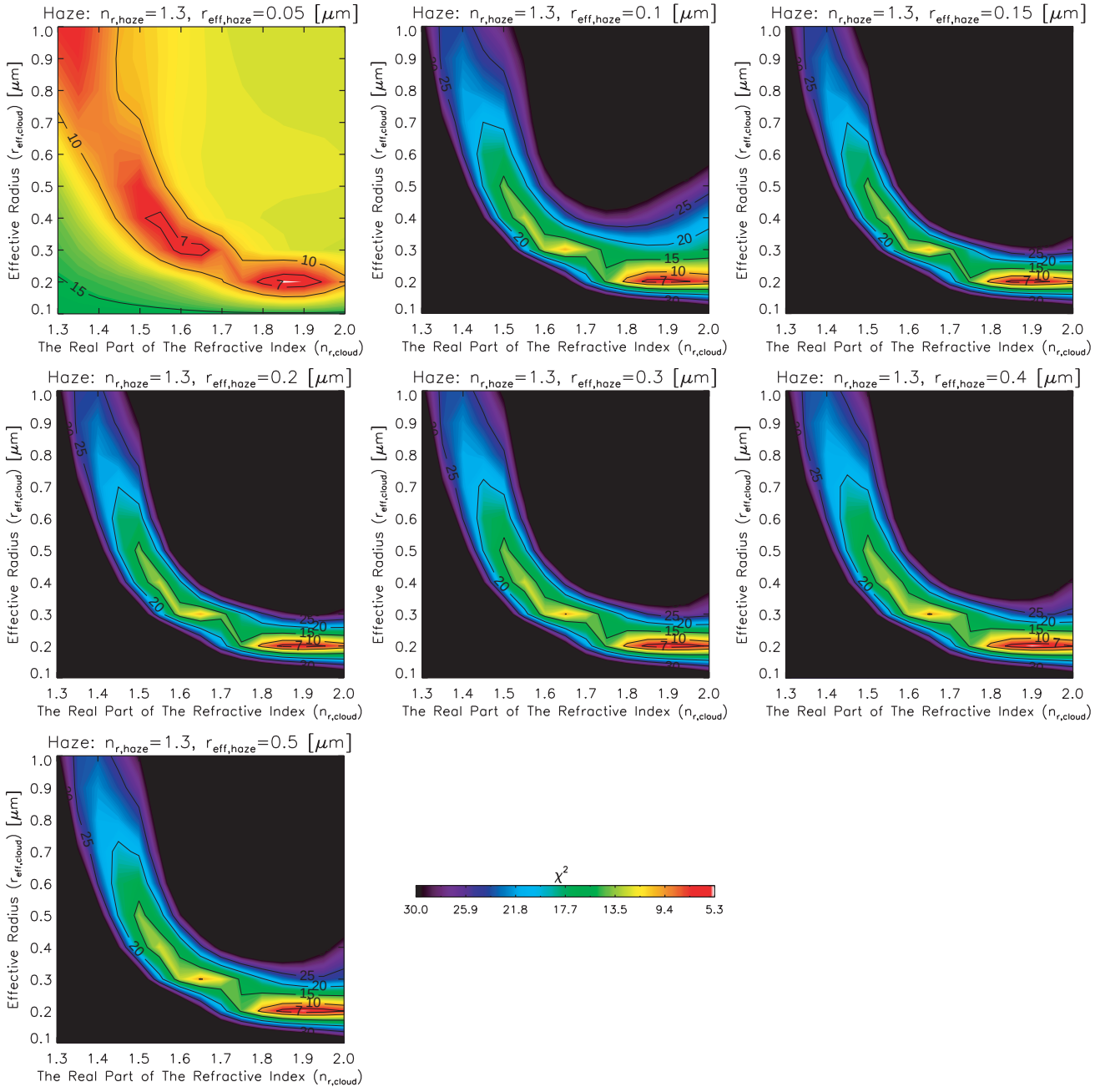

Figure 4.7. Same as Figure 4.2, except in the BL1/STrZ data set. For each $r_{\text{eff,haze}}$, the best-fit values of $n_{\text{r,cloud}}$ and $r_{\text{eff,cloud}}$, and χ^2 value for the best-fit model are presented in Table 4.5.

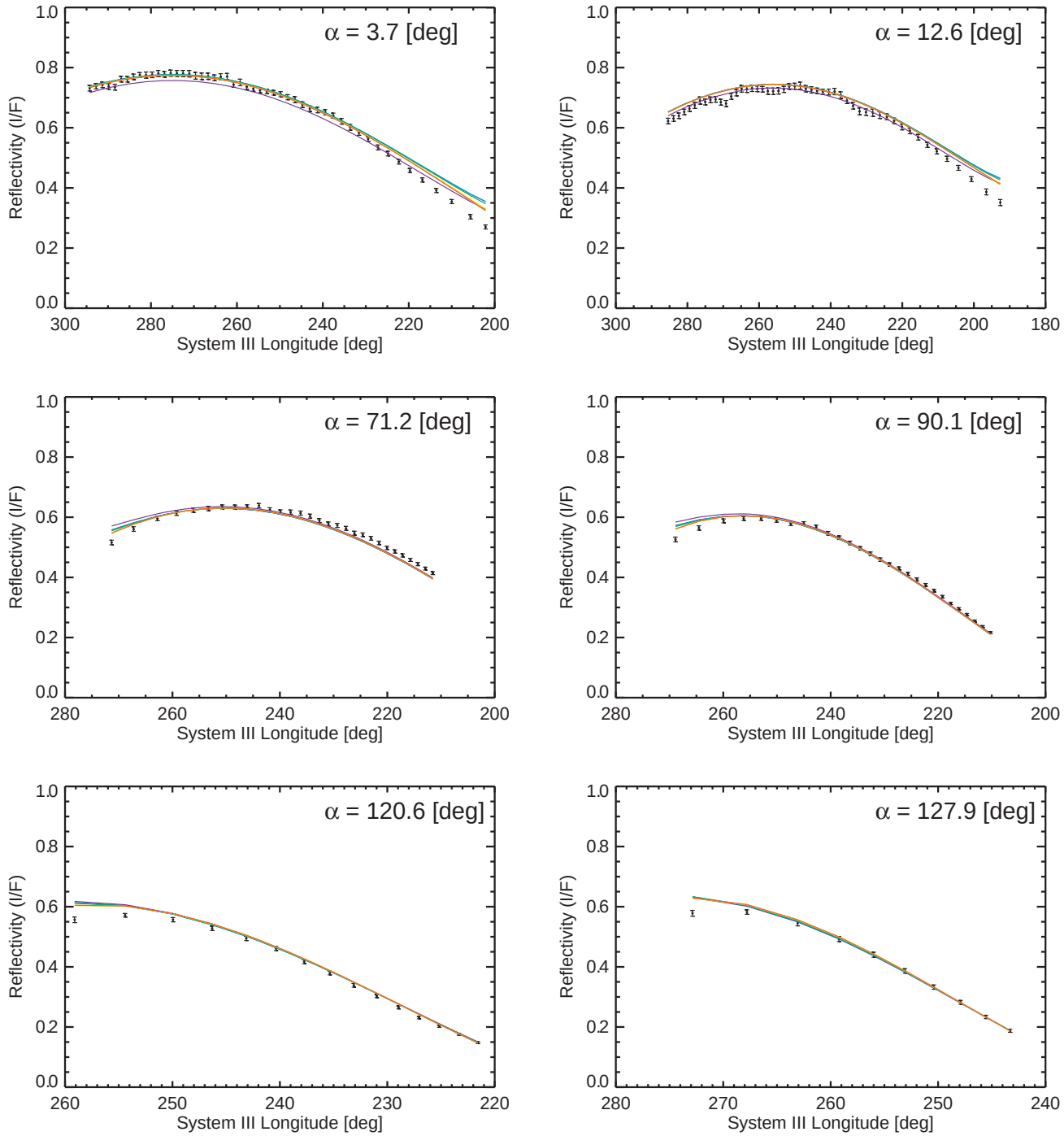

Figure 4.8. Same as Figure 4.4, except in the BL1/STrZ data set. The best-fit model in all assumed cases is obtained with $n_{\mathrm{r,cloud}}$ = 1.9 and $r_{\mathrm{eff,cloud}}$ = 0.2 μm for cloud particles and $n_{\mathrm{r,haze}}$ = 1.3 and $r_{\mathrm{eff,haze}}$ = 0.4 μm for the stratospheric haze. Even the best-fit model in all assumed cases cannot reproduce the observations, especially in some limb points at small solar phase angles (3.7°, 12.6°, and 18.8°).

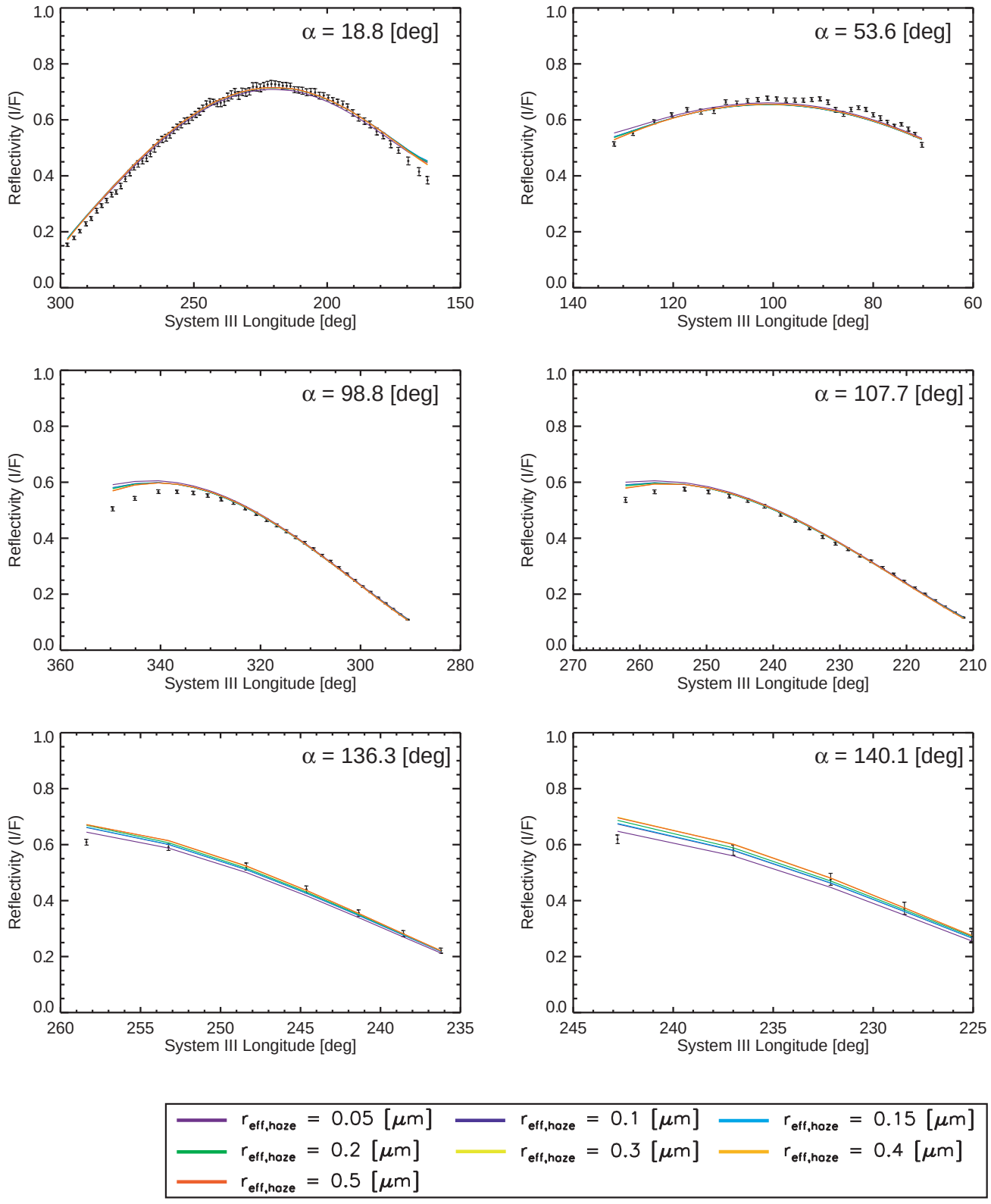

Figure 4.8–*Continued*

ΔP_1 and ΔP_2 dependence

As already noted in **Section 3.3**, the atmosphere seen in BL1 is optically thicker due to Rayleigh scattering compared with that seen in CB2. It means that the observed limb-darkening curves for the entire solar phase angles in BL1 are more sensitive to ΔP_1 and ΔP_2 than those in CB2. Therefore, it is possible to improve the model's fit by changing the pressure levels of the stratospheric haze ΔP_1 and the cloud top $(\Delta P_1 + \Delta P_2)$. To find out this effect, we perform the radiative transfer calculations with additional combinations of ΔP_1 and ΔP_2. In these calculations, we use the Mie scattering phase function for cloud with values of $n_{\mathrm{r,cloud}}$ = 1.9 and $r_{\mathrm{eff,cloud}}$ = 0.2 μm, and the function for haze with values of $n_{\mathrm{r,cloud}}$ = 1.3 and $r_{\mathrm{eff,cloud}}$ = 0.5 μm. Note that all other assumed parameters are not changed in this calculation. **Table 4.6** presents the assumed combinations of ΔP_1 and ΔP_2, and the best-fit χ^2 value for each combination. The comparisons of limb-darkening curves between the observations and model calculations for three cases (an already-described nominal case and two extreme cases) are shown in **Figure 4.9**.

As shown in **Table 4.6**, χ^2 value decreases with increasing ΔP_1 and ΔP_2 (lowering altitudes of the stratospheric haze and cloud top) and reaches the minimum value (= 4.37) when we use a cloud model (ΔP_1 = 0.15 bar and ΔP_2 = 0.3 bar). Such effect on modeled limb-darkening curves can be clearly seen in those at four high solar phase angles (120.6°, 127.9°, 136.3°, and 140.1°) because these data with relatively small μ and μ_0 are especially sensitive to the upper layer. However, even "the lowest-cloud model" represented by green curves in **Figure 4.9** shows little improvement in the model's fit for the near-limb points at three small solar phase angles (3.7°, 12.6°, and 18.8°). From this sensitivity test for ΔP_1 and ΔP_2, we find that the assumption of ΔP_1 and ΔP_2 is not the primary cause of these mismatches.

Table 4.6. Sensitivity of χ^2 value for two pressure differences (ΔP_1 and ΔP_2). In these calculations, we use the Mie scattering phase function for cloud with values of $n_{\mathrm{r,cloud}}$ = 1.9 and $r_{\mathrm{eff,cloud}}$ = 0.2 μm, and the function for haze with values of $n_{\mathrm{r,cloud}}$ = 1.3 and $r_{\mathrm{eff,cloud}}$ = 0.5 μm.

ΔP_1 and ΔP_2 dependence		ΔP_2 [bar]			
		0.0	0.1	0.2	0.3
ΔP_1 [bar]	0.0	12.89	9.10	6.71	5.26
	0.05	10.83	7.80	5.93	4.87
	0.1	9.20	6.79	5.36*	4.58
	0.15	7.91	6.02	4.94	4.37

* A cloud model with a combination of ΔP_1 = 0.1 bar and ΔP_2 = 0.2 bar is referred to as "nominal case".

ω_{haze} dependence

Although we succeed in reproducing the observed limb-darkening curves for all solar phase angles in CB2 with ω_{haze} = 1 (i.e., $n_{\mathrm{i,haze}}$ = 0), it is unclear whether such conservative scattering of the stratospheric haze is also true for those in BL1. In fact, West (1988) used n_{i} = 0.02 for the stratospheric haze particles, based on extrapolation of n_{i} curves derived by Tomasko et al. (1986) with UV data (see Figure 13 of their paper), to analyze the Voyager 2 images at 430 nm. Thus, we are motivated to perform the radiative transfer calculations to examine the sensitivity of χ^2 value for ω_{haze} variations. In practice, we vary $n_{\mathrm{i,haze}}$ in the range of 0.0001–0.8 ($n_{\mathrm{i,haze}} = p \times 10^{-q}$: p = 1, 2, 4, 6, 8 and q = 1, 2, 3, 4) and recalculate the Mie scattering phase functions for each $n_{\mathrm{i,haze}}$ with values of $n_{\mathrm{r,haze}}$ = 1.3 and seven different $r_{\mathrm{eff,haze}}$. The derived ω_{haze} in the Mie scattering calculations, which decreases with increasing $n_{\mathrm{i,haze}}$ regardless of $n_{\mathrm{r,haze}}$ and $r_{\mathrm{eff,haze}}$, is used as the single scattering albedo of the stratospheric haze. Note that all other assumed parameters (e.g., ΔP_1 and ΔP_2) are not changed from nominal values in this calculation.

Figure 4.10 shows the relationship of χ^2 value and two optimized parameters (ω_{cloud} and τ_{haze}) to $n_{\mathrm{i,haze}}$ for each $r_{\mathrm{eff,haze}}$ case. The values of best-fit parameters ($n_{\mathrm{r,cloud}}$, $r_{\mathrm{eff,cloud}}$, $n_{\mathrm{i,haze}}$, ω_{haze}, ω_{cloud}, and τ_{haze}) and χ^2 value for the best-fit model are summarized for each $r_{\mathrm{eff,haze}}$ case in **Table 4.7**.

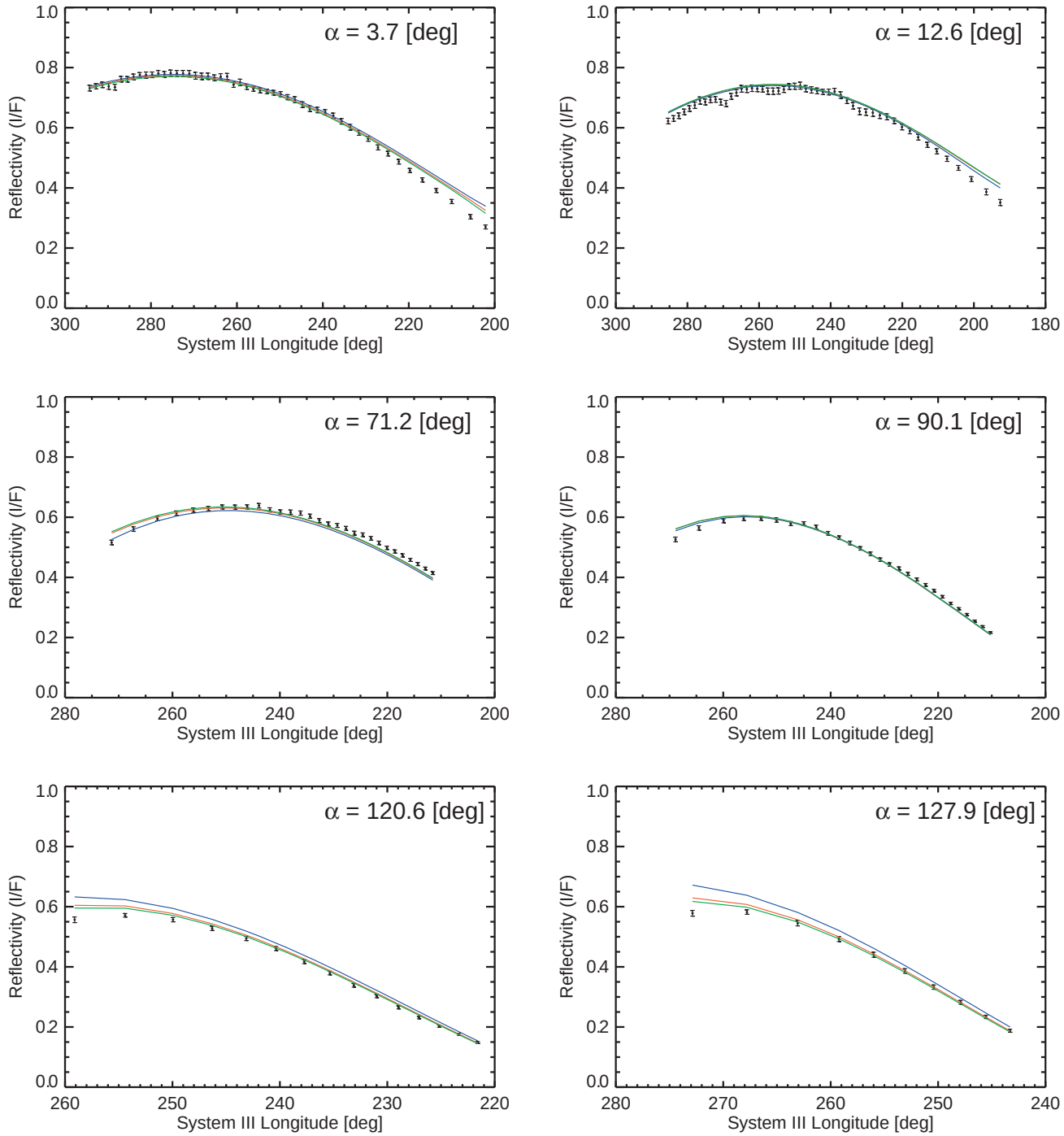

Figure 4.9. The sensitivity of modeled limb-darkening curves in BL1 for two pressure differences (ΔP_1 and ΔP_2). In this figure, three model calculation results (one nominal case and two extreme cases, see also Table 4.6) are presented.

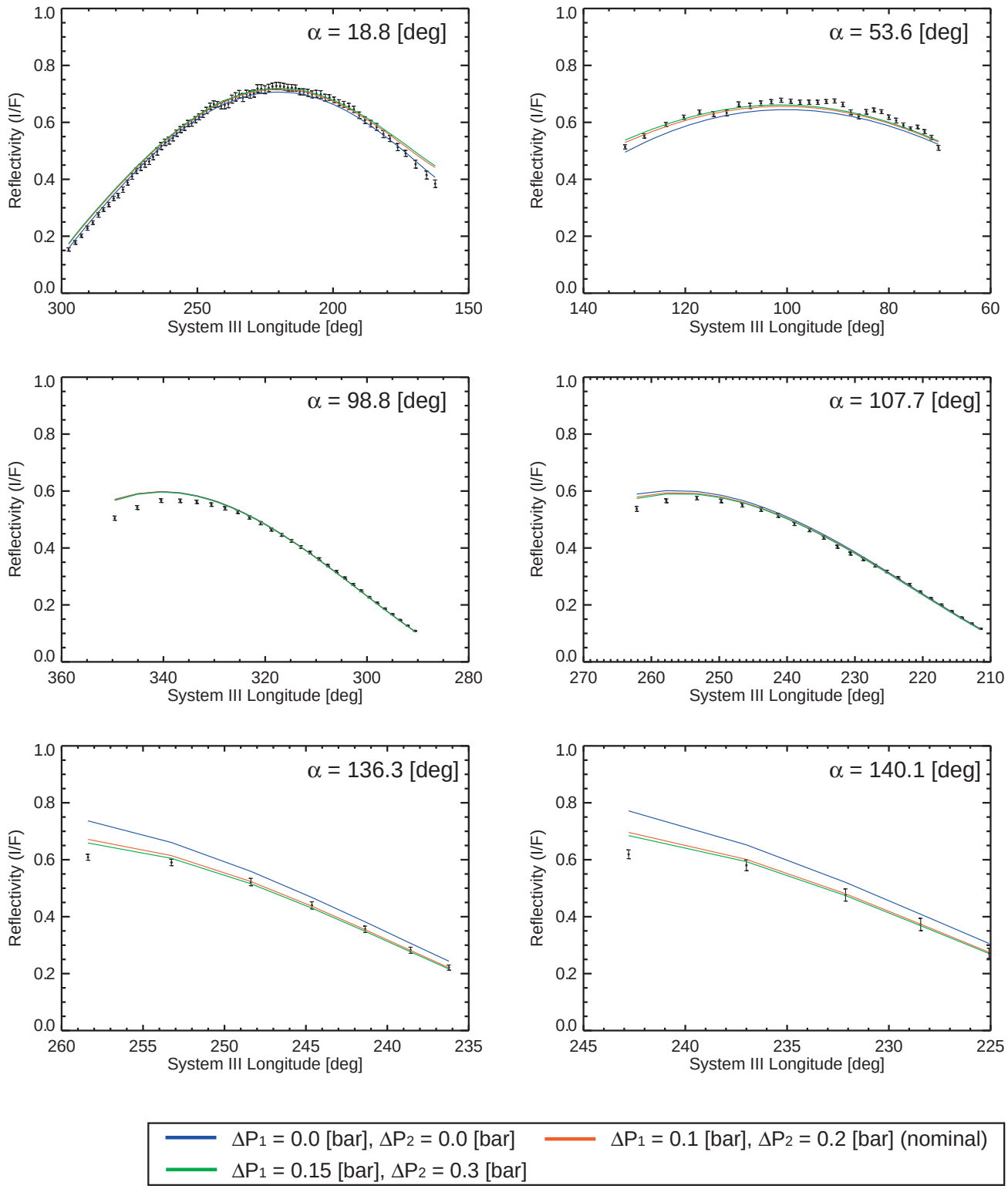

Figure 4.9–*Continued*

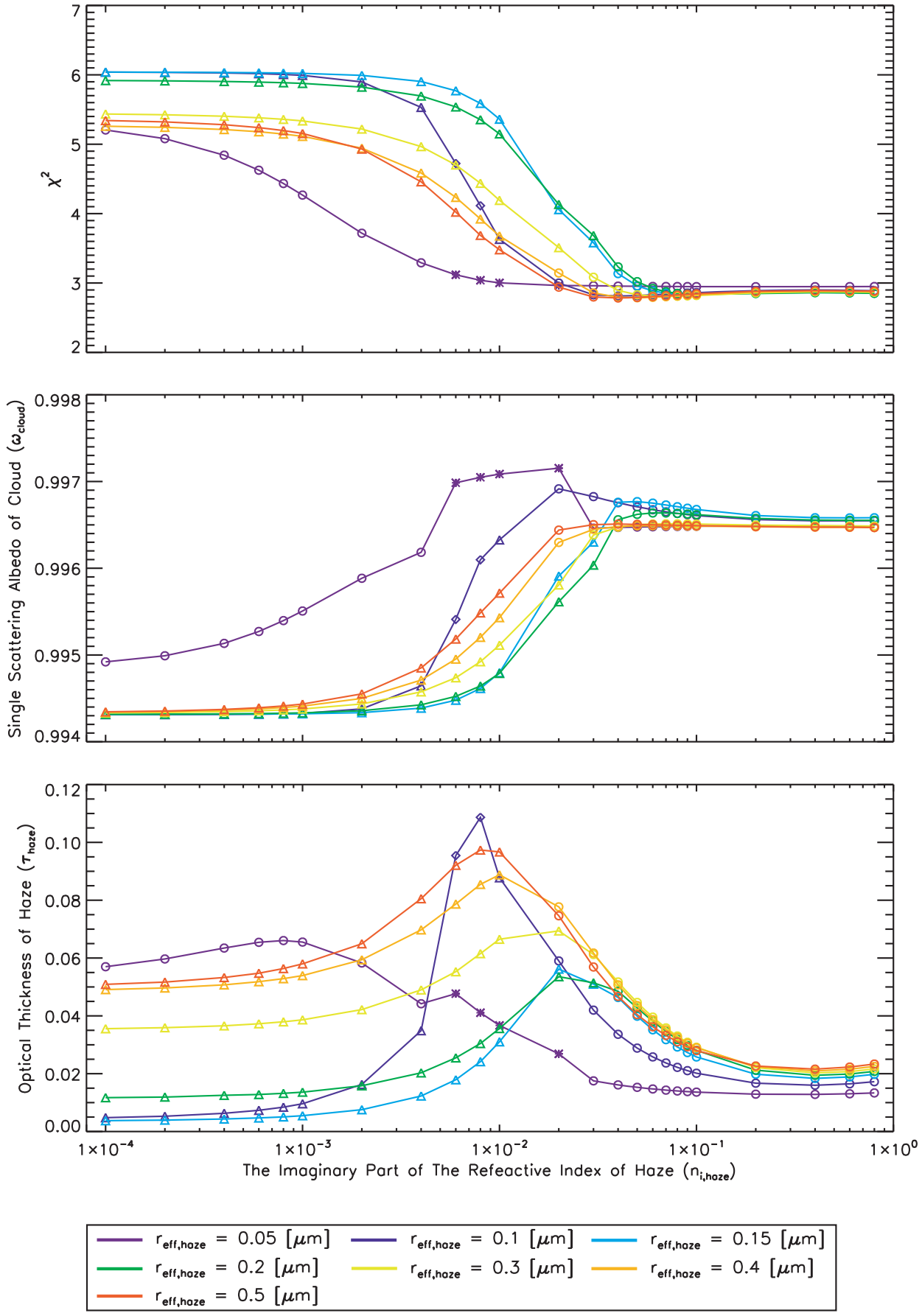
χ^2
Single Scattering Albedo of Cloud (ω_{cloud})
Optical Thickness of Haze (τ_{haze})
The Imaginary Part of The Refeactive Index of Haze ($n_{i,haze}$)
$r_{eff,haze}$ = 0.05 [μm]
$r_{eff,haze}$ = 0.1 [μm]
$r_{eff,haze}$ = 0.15 [μm]
$r_{eff,haze}$ = 0.2 [μm]
$r_{eff,haze}$ = 0.3 [μm]
$r_{eff,haze}$ = 0.4 [μm]
$r_{eff,haze}$ = 0.5 [μm]

As is evident in **Figure 4.10**, when $n_{\mathrm{i,haze}}$ is larger than ~0.001, the χ^2 value starts to monotonically decrease with increasing $n_{\mathrm{i,haze}}$ and reaches the minimum value at $n_{\mathrm{i,haze}}$ between 0.04 and 0.2, depending on $r_{\mathrm{eff,haze}}$. Once the χ^2 value gets the minimum value at such $n_{\mathrm{i,haze}}$, however, it shows little change with $n_{\mathrm{i,haze}}$ any more. In addition, the behavior of ω_{cloud} as a function of $n_{\mathrm{i,haze}}$ is also similar to that of χ^2 with the exception that ω_{cloud} increases with $n_{\mathrm{i,haze}}$. Although the optimized τ_{haze} varies with $n_{\mathrm{i,haze}}$, this parameter seems not to show a significant difference for change of $n_{\mathrm{i,haze}}$.

The best-fit modeled limb-darkening curves for each $r_{\mathrm{eff,haze}}$ case, together with the observed curves, are also shown in **Figure 4.11**. The improvement of the model's fit is apparent in the near-limb points at three small solar phase angles (3.7°, 12.6°, and 18.8°). Although the best-fit cloud model in all assumed cases is obtained with $r_{\mathrm{eff,haze}}$ = 0.5 μm and $n_{\mathrm{i,haze}}$ = 0.04, as can be seen from **Figure 4.10** and **Figure 4.11**, there is no remarkable difference in modeled limb-darkening curves due to a difference in $r_{\mathrm{eff,haze}}$. It should be noted that the optimized $n_{\mathrm{r,cloud}}$ is 1.85, which is unchanged from the best-fit value obtained from the CB2/STrZ data set. $r_{\mathrm{eff,cloud}}$ is optimized at 0.2 μm regardless of the value of $n_{\mathrm{i,haze}}$, which is slightly smaller than that (= 0.3 μm) from the CB2/STrZ data set, with the reason being unknown.

Table 4.7. The best-fit models of the Type II-Mie model for the case of $n_{\mathrm{r,haze}}$ = 1.3 in the BL1/STrZ data set when we allow $n_{\mathrm{i,haze}}$ to vary in the range of 0.0001–0.8.

The best-fit values							
$r_{\mathrm{eff,haze}}$ [μm]	$n_{\mathrm{r,cloud}}$	$r_{\mathrm{eff,cloud}}$ [μm]	$n_{\mathrm{i,haze}}$	ω_{haze}	ω_{cloud}	τ_{haze}	χ^2
0.05	1.85	0.2	0.2	0.1027	0.9965	0.013	2.95
0.1	1.85	0.2	0.04	0.5909	0.9968	0.034	2.81
0.15	1.85	0.2	0.1	0.4912	0.9967	0.026	2.83
0.2	1.85	0.2	0.1	0.5517	0.9966	0.028	2.84
0.3	1.85	0.2	0.07	0.6737	0.9965	0.036	2.81
0.4	1.85	0.2	0.05	0.7356	0.9965	0.044	2.79
0.5	1.85	0.2	0.04	0.7500	0.9965	0.047	2.78

Figure 4.10. The relationship of χ^2 value and two optimized parameters (ω_{cloud} and τ_{haze}) to $n_{\mathrm{i,haze}}$ for each $r_{\mathrm{eff,haze}}$ case. Four symbols denote four different best-fit cloud models: asterisk, $n_{\mathrm{r,cloud}}$ = 1.8; circle, $n_{\mathrm{r,cloud}}$ = 1.85; triangle, $n_{\mathrm{r,cloud}}$ = 1.9; diamond, $n_{\mathrm{r,cloud}}$ = 1.95. In all best-fit cloud models, $r_{\mathrm{eff,cloud}}$ is optimized at 0.2 μm.

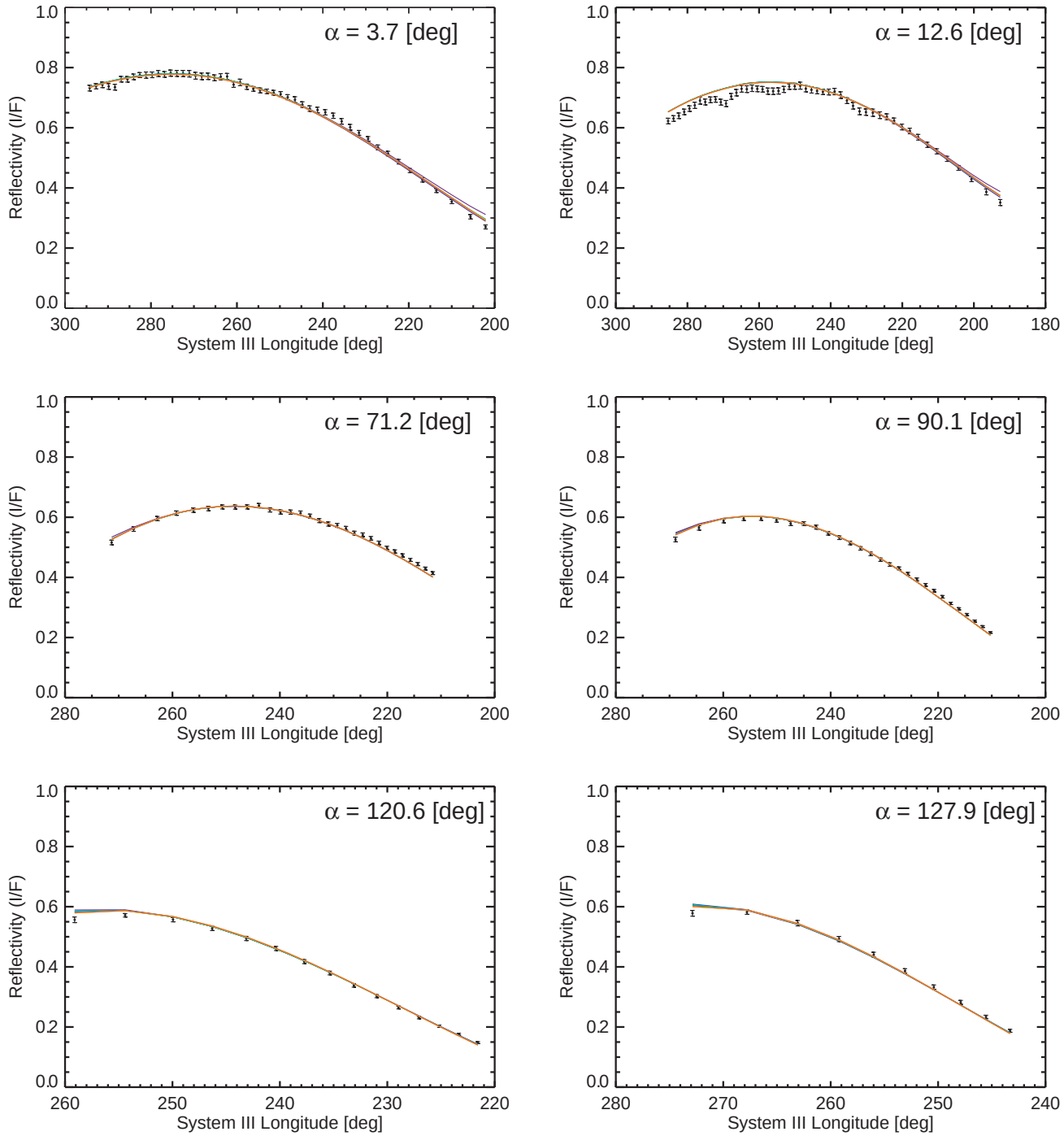

Figure 4.11. The best-fit models of the modified Type II-Mie model for seven different effective radii of haze ($r_{\mathrm{eff,haze}}$ = 0.05, 0.1, 0.15, 0.2, 0.3, 0.4, and 0.5 μm) in the BL1/STrZ data set. In this model, we allow $n_{\mathrm{i,haze}}$ to vary in the range of 0.0001–0.8. The best-fit model in all assumed cases is obtained with $n_{\mathrm{r,cloud}}$ = 1.85 and $r_{\mathrm{eff,cloud}}$ = 0.2 μm for cloud particles and $n_{\mathrm{r,haze}}$ = 1.3 and $r_{\mathrm{eff,haze}}$ = 0.5 μm for the stratospheric haze. The improvement of the model's fit is apparent in the near-limb points at small solar phase angles (3.7°, 12.6°, and 18.8°).

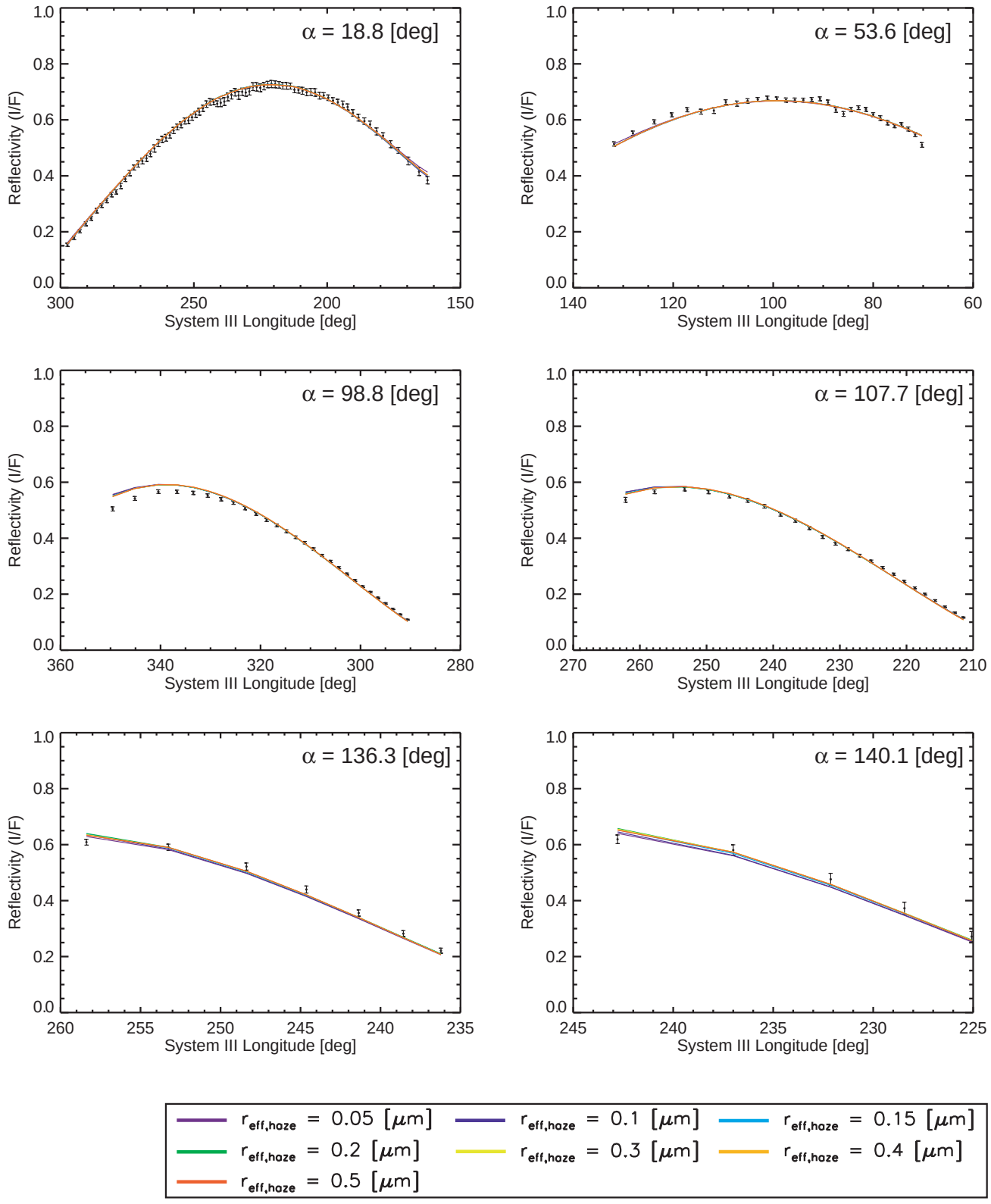

Figure 4.11–*Continued*

In closing this section, we should clarify why the observed limb-darkening curves can be reproduced by increasing $n_{\mathrm{i,haze}}$ in the cloud model. Note that increase of $n_{\mathrm{i,haze}}$ for particles causes not only decrease of the single scattering albedo but also change in the shape of the scattering phase function. When we use ω_{haze} = 1 (i.e., $n_{\mathrm{i,haze}}$ = 0) in the cloud model (referred to as nominal cloud model), the modeled limb-darkening curves show relatively flatter shapes than the observed curves at all three small solar phase angles (**Figure 4.8**). In general, since the limb-darkening curves at small solar phase angles are sensitive to the cloud layer rather than the stratospheric haze, if ω_{cloud} gets a larger value than 0.9943 which is obtained with the nominal cloud model, the modeled limb-darkening curves become steeper and can fit to these observations. However, such bright cloud particles combined with the stratospheric haze having conservative scattering yield excessively higher reflectivity compared with the observations for other solar phase angles, especially high solar phase angles (136.3° and 140.1°). This is why the nominal cloud model cannot reproduce the observations well and large $n_{\mathrm{i,haze}}$ of the stratospheric haze is required. To examine this in more detail, we focus on the behavior of ω_{haze} and $P_{\mathrm{Mie}}(\Theta)$ as a function of $n_{\mathrm{i,haze}}$ because the reflectivity at high solar phase angles is largely controlled by the albedo-weighted single scattering phase function $\omega P(\Theta)$. **Figure 4.12** indicates five scattering phase functions for the stratospheric haze with five different values of $n_{\mathrm{i,haze}}$. The values of single scattering albedo are also presented in **Figure 4.12**. We find that not only the single scattering albedo decreases but also the strengths of the scattering phase functions weaken over all scattering angles used in this study, as $n_{\mathrm{i,haze}}$ is larger. Therefore, both two effects: absorption of photons and decrease in strength of scattering due to the stratospheric haze, play a key role in obtaining higher ω_{cloud} (= 0.9965). Once ω_{cloud} gets a higher value of 0.9965, there are no need for improving the limb-darkening curves at small solar phase angles. Decrease of reflectivity at large solar phase angles due to further large $n_{\mathrm{i,haze}}$ can be compensated for by adjusting τ_{haze}. For this reason, χ^2 value keeps the similar value for large $n_{\mathrm{i,haze}}$.

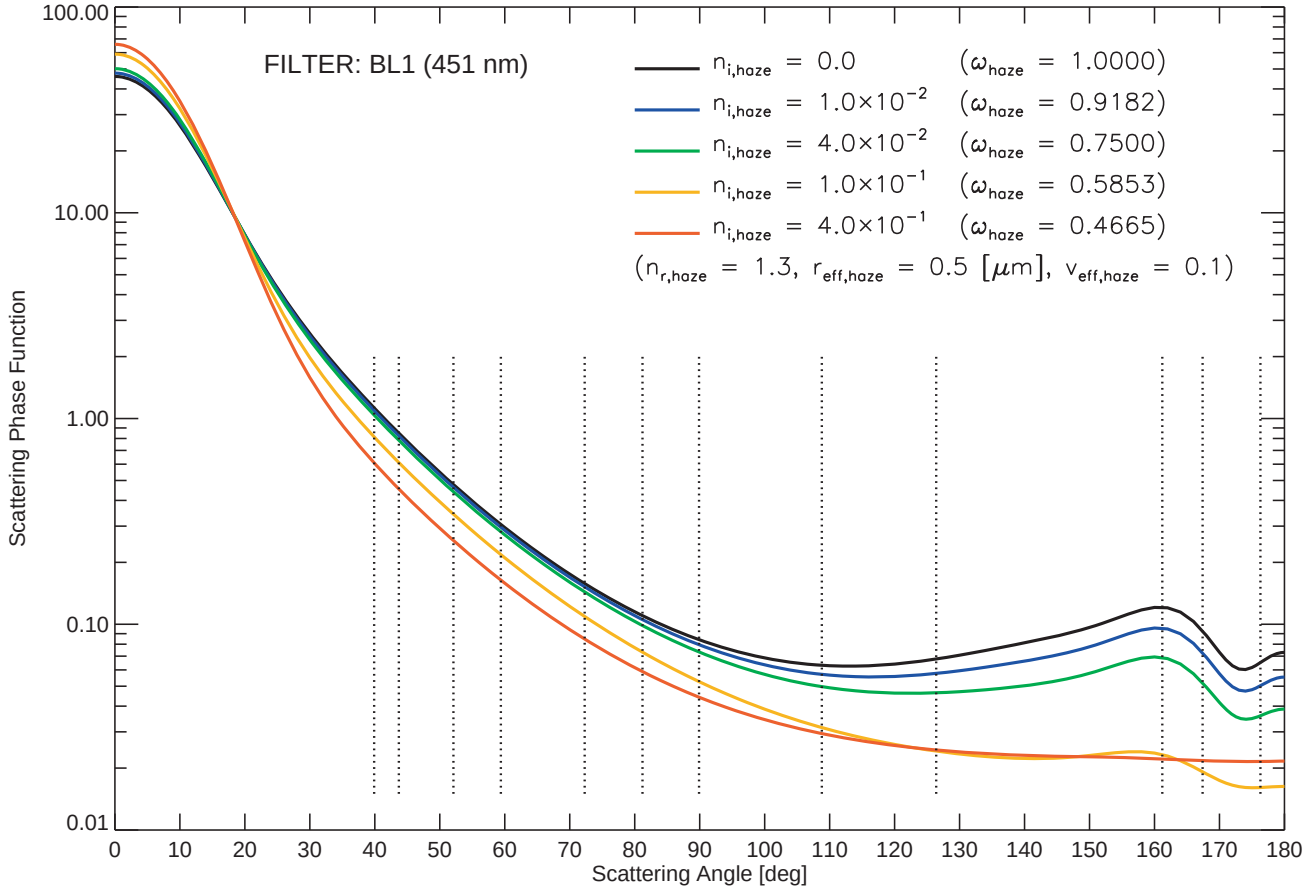

Figure 4.12. Five scattering phase functions in BL1 for the stratospheric haze with different $n_{\mathrm{i,haze}}$. The values of single scattering albedo are also presented in this figure. The vertical dotted lines indicate scattering angles sampled at the Cassini ISS observations used in this study.

4.4. The BL1/SEBn data set

For the BL1/SEBn data set, we also use the same approach as that applies to the already-described other data sets. The BL1/SEBn data set, which shows a significant difference in limb-darkening curves at small solar phase angles from other three data sets mentioned in **Section 2.6**, should yield valuable clues as to the visual difference between the zones and belts. **Figure 4.13** shows χ^2 variations as a function of $n_{\mathrm{r,cloud}}$ and $r_{\mathrm{eff,cloud}}$ for seven different $r_{\mathrm{eff,haze}}$ cases obtained with the nominal cloud model. The characteristics of χ^2 variations discussed in **Section 4.1** and **Section 4.3** are just as valid for this data set. For each $r_{\mathrm{eff,haze}}$ case, the values of best-fit parameters ($n_{\mathrm{r,cloud}}$, $r_{\mathrm{eff,cloud}}$, ω_{cloud}, and τ_{haze}) and χ^2 value for the best-fit model are tabulated in **Table 4.8**. The best-fit modeled limb-darkening curves for each $r_{\mathrm{eff,haze}}$ case, together with the observed curves, are presented in **Figure 4.14**.

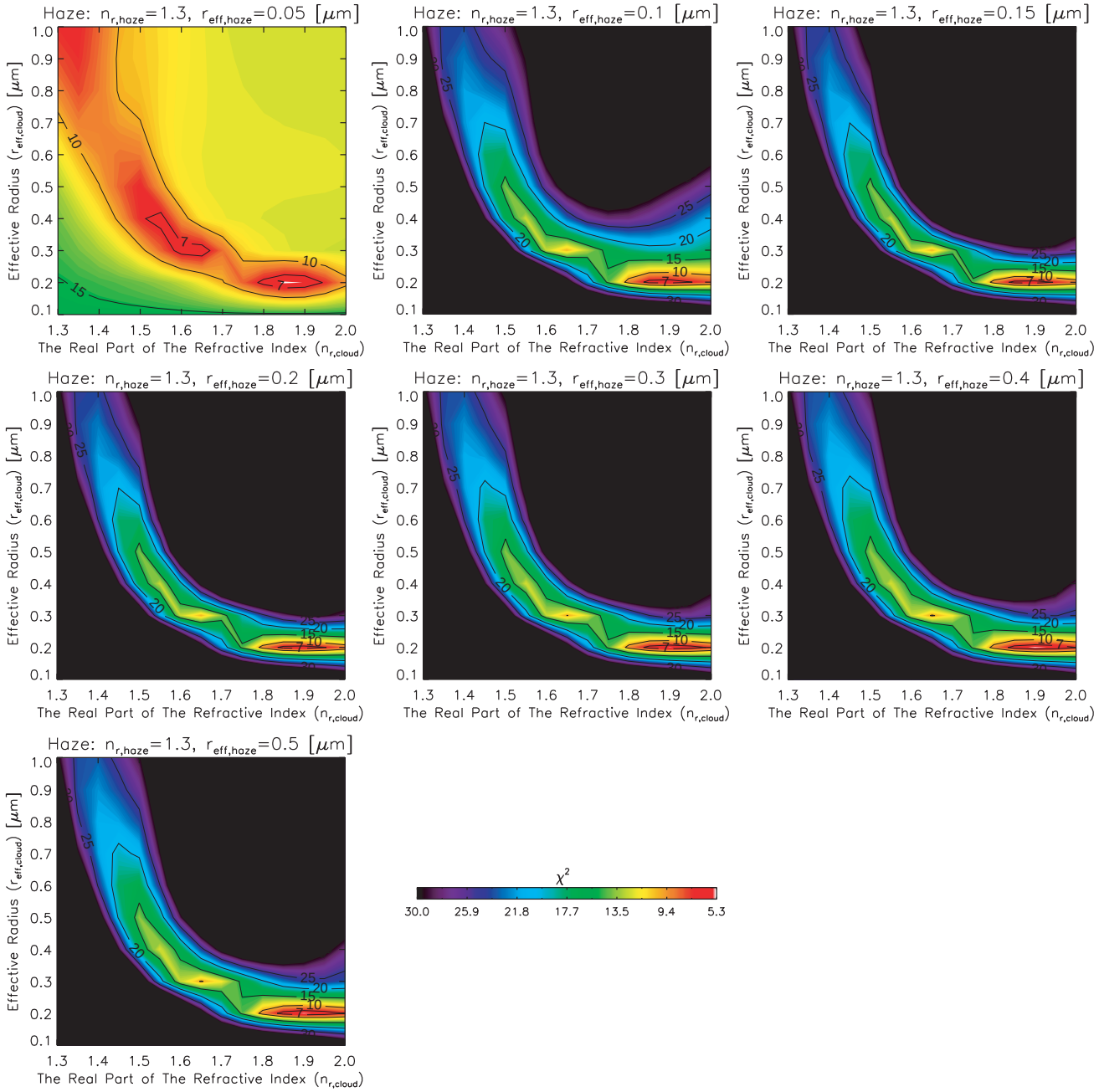

Figure 4.13. Same as Figure 4.2, except in the BL1/SEBn data set. For each $r_{\text{eff,haze}}$, the best-fit values of $n_{\text{r,cloud}}$ and $r_{\text{eff,cloud}}$, and χ^2 value for the best-fit model are presented in Table 4.8.

Table 4.8. Same as Table 4.1, except in the BL1/SEBn data set.

The best-fit values					
$r_{\mathrm{eff,haze}}$ [μm]	$n_{\mathrm{r,cloud}}$	$r_{\mathrm{eff,cloud}}$ [μm]	ω_{cloud}	τ_{haze}	χ^2
0.05	1.85	0.2	0.9687	0.044	7.26
0.1	1.85	0.2	0.9692	0.000	8.08
0.15	1.85	0.2	0.9692	0.000	8.08
0.2	1.85	0.2	0.9692	0.000	8.06
0.3	1.85	0.2	0.9691	0.000	8.05
0.4	1.85	0.2	0.9690	0.000	8.05
0.5	1.85	0.2	0.9691	0.000	8.05

In this data set as well as the CB2/SEBn data set, the best-fit combination of $n_{\mathrm{r,cloud}}$ and $r_{\mathrm{eff,cloud}}$ is determined regardless of the value of $r_{\mathrm{eff,haze}}$. In addition, such combination is same as that obtained from the BL1/STrZ data set, though the behaviors of the observed limb-darkening curves at small solar phase angles are quite different from each other. Note that the achieved χ^2 value (= 7.26 at best) is much larger than those for other three data sets due mainly to unwanted small cloud features prominently seen at small and intermediate solar phase angles.

The derived ω_{cloud}, the value of which is ~0.969, is significantly smaller compared with that (~0.9965) for the BL1/STrZ data set. That is, particles in cloud layer for the SEBn ($1-\omega$ = ~0.031) absorb about ten times as many photons as those for the STrZ ($1-\omega$ = ~0.0035) at this wavelength. As shown in **Table 4.8**, the stratospheric haze is not necessary to fit the observations for all $r_{\mathrm{eff,haze}}$ cases, which is same characteristic as that for the CB2/SEBn data set.

It can be seen in **Figure 4.14** that the cloud model with $r_{\mathrm{eff,haze}}$ = 0.05 μm, which is the best-fit model in all assumed cases, can reproduce the limb-darkening curves for two high solar phase angles (136.2° and 140.1°) well compared with no stratospheric haze models (i.e., $r_{\mathrm{eff,haze}}$ = 0.1–0.5 μm cases). The reason why no stratospheric haze model is preferred for all $r_{\mathrm{eff,haze}}$ cases except $r_{\mathrm{eff,haze}}$ = 0.05 μm case can be interpreted in the following way. Note that it is only necessary to compare the scattering phase functions for the stratospheric haze because the best-fit functions for cloud are all in the same shapes regardless of $r_{\mathrm{eff,haze}}$. At two high solar phase angles, no stratospheric haze model shows higher reflectivities than the observed ones. Therefore, to insert the stratospheric haze having conservative scattering (ω_{haze} = 1) to the Rayleigh gas layer, ω_{cloud} should get a lower value than ~0.969 (in fact, ω_{cloud} in the cloud model with $r_{\mathrm{eff,haze}}$ = 0.05 μm is lower than that in no stratospheric haze model). Then, the reflectivities at small solar phase angles become lower due to a lower value of ω_{cloud}.

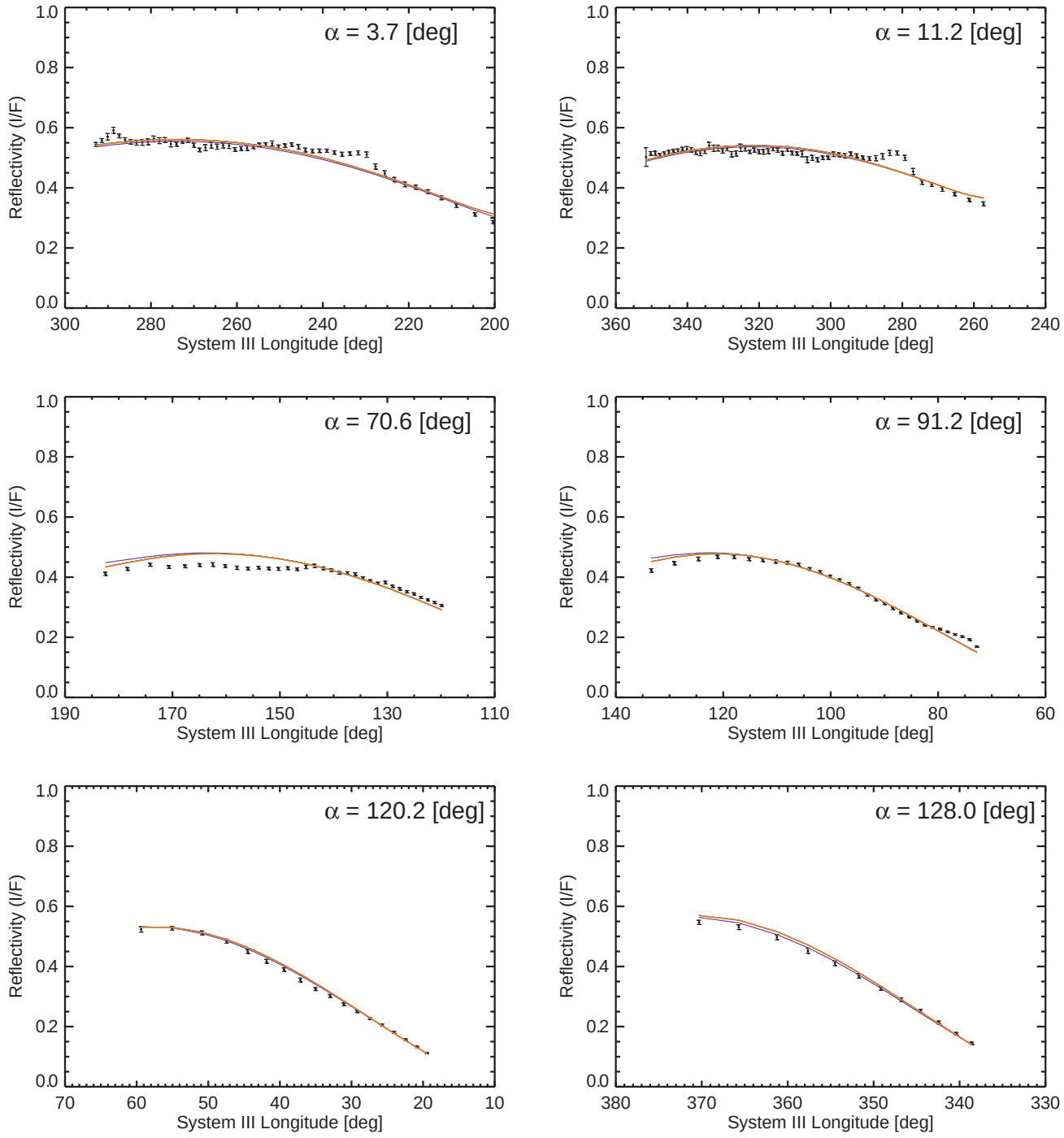

Figure 4.14. Same as Figure 4.4, except in the BL1/SEBn data set. The best-fit model in all assumed cases is obtained with $n_{\mathrm{r,cloud}}$ = 1.85 and $r_{\mathrm{eff,cloud}}$ = 0.2 μm for cloud particles and $n_{\mathrm{r,haze}}$ = 1.3 and $r_{\mathrm{eff,haze}}$ = 0.05 μm for the stratospheric haze. A significant mismatch seen in the nominal cloud model for the BL1/STrZ data set is not clear in the case of the BL1/SEBn data set.

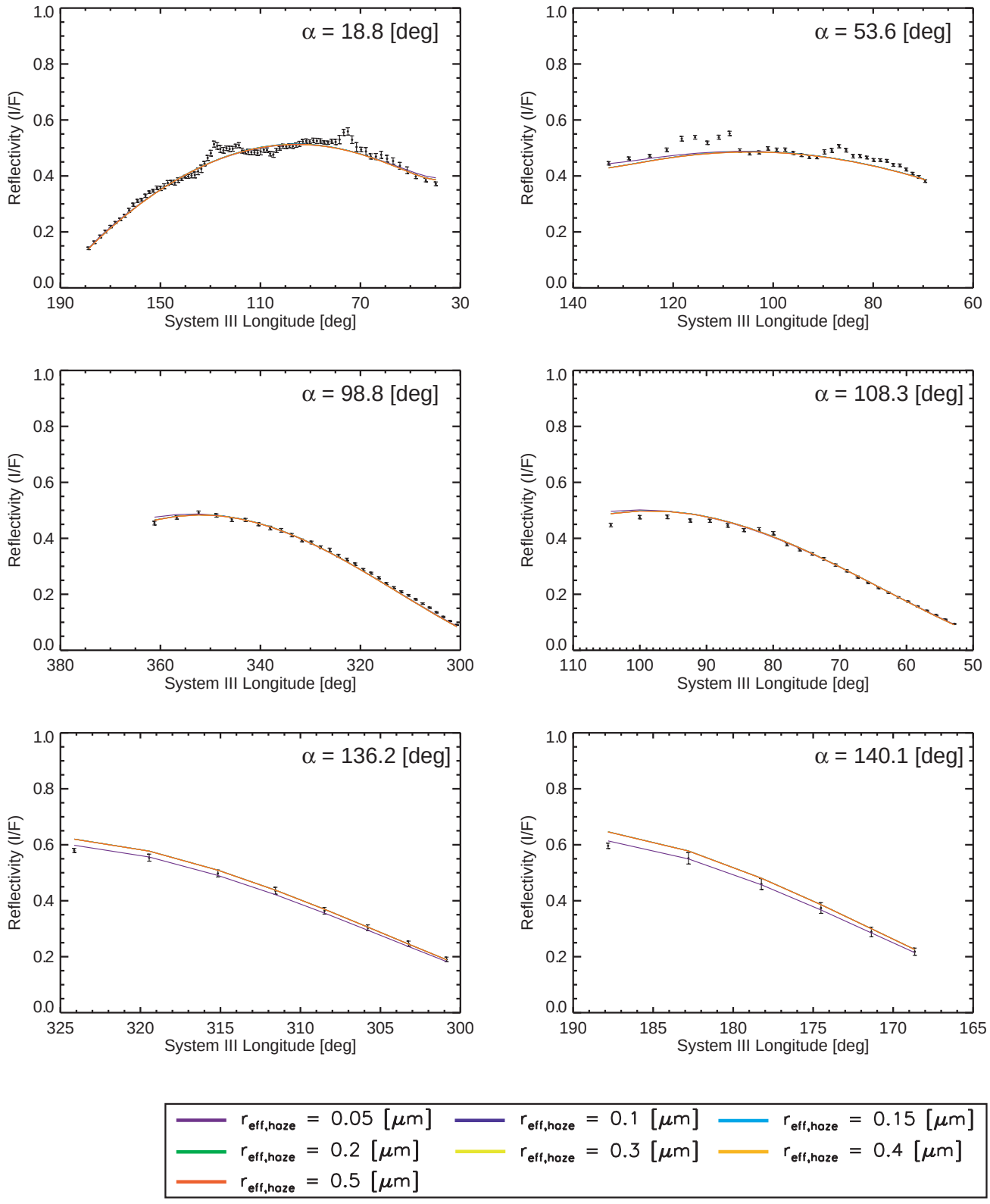

Figure 4.14–*Continued*

As shown in **Figure 4.15**, unlike the backward scattering of the scattering phase functions for $r_{\text{eff,haze}}$ = 0.05 μm, those for $r_{\text{eff,haze}}$ = 0.1–0.5 μm are not strong enough to overcome the effect of the decrease in reflectivity due to a lower value of ω_{cloud}. Because of this, the cloud model with the stratospheric haze is rejected in the above $r_{\text{eff,haze}}$ cases.

We also check the dependence of the χ^2 value on $n_{\text{i,haze}}$ in the same range described in **Section 4.3**. **Figure 4.16** shows the relationship of χ^2 value and two optimized parameters (ω_{cloud} and τ_{haze}) to $n_{\text{i,haze}}$ for each $r_{\text{eff,haze}}$ case.

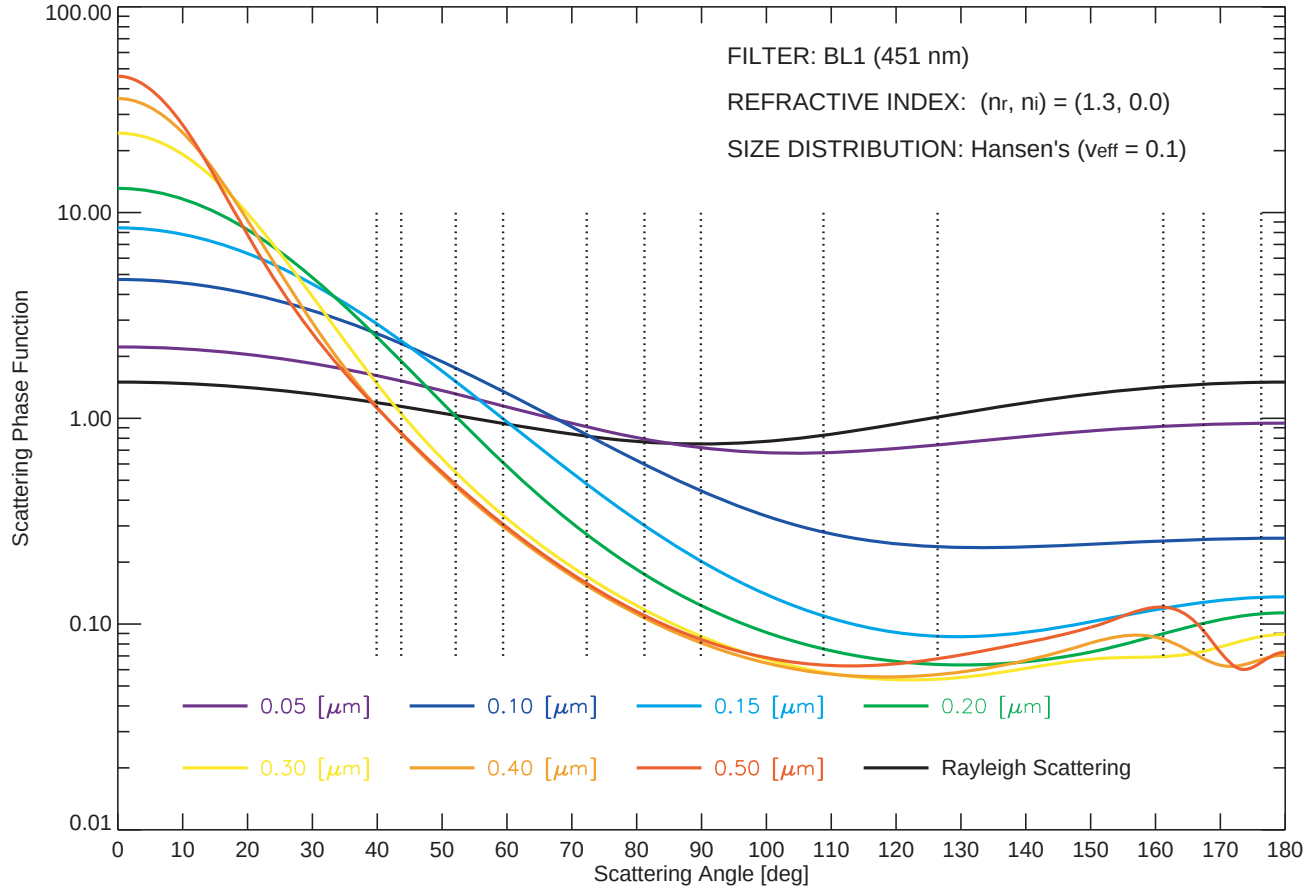

Figure 4.15. The Mie scattering phase functions in BL1 for the stratospheric haze used in the nominal cloud model. The backward scattering for $r_{\text{eff,haze}}$ = 0.05 μm is the strongest in all assumed $r_{\text{eff,haze}}$ cases.

Figure 4.16. Same as Figure 4.10, except in the BL1/SEBn data set.

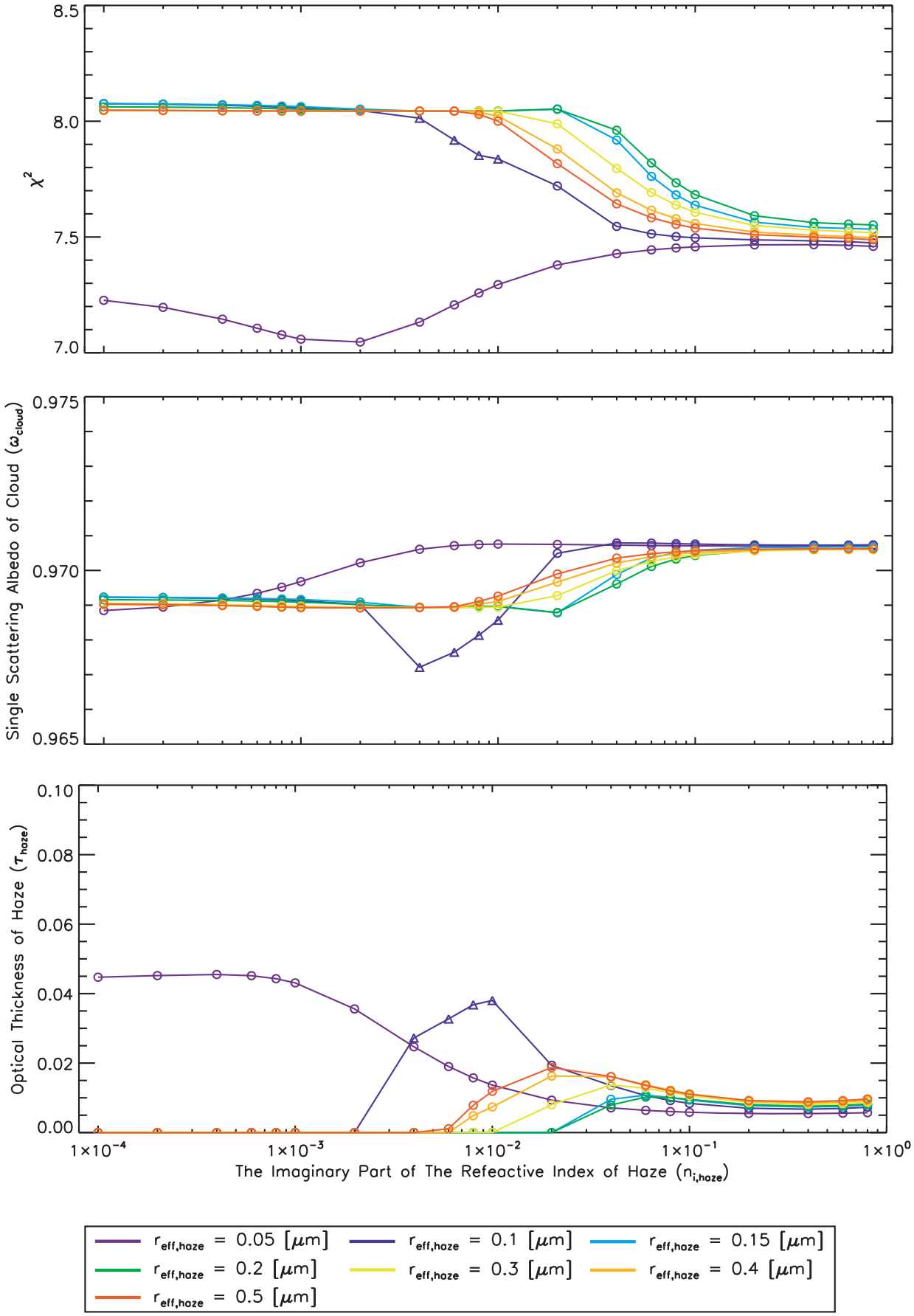
8.5
8.0
7.5
7.0
χ^2
0.975
0.970
0.965
Single Scattering Albedo of Cloud (ω_{cloud})
0.10
0.08
0.06
0.04
0.02
0.00
Optical Thickness of Haze (τ_{haze})
1×10^{-4}
1×10^{-3}
1×10^{-2}
1×10^{-1}
1×10^{0}
The Imaginary Part of The Refeactive Index of Haze ($n_{i,haze}$)
$r_{eff,haze}$ = 0.05 [μm]
$r_{eff,haze}$ = 0.1 [μm]
$r_{eff,haze}$ = 0.15 [μm]
$r_{eff,haze}$ = 0.2 [μm]
$r_{eff,haze}$ = 0.3 [μm]
$r_{eff,haze}$ = 0.4 [μm]
$r_{eff,haze}$ = 0.5 [μm]

Table 4.9. Same as Table 4.7, except in the BL1/SEBn data set.

The best-fit values							
$r_{\mathrm{eff,haze}}$ [μm]	$n_{\mathrm{r,cloud}}$	$r_{\mathrm{eff,cloud}}$ [μm]	$n_{\mathrm{i,haze}}$	ω_{haze}	ω_{cloud}	τ_{haze}	χ^2
0.05	1.85	0.2	0.002	0.8928	0.9702	0.0356	7.05
0.1	1.85	0.2	0.8	0.3005	0.9707	0.0073	7.47
0.15	1.85	0.2	0.8	0.3770	0.9707	0.0080	7.53
0.2	1.85	0.2	0.8	0.4200	0.9706	0.0082	7.55
0.3	1.85	0.2	0.8	0.4670	0.9706	0.0087	7.52
0.4	1.85	0.2	0.8	0.4931	0.9706	0.0093	7.50
0.5	1.85	0.2	0.8	0.5101	0.9706	0.0097	7.49

The values of best-fit parameters ($n_{\mathrm{r,cloud}}$, $r_{\mathrm{eff,cloud}}$, $n_{\mathrm{i,haze}}$, ω_{haze}, ω_{cloud}, and τ_{haze}) and χ^2 value for the best-fit model are listed for each $r_{\mathrm{eff,haze}}$ case in **Table 4.9**.

The behaviors of χ^2 and ω_{cloud} as a function of $n_{\mathrm{i,haze}}$ as mentioned in **Section 4.3** can also be read from those for $r_{\mathrm{eff,haze}}$ = 0.1–0.5 μm cases in **Figure 4.16**, although the behaviors at $r_{\mathrm{eff,haze}}$ = 0.05 μm is clearly different from all others. The difference in such behaviors may also be associated with the criterion of whether the size parameter of the stratospheric haze exceeds unity or not. The best-fit modeled limb-darkening curves for each $r_{\mathrm{eff,haze}}$ case, together with the observed curves when we allow $n_{\mathrm{i,haze}}$ to vary in the range from 0.0001–0.8, are presented in **Figure 4.17**. Although the χ^2 value decreases from ~8.0 to ~7.5 (for $r_{\mathrm{eff,haze}}$ = 0.1–0.5 μm cases) by changing the value of $n_{\mathrm{i,haze}}$, the improvement of the model's fit is not so evident unlike the case of the BL1/STrZ data set. Since the stratospheric haze is not indispensable for fitting the observations in BL1 for the SEBn over a wide range of $n_{\mathrm{i,haze}}$ (i.e., the obtained τ_{haze} is zero or very small), the effect of changing $n_{\mathrm{i,haze}}$ on the model's fit of the BL1/SEBn data set is relatively smaller compared with the case of the BL1/STrZ data set. Similarly, although the best-fit cloud model in all assumed cases is obtained with $r_{\mathrm{eff,haze}}$ = 0.05 μm and $n_{\mathrm{i,haze}}$ = 0.002, as is evident from the comparison between **Figure 4.14** and **Figure 4.17**, it is highly difficult to find out a remarkable difference in modeled limb-darkening curves due to differences in $r_{\mathrm{eff,haze}}$ and $n_{\mathrm{i,haze}}$. It means that it is impossible to constrain the value of $n_{\mathrm{i,haze}}$ from this data set.

Nevertheless, the essence of the BL1/SEBn data set is clearly evident in $n_{\mathrm{r,cloud}}$, $r_{\mathrm{eff,cloud}}$, and ω_{cloud}. That is, the best-fit combination of $n_{\mathrm{r,cloud}}$ (= 1.85) and $r_{\mathrm{eff,cloud}}$ (= 0.2 μm) is not changed with $n_{\mathrm{i,haze}}$ in the range of 0.0–0.8 and is the same as that at the best-fit model for the BL1/STrZ data set. ω_{cloud}, which varies slightly from 0.969 to 0.971 with increasing $n_{\mathrm{i,haze}}$, gets significantly

small value compared with those obtained from other three data sets.

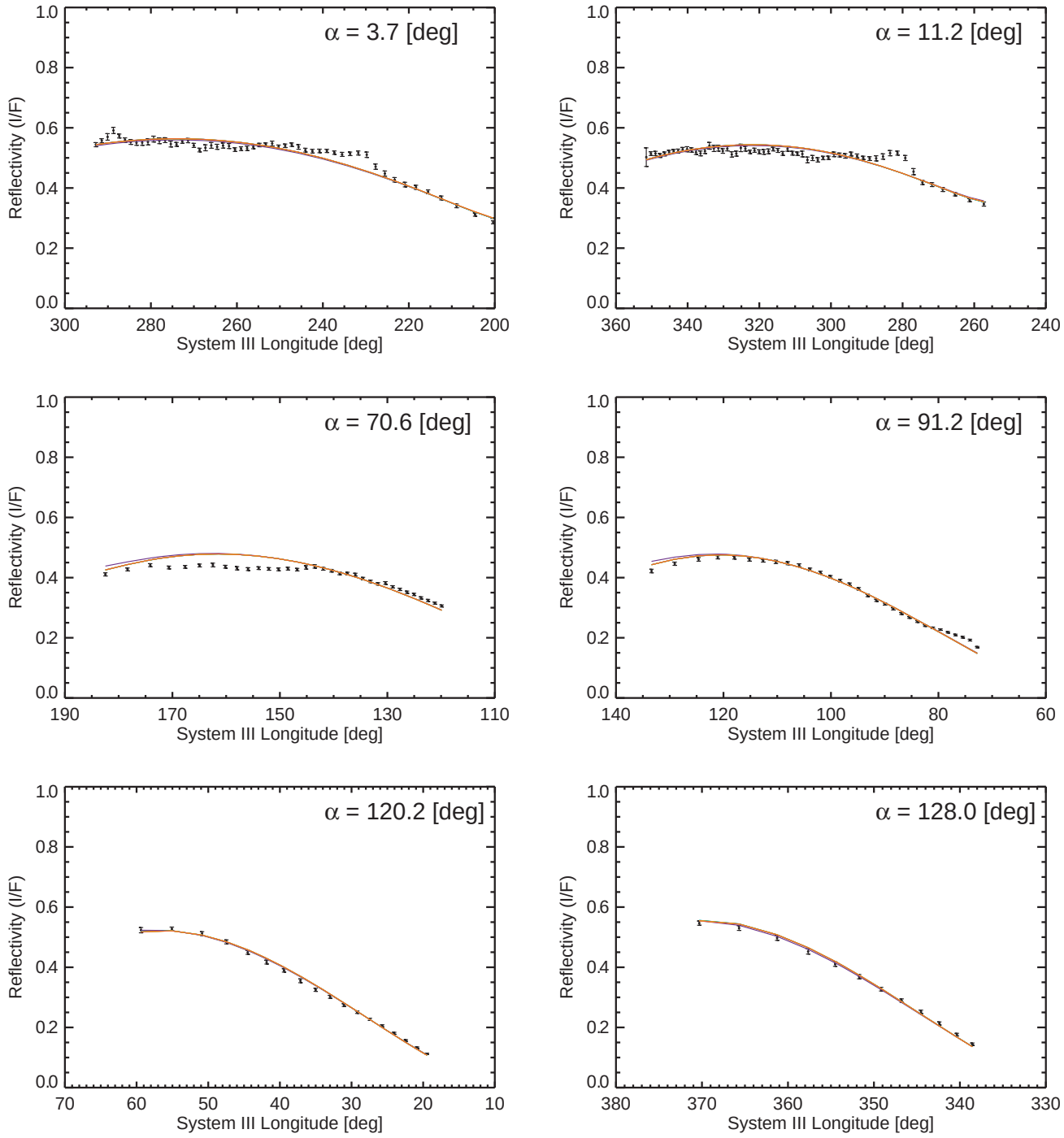

Figure 4.17. Same as Figure 4.11, except in the BL1/SEBn data set. The best-fit model in all assumed cases is obtained with $n_{\mathrm{r,cloud}}$ = 1.85 and $r_{\mathrm{eff,cloud}}$ = 0.2 μm for cloud particles and $n_{\mathrm{r,haze}}$ = 1.3 and $r_{\mathrm{eff,haze}}$ = 0.05 μm for the stratospheric haze. The improvement of the model's fit by changing the value of $n_{\mathrm{i,haze}}$ is not so evident unlike the case of the BL1/STrZ data set (see Figure 4.14).

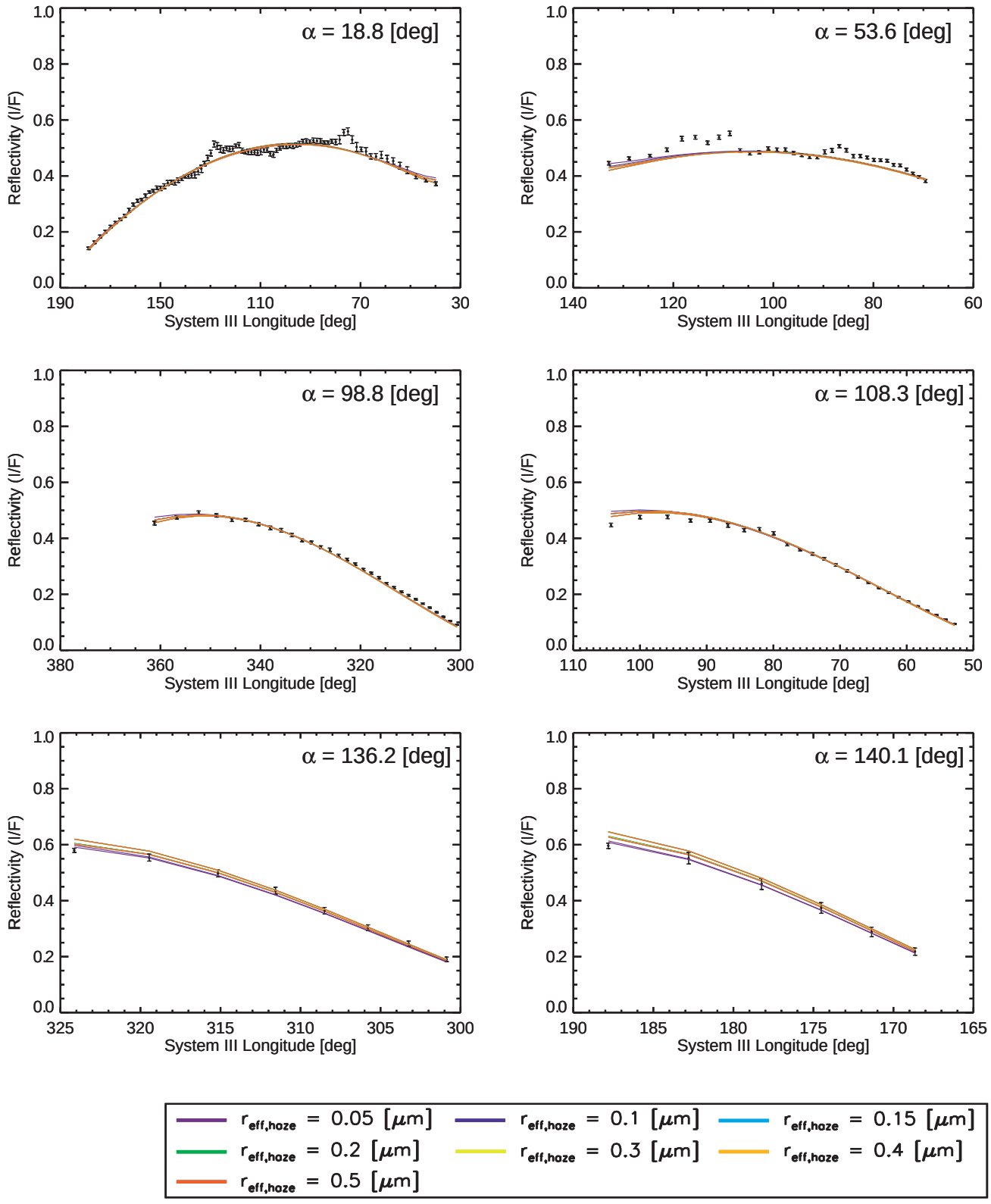

Figure 4.17–*Continued*

4.5. Summary of optical and physical properties of cloud and haze deduced from four data sets

As described in previous sections, we have successfully reproduced the limb-darkening curves in both CB2 and BL1 for two distinctly-different bands: the STrZ and the SEBn at a wide range of solar phase angles, assuming that cloud and haze properties can be approximated by Mie scattering for spherical particles (Type II-Mie model). In this section, we briefly summarize the results of optical and physical properties of cloud and haze deduced from four data sets. The parameters of the best-fit cloud model in all assumed cases for each data set are listed in **Table 4.10**.

Table 4.10. The cloud model parameters of the best-fit Type II-Mie model. The free parameters are shown in bold face.

	CB2 (effective wavelength: 750 nm)		BL1 (effective wavelength: 455 nm)	
	STrZ	SEBn	STrZ	SEBn
The upper Rayleigh gas layer	ΔP_1 = 0.1[a] τ_{total} = 0.00243 ω_{R} = 0.9614	ΔP_1 = 0.1[a] τ_{total} = 0.00249 ω_{R} = 0.9614	ΔP_1 = 0.1[a] τ_{total} = 0.0189 ω_{R} = 0.9991	ΔP_1 = 0.1[a] τ_{total} = 0.0193 ω_{R} = 0.9991
The stratospheric haze	$\boldsymbol{\tau_{\text{haze}}}$ **= 0.056** ω_{haze} = 1.0 $n_{\text{r,haze}}$ = 1.3 $n_{\text{i,haze}}$ = 0.0 $\boldsymbol{r_{\text{eff,haze}}}$ **= 0.5**[b] $v_{\text{eff,haze}}$ = 0.1	$\boldsymbol{\tau_{\text{haze}}}$ **= 0.0174** ω_{haze} = 1.0 $n_{\text{r,haze}}$ = 1.3 $n_{\text{i,haze}}$ = 0.0 $\boldsymbol{r_{\text{eff,haze}}}$ **= 0.5**[b] $v_{\text{eff,haze}}$ = 0.1	$\boldsymbol{\tau_{\text{haze}}}$ **= 0.047** ω_{haze} = 0.75 $n_{\text{r,haze}}$ = 1.3 $\boldsymbol{n_{\text{i,haze}}}$ **= 0.04** $\boldsymbol{r_{\text{eff,haze}}}$ **= 0.5**[b] $v_{\text{eff,haze}}$ = 0.1	$\boldsymbol{\tau_{\text{haze}}}$ **= 0.0356** ω_{haze} = 0.8928 $n_{\text{r,haze}}$ = 1.3 $\boldsymbol{n_{\text{i,haze}}}$ **= 0.002** $\boldsymbol{r_{\text{eff,haze}}}$ **= 0.05**[b] $v_{\text{eff,haze}}$ = 0.1
The lower Rayleigh gas layer	ΔP_2 = 0.2[a] τ_{total} = 0.00487 ω_{R} = 0.9614	ΔP_2 = 0.2[a] τ_{total} = 0.00498 ω_{R} = 0.9614	ΔP_2 = 0.2[a] τ_{total} = 0.0377 ω_{R} = 0.9991	ΔP_2 = 0.2[a] τ_{total} = 0.0386 ω_{R} = 0.9991
The semi-infinite cloud	$\boldsymbol{\omega_{\text{cloud}}}$ **= 0.9968** $\boldsymbol{n_{\text{r,cloud}}}$ **= 1.85** $n_{\text{i,cloud}}$ = 0.0 $\boldsymbol{r_{\text{eff,cloud}}}$ **= 0.3**[b] $v_{\text{eff,clud}}$ = 0.1	$\boldsymbol{\omega_{\text{cloud}}}$ **= 0.9932** $\boldsymbol{n_{\text{r,cloud}}}$ **= 1.8** $n_{\text{i,cloud}}$ = 0.0 $\boldsymbol{r_{\text{eff,cloud}}}$ **= 0.3**[b] $v_{\text{eff,clud}}$ = 0.1	$\boldsymbol{\omega_{\text{cloud}}}$ **= 0.9965** $\boldsymbol{n_{\text{r,cloud}}}$ **= 1.85** $n_{\text{i,cloud}}$ = 0.0 $\boldsymbol{r_{\text{eff,cloud}}}$ **= 0.2**[b] $v_{\text{eff,clud}}$ = 0.1	$\boldsymbol{\omega_{\text{cloud}}}$ **= 0.9702** $\boldsymbol{n_{\text{r,cloud}}}$ **= 1.85** $n_{\text{i,cloud}}$ = 0.0 $\boldsymbol{r_{\text{eff,cloud}}}$ **= 0.2**[b] $v_{\text{eff,clud}}$ = 0.1
χ^2	2.61	2.92	2.78	7.05

a: The pressure differences ΔP_1 and ΔP_2 are in units of bars.
b: The effective radii $r_{\text{eff,haze}}$ and $r_{\text{eff,cloud}}$ are in units of μm.

The major findings obtained from our radiative transfer calculations are described as follows.

- The best-fit $n_{\mathrm{r,cloud}}$ for all four data sets except the CB2/SEBn data set show an identical value (= 1.85), which is significantly higher than those of n_{r} for NH_3 ice particles reported by Martonchik et al. (1984) (e.g., 1.449 at ~430 nm and 1.423 at ~670 nm). The only exception, the CB2/SEBn data set, can also be reproduced fairly well with $n_{\mathrm{r,cloud}}$ = 1.85, which is somewhat larger than the best-fit value (= 1.8).
- The best-fit $r_{\mathrm{eff,cloud}}$ is optimized at two different values, depending on the wavelength: 0.3 μm in CB2 and 0.2 μm in BL1. In most cases, these values are robust against small changes of other free parameters such as $r_{\mathrm{eff,haze}}$ and $n_{\mathrm{i,haze}}$.
- While the difference of the best-fit ω_{cloud} between the STrZ (= 0.9968) and the SEBn (= 0.9932) in CB2 is not so evident, the difference between the STrZ (= 0.9965) and the SEBn (= 0.9702) in BL1 is remarkable. This trend is unaffected by change of other free parameters such as $r_{\mathrm{eff,haze}}$ and $n_{\mathrm{i,haze}}$.
- The optical and physical properties of the stratospheric haze are not well constrained. There seems to be no characteristic common to all data sets with the exception that the stratospheric haze is optically thin (<0.06) when it exists. The CB2/STrZ data, either by the behavior of the near-limb points in most solar phase angles or by higher reflectivity seen in the two largest solar phase angles (136.2° and 140.1°), favor the presence of conservatively-scattering large particles ($r_{\mathrm{eff,haze}}$ = 0.5 μm). In contrast to the CB2/STrZ data set, large $n_{\mathrm{i,haze}}$ (≥0.04) is required to reproduce the BL1/STrZ data set well. The stratospheric haze is not indispensable for fitting the observed limb-darkening curves for the CB2/SEBn data set and the BL1/SEBn data set.
- No change of two assumed pressure differences ΔP_1 (= 0.1 bar) and ΔP_2 (= 0.2 bar) is required to reproduce the observations for every data sets.

Chapter 5

Discussion

In **Section 5.1**, we compare our results obtained in **Chapter 4** with those deduced by previous studies. We focus on the shapes of the derived Mie scattering phase functions, two most important physical quantities of $n_{\mathrm{r,cloud}}$ and $r_{\mathrm{eff,cloud}}$, and the stratospheric haze properties in **Section 5.1.1**–**5.1.4**. We mention what model parameter determined in this study can explain the visual difference between two distinctly-different bands in **Section 5.1.5**. In **Section 5.2**, we test the sensitivity of our results for several assumptions used in this study. We apply our Mie scattering phase functions to the P10/IPP data to demonstrate the utility of these functions in **Section 5.3**. Finally, we show the limitation of the Pioneer HG function by applying this function to the Cassini ISS data in **Section 5.4**.

5.1. Cloud and haze properties deduced from the Cassini ISS limb-darkening analyses

5.1.1. Shapes of the best-fit Mie scattering phase functions of cloud particles

First of all, we compare the shapes of our best-fit Mie scattering phase functions of cloud particles in CB2 and BL1 for the STrZ and the SEBn with other published scattering phase functions. The best-fit parameters of our obtained scattering phase functions are summarized with other cloud model parameters in **Table 4.10**.

Comparisons with the Pioneer HG functions (for cloud in both the STrZ and the SEBn at both blue-channel: 440 nm and red-channel: 640 nm) are plotted according to wavelength in **Figure 5.1**.

The vertical dotted lines indicate scattering angles of the Cassini ISS observations used in this study. Again, the Pioneer HG function is described by three parameters as defined by equations (1.1) and (1.2). The best-fit parameters of such functions are listed in **Table 1.2**. Here, we take a comparison between our Mie scattering phase function in CB2 for the STrZ and the Pioneer HG function in red-channel for the STrZ as an example. First, the overall shape of our best-fit Mie scattering phase function is much flatter than the Pioneer HG function: ours is lower than the Pioneer HG function for the three smallest solar phase angles, and is higher for all other solar phase angles. This implies that the Pioneer HG function would yield more dynamic range between brighter phase angles and darker ones than ours. This can be understood by examining **Figure 2.18(a)** and **Figure 2.19(a)**: the brightness peak of the P10/IPP data reaches (I/F) ~0.78 for 12º and ~0.58 for 127º, while it is ~0.75 for 12.6º and ~0.68 for 127.9º in the Cassini ISS data. Therefore, the brightening in smaller phase angles (often called an opposition surge) is more pronounced in the P10/IPP data, requiring a more peaked phase function in the backward scattering portion. The feature that our scattering phase function has much flatter shape compared with the Pioneer HG function is also true in other three corresponding scattering phase functions.

Second, the forward scattering in our best-fit scattering phase function is strong enough to give sufficient brightness to the curves for large solar phase angles. Although the largest solar phase angle in the Cassini ISS data, 140.1º, is somewhat smaller than the P10/IPP's 150º, the scattering phase function $P_{\mathrm{Mie}}(\Theta = 30°)$ is still higher than $P_{\mathrm{DHG}}(\Theta = 30°)$. Therefore, the Mie scattering phase function for cloud, together with the Mie scattering phase function for haze, would reproduce the data for even larger solar phase angles than the Cassini ISS's limit. We examine this for all the four Mie scattering phase functions in **Section 5.3**.

Third, it should be noted that the best-fit Mie scattering phase function for the range of scattering angles from 80° to 130° (i.e., 50°–100° for solar phase angle), which corresponds to the range that the P10/IPP observations did not cover, is stronger by a factor of two and is more gradual in shape compared with the Pioneer HG function. These characteristics of cloud particles are detectable only after consideration of the limb-darkening curves at intermediate solar phase angles (53.6°, 71.2°, 90.1°, and 98.8°) in addition to those at small and large solar phase angles. The same holds true for the other Mie scattering phase functions.

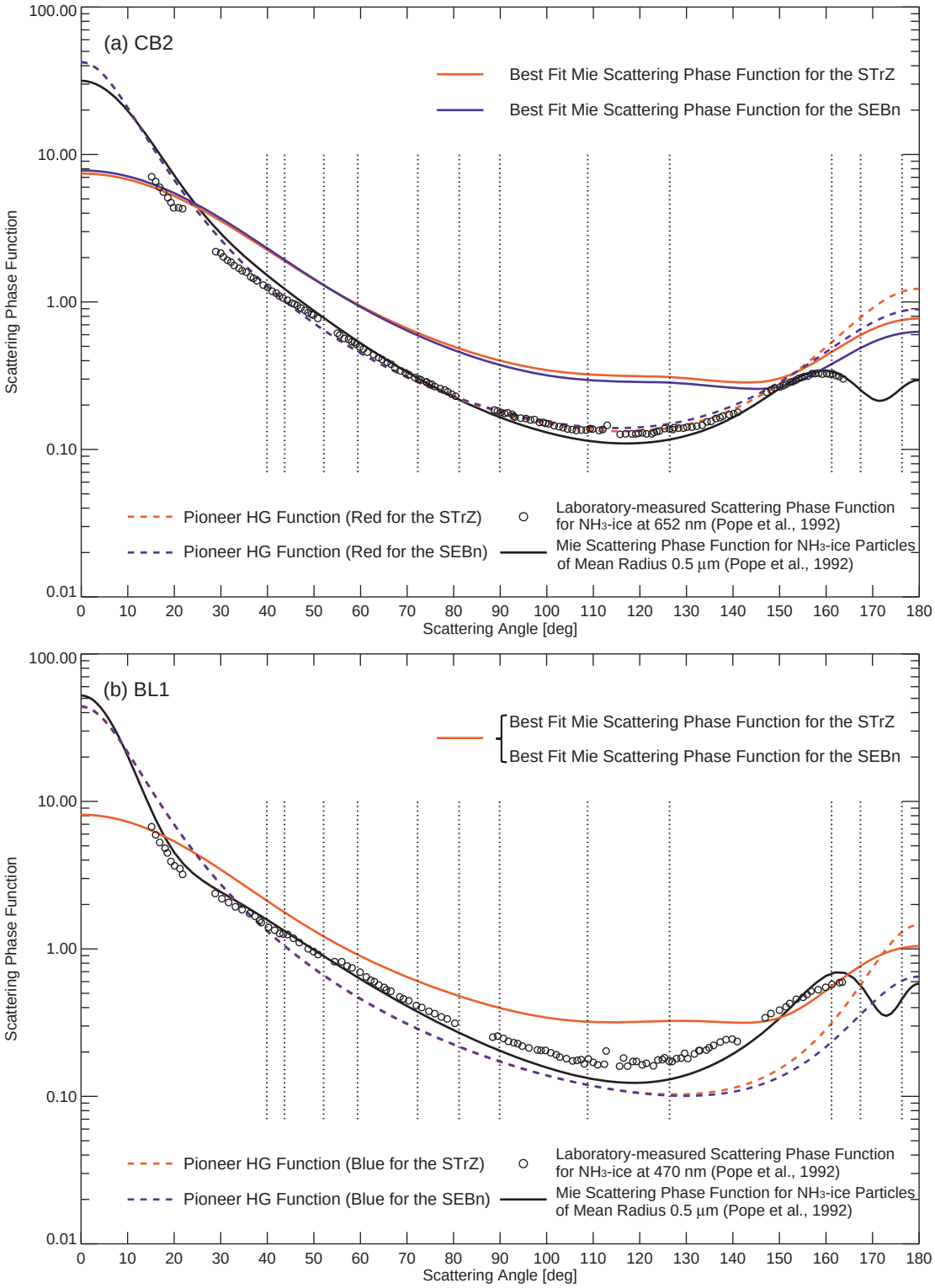

Figure 5.1. (a) Comparisons of our best-fit Mie scattering phase functions (red and blue solid curves) in CB2 with the Pioneer HG functions (red and blue dashed curves), and the laboratory measured scattering phase functions for NH_3 ice particles (circles) with Mie scattering curves of mean radius 0.5 µm (black curve) (Pope et al., 1992). (b) Same as (a), except in BL1. The vertical dotted lines indicate the observed scattering angles.

We are motivated to compare our best-fit Mie scattering phase functions of cloud with those of NH_3 ice particles. NH_3 ice has been considered as condensate clouds in the upper troposphere we see at visible wavelengths. In **Figure 5.1**, we compare our best-fit Mie scattering phase functions with the laboratory measurements at blue (470 nm) and red (652 nm) wavelengths of Pope et al. (1992). They claimed that the measured scattering phase functions could be fit by Mie scattering curve for NH_3 ice particles (n_r = 1.441 at blue and n_r = 1.424 at red) of mean radius 0.5 μm (see Figure 4 of their paper). There are, however, significant deviations between our scattering phase functions and Pope et al.'s measurements regardless of wavelength. Although the exact reason is unclear, probably the published scattering phase functions are one of many variations actually measured, and those which most resemble the Pioneer HG functions are highlighted. Obviously, more laboratory measurements of NH_3 ice to sample many different and possible scattering phase functions are required.

5.1.2. The effective radius of cloud particles

By compiling the knowledge accumulated through decades of visible and infrared observations, West et al. (2004) described the upper tropospheric cloud as consisting of two components: one is a diffuse layer of small aerosol particles (~0.5 μm) with visible optical depth of 2–10, extending up to 0.2–0.3 bar pressure level; and the other is a compact layer of larger particles (3–100 μm) located near the base of the diffuse layer (~0.75 bar). Our best-fit effective radii of cloud particles $r_{\mathrm{eff,cloud}}$, which are obtained at 0.3 μm in CB2 and at 0.2 μm in BL1, correspond to that of West et al.'s diffuse cloud layer. It is, of course, likely that larger particles populate the lower part of the cloud layer of our model. Even so, the Cassini ISS measurements would not be very sensitive to cloud properties below the upper two or three optical depths due to the effects of multiple light scattering.

Irwin et al. (1998) retrieved, from the Galileo NIMS spectra (0.7–5.2 μm), the vertical cloud structure at a "warm" spot (5°N, 85°W) and showed evidence of 0.75-μm NH_3 ice particles at ~0.7 bar and 0.5-μm tholins at ~0.2 bar in the upper troposphere. Sromovsky et al. (1998) derived NH_3 ice particles (0.5–0.75 μm) near 0.45 bar from the Galileo probe Net Flux Radiometer. The particle size estimated in this study (0.2 μm in BL1 and 0.3 μm in CB2) is somewhat smaller than those obtained in these studies. However, the STrZ is a latitude region of optically thick cloud cover (a "cold" region in the thermal infrared) in contrast to the warm spot of Irwin et al. (1998) or the hot spot where the Galileo probe descended into the Jovian atmosphere. It would be possible that dynamically

different regions have different populations of cloud particles, larger or smaller. Therefore, our results are consistent with other studies in the sense that the Jovian upper troposphere is covered with a layer of smaller (micron to sub-micron size) aerosol particles. As deduced from the polarimetry with the Pioneer 10 and 11 IPP (Smith and Tomasko, 1984), such a layer should be ubiquitous over the zones and belts. It is worth noting that we obtain the same value for $r_{\mathrm{eff,cloud}}$ at both two wavelengths regardless of latitude regions.

Finally, we need to refer to the difference in $r_{\mathrm{eff,cloud}}$ deduced form the BL1 and the CB2 data sets. Such small difference (only 0.1 μm) cannot be cleared up because this dramatically changes the goodness of fit. For example, when we analyze the CB2/STrZ data set with the stratospheric haze of $n_{\mathrm{r,haze}}$ = 1.3 and $r_{\mathrm{eff,haze}}$ = 0.5 μm, a cloud model with values of $n_{\mathrm{r,cloud}}$ = 1.85 and $r_{\mathrm{eff,cloud}}$ = 0.2 μm gets a large χ^2 value (= 19.43), although a cloud model (the best-fit model) with values of $n_{\mathrm{r,cloud}}$ = 1.85 and $r_{\mathrm{eff,cloud}}$ = 0.3 μm achieves the smallest χ^2 value (= 2.61) (see **Figure 4.2**). The same trend can also be seen in BL1 data sets. This is, perhaps, because the assumed cloud model is over simplified and does not reflect the distribution of aerosols and their properties in the real Jovian atmosphere. In the real atmosphere, of course, the radii of aerosols vary with altitude and are not characterized by single effective radius. Even so, we have very few information about them and it is worth mentioning that such simple cloud model can reproduce the limb-darkening curves at a wide variety of solar phase angles obtained at two different wavelengths. The improvement of our cloud model to solve this problem should be conducted in future.

5.1.3. Implication for cloud composition –the refractive index of cloud particles

As can be seen in **Figure 5.2**, the evidence of strong depletion of NH_3 vapor at pressures less than 0.5 bar has been observationally suggested by ground-based microwave observations (e.g., de Pater and Massie, 1985), the Galileo probe Net Flux Radiometer (Sromovsky et al., 1998), and the ISO observations (Fouchet et al., 2000). Such depletion is considered to be consistent with the prediction of thermochemical equilibrium theory that NH_3 condensation is expected to start at ~0.7 bar. Both the observation and the theory support the existence of condensation clouds of NH_3 ice, not droplets because of the low temperature, in the upper troposphere to which the Cassini ISS data are sensitive (the pressure levels where the putative NH_3 ice cloud layer as well as the stratospheric haze would be exist are also shown in **Figure 5.2**). However, as mentioned in **Chapter 4**, the best-fit values of $n_{\mathrm{r,cloud}}$, which are 1.85 for all data sets except for the CB2/SEBn data set (= 1.80), obtained from

our analyses are significantly higher than that of NH_3 ice measured in the laboratory (Martonchik et al., 1984). This discrepancy suggests that some sort of impurity or alteration may exist with the NH_3 ice particles after they condense out.

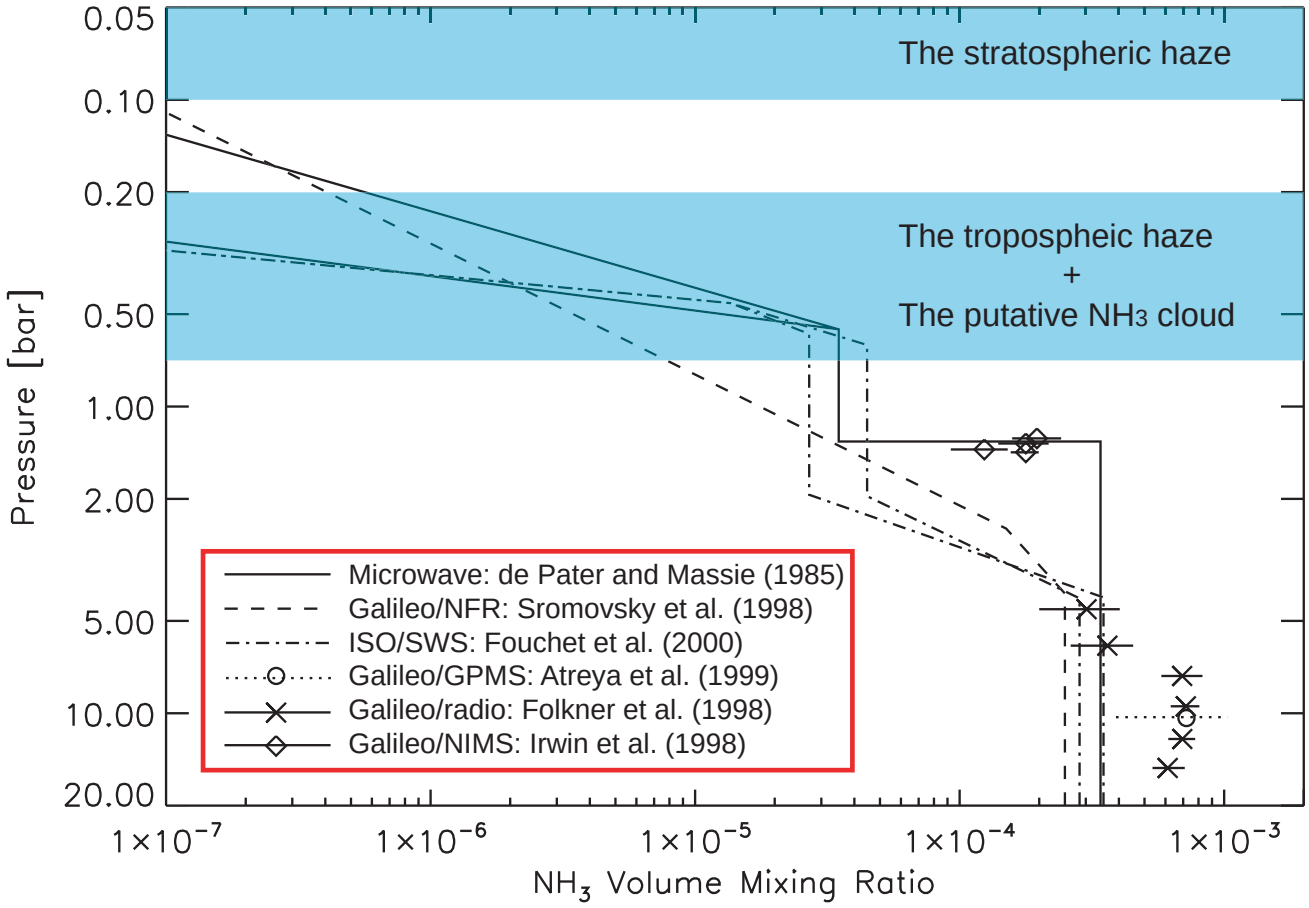

Figure 5.2. The vertical profiles of NH_3 volume mixing ratio with the location of the putative NH_3 ice cloud layer and the stratospheric haze (from Taylor et al., 2004). The estimate deduced from the ground-based microwave data (de Pater and Massie, 1985) is shown by solid line. The dashed line, the circle, the diamonds, and the cross symbols represent the profiles inferred from data obtained by the Galileo probe Net Radiometer (NFR) (Sromovsky et al., 1998); the Galileo probe Mass Spectrometer (GPMS) (Atreya et al., 1999); the Galileo Near Infrared Mapping Spectrometer (NIMS) (Irwin et al., 1998); and the Galileo probe uplink signal attenuation (Folkner et al., 1998), respectively. The dot-dashed line shows the profiles derived by Fouchet et al. (2000) from the Infrared Space Observatory (ISO) Short Wavelength Spectrometer (SWS) observations.

Baines et al. (2002) revealed from the Galileo NIMS spectra that spectrally identifiable ammonia clouds (SIACs) were significantly localized to specific regions and covered only <1% of the Jovian surface. Because our limb-darkening analyses assume longitudinal uniformity, small anomalous regions do not affect our results. In other words, our results represent the properties of the majority of clouds, other than SIACs.

Sromovsky and Fry (2010a, 2010b) analyzed, with improved NH_3 gas absorption models, the spectra (2.9–3.1 μm) obtained from the ISO and the Cassini VIMS. Their best-fit model consists of four distinct layers: a small particle stratospheric haze layer, a layer of *ammonia-coated* particles (~0.3 μm) overlying or close to a layer of much larger NH_4SH particles (~10–15 μm), and a deeper optically thick layer. It is noteworthy that the data preferred a model with cloud particles in the second layer consisting of highly-refractive core material (n_{r} = 1.8) coated with NH_3 ice. Our best-fit values of $n_{\mathrm{r,cloud}}$ and $r_{\mathrm{eff,cloud}}$ are in excellent agreement with their findings. They also noted that large NH_4SH particles in the third layer would be responsible for the 3-μm absorption anomaly rather than the NH_3 ice supported by Brooke et al. (1998), and the small NH_3 ice particles would only contribute to an improvement of model fit in the form of a coating or core materials, not as pure NH_3 ice particles.

To satisfy conflicting observations (the strong depletion of NH_3 vapor and the lack of an absorption feature of NH_3 ice), masking of the spectral NH_3 ice signature by other materials is an intriguing idea. Rossow (1978) pointed out that the population consisting of small particles (<1 μm) had a long lifetime against sedimentation in the upper troposphere, being maintained by small amplitude turbulent motions. Thus, the characteristics of small cloud particles would have much chance to be altered. Recently, Atreya et al. (2005) proposed that NH_3 ice particles were coated by haze materials photochemically generated in the stratosphere as illustrated in **Figure 5.3**. Kalogerakis et al. (2008) demonstrated that hydrocarbon-coated NH_3 ice could alter or suppress NH_3 ice absorption features from laboratory measurements (one example is presented in **Figure 5.4**). Their scenario is the inverse of the traditional scenario that the sedimenting photochemical stratospheric haze would serve as condensation nuclei for NH_3 ice particles (West et al., 1986). The assessment of production and sedimentation rates of photochemical material(s) and the production rate of NH_3 ice particles would be necessary to clarify which scenario accounts for masking of the spectroscopic NH_3 ice signature. Nevertheless, whichever scenario is correct, the values of $n_{\mathrm{r,cloud}}$ obtained here may describe the characteristics of masking materials.

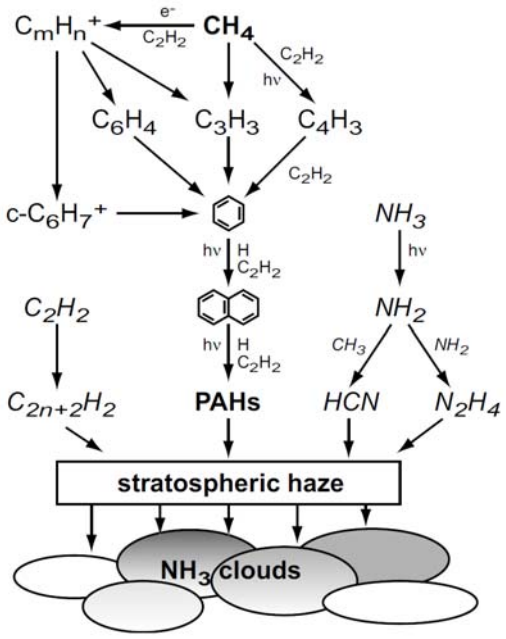

Figure 5.3. Illustration of chemical schemes leading to the stratospheric haze formation on Jupiter. The chemical schemes beginning with C_2H_2 and leading to polyyne polymerization (*lower left branch*) and the HCN polymerization (*right branch*) are minor contributors to haze formation. In the auroral regions, ion chemistry plays an important in the hydrocarbon chemistry, so that nearly all of the "auroral" C_6H_6 (precursor to polycyclic aromatic hydrocarbons: PAH) is produced through the electron recombination of ring ion c-$C_6H_7^+$. The stratospheric haze has a distinct possibility that it can mask the spectral signature of the NH_3 ice clouds (from Atreya and Wong, 2005; see also Wong et al., 2003).

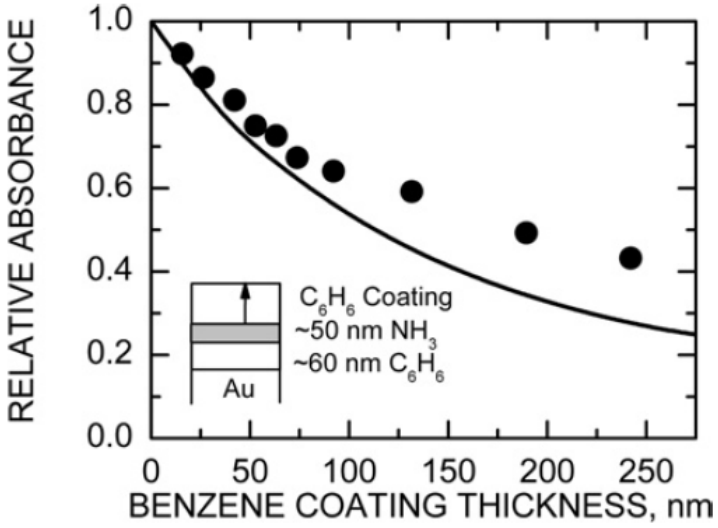

Figure 5.4. Effect of a C_6H_6 coating on the magnitude of the 3-μm absorbance feature of a ~50 nm NH_3 ice film deposited on a ~60 nm C_6H_6 ice film. The experimental data which were measured at 100 K and the result of thin film optical computations are shown by circles and solid curve, respectively (from Kalogerakis et al., 2008).

5.1.4. Characteristics of the stratospheric haze

As already mentioned in **Section 4.5**, we cannot constrain well the optical and physical properties of the stratospheric haze, even when using the limb-darkening curves at a wide variety of solar phase angles. Although there are no characteristic common to all data sets with the exception that the stratospheric haze is optically thin, we find several key points of the stratospheric haze.

First, from the analysis of the CB2/STrZ data set, we find that $r_{\mathrm{eff,haze}}$ mainly has the effect of varying the magnitude of modeled reflectivity at two high solar phase angles (136.3° and 140.1°). A large $r_{\mathrm{eff,haze}}$ is needed for reproducing the relatively high observed reflectivity at two large solar phase angles. This effect can also be seen from those when we analyze the BL1/STrZ data set with $n_{\mathrm{i,haze}}$ = 0.0 (see **Figure 4.8**). Tomasko et al. (1978) mentioned that the stratospheric haze should have a relatively strong forward scattering phase function (asymmetry parameter $g \geq 0.75$) in both red- and blue-channels to provide enough intensity at high solar phase angle (150°). The asymmetry parameters g calculated with the best-fit combination of $n_{\mathrm{r,haze}}$, $n_{\mathrm{i,haze}}$ and $r_{\mathrm{eff,haze}}$ for the CB2/STrZ data set and the BL1/STrZ data set (these parameter are listed in **Table 4.10**) correspond to ~0.84 and ~0.89, respectively. The best-fit value of $r_{\mathrm{eff,haze}}$ is consistent with their observational results.

Rages et al. (1999) analyzed limb intensity variations obtained from the Galileo SSI at high solar phase angles (146° and 157°) to retrieve the vertical profiles of aerosol extinction at two wavelengths (violet: 410 nm and near-infrared: 756 nm). For the equatorial region (9°N), the best-fit model was obtained with r ~ 0.32 μm at ~16 mbar probed primarily in violet and r ~ 0.45 μm at ~96 mbar sensed in near-infrared. Although the Cassini ISS images at high solar phase angle have too low spatial resolution (~300 km/pixel at a solar phase angle of 140.1°) to resolve limb intensity variations compared with the Galileo SSI images (~15 km/pixel), their best-fit model for near-infrared images supports our best-fit value of $r_{\mathrm{eff,haze}}$ and our assumption of altitude of haze particles (= 0.1 bar) for the CB2 data sets. While the sensing altitude inferred from violet images in their analysis is somewhat higher than our assumed one, we find that it is highly difficult to distinguish the effect of haze altitude change on the limb-darkening curve even at the highest solar phase angle used in this study from the effect of $r_{\mathrm{eff,haze}}$ change. To constrain the haze altitude based on the Cassini ISS data, we need to conduct a further analysis of both UV (UV1, effective wavelength: 264 nm) data and strong CH_4 band data (MT3, effective wavelength: 889 nm) at high solar phase angles in future.

Tomasko et al. (1986) likewise concluded from the IUE ultraviolet observations (the longest wavelength is 330 nm) at small solar phase angles that stratospheric haze particles with radii between

0.2 μm and 0.5 μm were required for an acceptable fit to the reflectivity and limb-darkening curves. They also pointed out the fact that particles with radii larger than 0.5 μm seemed unlikely because of the high mass production rate required to sustain a large number of particles in the stratosphere.

Second, for the BL1/STrZ data set, we find that large $n_{\mathrm{i,haze}}$ (≥0.04, depending on $r_{\mathrm{eff,haze}}$) is required to reproduce the limb-darkening curves. It is worth noting that the best-fit value of $n_{\mathrm{i,haze}}$ (= 0.04) obtained in this study is in good agreement with the value (n_{i} = 0.02 for 430 nm) adopted by West (1988) based on the study of Tomasko et al. (1986). Conversely, ω_{haze} for the STrZ determined by Tomasko et al. (1978) with the P10/IPP blue-channel data was ~0.995, close to unity. To obtain such nearly conservative scattering for the stratospheric haze being approximated by Mie particles with $n_{\mathrm{r,haze}}$ = 1.3 and $r_{\mathrm{eff,haze}}$ = 0.5 μm, we need only small n_{i} (= 5.0×10^{-4}). To examine this discrepancy in detail, we compare the fitting results of the P10/IPP data obtained with two different Mie scattering phase functions for an absorbing case ($n_{\mathrm{i,haze}}$ = 0.04) and a conservative scattering case ($n_{\mathrm{i,haze}}$ = 0.0) in **Section 5.3**.

In order to validate our assumption of $n_{\mathrm{i,haze}}$ (= 0.0) for the CB2 data, we conduct a sensitivity test for $n_{\mathrm{i,haze}}$. The same approach as that for the BL1/STrZ data set is applied to the CB2/STrZ data set. **Figure 5.5** shows the relationship of χ^2 value and two optimized parameters (ω_{cloud} and τ_{haze}) to $n_{\mathrm{i,haze}}$ for each $r_{\mathrm{eff,haze}}$. The values of best-fit parameters ($n_{\mathrm{r,cloud}}$, $r_{\mathrm{eff,cloud}}$, $n_{\mathrm{i,haze}}$, ω_{haze}, ω_{cloud}, and τ_{haze}) and χ^2 value for the best-fit model are summarized for each $r_{\mathrm{eff,haze}}$ case in **Table 5.1**.

Figure 5.5. The relationship of χ^2 value and two optimized parameters (ω_{cloud} and τ_{haze}) to $n_{\mathrm{i,haze}}$ for each $r_{\mathrm{eff,haze}}$ case in the CB2/STrZ data set. Three symbols denote three different best-fit cloud models: asterisk, $n_{\mathrm{r,cloud}}$ = 1.8 and $r_{\mathrm{eff,cloud}}$ = 0.3 μm; circle, $n_{\mathrm{r,cloud}}$ = 1.85 and $r_{\mathrm{eff,cloud}}$ = 0.3 μm; plus, $n_{\mathrm{r,cloud}}$ = 1.65 and $r_{\mathrm{eff,cloud}}$ = 0.4 μm.

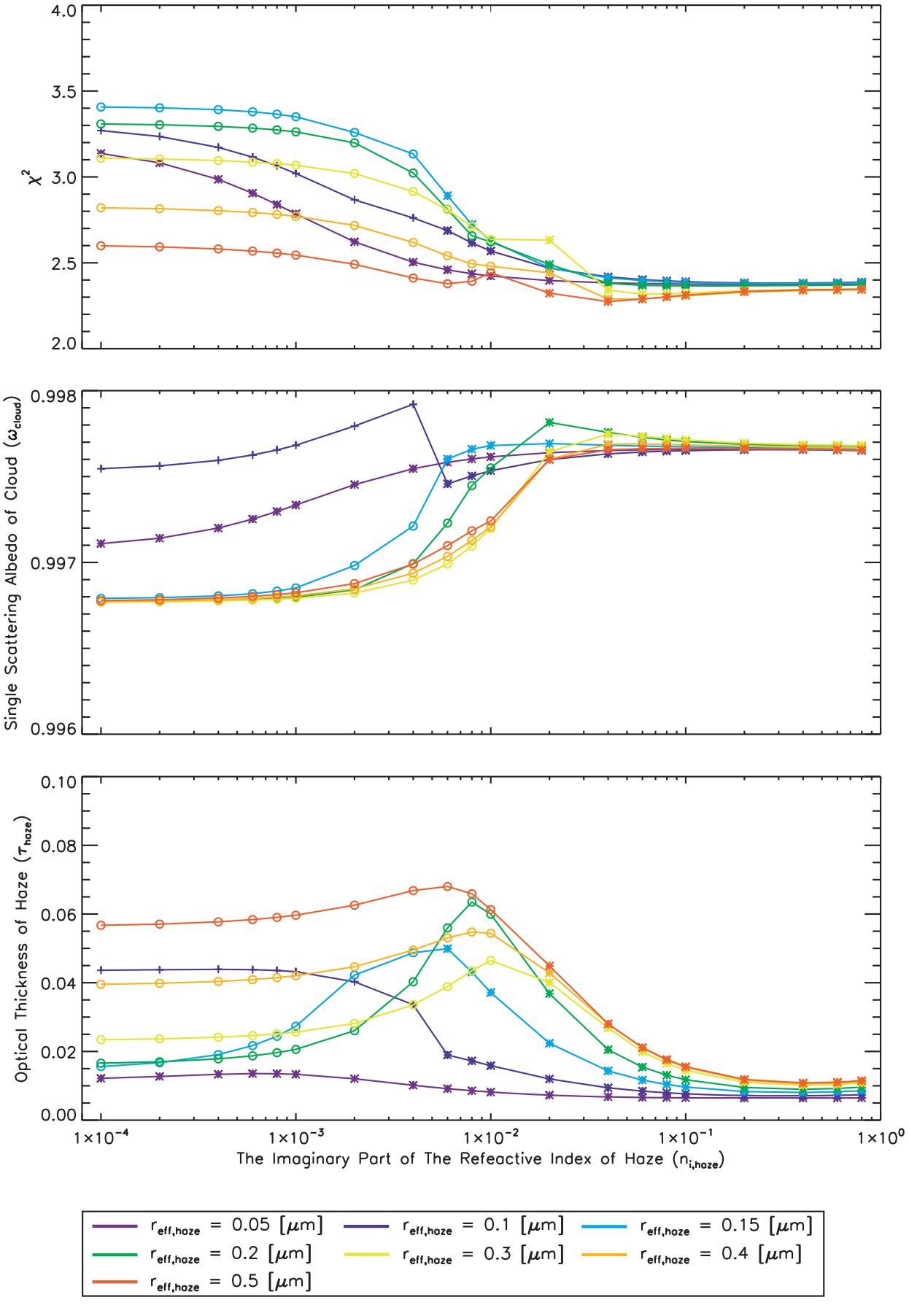
4.0
3.5
3.0
2.5
2.0
χ^2
0.998
0.997
0.996
Single Scattering Albedo of Cloud (ω_{cloud})
0.10
0.08
0.06
0.04
0.02
0.00
Optical Thickness of Haze (τ_{haze})
1×10^{-4}
1×10^{-3}
1×10^{-2}
1×10^{-1}
1×10^{0}
The Imaginary Part of The Refeactive Index of Haze ($n_{i,haze}$)
$r_{eff,haze}$ = 0.05 [μm]
$r_{eff,haze}$ = 0.1 [μm]
$r_{eff,haze}$ = 0.15 [μm]
$r_{eff,haze}$ = 0.2 [μm]
$r_{eff,haze}$ = 0.3 [μm]
$r_{eff,haze}$ = 0.4 [μm]
$r_{eff,haze}$ = 0.5 [μm]

Table 5.1. The best-fit models of the Type II-Mie model for the case of $n_{\mathrm{r,haze}}$ = 1.3 in the CB2/STrZ data set when we allow $n_{\mathrm{i,haze}}$ to vary in the range of 0.0001–0.8.

The best-fit values							
$r_{\mathrm{eff,haze}}$ [μm]	$n_{\mathrm{r,cloud}}$	$r_{\mathrm{eff,cloud}}$ [μm]	$n_{\mathrm{i,haze}}$	ω_{haze}	ω_{cloud}	τ_{haze}	χ^2
0.05	1.80	0.3	0.4	0.031	0.9977	0.064	2.37
0.1	1.80	0.3	0.4	0.133	0.9977	0.0071	2.38
0.15	1.80	0.3	0.4	0.222	0.9977	0.0081	2.38
0.2	1.80	0.3	0.1	0.432	0.9977	0.012	2.37
0.3	1.80	0.3	0.06	0.648	0.9977	0.020	2.32
0.4	1.80	0.3	0.04	0.768	0.9977	0.028	2.29
0.5	1.80	0.3	0.04	0.780	0.9977	0.028	2.27

The behaviors of χ^2 and ω_{cloud} as a function of $n_{\mathrm{i,haze}}$ as discussed in **Section 4.3** is found to be just as valid for the CB2/STrZ data set for the same reason. To check the effect of $n_{\mathrm{i,haze}}$ on the model's fit, we show the best-fit modeled limb-darkening curves for two cloud model cases ($n_{\mathrm{i,haze}}$ = 0.0 and $n_{\mathrm{i,haze}}$ = 0.04) obtained under $r_{\mathrm{eff,haze}}$ = 0.5 μm in **Figure 5.6**. Compared with a conservative scattering case ($n_{\mathrm{i,haze}}$ = 0.0), the improvement of the model's fit is certainly confirmed in the near-limb points for three small solar phase angles (3.7°, 12.6°, and 18.8°). Conversely, the goodness of fit for two large solar phase angles (136.3° and 140.1°) becomes worse because of absorption of photons and decrease in strength of scattering due to the stratospheric haze. It should be noted that amount of change in χ^2 value due to change of $n_{\mathrm{i,haze}}$ for the CB2/STrZ data set is not so large compared with that for the BL1/STrZ data set. For example, in the case of $r_{\mathrm{eff,haze}}$ = 0.5 μm, while χ^2 value decreases from 5.36 ($n_{\mathrm{i,haze}}$ = 0.0) to 2.78 ($n_{\mathrm{i,haze}}$ = 0.04) for the BL1/STrZ data set, χ^2 value decreases only 0.34 (from 2.61 at $n_{\mathrm{i,haze}}$ = 0.0 to 2.27 at $n_{\mathrm{i,haze}}$ = 0.04) for the CB2/STrZ data set. In addition, West (1988) suggested that the value of $n_{\mathrm{i,haze}}$ at 600 nm would be smaller than that at 430 nm and adopted the considerably small value ($n_{\mathrm{i,haze}}$ = 0.0002) at 600 nm for obtaining a reasonable fit in his analyses of Voyager 2 images during eclipse. Tomasko et al. (1978) determined that ω_{haze} in red-channel for the STrZ was equal to or larger than 0.95. This value leads to n_{i} = 0.008, if the stratospheric haze can be approximated by Mie particles with $n_{\mathrm{r,haze}}$ = 1.3 and $r_{\mathrm{eff,haze}}$ = 0.5 μm. From these reasons, we consider that there is no need to change the value of $n_{\mathrm{r,haze}}$ significantly, at least in CB2.

Finally, we make reference to the value of τ_{haze}. As mentioned before, the stratospheric haze is found to be optically thin without regard to regions and wavelengths. For example, in the case of the

CB2/STrZ data set, the obtained τ_{haze} is only 0.06 even at the optically thickest case. Smith (1980) determined the vertical aerosol optical thickness above the troposphere for the STrZ was ~0.05 at 1.05 μm from the satellite eclipse observations. Simon-Miller et al. (2001) retrieved the optical thickness of the stratospheric haze for the STrZ from the Galileo SSI high spatial images, the value of which was 0.03 at 756 nm. The optically thin stratospheric haze deduced in this study is in good agreement with these previous studies. Conversely, values significantly larger than ours (τ_{haze} = 0.4–0.6) were found by previous limb-darkening analyses with ground-based continuum (~750 nm) data (e.g., Satoh and Kawabata, 1992, 1994; Kuehn and Beebe, 1993). This discrepancy would probably be caused by the difference between the Pioneer HG function and our Mie scattering phase function in the amplitude of backward scattering. A detailed analysis of previous published ground-based and spacecraft data with our Mie scattering phase functions is required to support this hypothesis in future.

5.1.5. Visual difference between the STrZ and the SEBn –the single scattering albedo of cloud particles

As already noted, there are no key parameters discussed above to explain the visual difference between the STrZ and the SEBn. Especially, it is noteworthy that the scattering properties of cloud particles for both the STrZ and the SEBn are found to show much the same characteristics from our analyses of the Cassini ISS data. Only the single scattering albedo of cloud (ω_{cloud}), the last variable parameter left in our assumed cloud model, shows a remarkable difference between two regions. That is, ω_{cloud} gets a higher value for the STrZ than one for the SEBn regardless of wavelengths. The difference in absorption ($1-\omega_{\mathrm{cloud}}$) occurred in the cloud layer between two regions is remarkable in BL1 and becomes less prominent in CB2. Thus, we conclude that only the single scattering albedo of cloud in the assumed cloud model is one key parameter which causes the visual difference between the zones and belts. Our results obtained with the Cassini ISS data support the idea proposed by West et al. (1986) that the main difference between two distinctly-different bands is caused by the lower continuum single scattering albedo in the belt. However, in principle, we cannot judge from our results of the radiative transfer calculation whether such difference ($1-\omega_{\mathrm{cloud}}$) is caused by cloud particles themselves or some absorbents (i.e., coloring agents, referred to as chromophores) amongst the cloud particles.

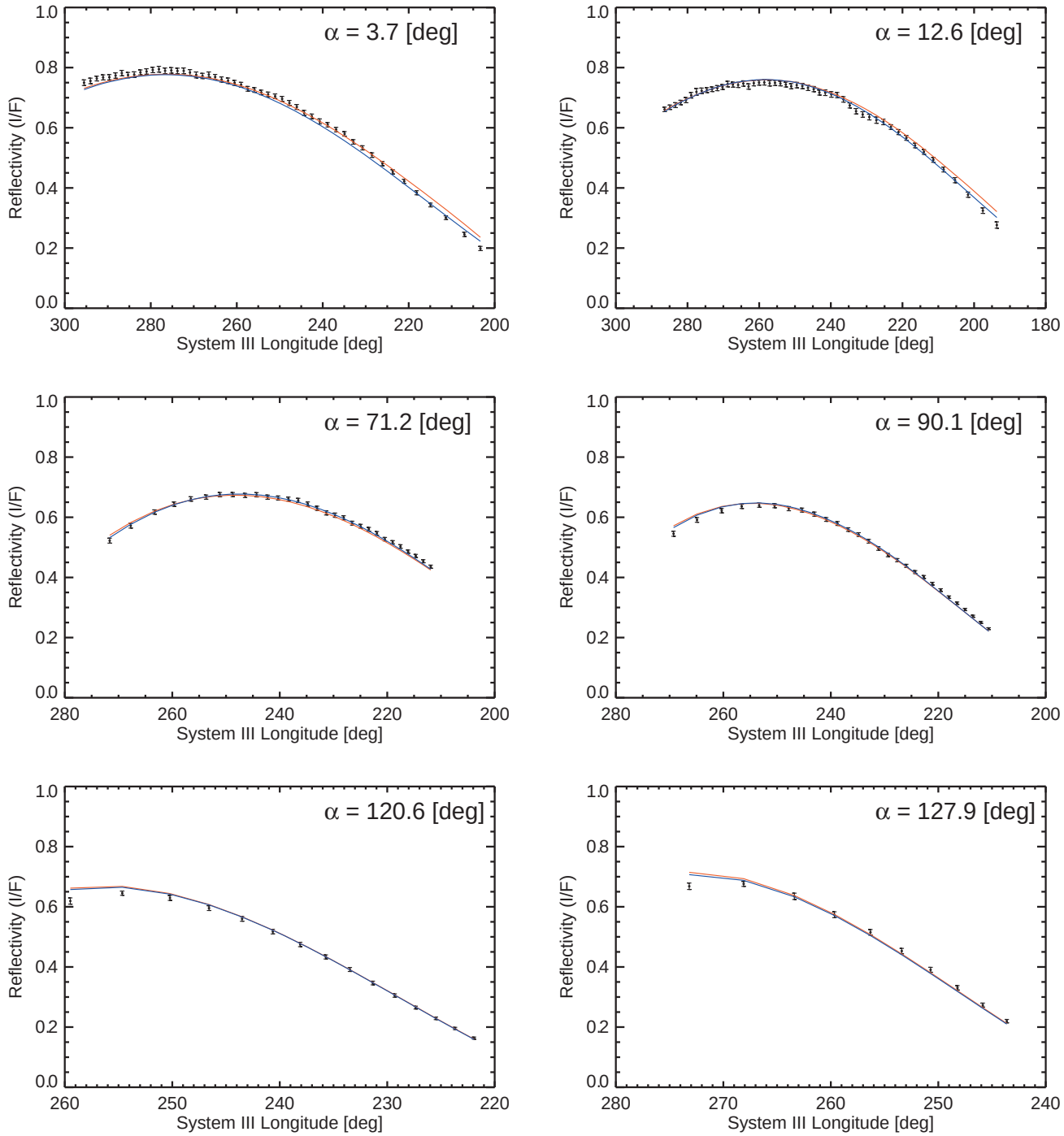

Figure 5.6. The sensitivity of modeled limb-darkening curves in CB2/STrZ data set for $n_{\mathrm{i,haze}}$. In this figure, two model calculation results ($n_{\mathrm{i,haze}}$ = 0.0 and $n_{\mathrm{i,haze}}$ = 0.04) obtained under $n_{\mathrm{r,haze}}$ = 1.3 and $r_{\mathrm{eff,haze}}$ = 0.5 μm are presented (see also Table 4.1 and Table 5.1).

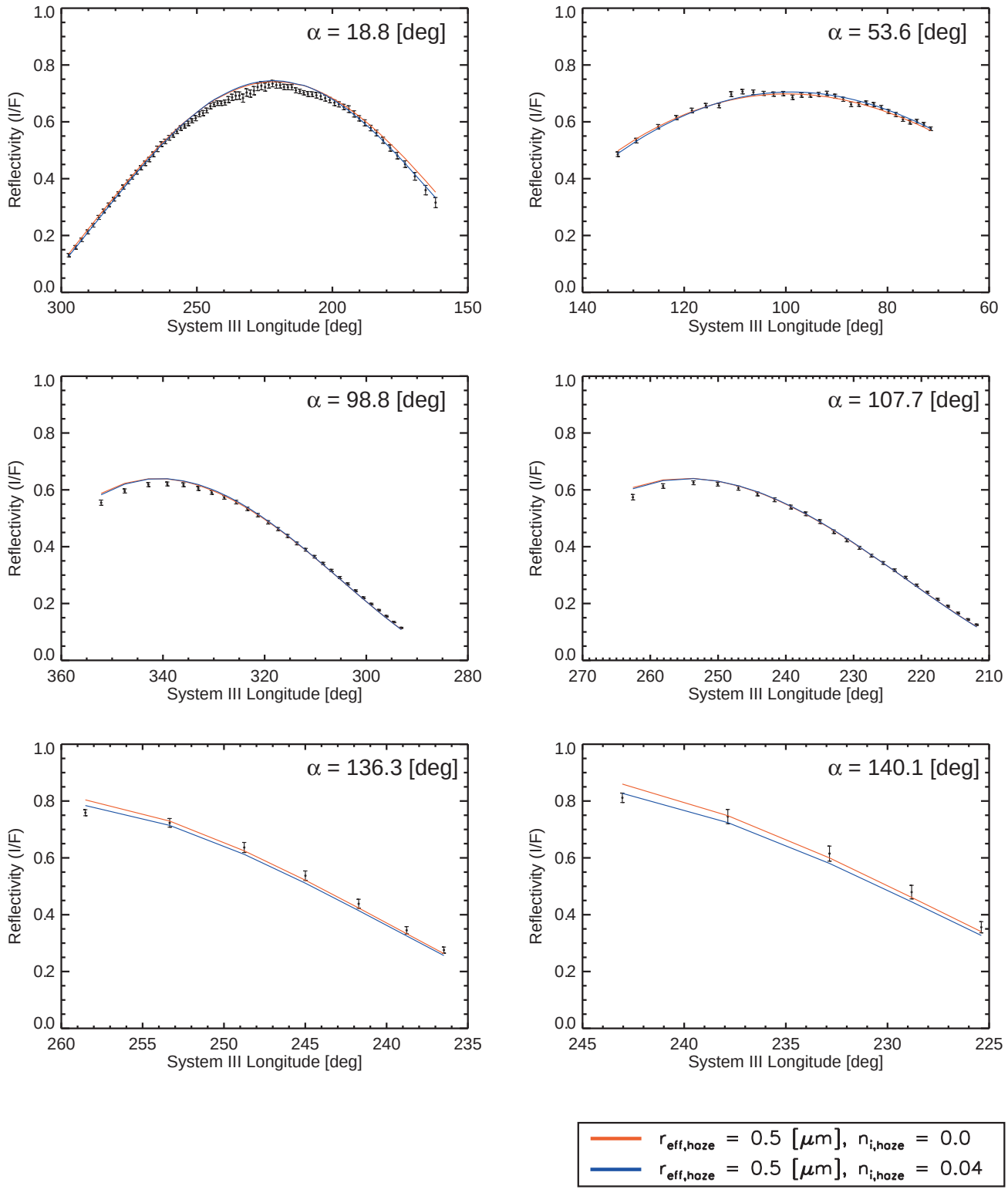

Figure 5.6–*Continued*

Nevertheless, this would be likely to be due to chromophores since all of condensate clouds predicted from thermochemical equilibrium theory and photochemically produced stratospheric haze are white at visible wavelengths and the optical and physical properties of cloud particles obtained in this study remain unchanged regardless of regions.

In this study, we can reproduce the entire limb-darkening curves in CB2 and BL1 with Type II-Mie model which has a stratospheric haze and a semi-infinite cloud layer containing vertically well-mixed chromophores. This model is the same as the model used by Tomasko et al. (1978) and Smith and Tomasko (1984). Simon-Miller et al. (2001) analyzed the Galileo SSI images at four wavelengths including 410 nm sampled at a limited range of solar phase angles with their different cloud model (a stratospheric haze, a tropospheric haze and a cloud sheet at the base of the tropospheric haze). They concluded that chromophores (absorption) in the tropospheric haze layer were responsible primarily for color variations at 410 nm. It is important whether or not such cloud model can also satisfy the limb-darkening cures over a wide range of solar phase angles used in this study because the wide solar phase angle behaviors of the limb-darkening curves can give stricter constraint on the vertical distribution of chromophores.

It should be noted that our conclusion is not a unique solution for the case in near-infrared. Banfield et al. (1998) used a cloud model with the particles as conservative scattering (in near-infrared) and the optically thick Rayleigh gas layer below the finite tropospheric cloud layer. They concluded that visual difference was primarily due to the optical thickness variations of the tropospheric cloud. After that, Sromovsky and Fry (2002) made a similar conclusion from the analysis of the HST data. Although their analyses were conducted with data at limited solar phase angle coverage, they showed the possibility of very different consequence for Jovian cloud model. To differentiate these two possibilities for Jovian cloud model, we should conduct further analyses using the Cassini ISS data with the combination of the wide solar phase angle and wavelength (from UV to near-infrared, including CH_4 bands) coverage in future.

5.2. Sensitivity of our results for the assumed parameters

As is well known, the assessment of uncertainty for each free parameter determined in **Chapter 4** is highly difficult because of complex mutual correlation among these parameters. However, it is important to know how fixed parameters in our assumed cloud model have an effect on our results (several sensitivity tests are already shown in **Chapter 4** and **Section 5.1.4**). In this section, instead of determining uncertainty for each parameter, we conduct several sensitivity tests for the assumed parameters.

5.2.1. Sensitivity test for pressure differences ΔP_1 and ΔP_2

As already tested in **Section 4.3** for the BL1/STrZ data set, we also examine the sensitivity of χ^2 value and two free parameters ω_{cloud} and τ_{haze} for two pressure differences (ΔP_1 and ΔP_2) with the CB2/STrZ data set. Again, the atmospheric opacity τ_{total} seen in CB2 is only one-eighth of that seen in BL1. In this sensitivity test, we use the same approach as that applies to the BL1/STrZ data set with the exception of the Mie scattering phase function for cloud with values of $n_{\mathrm{r,cloud}}$ = 1.85 and $r_{\mathrm{eff,cloud}}$ = 0.3 μm. The best-fit χ^2 value and two optimized parameters (ω_{cloud} and τ_{haze}) for each combination of ΔP_1 and ΔP_2 are listed in **Table 5.2**. Although, in the case of the BL/STrZ data set, the χ^2 value decreases from 12.89 at a combination of ΔP_1 = 0.0 bar and ΔP_2 = 0.0 bar to 4.37 at a combination of ΔP_1 = 0.15 bar and ΔP_2 = 0.3 bar, the difference of χ^2 value for the CB2/STrZ data set between the above two extreme cases is only 0.3. In general, the limb-darkening curves for large solar phase angles are more sensitive to these parameters. There are, however, no remarkable differences in reflectivity at solar phase angles smaller than the Cassini's upper limit (= 140.1°) as presented in **Figure 5.7**. Therefore, our assumption of these parameters at this wavelength is valid for even such large solar phase angle.

Table 5.2. Sensitivity of χ^2 value and two parameters (ω_{cloud} and τ_{haze}) for two pressure differences (ΔP_1 and ΔP_2) with the CB2/STrZ data set. In these calculations, we use the Mie scattering phase function for cloud with values of $n_{\text{r,cloud}}$ = 1.85 and $r_{\text{eff,cloud}}$ = 0.3 μm, and the function for haze with values of $n_{\text{r,haze}}$ = 1.3 and $r_{\text{eff,haze}}$ = 0.5 μm.

ΔP_1 and ΔP_2 dependence		ΔP_2 [bar]			
		0.0	0.1	0.2	0.3
ΔP_1 [bar]	0.0	χ^2 = 2.85 τ_{haze} = 0.039 ω_{cloud} = 0.9967	χ^2 = 2.74 τ_{haze} = 0.045 ω_{cloud} = 0.9967	χ^2 = 2.66 τ_{haze} = 0.050 ω_{cloud} = 0.9967	χ^2 = 2.59 τ_{haze} = 0.056 ω_{cloud} = 0.9968
	0.05	χ^2 = 2.80 τ_{haze} = 0.042 ω_{cloud} = 0.9967	χ^2 = 2.70 τ_{haze} = 0.048 ω_{cloud} = 0.9967	χ^2 = 2.63 τ_{haze} = 0.053 ω_{cloud} = 0.9968	χ^2 = 2.58 τ_{haze} = 0.059 ω_{cloud} = 0.9968
	0.1	χ^2 = 2.76 τ_{haze} = 0.045 ω_{cloud} = 0.9967	χ^2 = 2.67 τ_{haze} = 0.051 ω_{cloud} = 0.9967	χ^2 = 2.61* τ_{haze} = 0.056 ω_{cloud} = 0.9968	χ^2 = 2.56 τ_{haze} = 0.062 ω_{cloud} = 0.9968
	0.15	χ^2 = 2.72 τ_{haze} = 0.048 ω_{cloud} = 0.9967	χ^2 = 2.64 τ_{haze} = 0.054 ω_{cloud} = 0.9968	χ^2 = 2.59 τ_{haze} = 0.060 ω_{cloud} = 0.9968	χ^2 = 2.55 τ_{haze} = 0.065 ω_{cloud} = 0.9968

* A cloud model with a combination of ΔP_1 = 0.1 bar and ΔP_2 = 0.2 bar is referred to as "nominal case".

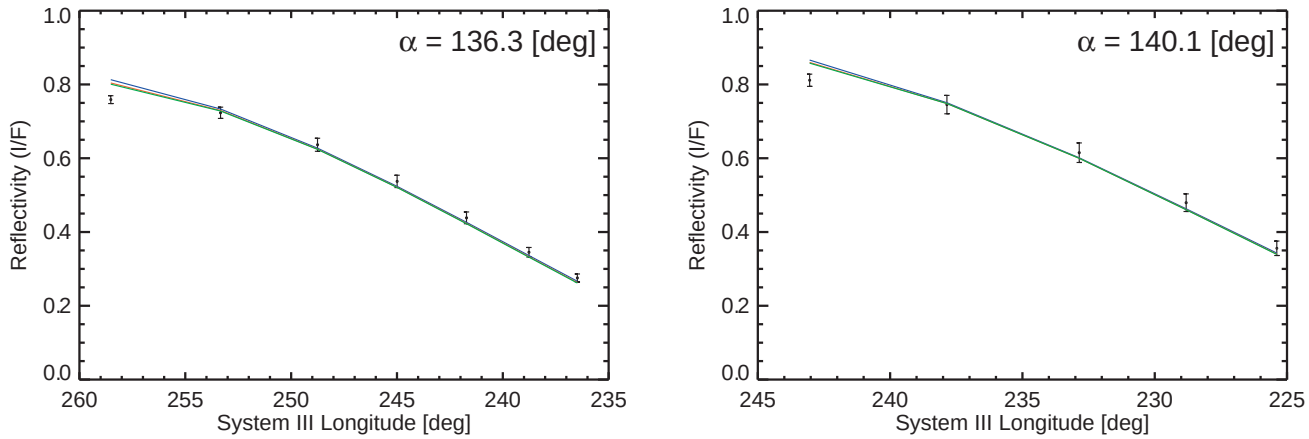

Figure 5.7. The sensitivity of modeled limb-darkening curves in the CB2/STrZ data set for two pressure differences (ΔP_1 and ΔP_2). Three colors denote three different model calculation results: red, nominal case (ΔP_1 = 0.1 bar and ΔP_2 = 0.2 bar); blue, an extreme case (ΔP_1 = 0.0 bar and ΔP_2 = 0.0 bar); green, another extreme case (ΔP_1 = 0.15 bar and ΔP_2 = 0.3 bar). In this figure, only the modeled limb-darkening curves for two large solar phase angles (136.3° and 140.1°) are presented.

5.2.2. Sensitivity test for variance of the Hansen's size distribution $v_{\mathrm{eff,cloud}}$

Through our radiative transfer calculations, the effective variances v_{eff} of the Hansen's size distributions for cloud and haze are assumed to be 0.1. Next, we verify the dependence of $v_{\mathrm{eff,cloud}}$ by comparing the nominal size distribution with two cases: narrower ($v_{\mathrm{eff,cloud}}$ = 0.05) and broader ($v_{\mathrm{eff,cloud}}$ = 0.2) ones described in **Figure 3.5**. Except for using the fixed value of $n_{\mathrm{r,haze}}$ (= 1.3), the Type II-Mie model and the fitting strategy mentioned in **Section 3.3** and **Section 3.4**, respectively, are directly applied to the CB2/STrZ data set. As a result, in both cases, the best-fit model for the case of $r_{\mathrm{eff,haze}}$ = 0.5 μm is preferred to those for other $r_{\mathrm{eff,haze}}$ cases. For the case of $r_{\mathrm{eff,haze}}$ = 0.5 μm, the values of best-fit parameters ($n_{\mathrm{r,cloud}}$, $r_{\mathrm{eff,cloud}}$, ω_{cloud}, and τ_{haze}) and χ^2 value for the best-fit model are summarized in **Table 5.3**. Even though the largest difference in χ_{i}^2 ($\Delta\chi_{\mathrm{i}}^2 \geq 2$) between the narrower (broader) and the nominal size distributions is found in the limb-darkening curves at 3.7° (120.6°) as shown in **Figure 5.8**, there are little remarkable differences required to constrain this parameter well. Actually, we have very few information on what size and type of aerosols are distributed in the Jovian atmosphere. The determination of the particle size distribution by in-situ measurements (such as the cloud particle size spectrometer on board Pioneer Venus), of course, is needed to know more accurate information on aerosols' distributions and their properties.

Table 5.3. The best-fit models in the CB2/STrZ data set for three different $v_{\mathrm{eff,cloud}}$ when we use the Mie scattering phase function for haze with values of $n_{\mathrm{r,haze}}$ = 1.3 and $r_{\mathrm{eff,haze}}$ = 0.5 μm.

The best-fit values					
$v_{\mathrm{eff,haze}}$	$n_{\mathrm{r,cloud}}$	$r_{\mathrm{eff,cloud}}$ [μm]	ω_{cloud}	τ_{haze}	χ^2
0.05	1.85	0.3	0.9970	0.026	2.93
0.1	1.85	0.3	0.9968	0.056	2.61
0.2	1.80	0.3	0.9967	0.054	2.84

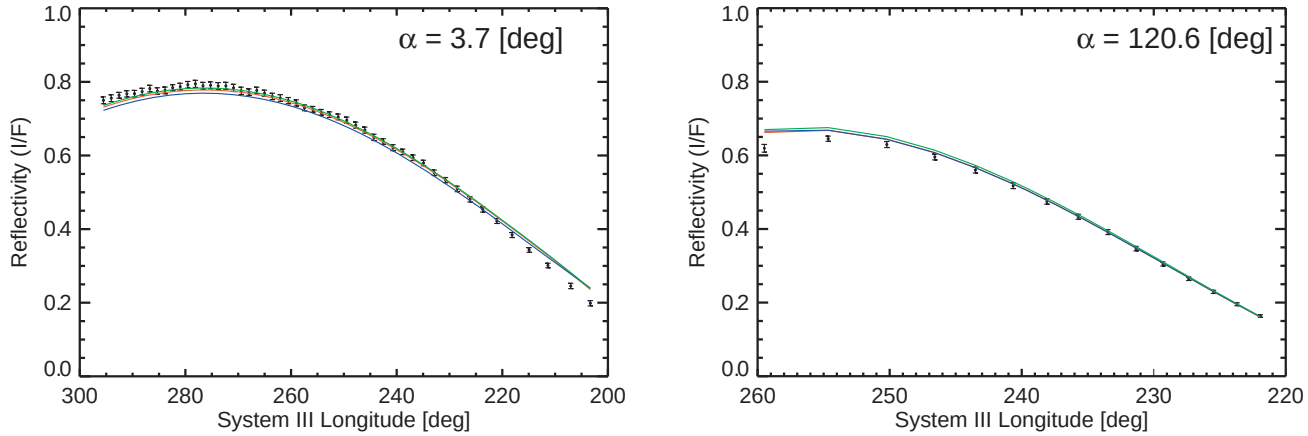

Figure 5.8. The sensitivity of modeled limb-darkening curves in the CB2/STrZ data set for the effective variance of the Hansen's size distribution ($v_{\mathrm{eff,cloud}}$). Three colors denote three different model calculation results: red, nominal size distribution ($v_{\mathrm{eff,cloud}}$ = 0.1); blue, a narrower size distribution ($v_{\mathrm{eff,cloud}}$ = 0.05); green, a broader size distribution ($v_{\mathrm{eff,cloud}}$ = 0.2). In this figure, we present only the modeled limb-darkening curves for two solar phase angles (3.7° and 120.6°) in which the largest difference in χ_{i}^2 ($\Delta\chi_{\mathrm{i}}^2 \geq 2$) between the narrower (broader) and the nominal size distributions is found.

5.2.3. Sensitivity test for uncertainty of absolute reflectivity C_{abs}

As pointed out in **Section 2.3**, the estimated absolute calibration error is ±10% for the CISSCAL-calculated values. We conduct a further sensitivity test for such uncertainty of absolute reflectivity to examine how values of variable parameters change with this uncertainty. In this sensitivity test, the absolute level of *all* limb-darkening curves is allowed to shift up or down from the nominal value calculated by CISSCAL. Such brightening or darkening is given by multiplying the CISSCAL-calculated values by an absolute scale factor C_{abs} ($0.9 \leq C_{\mathrm{abs}} \leq 1.1$) defined in **Section 2.3**. Note that the both correction factors, C_{abs} = 0.952 for CB2 and C_{abs} = 0.932 for BL1, presented in **Table 2.6**, are within this uncertainty range. For these limb-darkening curves at each C_{abs}, we search for the best-fit combination of two parameters ($n_{\mathrm{r,cloud}}$ and $r_{\mathrm{eff,cloud}}$) in the same manner as described in **Section 3.3** and **Section 3.4**. For simplicity, three less-significant parameters are fixed: $n_{\mathrm{r,haze}}$ = 1.3, $n_{\mathrm{i,haze}}$ = 0.0 (i.e., ω_{haze} = 1.0), and $r_{\mathrm{eff,haze}}$ = 0.5 μm. Here, we present the model calculation results of the CB2/STrZ data set and the BL1/SEBn data set.

For the CB2/STrZ data set, the best-fit combinations of $n_{\mathrm{r,cloud}}$ and $r_{\mathrm{eff,cloud}}$ with corresponding χ^2 values as well as the other optimized parameters (ω_{cloud} and τ_{haze}) as a function of C_{abs} are shown with black curves in **Figure 5.9**. Red curves in **Figure 5.9** show the relationship of χ^2 and

the other optimized parameters (ω_{cloud} and τ_{haze}) to C_{abs} when we use the best-fit Mie scattering phase function ($n_{\mathrm{r,cloud}}$ = 1.85 and $r_{\mathrm{eff,cloud}}$ = 0.3 μm) determined from the corrected limb-darkening curves (C_{abs} = 0.952 for CB2) in **Chapter 4**. The vertical solid and dashed lines denote the nominal reflectivity (C_{abs} = 1.0) and the corrected one (C_{abs} = 0.952).

We find that the best-fit combination of $n_{\mathrm{r,cloud}}$ and $r_{\mathrm{eff,cloud}}$ changes with C_{abs}; a smaller $n_{\mathrm{r,cloud}}$ and larger $r_{\mathrm{eff,cloud}}$ are required to reproduce the observations with increasing C_{abs}. Thus, the best-fit combination of $n_{\mathrm{r,cloud}}$ and $r_{\mathrm{eff,cloud}}$ obtained at C_{abs} = 0.952 is not a unique solution through all possible ranges of C_{abs}. Although the difference in χ^2 values obtained from both the best-fit cloud model and the cloud model with $n_{\mathrm{r,cloud}}$ = 1.85 and $r_{\mathrm{eff,cloud}}$ = 0.3 μm is more significant with increasing C_{abs} (>1.0), when C_{abs} is smaller than 1.0, the Mie scattering phase function ($n_{\mathrm{r,cloud}}$ = 1.85 and $r_{\mathrm{eff,cloud}}$ = 0.3 μm) is found to give an excellent fit to the observations by adjusting the values of ω_{cloud} and τ_{haze}.

As shown in **Figure 5.10**, the same holds true for the BL1/SEBn data set. In this case, the best-fit combination of $n_{\mathrm{r,cloud}}$ = 1.85 and $r_{\mathrm{eff,cloud}}$ = 0.2 μm obtained at C_{abs} = 0.932 is preferred in a broader range of C_{abs} compared with the case of the CB2/STrZ data set. We find that there is no need for inserting the stratospheric haze to our cloud model in most range of C_{abs}. The value of ω_{cloud} increases with C_{abs} and reaches ~0.99 at C_{abs} = 1.1 which is significantly lower value than those obtained at C_{abs} = 0.9 for other three data sets.

We still do not have an acceptable reason why the nominal full-disk albedo calculated by CISSCAL is higher than those measured by Karkoschka (1998) by 5–10 %, depending on filter, at the same solar phase angle. The “true” temporal changes of cloud brightness may be partially responsible for this difference. Nevertheless, the best-fit cloud parameters ($n_{\mathrm{r,cloud}}$ and $r_{\mathrm{eff,cloud}}$) obtained from the CB2/STrZ data set and the BL1/SEBn data set are still valid for most reliable C_{abs} intervals (i.e., 0.952–1.0 for CB2 and 0.932–1.0 for BL1).

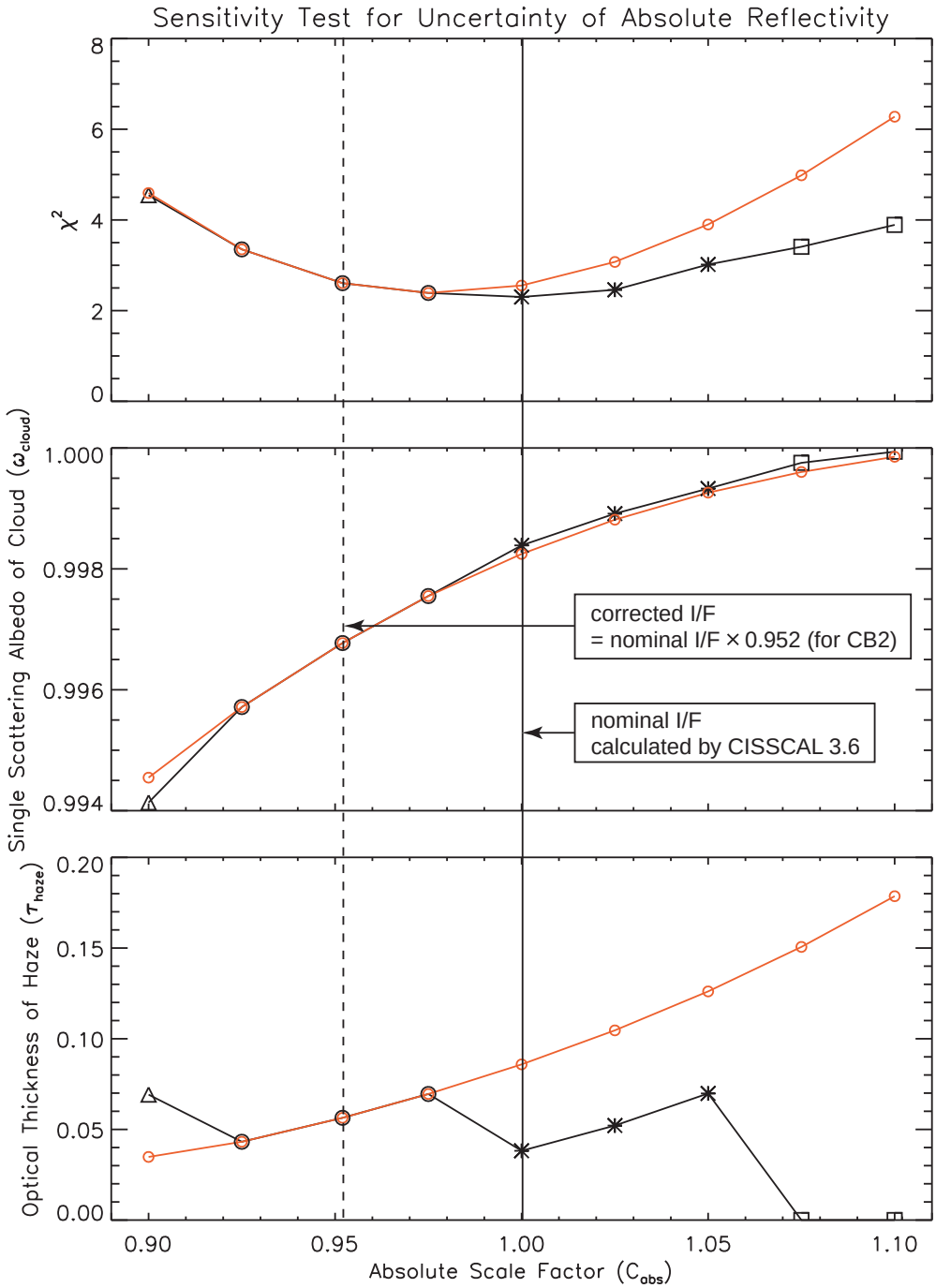

Figure 5.9. The best-fit combinations of $n_{\mathrm{r,cloud}}$ and $r_{\mathrm{eff,cloud}}$ with corresponding χ^2 values and the other optimized parameters (ω_{cloud} and τ_{haze}) as a function of absolute scale factor C_{abs} (black curves) in the CB2/STrZ data set. The relationship of χ^2 and the other parameters (ω_{cloud} and τ_{haze}) to C_{abs} when using the best-fit Mie scattering phase function ($n_{\mathrm{r,cloud}}$ = 1.85 and $r_{\mathrm{eff,cloud}}$ = 0.3 μm) (red curves). The vertical solid and dashed lines indicate the nominal (C_{abs} = 1.0) and the corrected (C_{abs} = 0.952) reflectivities. Four symbols denote four different best-fit cloud models: square, $n_{\mathrm{r,cloud}}$ = 1.6; asterisk, $n_{\mathrm{r,cloud}}$ = 1.8; circle, $n_{\mathrm{r,cloud}}$ = 1.85; triangle, $n_{\mathrm{r,cloud}}$ = 1.9. In all models except for the case of $n_{\mathrm{r,cloud}}$ = 1.6 ($r_{\mathrm{eff,cloud}}$ = 0.4 μm), $r_{\mathrm{eff,cloud}}$ is optimized at 0.3 μm.

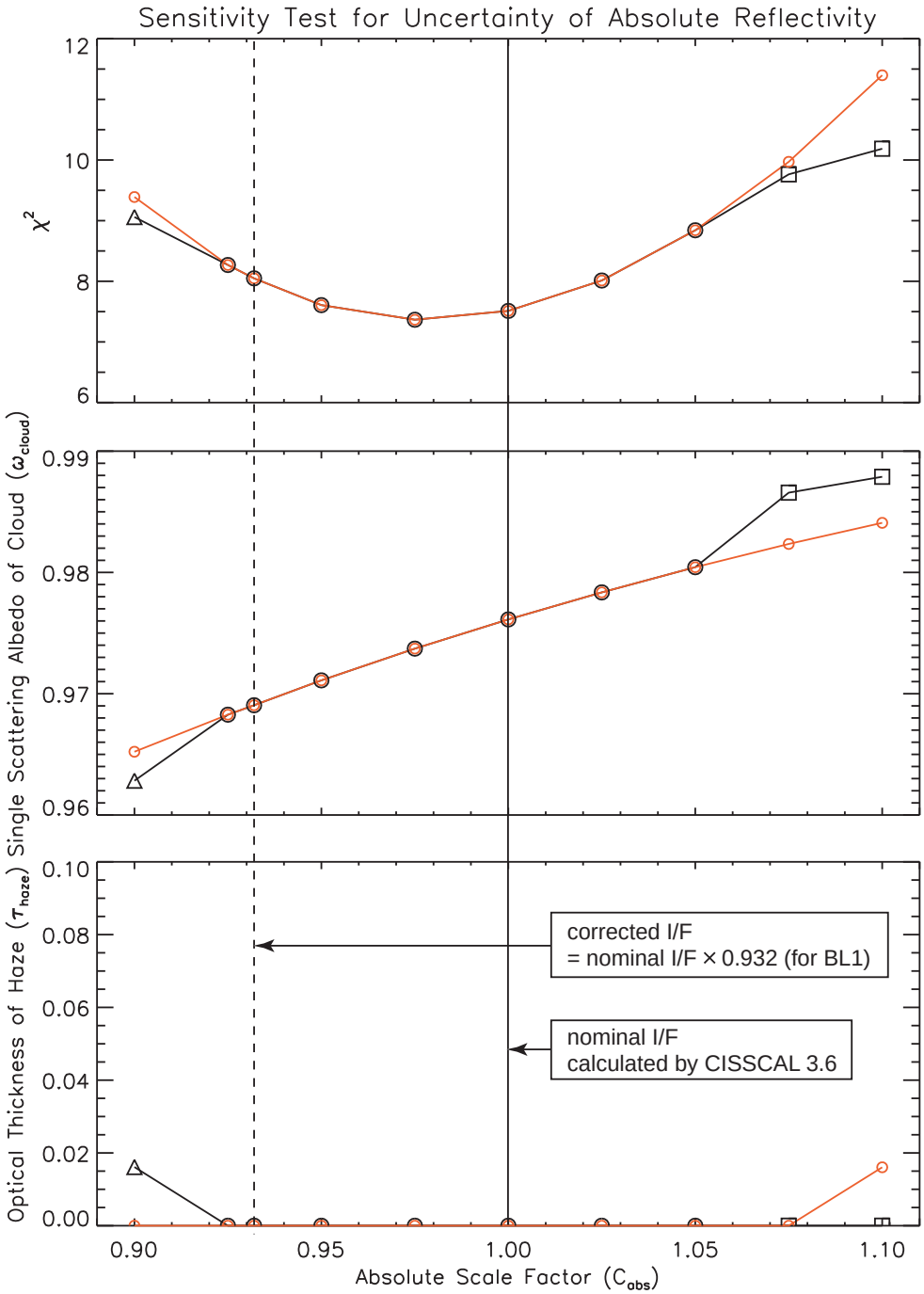

Figure 5.10. The best-fit combinations of $n_{\mathrm{r,cloud}}$ and $r_{\mathrm{eff,cloud}}$ with corresponding χ^2 values and the other optimized parameters (ω_{cloud} and τ_{haze}) as a function of absolute scale factor C_{abs} (black curves) in the BL1/SEBn data set. The relationship of χ^2 and the other parameters (ω_{cloud} and τ_{haze}) to C_{abs} when using the best-fit Mie scattering phase function ($n_{\mathrm{r,cloud}}$ = 1.85 and $r_{\mathrm{eff,cloud}}$ = 0.2 μm) (red curves). The vertical solid and dashed lines indicate the nominal (C_{abs} = 1.0) and the corrected (C_{abs} = 0.932) reflectivities. Three symbols denote three different best-fit cloud models: square, $n_{\mathrm{r,cloud}}$ = 1.6; circle, $n_{\mathrm{r,cloud}}$ = 1.85; triangle, $n_{\mathrm{r,cloud}}$ = 1.9. In all models except for the case of $n_{\mathrm{r,cloud}}$ = 1.6 ($r_{\mathrm{eff,cloud}}$ = 0.3 μm), $r_{\mathrm{eff,cloud}}$ is optimized at 0.2 μm.

5.3. Application of the best-fit Mie scattering phase functions to the Pioneer 10 IPP data

In this section, we demonstrate whether our best-fit Mie scattering phase functions can reproduce the P10/IPP data. This demonstration is conducted for all derived Mie scattering phase functions. The total optical thickness as a function of ΔP and the single scattering albedo of the Rayleigh gas layer in blue (440 nm) and red (640 nm) channels are calculated by convolving the spectral responsivity of the IPP (Pellicori et al., 1973). **Table 5.4** presents these parameters at two wavelengths for the STrZ and the SEBn. We explain the approach of this demonstration for the Red/STrZ data set as an example. We calculate the Mie scattering phase function for cloud at 640 nm wavelength with our best-fit values of $n_{\mathrm{r,cloud}}$ = 1.85 and $r_{\mathrm{eff,cloud}}$ = 0.3 μm obtained from the CB2/STrZ data set. The scattering phase functions for the stratospheric haze are also calculated with $n_{\mathrm{r,haze}}$ = 1.3 and $r_{\mathrm{eff,haze}}$ = 0.1–0.5 μm at intervals of 0.1 μm. With the Type II-Mie model, we optimize ω_{cloud} and τ_{haze} by allowing adjustment of F_{p} ($72.3 \leq F_{\mathrm{p}} \leq 79.6$ for red-channel) as discussed in Tomasko et al. (1978). Note that F_{p} is the solar incident flux divided by π in units of the P10/IPP's count. In the case of the CB2/SEBn data set, the best-fit combination of $n_{\mathrm{r,cloud}}$ = 1.8 and $r_{\mathrm{eff,cloud}}$ = 0.3 μm is used.

Table 5.4. Total optical thickness and single scattering albedo of the Rayleigh gas layer calculated for the Pioneer 10 IPP red- and blue-channels in the STrZ and the SEBn.

	Red		Blue	
	STrZ	SEBn	STrZ	SEBn
τ_R	$0.0460\Delta P$	$0.0467\Delta P$	$0.208\Delta P$	$0.211\Delta P$
τ_M	$1.03 \times 10^{-2}\Delta P$	$1.05 \times 10^{-2}\Delta P$	$1.41 \times 10^{-4}\Delta P$	$1.44 \times 10^{-4}\Delta P$
τ_{total}	$0.0563\Delta P$	$0.0572\Delta P$	$0.208\Delta P$	$0.212\Delta P$
ω_R	0.8167	0.8167	0.9993	0.9993

Figure 5.11 and **Figure 5.12** show the comparisons of the model-computed curves for five $r_{\mathrm{eff,haze}}$ cases with the P10/IPP limb-darkening curves in red-channel for the STrZ and the SEBn, respectively. In the fitting process, data points too close to the limb or to the terminator (shown by triangles in **Figure 5.11** and **Figure 5.12**) are null weighted because inaccuracy of the plane-parallel approximation is expected to be significant for such geometries (the criterion we use is that either μ_0

or μ is smaller than 0.15). Such treatment actually excludes all data points for the STrZ at the solar phase angle of 150° from the evaluation of the goodness of fit, although only one data point for the SEBn passes this criterion. The best-fit values of ω_{cloud} and τ_{haze}, together with F_{p} for each $r_{\mathrm{eff,haze}}$ case in the Red/STrZ data set and the Red/SEBn data set are tabulated in **Table 5.5** and **Table 5.6**, respectively. We find that the best-fit models are obtained with $r_{\mathrm{eff,haze}}$ = 0.5 μm and F_{p} = 72.3, regardless of regions. In two data sets, the χ^2 value monotonically decreases with increasing $r_{\mathrm{eff,haze}}$. The best-fit values of ω_{cloud} (= 0.996) and τ_{haze} (= 0.15) at $r_{\mathrm{eff,haze}}$ = 0.5 μm for the STrZ are within acceptable ranges mentioned in previous studies. In the case of the SEBn, although the best-fit value of ω_{cloud} (= 0.988) is somewhat lower than those deduced from previous studies (e.g., 0.991 in Tomasko et al., 1978), such adjustment of variable parameters is likely to be required for reproducing the limb-darkening curves because the shape of our Mie scattering phase function is quite different from that of the Pioneer HG function as discussed in **Section 5.1.1**. Rather, such difference tells us how the scattering phase functions of aerosols have impact on determining other variable parameters. As **Figure 5.11** and **Figure 5.12** show, our best-fit Mie scattering phase functions reproduce the P10/IPP observations in red-channel for both regions well in spite of a gap of 27 years between the Pioneer 10 and the Cassini observations.

From these analyses of the P10/IPP red-channel data as well as the Cassini ISS CB2 data, it is found that large haze particles are needed to improve the model's fit for the near-limb points at high solar phase angles (109°, 120°, and 127°). Furthermore, at a solar phase angle of 150°, a remarkable dependence of $r_{\mathrm{eff,haze}}$ can be seen that is not so obvious for the solar phase angle of 140.1° in the Cassini ISS data (see **Figure 4.4**). The modeled reflectivity at the solar phase angle of 150° for the STrZ obtained with $r_{\mathrm{eff,haze}}$ = 0.1 μm is significantly lower than the observed one, beyond the expected errors of the plane-parallel approximation for such geometries (Herman et al., 1994). The same holds for the modeled reflectivity at 150° in the Red/SEBn data set. The best-fit cloud model with $r_{\mathrm{eff,haze}}$ = 0.2 μm for the Red/SEBn data set seems to yield excessively higher reflectivity compared with the observations at high solar phase angles (109°, 120°, and 127°) to reach the intensity of one data point at 150° which meets the criterion. To reproduce the high reflectivity variation at 150°, it seems that stratospheric haze consisting of particles larger than at least 0.2 μm is required.

Table 5.5. The best-fit parameters of the Type II-Mie model for the Pioneer 10 IPP Red/STrZ data set. In this demonstration, we use the best-fit Mie scattering phase function for cloud with values of $n_{\mathrm{r,cloud}}$ = 1.85 and $r_{\mathrm{eff,cloud}}$ = 0.3 μm.

The best-fit values				
$r_{\mathrm{eff,haze}}$ [μm]	ω_{cloud}	τ_{haze}	F_{p}	χ^2
0.1	0.9961	0.095	72.3	3.28
0.2	0.9958	0.039	72.3	3.11
0.3	0.9958	0.078	72.3	2.48
0.4	0.9959	0.119	72.3	2.13
0.5	0.9959	0.145	72.3	2.06

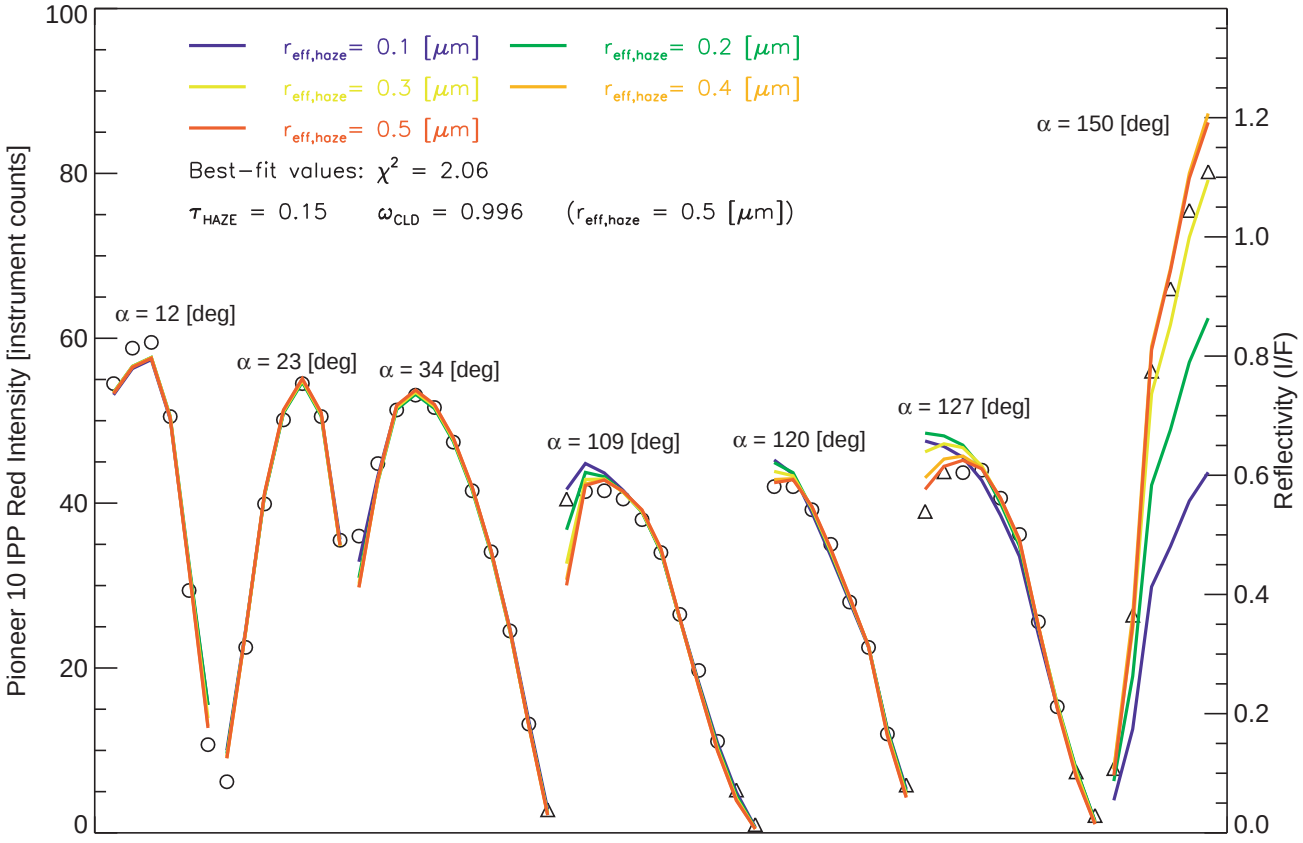

Figure 5.11. The comparisons of the best-fit modeled limb-darkening curves for five different effective radii of haze ($r_{\mathrm{eff,haze}}$: 0.1, 0.2, 0.3, 0.4, and 0.5 μm) with the Pioneer 10 IPP limb-darkening curves in red-channel for the STrZ. This calculation is performed for a demonstration of the best-fit Mie scattering phase function obtained in this study. Circles and triangles represent the Pioneer 10 IPP data which are used for the fitting process or not used, respectively. The reflectivity displayed in the right vertical axis is calculated by dividing the intensity by F_{p} = 72.3.

Table 5.6. The best-fit parameters of the Type II-Mie model for the Pioneer 10 IPP Red/SEBn data set. In this demonstration, we use the best-fit Mie scattering phase function for cloud with values of $n_{\mathrm{r,cloud}}$ = 1.80 and $r_{\mathrm{eff,cloud}}$ = 0.3 μm.

The best-fit values				
$r_{\mathrm{eff,haze}}$ [μm]	ω_{cloud}	τ_{haze}	F_{p}	χ^2
0.1	0.9833	0.000	79.6	44.18
0.2	0.9803	0.137	79.6	17.17
0.3	0.9878	0.129	72.3	2.19
0.4	0.9881	0.114	72.3	1.40
0.5	0.9882	0.127	72.3	1.38

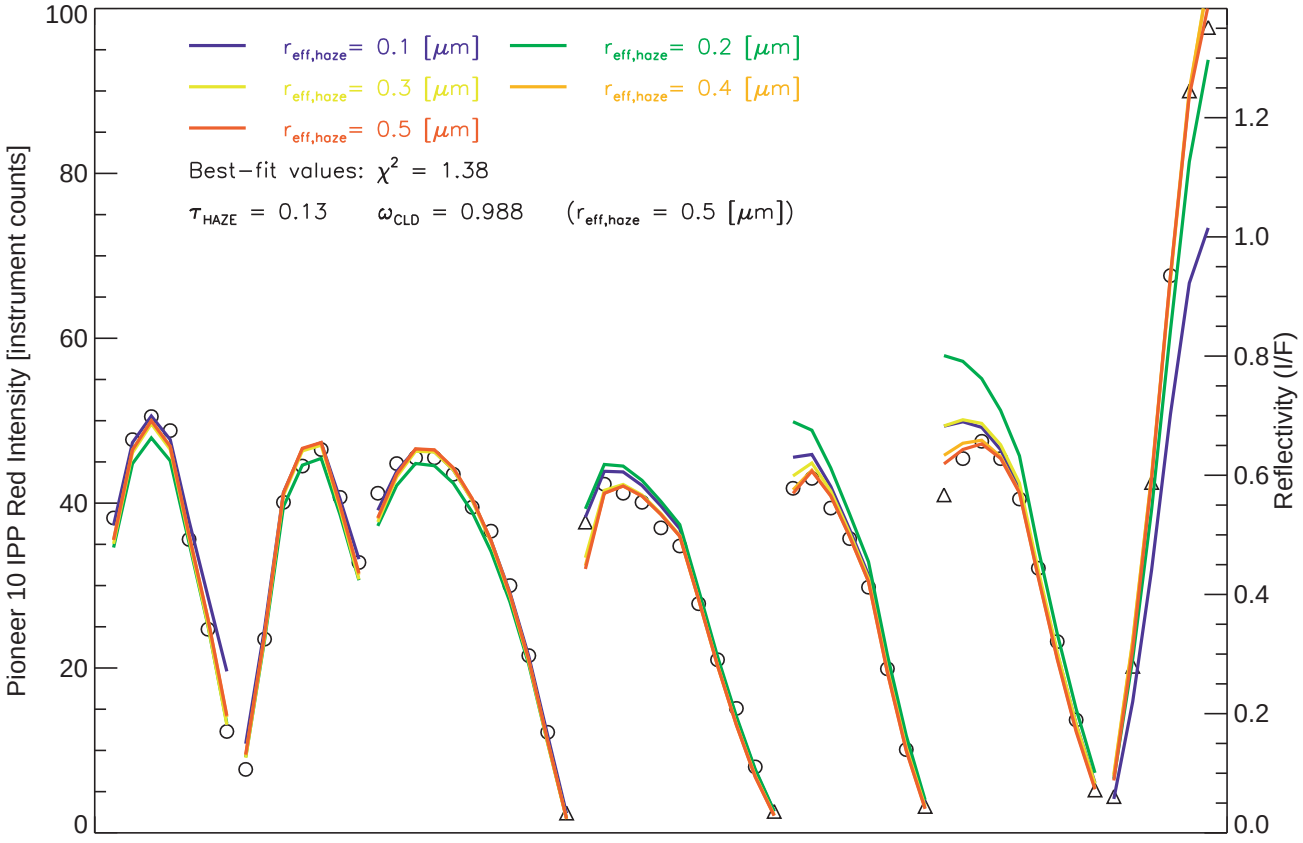

Figure 5.12. Same as Figure 5.11, except for the Red/SEBn data set. The reflectivity displayed in the right vertical axis is calculated by dividing the intensity by F_{p} = 72.3. Thus, the right vertical axis is not valid for the best-fit models obtained with $r_{\mathrm{eff,haze}}$ = 0.1 μm and 0.2 μm cases.

We also use the same approach mentioned above for the Blue/STrZ data set and the Blue/SEBn data set. In blue-channel, F_{p} is allowed to vary from 57.7 to 66.0. In this demonstration, we use the best-fit Mie scattering phase function for cloud with values of $n_{\mathrm{r,cloud}}$ = 1.85 and $r_{\mathrm{eff,cloud}}$ = 0.2 μm and set $n_{\mathrm{i,haze}}$ to 0.0 for both data sets. In the case of the Blue/STrZ data set, we perform an additional calculation with the best-fit Mie scattering phase functions for the stratospheric haze ($n_{\mathrm{i,haze}}$ = 0.04). **Figure 5.13** and **Figure 5.14** show the comparisons of the observed limb-darkening curves in blue-channel for the STrZ with the best-fit modeled curves for each $r_{\mathrm{eff,haze}}$ case calculated with a conservative scattering case ($n_{\mathrm{i,haze}}$ = 0.0) and an absorbing case ($n_{\mathrm{i,haze}}$ = 0.04), respectively. The best-fit values of ω_{cloud} and τ_{haze}, together with F_{p} for each $r_{\mathrm{eff,haze}}$ case in two $n_{\mathrm{i,haze}}$ cases are summarized in **Table 5.7** and **Table 5.8**. The comparisons for the Blue/SEBn data set are also shown in **Figure 5.15** and the best-fit values are listed in **Table 5.9**. From these figures, it is confirmed that our Mie scattering phase functions can reproduce the P10/IPP limb-darkening curves in blue-channel as well as red-channel without evident deviations.

It should be noted that the difference in the modeled reflectivity between two cloud models for the Blue/STrZ data set shown in **Figure 5.13** and **Figure 5.14** is apparent only at a solar phase angle of 150°. That is, the best-fit modeled reflectivity at 150° calculated with an absorbing case ($n_{\mathrm{i,haze}}$ = 0.04) is significantly lower than that calculated with a conservative scattering case ($n_{\mathrm{i,haze}}$ = 0.0). As can be seen from **Figure 5.13**, it is natural that the higher value of ω_{haze} (~0.995) obtained from their analysis was required to fit the observed reflectivity at 150° since Tomasko et al. (1978) included these data in the evaluation of the goodness of fit. At this time, we cannot constrain the optical and physical properties of the stratospheric haze well because of two reasons. One is that the observed limb-darkening curves obtained by the Cassini ISS are not sensitive to these properties enough to constrain them strictly. The other is that the observed limb-darkening curve at 150°, which shows the remarkable difference for $r_{\mathrm{eff,haze}}$, prevents us from evaluating this data by the radiative transfer calculation based on the plane-parallel approximation. In future, we need to analyze the limb-darkening curve at the solar phase angle of 150° obtained from the P10/IPP with a radiative transfer model considering the atmospheric curvature effect, in order to obtain more accurate information on the stratospheric haze.

Table 5.7. The best-fit parameters of the Type II-Mie model for the Pioneer 10 IPP Blue/STrZ data set. In this demonstration, we use the best-fit Mie scattering phase function for cloud with values of $n_{\mathrm{r,cloud}}$ = 1.85 and $r_{\mathrm{eff,cloud}}$ = 0.2 μm, and the functions for haze having conservative scattering ($n_{\mathrm{i,haze}}$ = 0.0).

The best-fit values				
$r_{\mathrm{eff,haze}}$ [μm]	ω_{cloud}	τ_{haze}	F_{p}	χ^2
0.1	0.9914	0.080	61.6	2.24
0.2	0.9873	0.075	66.0	2.13
0.3	0.9873	0.131	66.0	1.97
0.4	0.9873	0.156	66.0	2.00
0.5	0.9873	0.165	66.0	2.06

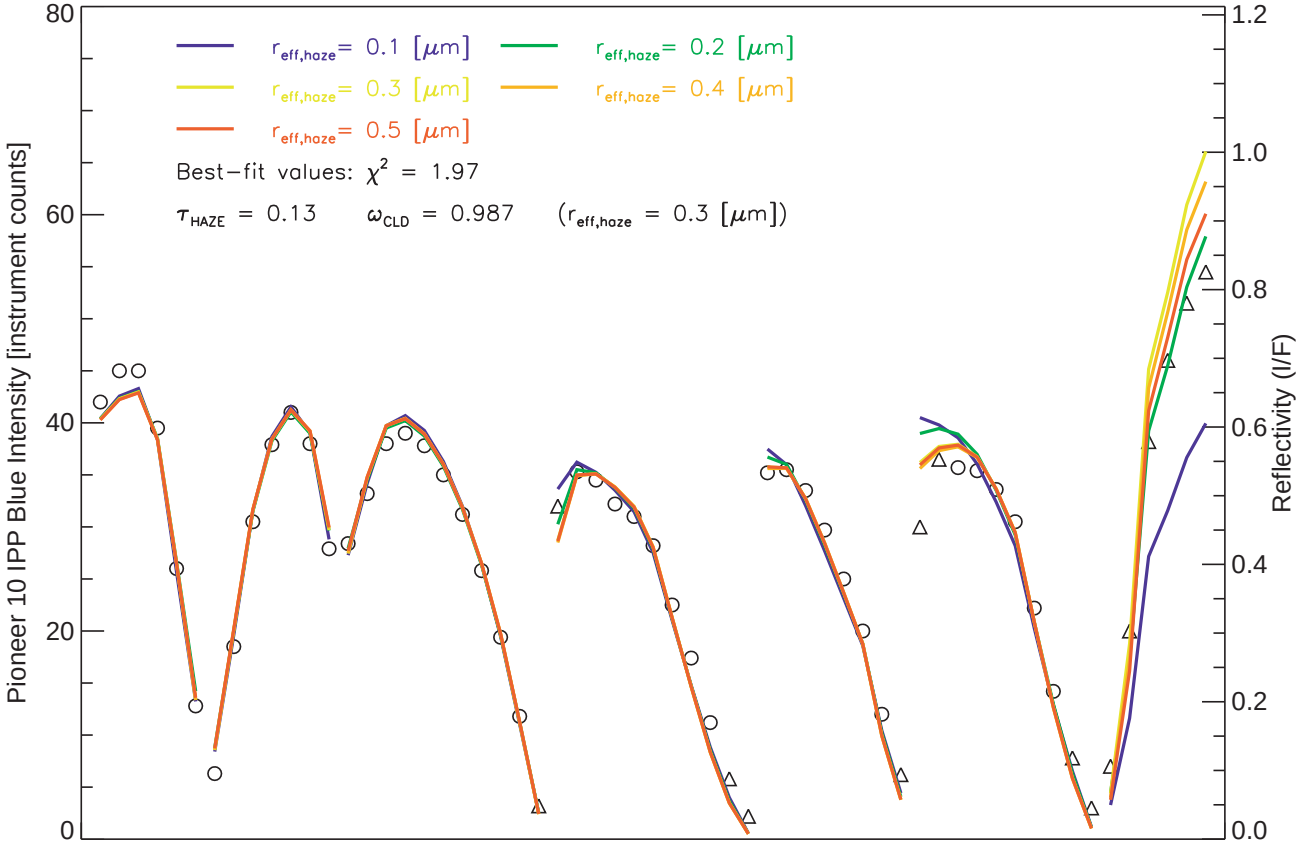

Figure 5.13. Same as Figure 5.11, except for the Blue/STrZ data set. In this calculation, we calculate the Mie scattering phase function for the stratospheric haze with a value of $n_{\mathrm{i,haze}}$ = 0.0. The reflectivity displayed in the right vertical axis is calculated by dividing the intensity by F_{p} = 66.0. Thus, the right vertical axis is not valid for the best-fit models obtained with $r_{\mathrm{eff,haze}}$ = 0.1 μm case.

Table 5.8. The best-fit parameters of the Type II-Mie model for the Pioneer 10 IPP Blue/STrZ data set. In this demonstration, we use the best-fit Mie scattering phase function for cloud with values of $n_{\mathrm{r,cloud}}$ = 1.85 and $r_{\mathrm{eff,cloud}}$ = 0.2 μm, and the functions for haze with a value of $n_{\mathrm{i,haze}}$ = 0.04.

The best-fit values				
$r_{\mathrm{eff,haze}}$ [μm]	ω_{cloud}	τ_{haze}	F_{p}	χ^2
0.1	0.9883	0.008	66.0	2.89
0.2	0.9884	0.015	66.0	2.85
0.3	0.9881	0.011	66.0	2.91
0.4	0.9880	0.009	66.0	2.92
0.5	0.9880	0.007	66.0	2.94

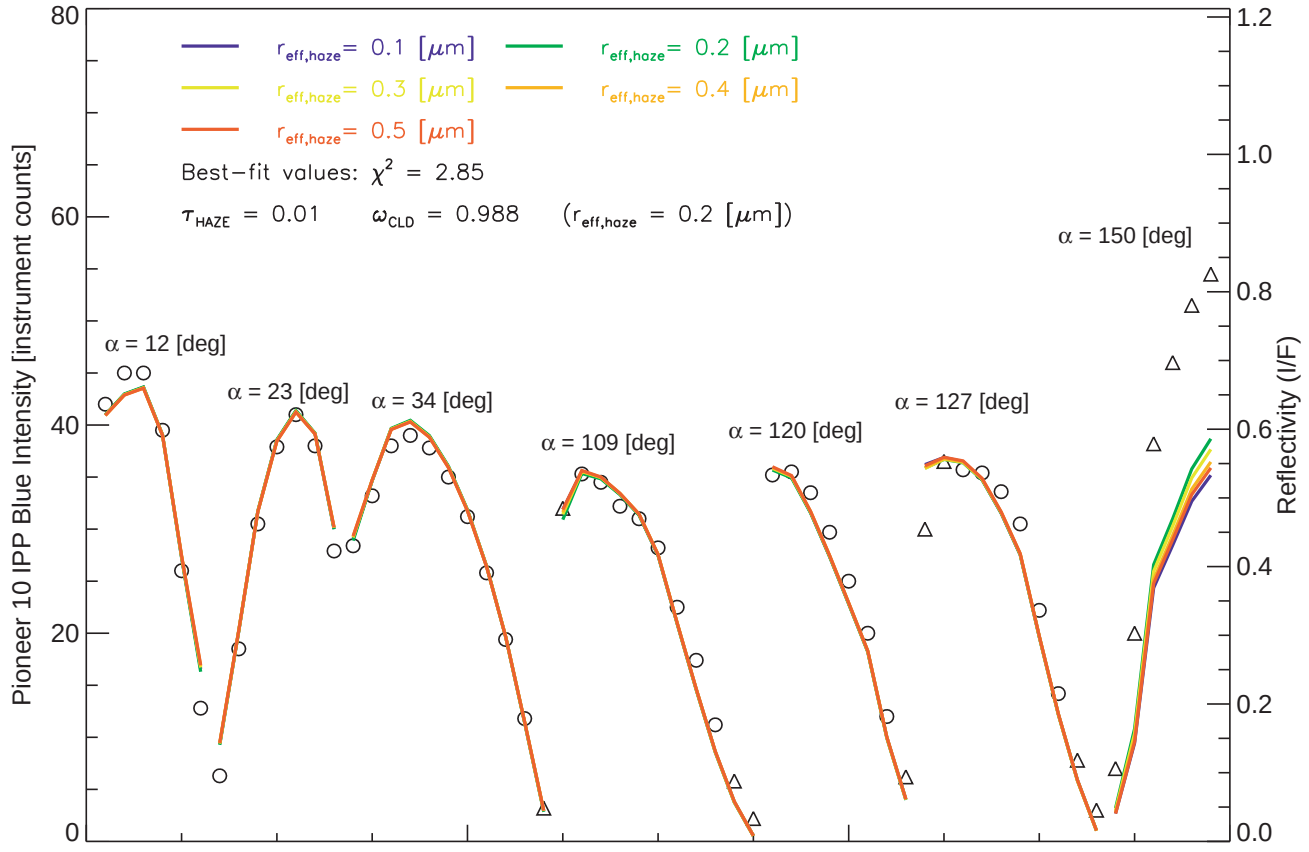

Figure 5.14. Same as Figure 5.11, except for the Blue/STrZ data set. In this calculation, we calculate the Mie scattering phase function for the stratospheric haze with a value of $n_{\mathrm{i,haze}}$ = 0.04. The reflectivity displayed in the right vertical axis is calculated by dividing the intensity by F_{p} = 66.0.

Table 5.9. The best-fit parameters of the Type II-Mie model for the Pioneer 10 IPP Blue/SEBn data set. In this demonstration, we use the best-fit Mie scattering phase function for cloud with values of $n_{\mathrm{r,cloud}} = 1.85$ and $r_{\mathrm{eff,cloud}} = 0.2$ μm.

The best-fit values				
$r_{\mathrm{eff,haze}}$ [μm]	ω_{cloud}	τ_{haze}	F_{p}	χ^2
0.1	0.9211	0.285	66.0	34.5
0.2	0.930	0.132	66.0	1.29
0.3	0.933	0.121	66.0	1.48
0.4	0.933	0.144	66.0	1.53
0.5	0.932	0.170	66.0	1.44

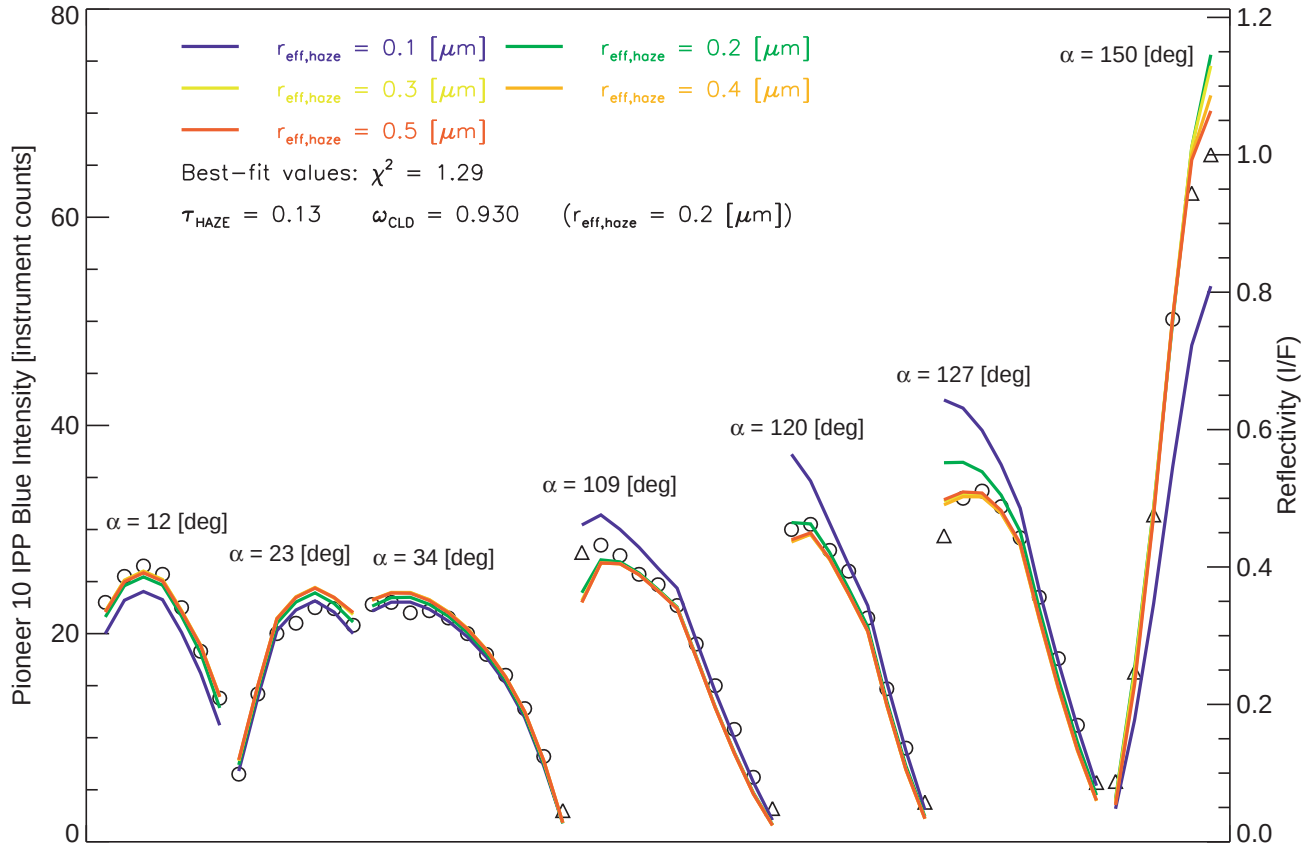

Figure 5.15. Same as Figure 5.11, except for the Blue/SEBn data set. The reflectivity displayed in the right vertical axis is calculated by dividing the intensity by $F_{\mathrm{p}} = 66.0$.

5.4. Limitation of the Pioneer HG function

Because the solar phase angle coverage of the Cassini ISS data is more uniform than the P10/IPP data (**Table 5.10**), it is possible to test the Pioneer HG function against the Cassini ISS limb-darkening curves. For this validation, we perform the radiative transfer calculations using the same configuration in the Type II model of Tomasko et al. (1978) (hereafter Type II-HG model). No modification is made to the scattering phase functions for both cloud and haze. Parameters for the Type II-HG model are summarized in **Table 5.11**. For the Type II-HG model, we search for the best-fit combination of two free parameters, τ_{haze} and ω_{cloud}, in the same manner as described in **Section 3.4**. In this validation, we conduct this test only for the CB2/STrZ data set.

Table 5.10. Solar phase angle coverage of the Cassini ISS and the Pioneer 10 IPP observations. The Cassini ISS data used in Case 1 and Case 2 are represented by circles.

Cassini's solar phase angle $\alpha_{\mathrm{Cassini}}$	Similar solar phase angle α_{P10} by the Pioneer 10 observations ($\alpha_{\mathrm{P10}} = \alpha_{\mathrm{Cassini}} \pm 10°$)	Case 1	Case 2
3.7°	12°	○	○
12.6°	12°	○	○
18.8°	12°, 23°	○	○
53.6°		○	
71.2°		○	
90.1°		○	
98.8°	109°	○	
107.7°	109°	○	○
120.6°	120°, 127°	○	○
127.9°	120°, 127°	○	○
136.3°	127°	○	○
140.1°	150°	○	○

Table 5.11. Model parameters for the Type II-HG model.

Layer	Parameter	Values	References
Stratospheric haze	τ_{haze}	variable	
	ω_{haze}	≥ 0.95	Tomasko et al. (1978)
	$P_{\mathrm{HG}}(\Theta)$	single HG function: g = 0.75	Tomasko et al. (1978)
Semi-infinite cloud	τ_{cloud}	128	
	ω_{cloud}	Variable	
	$P_{\mathrm{DHG}}(\Theta)$	double HG function: (f, g_1, g_2) = (0.938, 0.80, –0.70)	Tomasko et al. (1978)

Figure 5.16 shows the best-fit models with the Cassini ISS limb-darkening curves at 12 solar phase angles. Even with variations of ω_{haze} (= 0.96, 0.97, 0.98, 0.99, and 1.00), in addition to the nominal value (ω_{haze} = 0.95) of Tomasko et al. (1978), none of these models satisfactorily reproduces the Cassini ISS observations. The modeled limb-darkening curves at small solar phase angles (3.7°, 12.6°, and 18.8°) are steeper than observed curves for all ω_{haze} cases. The peak values of the modeled limb-darkening curves are also significantly higher than those observed at several solar phase angles (3.7°, 12.6°, 18.8°, 120.6°, 127.9°, 136.3°, and 140.1°). The best-fit parameters (ω_{cloud} and τ_{haze}) and χ^2 value for six different ω_{haze} cases are summarized as "Case 1" in **Table 5.12**.

The above result seems to be quite puzzling, as newly derived Mie scattering phase functions are able to reproduce both the Cassini ISS CB2 data and the P10/IPP red-channel data as demonstrated in **Section 5.3**. Therefore, we are motivated to make the Cassini ISS data as similar to the P10/IPP data as possible by selecting eight solar phase angles (3.7°, 12.6°, 18.8°, 107.7°, 120.6°, 127.9°, 136.3°, and 140.1°) as listed in **Table 5.10**. The data at the other four solar phase angles are null-weighted in the evaluation of χ^2. We name this experiment "Case 2". The model calculation results are shown in **Figure 5.17**, and the best-fit parameters and χ^2 values are presented in **Table 5.12**. Surprisingly, the selected limb-darkening curves, especially those at small solar phase angles (3.7°, 12.6°, and 18.8°), are better reproduced in Case 2 than Case 1. With the best-fit model, the calculated limb-darkening curves at the other solar phase angles (53.6°, 71.2°, 90.1°, and 98.8°), which are not used in the χ^2 evaluation, are also presented in **Figure 5.17**. The calculated reflectivities at these solar phase angles are found to be systematically lower than the observed ones by 5–10%, which cannot be explained by the uncertainty of reflectivity of the Cassini ISS data.

Table 5.12. The best-fit models of the Type II-HG model for Case 1 and Case 2.

ω_{haze}	Case 1			Case 2*		
	ω_{cloud}	τ_{haze}	χ^2	ω_{cloud}	τ_{haze}	χ^2
0.95	0.9996	0.60	12.49	0.9983	0.39	7.62
0.96	0.9994	0.65	10.32	0.9981	0.40	6.22
0.97	0.9991	0.65	9.41	0.9976	0.39	5.64
0.98	0.9987	0.61	9.85	0.9972	0.37	5.84
0.99	0.9981	0.54	11.39	0.9967	0.33	6.60
1.00	0.9977	0.47	13.62	0.9962	0.29	7.71

* In Case 2, we conduct the fitting process with selected limb-darkening curves at eight solar phase angles. Note that χ^2 values for Case 2 are calculated with equations (3.68) and (3.69) for n = 8.

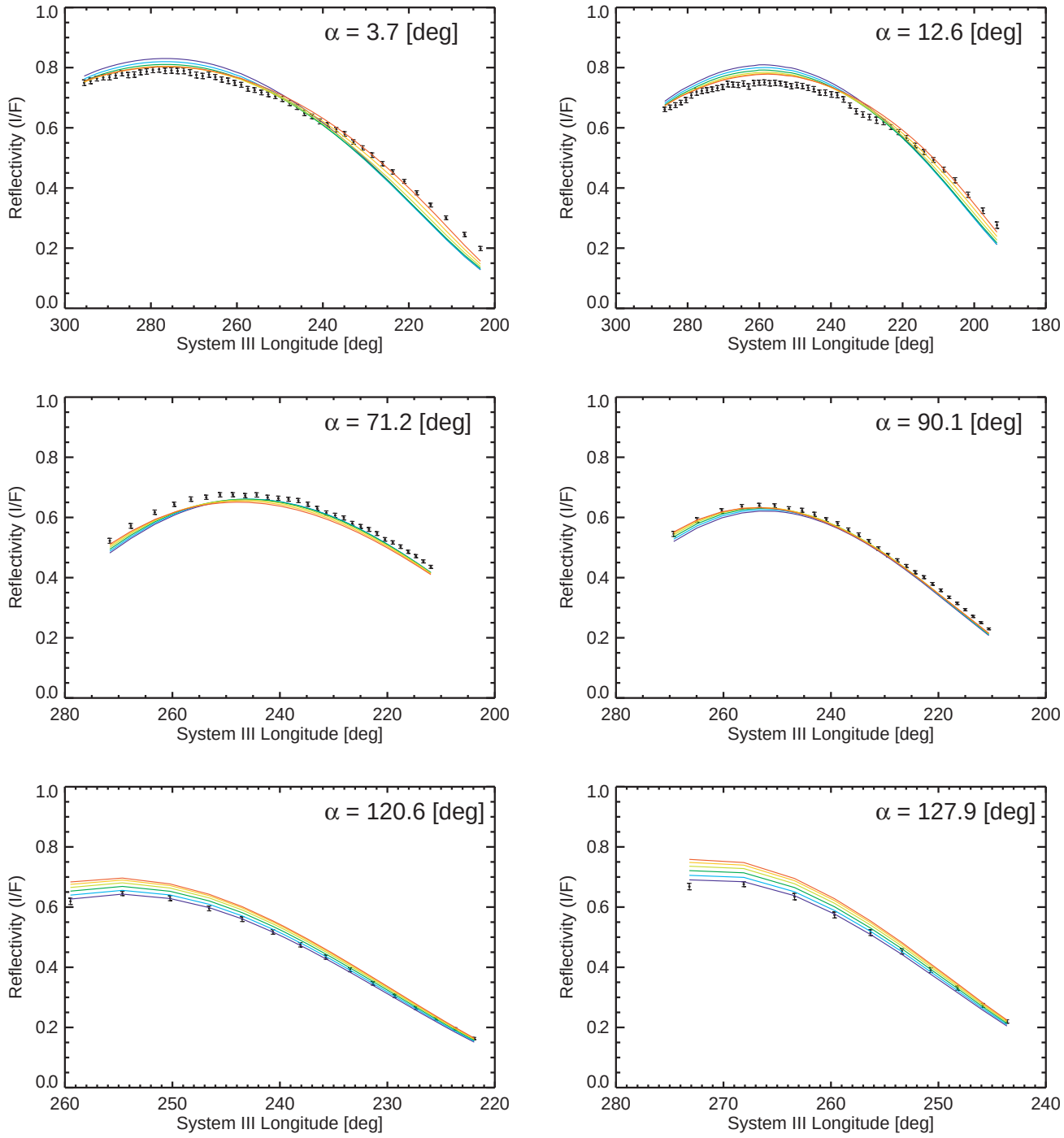

Figure 5.16. The best-fit models of the Type II-HG model (Case 1). The Pioneer HG functions are directly applied to scattering of the stratospheric haze and cloud particles. The dependence of single scattering albedo of the stratospheric haze (ω_{haze}: 0.95–1.0) is also investigated.

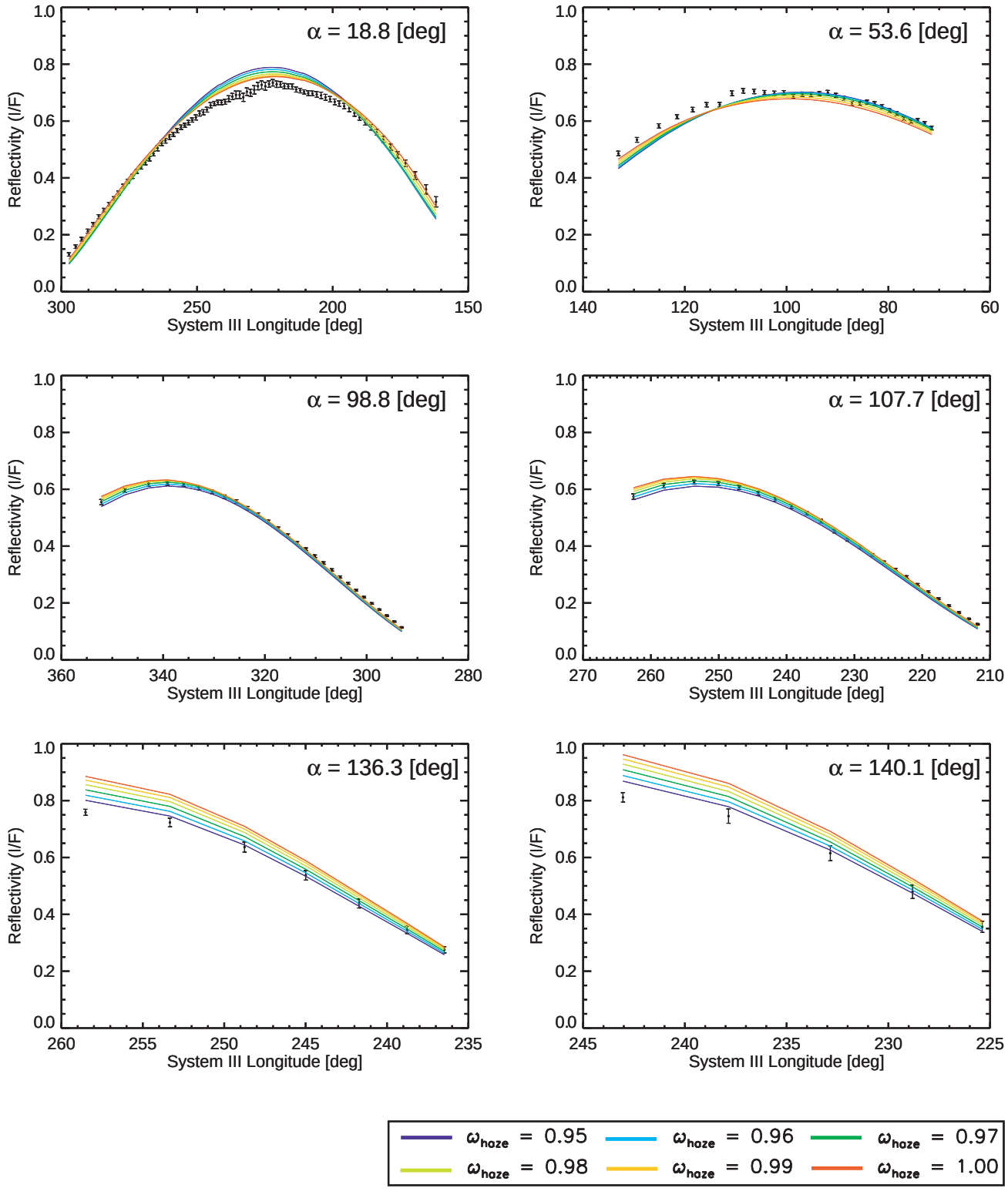

Figure 5.16–*Continued*

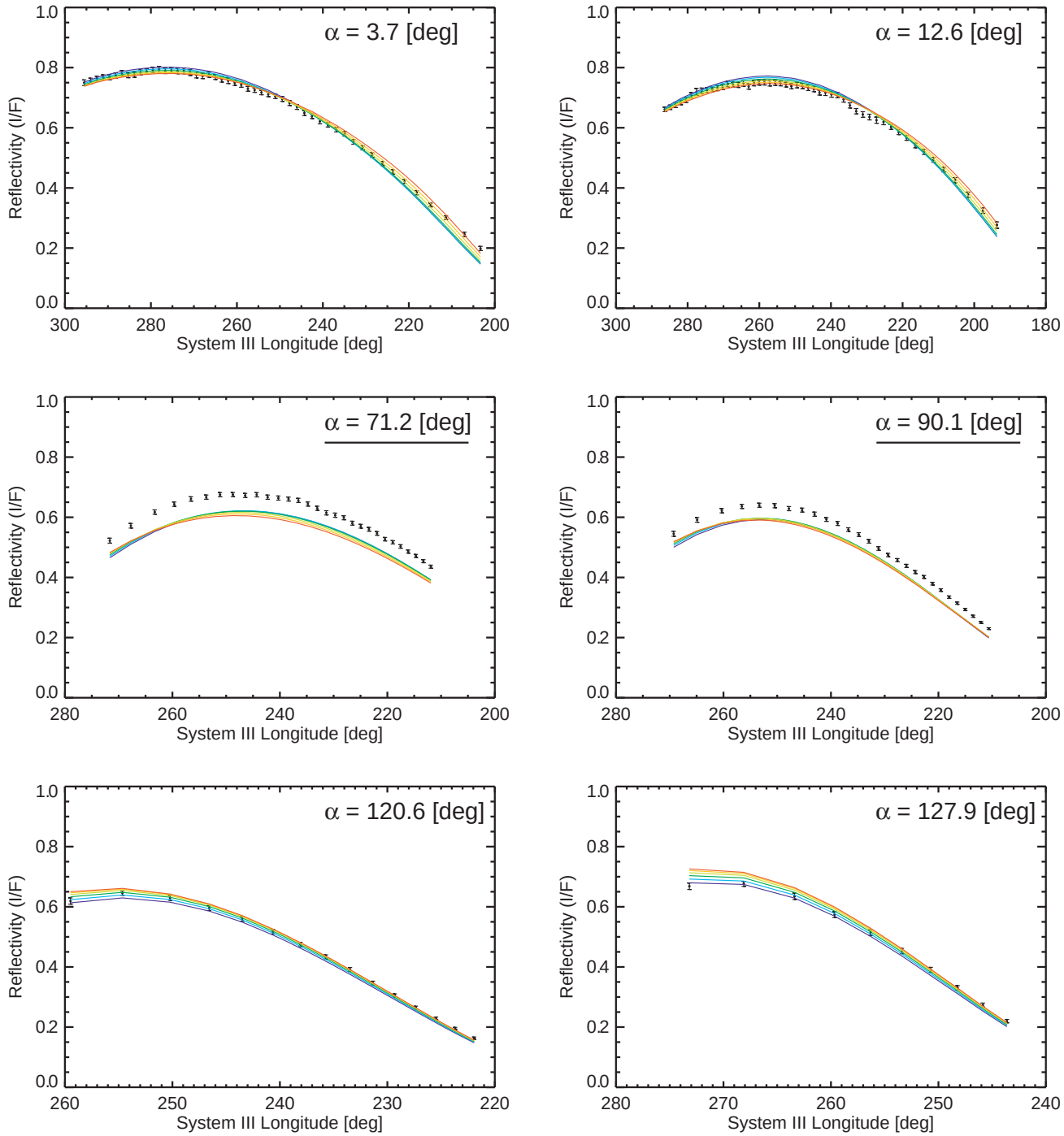

Figure 5.17. The best-fit models of the Type II-HG model (Case 2). In Case 2, we conduct the fitting process using the Cassini ISS limb-darkening curves at eight solar phase angles (3.7°, 12.6°, 18.8°, 107.7°, 120.6°, 127.9°, 136.3°, and 140.1°) which give similar coverage for solar phase angles as the Pioneer 10 IPP observations. The limb-darkening curves at the other solar phase angles with a single underline (53.6°, 71.2°, 90.1°, and 98.8°) are also calculated with the best-fit values of ω_{cloud} and τ_{haze}.

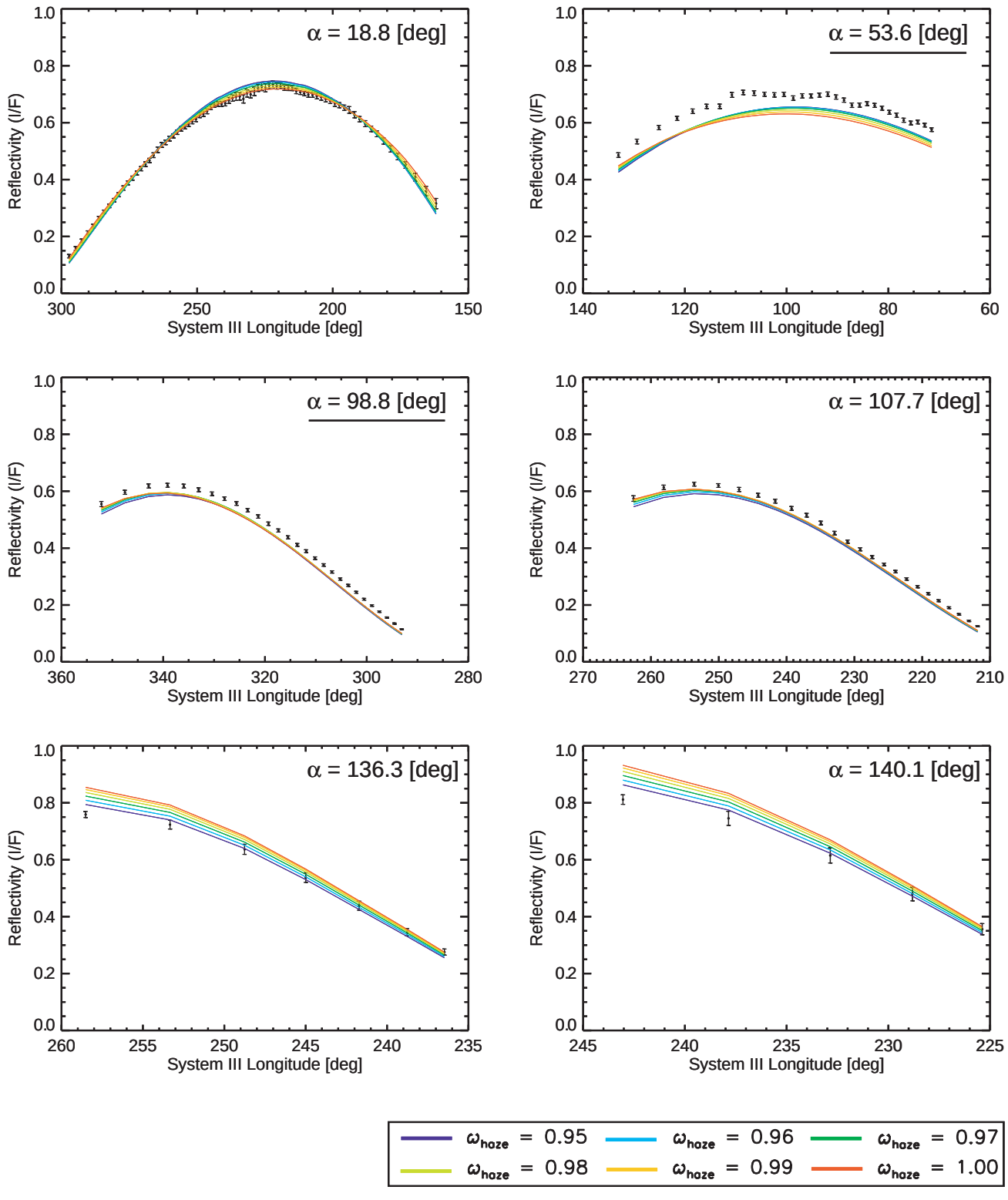

Figure 5.17–*Continued*

These results strongly suggest the following:

(1) In the overlapping solar phase angles (small solar phase angles: 3.7°–18.8° and large solar phase angles: 107.7°–140.1°), the characteristics of limb-darkening curves obtained by the Cassini ISS CB2 seem to be similar to those (small solar phase angles: 12°–34° and large solar phase angles: 109°–150°) obtained by the P10/IPP red-channel;

(2) Because of (1), the Pioneer HG function can roughly reproduce the Cassini ISS data at such solar phase angles; however,

(3) The Pioneer HG function is not compatible with the Cassini ISS data at intermediate solar phase angles (53.6°–98.8°).

Tomasko et al. (1978) claimed that their scattering phase functions were much better constrained compared to their preliminary analysis (Tomasko et al., 1974) with only the 34° and 109° subset of the P10/IPP data. However, based on the above examinations, we conclude that the lack of information between 34° and 109° has likely given the Pioneer HG functions an incompatible shape with the data at corresponding solar phase angles.

Chapter 6

Summary and conclusion

In order to derive the scattering properties of aerosols in the Jovian upper troposphere and stratosphere observationally, we have analyzed new and high-quality imaging data during the Cassini flyby of Jupiter (October 2000–March 2001) by utilizing its onboard Imaging Science Subsystem (ISS). The Cassini data, covering a wide range of solar phase angles (0°–140°), provide the first opportunity to improve observationally-based scattering phase functions for the Jovian aerosols since Tomasko et al. (1978) derived those from the Pioneer 10 Imaging Photopolarimeter (IPP) data.

In this thesis, we present the analysis results of four sets of limb-darkening curves extracted along a bright zone (the South Tropical Zone: STrZ) and a dark belt (the north component of the South Equatorial Belt: SEBn) from Jovian images in BL1 (effective wavelength: 455 nm) and CB2 (effective wavelength: 750 nm). The advantages of the Cassini data sets used in this study over the Pioneer 10 data sets are as follows:

- the Cassini data sets were taken at a constant gain setting for all solar phase angles, which is theoretically free from unwanted photometric inconsistency due to cross-calibration of the data acquired at different settings like the Pioneer 10 data;
- the transmission bandwidth of the Cassini ISS CB2 filter is so narrow that we can infer more monochromatic optical properties of aerosols, which is suitable for applying the Mie scattering theory, than the Pioneer 10 IPP red-channel (660 nm) data;
- the Cassini data sets have a better solar phase angle coverage with much smaller gap in solar phase angles (19°–54°) than the Pioneer 10 IPP's larger gap (34–109°), although the largest available solar phase angle of the Pioneer 10 data (150°) surpasses the Cassini data (140.1°) by 10 degrees.

To explain the solar phase angle behaviors of limb-darkening curves for each data set, we perform the radiative transfer calculations with a simple cloud model and the Mie scattering theory applied to scattering of aerosols (Type II-Mie model), and successfully derive the scattering properties of aerosols for all data sets. The major findings of this thesis are described as the answers to the major questions listed in **Section 1.4**.

(1) What optical and physical properties does the tropospheric haze have?

(Instead of the term "the tropospheric haze", we use the term "cloud" in **Chapter 3–5**.)

- The best-fit effective radius of cloud, $r_{\mathrm{eff,cloud}}$ is optimized at two different values, depending on the wavelength (not on the region): $r_{\mathrm{eff,cloud}}$ = 0.3 μm in CB2 and $r_{\mathrm{eff,cloud}}$ = 0.2 μm in BL1. These values are in good agreement with those inferred from previous studies (Sromovsky and Fry, 2010a, 2010b) for the diffuse and ubiquitous layer of small particles in the upper troposphere as described in the synthesis works by West et al. (1986, 2004).
- The best-fit values of the real part of the refractive index of cloud, $n_{\mathrm{r,cloud}}$ are 1.85 for all data sets except for the CB2/SEBn data set ($n_{\mathrm{r,cloud}}$ = 1.8). Such values of $n_{\mathrm{r,cloud}}$ are found to be significantly higher than experimental values of n_{r} for NH_3 ice particles (n_{r} ~ 1.4) measured by Martonchik et al. (1984). This strongly suggests that the primary constituent of the tropospheric haze would not be pure NH_3 ice. This suggestion does not conflict with lack of spectrally identifiable ammonia clouds (SIACs) (Baines et al., 2002) and source of the 3-μm absorption anomaly (Sromovsky and Fry, 2010a, 2010b) inferred from near-infrared spectra. What actually eliminates the spectral signature of NH_3 ice around the 3-μm wavelength, despite the fact that significant depletion of NH_3 vapor has been observed for pressure levels of visible cloud layer, is unclear at this moment. The high real refractive index obtained in this study may hint at the composition of cloud particles for further studies.

(2) What cause the visual difference between two distinctly-different bands: zones and belts?

- As described above, the scattering properties of cloud particles for both the STrZ and the SEBn are found to show much the same characteristics, which suggests that the cloud particles themselves are less likely to be related to the visual difference between the zones and belts.
- We find that only the single scattering albedo of cloud (ω_{cloud}) shows a remarkable difference between two regions (ω_{cloud} gets a higher value for the STrZ than that for the SEBn). Particles in cloud layer for the SEBn ($1-\omega_{\mathrm{cloud}}$ = 0.031) absorb about ten times as many photons as

those for the STrZ ($1-\omega_{\mathrm{cloud}}$ = 0.0035) in BL1, while particles for the SEBn ($1-\omega_{\mathrm{cloud}}$ = 0.0068) absorb twice as many photons as those for the STrZ ($1-\omega_{\mathrm{cloud}}$ = 0.0032) in CB2. We conclude that only ω_{cloud} is one key parameter which causes the visual difference between the zones and belts. Our results support the idea proposed by West et al. (1986). Such difference in absorption would be likely to be due to chromophores (unknown coloring agents) since all of condensate clouds predicted from thermochemical equilibrium theory and photochemically produced stratospheric haze are white at visible wavelengths.

- Our results do not rule out the opposite view proposed by Banfield et al. (1998) and Sromovsky and Fry (2002) who argued from their analyses that visual difference at near-infrared wavelengths was primarily due to the optical thickness variations of the tropospheric cloud.

Along with these major findings, although the optical and physical properties of the stratospheric haze are not well constrained, we find several key characteristics of the stratospheric haze.

- From the analysis of the CB2/STrZ data set, the large haze particles ($r_{\mathrm{eff,haze}}$ = 0.5 μm) are preferred to improve the model's fit either for the near-limb points in most solar phase angles or for higher reflectivity seen at the two largest solar phase angles. The deduced particle size is consistent with those inferred from previous studies (Tomasko et al., 1986; Rages et al., 1999). The need for strongly forward scattering (large) particles is also suggested by the Pioneer 10 IPP data at a high solar phase angle of 150° (Tomasko et al., 1978).
- The large value (≥0.04) of the imaginary part of the refractive index, $n_{\mathrm{i,haze}}$ is required to reproduce the BL1/STrZ data set well. This value is in good agreement with that (= 0.02 for 440 nm) adopted by West (1988) based on the study of Tomasko et al. (1986). This requirement becomes less important for fitting the CB2/STrZ data set.
- The characteristic common to all data sets is that the stratospheric haze is optically thin (τ_{haze} = 0.06 even at the optically thickest case for the CB2/STrZ data set). Our results are consistent with those inferred from previous studies (Smith, 1980; Simon-Miller et al., 2001). Conversely, we find that there are a considerable gap in the value of τ_{haze} between ours and those deduced from previous studies in which the Pioneer HG functions were used to reproduce the ground-based photometric data (e.g., Satoh and Kawabata, 1992, 1994; Kuehn and Beebe, 1993).

(3) Can new scattering phase functions for aerosols reproduce other photometric data?

- It is demonstrated that the best-fit Mie scattering phase functions obtained from all data sets can reproduce the Pioneer 10 observations well in spite of an interval of 27 years between the Pioneer 10 and the Cassini observations. These Mie scattering phase functions can be used at other wavelengths for determination of vertical cloud structure.
- We find that the limb-darkening curve at a solar phase angle of 150° is significantly sensitive to the properties of the stratospheric haze, yet we cannot accurately assess this data by a radiative transfer calculation based on the plane-parallel approximation.

(4) Can conventional scattering phase functions for aerosols also reproduce new Cassini imaging data?

- The Mie scattering phase functions for NH_3 ice particles (n_r ~ 1.4, much smaller than our best-fit value, 1.85) do not reproduce the Cassini observations in any of the assumed cloud model cases.
- Taking the CB2/STrZ data set as an example, we show that the Pioneer HG function does not reproduce the Cassini limb-darkening curves obtained at wide solar phase angles in spite of using the same model as Tomasko et al.'s (Type II-HG model). This is attributed to under-constraint of the Pioneer HG function, due to lack of information in the intermediate solar phase angle range (34°–109°).

As stated above, this thesis succeeds in providing new insights into the optical and physical properties of aerosols in the Jovian upper troposphere and stratosphere. By the contribution of this thesis, we now have a set of reliable baseline scattering phase functions that can be used to interpret the ever-changing appearance of Jovian clouds as changes of the vertical cloud structure and/or distribution of chromophores in the atmosphere. A part of this study is already submitted by Sato et al. (2011) for publication.

Chapter 7

Future Directions

The study conducted in this thesis has a potential to be further expanded and improved by using other data sets obtained by the Cassini ISS, along with those obtained by the ground-based telescopes and the HST and by developing more universal radiative transfer code. In this chapter, we briefly summarize the future directions of this study.

(1) Further analysis with the Cassini ISS data obtained by CH_4 band and UV filters

In this thesis, we succeeded in obtaining scattering properties of aerosols in the Jovian upper troposphere and stratosphere. We also clarified the primary cause of visual difference between two distinctly-different bands. In contrast, the optical and physical properties of the stratospheric haze were not well constrained even by the limb-darkening curves in BL1 and CB2 obtained at a wide variety of solar phase angles. In addition, we could not extract any information on the vertical distribution of aerosols from these data sets used in this thesis (this is, of course, because we chose such data sets to deduce the scattering properties without ambiguity due to the effect of other cloud model parameters). To obtain the above information, it is essential to analyze CH_4 band and UV images obtained by the Cassini ISS. During the Cassini flyby of Jupiter, the Cassini ISS took a set of Jovian images mainly with three CH_4 band filters (MT1, effective wavelength: 619 nm; MT2, 727 nm; and MT3, 889 nm) and a UV filter (UV1, 264 nm). It is worth noting that the Cassini ISS provided for the first time these images at a wide variety of solar phase angles with fine sampling interval. Since the strengths of absorption in three CH_4 band filters are greatly different from one another, the limb-darkening curves extracted from these images enable us to deduce the vertical aerosol distributions in the Jovian upper troposphere and stratosphere. In addition, because the sensing altitudes vary with solar phase angles at which images are obtained, the data set consisting of

three CH_4 band images taken from wide solar phase angles will constrain the cloud model more strictly than ever before. Furthermore, because of the opacity due to the Rayleigh scattering, the optical and physical properties of the stratospheric haze can be extracted from UV images. An analysis of solar phase angle behavior of limb-darkening curves should constrain the particle size and the complex refractive index of the particle in the stratosphere.

(2) Reanalysis of the published data obtained by ground-based telescopes and the Hubble Space Telescope

As remarked in **Section 5.1.4**, the optical thickness of the stratospheric haze deduced from previous studies in which the Pioneer HG functions were used to reproduce the ground-based photometric data, is approximately ten times as thick as those obtained from this study. In this thesis, we suggested that such discrepancy would be likely due to the difference in the amplitude of backward scattering between two different scattering phase functions. To make sure of this hypothesis, we need to analyze the published CH_4 band photometric data obtained by ground-based and Earth-orbit telescopes. It is suitable to use the data obtained by the HST because these data are, of course, unaffected by weather and do not contain the ambiguity due to different observational system and data reduction process. An analysis of the HST data with our Mie scattering phase functions will give us “true” spatial and temporal variations of vertical cloud structure in the Jovian atmosphere.

(3) Improvement of our radiative transfer code

Our radiative transfer code was developed based on the plane-parallel approximation. It means that we cannot use the data points to close to the limb or to the terminator for constraint of cloud model parameters. As mentioned before, the limb-darkening curve at a solar phase angle of 150º is significantly sensitive to the properties of the stratospheric haze. The further development of a radiative transfer code considering the atmospheric curvature effect will enable us to obtain more accurate information on the optical and physical properties of the stratospheric haze. Furthermore, there are several interesting research themes we cannot conduct with a radiative transfer code based on the plane-parallel approximation. For example, the UV and near-infrared limb images obtained by Venus Monitoring Camera (VMC) on board Venus Express have a wealth of information on vertical distribution of unknown UV absorber and aerosols. Especially, the accurate vertical distribution of unknown UV absorber and their latitudinal and longitudinal dependences will give us a clue to the

nature of such absorber.

(4) Application of our approach to other planets and Titan

As described in this thesis, the analysis of solar phase angle behavior of limb-darkening curves is one of the powerful tools in remote sensing for deducing the scattering properties of aerosols in the top-most layer. The same approach used in this thesis can also be directly applied to other planets and Titan that have atmosphere. As a first step, we will apply this approach to the Saturnian atmosphere because the Cassini ISS has recorded huge volumes of the Saturnian images since its Saturn orbit insertion (July 2004). Before now, Tomasko and Doose (1984) derived the scattering phase functions of aerosols in blue- and red-channels for a zone and a mid-latitude belt from the Pioneer 11 IPP data at solar phase angles in the range from 9º to 150º. Compared with Jovian photometric data obtained by the Pioneer 10 IPP, this data have relatively small gap in solar phase angle. It is expected that the above scattering phase functions for the Saturnian aerosols are more constrained compared with those for the Jovian aerosols (i.e., Pioneer HG functions). NH_3 ice is also believed to compose the visual cloud layer in the Saturnian atmosphere. What optical and physical properties does such cloud layer have, same as those of Jupiter or not? In addition, the remarkable color difference in visual cloud layer between Jupiter and Saturn should be caused by the difference of single scattering albedo of cloud. How is the wavelength dependence of such parameter different from each other? The detailed comparison of these parameters based on the data obtained by the same instrument will shed light on these questions.

Bibliography

Atreya, S.K., Wong, A.-S., 2005. Coupled clouds and chemistry of the giant planets – a case for multiprobes. Space Sci. Rev. 116, 121–136.

Atreya, S.K., Wong, M.H., Owen, T.C., Niemann, H.B., Mahaffy, P.R., 1997. Chemistry and clouds of the Jupiter's atmosphere: A Galileo perspective. In: Barbieri, C., Rahe, J.H., Johnson, T.V., Sohus, A.M. (Eds.), The Three Galileos: The Man, the Spacecraft, the Telescope, Kluwer Academic, Dordrecht, The Netherlands, pp. 249–260.

Atreya, S.K., Wong, M.H., Owen, T.C., Mahaffy, P.R., Niemann, H.B., de Pater, I., Drossart, P., Encrenaz, T., 1999. A comparison of the atmospheres of Jupiter and Saturn: deep atmospheric composition, cloud structure, vertical mixing, and origin. Planet. Space Sci. 47, 1243–1262.

Atreya, S.K., Wong, A.S., Baines, K.H., Wong, M.H., Owen, T.C., 2005. Jupiter's ammonia clouds – localized or ubiquitous? Planet. Space Sci. 53, 498–507.

Baines, K.H., Carlson, R.W., Kamp, L.W., 2002. Fresh ammonia ice clouds in Jupiter. I. Spectroscopic identification, spatial distribution, and dynamical implications. Icarus 159, 74–94.

Banfield, D., Gierasch, P.J., Bell, M., Ustinov, E., Ingersoll, A.P., Vasavada, A.R., West, R.A., Belton, M.J.S., 1998. Jupiter's cloud structure from Galileo imaging data. Icarus 135, 230–250.

Bohren, C.F., Huffman, D.R., 1998. Absorption and Scattering of Light by Small Particles. Wiley, New York, 544pp.

Brooke, T.Y., Knacke, R.F., Encrenaz, T., Drossart, P., Crisp, D., Feuchtgruber, H., 1998. Models of the ISO 3-μm reflection spectrum of Jupiter. Icarus 136, 1–13.

Burton, M.E., Buratti, B., Matson, D.L., Lebreton, J.-P., 2001. The Cassin/Huygens Venus and Earth flybys: An overview of operations and results. J. Geophys. Res. 106, 30,099–30,107.

Chandrasekhar, S., 1960. Radiative transfer. Dover, New York, 393pp.

Chanover, N.J., Kuehn, D.M., Beebe, R.F., 1997. Vertical structure of Jupiter's atmosphere at the Galileo probe entry latitude. Icarus 128, 294–305.

Conrath, B.J., Flasar, F.M., Pirraglia, J.A., Gierasch, P.J., Hunt, G.E., 1981. Thermal structure and dynamics of the Jovian atmosphere. II – Visible cloud features. J. Geophys. Res. 86, 8769–8775.

Conrath, B.J., Gierasch, P.J., Ustinov, E.A., 1998. Thermal structure and para hydrogen fraction on the outer planets from Voyager IRIS measurements. Icarus 135, 501–517.

de Pater, I., Massie, S.T., 1985. Models of the millimeter-centimeter spectra of the giant planets. Icarus 62, 143–171.

de Pater, I., Lissauer, J. J., 2010. Planetary Sciences Second Edition, Cambridge University Press, Cambridge, 674pp.

Doose, L.R., Tomasko, M.G., Castillo, N.D., 1986. The single scattering phase function of Jupiter's clouds, in Jovian Atmospheres, pp. 83–93.

Dyudina, U.A., Del Genio, A. D., Ingersoll, A.P., Porco, C.C., West, R.A., Vasavada, A.R., Barbara, J.M., 2004. Lightning on Jupiter observed in the H_α line by the Cassini imaging science subsystem. Icarus 172, 24–36.

Flasar, F.M., Conrath, B.J., Pirraglia, J., Clark, P.C., French, R.G., Gierasch, P.J., 1981. Thermal structure and dynamics of the Jovian atmosphere. I – The Great Red Spot. J. Geophys. Res. 86, 8759–8767.

Folkner, W.M., Woo, R., Nandi, S., 1998. Ammonia abundance in Jupiter's atmosphere derived from the attenuation of the Galileo probe's radio signal. J. Geophys. Res. 103, 22,847–22,856.

Fouchet, T., Lellouch, E., Bézard, B., Encrenaz, T., Drossart, P., Feuchtgruber, H., de Graauw, T., 2000. ISO-SWS observations of Jupiter: Measurement of the ammonia tropospheric profile and of the $^{15}N/^{14}N$ isotopic ratio. Icarus 143, 223–243.

Gierasch, P.J., Conrath, B.J., Magalhaes, J. A., 1986. Zonal mean properties of Jupiter's upper troposphere from Voyager infrared observations. Icarus 67, 456–483.

Gierasch, P.J., Ingersoll, A.P., Banfield, D., Ewald, S.P., Helfenstein, P., Simon-Miller, A., Vasavada, A., Breneman, H.H., Senske, D.A., the Galileo Imaging Team, 2000. Observation of moist convection in Jupiter's atmosphere. Nature 403, 628–630.

Goody, R.M., Yung, Y.L., 1989. Atmospheric Radiation: Theoretical Basis. Oxford University Press, Oxford, 519pp.

Hansen, J.E., Travis, L.D., 1974. Light scattering in planetary atmospheres. Space Sci. Rev. 16, 527–610.

Herman, B.M., Ben-David, A., Thome, K.J., 1994. Numerical technique for solving the radiative transfer equation for a spherical shell atmosphere. Appl. Opt. 33, 1760–1770.

Ingersoll, A.P., Dowling, T.E., Gierasch, P.J., Orton, G.S., Read, P.L., Sánchez-Lavega, A., Showman, A.P., Simon-Miller, A.A., Vasavada, A.R., 2004. Dynamics of Jupiter's atmosphere. In: Bagenal,

F., Dowling, T.E., McKinnon, W.B. (Eds.), Jupiter: The Planet, Satellites and Magnetosphere. Cambridge University Press, Cambridge, pp. 105–128.

Irwin, P.G.J., 1999. Cloud structure and composition of Jupiter's atmosphere. Surveys in Geophysics 20, 505–535.

Irwin, P.G.J., Weir, A.L., Smith, S.E., Taylor, F.W., Lambert, A.L., Calcutt, S.B., Cameron-Smith, P.J., Carlson, R.W., Baines, K., Orton, G.S., Drossart, P., Encrenaz, T., Roos-Serote, M., 1998. Cloud structure and atmospheric composition of Jupiter retrieved from Galileo near-infrared mapping spectrometer real-time spectra. J. Geophys. Res. 103, 23,001–23,022.

Irwin, P.G.J., Weir, A.L., Talor, F.W., Calcutt, S.B., Carlson, R.W., 2001. The origin of belt/zone contrast in the atmosphere of Jupiter and their correlation with 5-μm opacity. Icarus 149, 397–415.

Kalogerakis, K.S., Marschall, J., Oza, A.U., Engel, P.A., Meharchand, R.T., Wong, M.H., 2008. The coating hypothesis for ammonia ice particles in Jupiter: Laboratory experiments and optical modeling. Icarus 196, 202–215.

Karkoschka, E., 1998. Methane, ammonia, and temperature measurements of the jovian planets and Titan from CCD-spectrophotometry. Icarus 133, 134–146.

Kuehn, D.M., Beebe, R.F., 1993. A study of the time variability of Jupiter's atmospheric structure. Icarus 101, 282–292.

Lewis, J.S., 1969. The clouds of Jupiter and the NH_3-H_2O and NH_3-H_2S systems. Icarus 10, 365–378.

Limaye, S.S., 1986. Jupiter: New estimates of the mean zonal flow at the cloud level. Icarus 65, 335–352.

Lindal, G.F., Wood, G.E., Levy, G.S., Anderson, J.D., Sweetnam, D.N., Hotz, H.B., Buckles, B.J., Holmes, D.P., Doms, P.E., Eshleman, V.R., Tyler, G.L., Croft, T.A., 1981. The atmosphere of Jupiter: An analysis of the Voyager radio occultation measurements. J. Geophys. Res. 86, 8721–8727.

Liou, K.N., 1980. An Introduction to Atmospheric Radiation. Academic Press, New York, 404pp.

Liou, K.N., 2002. An Introduction to Atmospheric Radiation Second Edition. Academic Press, New York, 583pp.

Little, B., Anger, C.D., Ingersoll, A.P., Vasavada, A.R., Senske, D.A., Breneman, H.H., Borucki, W., the Galileo SSI Team, 1999. Galileo images of lightning on Jupiter. Icarus 142, 306–323.

Martonchik, J.V., Orton, G.S., Appleby, J.F., 1984. Optical properties of NH_3 ice from the far infrared to the near ultraviolet. Appl. Opt. 23, 541–547.

Matson, D.L., Spilker, L.J., Lebreton, J.-P., 2002. The Cassini/Huygens mission to the Saturnian system. Space Sci. Rev. 104, 1–58.

Pellicori, S.F., Russell, E.E., Watts, L.A., 1973. Pioneer imaging photopolarimeter optical system. Appl. Opt. 12, 1246–1258.

Pope, S.K., Tomasko, M.G., Williams, M.S., Perry, M.L., Doose, L.R., Smith, P.H., 1992. Cloud of ammonia ice – Laboratory measurements of the single-scattering properties. Icarus 100, 203–220.

Porco, C.C., West, R.A., McEwen, A., Del Genio, A.D., Ingersoll, A.P., Thomas, P., Squyres, S., Dones, L., Murray, C.D., Johnson, T.V., Veverka, J., Barbara, J.M., Denk, T., Evans, M., Ferrier, J.J., Geissler, P., Helfenstein, P., Roatsch, T., Throop, H., Tiscareno, M., Vasavada, A.R., 2003. Cassini imaging of Jupiter's atmosphere, satellites, and rings. Science 299, 1541–1547.

Porco, C.C., West, R.A., Squyres, S., McEwen, A., Thomas, P., Murray, C.D., Del Genio, A., Ingersoll, A.P., Johnson, T.V., Neukum, G., Veverka, J., Dones, L., Brahic, A., Burns, J.A., Haemmerle, V., Knowles, B., Dawson, D., Roatsch, T., Beurle, K., Owen, W., 2004. Cassini imaging science: Instrument characteristics and anticipated scientific investigations at Saturn. Space Sci. Rev. 115, 363–497.

Ragent, B., Colburn, D.S., Rages, K.A., Knight, T.C.D., Avrin, P., Orton, G.S., Yanamandra-Fisher, P.A., Grams, G.W., 1998. The clouds of Jupiter: Results of the Galileo Jupiter mission probe nephelometer experiment. J. Geophys. Res. 103, 22,891–22,909.

Rages, K., Beebe, R., Senske, D., 1999. Jovian stratospheric hazes: The high phase angle view from Galileo. Icarus 139, 211–226.

Rossow, W.B., 1978. Cloud microphysics – Analysis of the clouds of Earth, Venus, Mars, and Jupiter. Icarus 36, 1–50.

Sato, T.M., Satoh, T., Kasaba, Y., 2011. Retrieval of Jovian cloud structure from the Cassini ISS limb-darkening data. I. Continuum scattering phase functions for cloud and haze in the South Tropical Zone. Submitted to Icarus.

Satoh, T., Kawabata, K., 1992. Methane band photometry of the faded South Equatorial Belt of Jupiter. Astrophys. J. 384, 298–304.

Satoh, T., Kawabata, K., 1994. A change of upper cloud structure in Jupiter's South Equatorial Belt during the 1989–1990 event. J. Geophys. Res. 99, 8425–8440.

Seiff, A., Kirk, D.B., Knight, T.C.D., Young, R.E., Mihalov, J.D., Young, L.A., Milos, F.S., Schubert, G., Blanchard, R.C., Atkinson, D., 1998. Thermal structure of Jupiter's atmosphere near the edge of a 5-μm hot spot in the north equatorial belt. J. Geophys. Res. 103, 22,857–22,889.

Simon-Miller, A.A., Banfield, D., Gierasch, P.J., 2001. Color and the vertical structure in Jupiter's belts, zones, and weather systems. Icarus 154, 459–474.

Smith, D.W., 1980. Galilean satellite eclipse studies. II – Jovian stratospheric and tropospheric aerosol content. Icarus 44, 116–133.

Smith, P.H., 1986. The vertical structure of the Jovian atmosphere. Icarus 65, 264–279.

Smith, P.H., Tomasko, M.G., 1984. Photometry and polarimetry of Jupiter at large phase angles. II – Polarimetry of the south tropical zone, south equatorial belt, and the polar regions from the Pioneer 10 and 11 missions. Icarus 58, 35–73.

Sromovsky, L.A., Fry, P.M., 2002. Jupiter's cloud structure as constrained by Galileo probe and HST observations. Icarus 157, 373–400.

Sromovsky, L.A., Fry, P.M., 2010a. The source of 3-μm absorption in Jupiter's clouds: Reanalysis of ISO observations using new NH_3 absorption models. Icarus 210, 211–229.

Sromovsky, L.A., Fry, P.M., 2010b. The source of widespread 3-μm absorption in Jupiter's clouds: Constraints from 2000 Cassini VIMS observations. Icarus 210, 230–257.

Sromovsky, L.A., Collard, A.D., Fry, P.M., Orton, G.S., Lemmon, M.T., Tomasko, M.G., Freedman, R.S., 1998. Galileo probe measurements of thermal and solar radiation fluxes in the Jovian atmosphere. J. Geophys. Res. 103, 22,929–22,978.

Stokes, G.G., 1862. On the intensity of the light reflected from of transmitted through a pile of plates. Proc. Roy. Soc. London 11, 545–556.

Taylor, F.W., Atreya, S.K., Encrenaz, T., Hunten D.M., Irwin, P.G.J, Owen, T.C., 2004. The composition of the atmosphere of Jupiter. In: Bagenal, F., Dowling, T.E., McKinnon, W.B. (Eds.), Jupiter: The Planet, Satellites and Magnetosphere. Cambridge University Press, Cambridge, pp. 59–78.

Temma, T., 2005. Vertical structure modeling of Saturn with high spectral resolution imaging. Ph. D. thesis, New Mexico State University, Las Cruces, 268pp.

Tomasko, M.G., Doose, L.R., 1984. Polarimetry and photometry of Saturn from Pioneer 11: Observations and constraints on the distribution and properties of cloud and aerosol particles. Icarus 58, 1–34.

Tomasko, M.G., Clements, A.E., Castillo, N.D., 1974. Limb darkening of two latitudes of Jupiter at phase angles of 34° and 109°. J. Geophys. Res. 79, 3653–3660.

Tomasko, M.G., West, R.A., Castillo, N.D., 1978. Photometry and polarimetry of Jupiter at large phase angles. I – Analysis of imaging data of a prominent belt and a zone from Pioneer 10. Icarus 33, 558–592.

Tomasko, M.G., Karkoschka, E., Martinek, S., 1986. Observations of the limb darkening of Jupiter at ultraviolet wavelengths and constraints on the properties and distribution of stratospheric aerosols. Icarus 65, 218–243.

van de Hulst, H. C., 1963. A New Look at Multiple Scattering. Tech. Rep., Goddard Institute for Space Studies, NASA, New York, 81pp.

van de Hulst, H. C., 1980. Multiple light scattering: Tables, Formulas, and Applications, Vols. 1 and 2. Academic Press, New York.

Vasavada, A.R., Showman, A.P., 2005. Jovian atmospheric dynamics: an update after Galileo and Cassini. Rep. Prog. Phys. 68, 1935–1996.

Weast, R.C., Lide, D.R., Astle,M.J., Beyer, W.H., 1990. CRC Handbook of Chemistry and Physics, 70th Edition. Boca Raton: CRC Press, Inc.

Weidenschilling, S.J., Lewis, J.S., 1973. Atmospheric and cloud structures of the jovian planets. Icarus 20, 465–476.

West, R.A., 1979. Spatially resolved methane band photometry of Jupiter. II. Analysis of the South Equatorial Belt and South Tropical Zone reflectivity. Icarus 38, 34–53.

West, R.A., 1988. Voyager 2 imaging eclipse observations of the Jovian high altitude haze. Icarus 75, 381–398.

West, R.A., Tomasko, M.G., 1980. Spatially resolved methane band photometry of Jupiter. III. Cloud vertical structures for several axisymmetric bands and the Great Red Spot. Icarus 41, 278–292.

West, R.A., Strobel, D.F., Tomasko, M.G., 1986. Clouds, aerosols, and photochemistry in the Jovian atmosphere. Icarus 65, 161–217.

West, R.A., Baines, K.H., Friedson, A.J., Banfield, D., Ragent, B., Taylor, F.W., 2004. Jovian clouds and haze. In: Bagenal, F., Dowling, T.E., McKinnon, W.B. (Eds.), Jupiter: The Planet, Satellites and Magnetosphere. Cambridge University Press, Cambridge, pp. 79–104.

West, R.A., Knowles, B., Birath, E., Charnoz, S., Nino, D.D., Hedman, M., Helfenstein, P., McEwen, A., Perry, J., Porco, C., Salmon, J., Throop, H., Wilson, D., 2010. In-flight calibration of the Cassini imaging science sub-system cameras. Planet. Space Sci. 58, 1475–1488.

Wong, A.-S., Yung, Y.L., Friedson, A.J., 2003. Benzene and haze formation in the polar atmosphere of Jupiter. Geophys. Res. Lett. 30(8), 1447.

Wong, M.H., Bjoraker, G.L., Smith, M.D., Flasar, F.M., Nixon, C.A., 2004. Identification of the 10-μm ammonia ice feature on Jupiter. Planet. Space Sci. 52, 385–395.

Young, R.E., 1998. The Galileo probe mission to Jupiter: Science overview. J. Geophys. Res. 103, 22,775–22,790.